

## ABSTRACT

Title of Dissertation: **PHASE TRANSITIONS AFFECTED BY  
MOLECULAR INTERCONVERSION**

**Thomas Joseph Longo**  
Doctor of Philosophy, 2023

Dissertation Directed by: **Professor Mikhail A. Anisimov**  
Institute for Physical Science and Technology &  
Department of Chemical and Biomolecular Engineering

Typically, pure substances may be found with only one gaseous or liquid state, while their solid state may exist in various polymorphic states. The existence of two distinct liquid forms in a single component substance is more unusual since liquids lack the long-range order common to crystals. Yet, the existence of multiple amorphous states in a single component substance, a phenomenon known as “liquid polyamorphism,” has been observed or predicted in a wide variety of substances. In contrast to standard phase transitions, it has been suggested that polyamorphic liquid-liquid transitions are caused by the interconversion of molecular or supramolecular states. To investigate this phenomenon, a nonequilibrium thermodynamic model was developed to quantitatively describe the interplay between the dynamics of molecular interconversion and fluid-phase separation. The theory has been compared to a variety of interconverting systems,

and has demonstrated a quantitative agreement with the results of Monte Carlo and Molecular Dynamics simulations.

In this thesis, it is shown that there are two major effects of molecular interconversion on the thermodynamics and the kinetics of fluid-phase separation: if the system evolves to an equilibrium state, then the growth of one of the alternative phases may result in the destruction of phase coexistence - a phenomenon referred to as “phase amplification.” It is demonstrated that depending on the experimental or simulation conditions, either phase separation or phase amplification would be observed. Previous studies of polyamorphic substances report conflicting observations of phase formation, which may be explained by the possibility of phase amplification occurring. Alternatively, if the system evolves to a nonequilibrium steady state, the phase domain growth could be restricted at a mesoscopic length scale. This phenomenon (referred to as “microphase separation”) is one of the simplest examples of steady-state dissipative structures, and may be applicable to active matter systems, hydrodynamic instabilities, and bifurcations in chemical reactions, in which the nonequilibrium conditions could be imposed by an external flux of matter or energy.

PHASE TRANSITIONS AFFECTED BY  
MOLECULAR INTERCONVERSION

by

Thomas J. Longo

Dissertation submitted to the Faculty of the Graduate School of the  
University of Maryland, College Park in partial fulfillment  
of the requirements for the degree of  
Doctor of Philosophy  
2023

Advisory Committee:

Professor Mikhail Anisimov, Chair  
Professor Christopher Jarzynski  
Professor Jeffery Klauda  
Professor Pratyush Tiwary  
Professor John Weeks

© Copyright by  
Thomas J. Longo  
2023

## Preface

This thesis consists of results from my original research performed in collaboration with my co-authors. The contents of this thesis have been adopted with permission from our publications, of which I am either the first or second author. The investigation of the fluid-fluid phase transition in high-pressure hydrogen (Section 2.2), high-density sulfur (Section 2.3), and fluids exhibiting water-like anomalies (Section 2.4) was conducted in Refs. [1–3], respectively. The phenomenological theory that describes the dynamics of phase transitions affected by molecular interconversion (Chapter 3) was developed in Refs. [4, 5]. This theory was verified via Monte Carlo (MC) and molecular dynamics (MD) simulations of three physically distinct microscopic models of mixtures with species interconversion (Chapter 4), which were investigated in Refs. [6–8].

Throughout my Ph.D. project, I developed the theory, participated in the computer simulations of the microscopic models, performed the data analysis, made the figures (except Figs. 4.10–4.13, which were created by Betül Uralcan), and was a major contributor to the text of the published manuscripts. I would like to ascribe appropriate credit to my research advisor, who conceived the project and supervised the research, and to our collaborators, whose contribution was crucial for the success of the project.

The two-state thermodynamic approach (Section 2.1) was originally developed by my advisor, Mikhail Anisimov, and his co-workers [9]. The equation-of-state of high-pressure hydrogen (Section 2.2) was developed in collaboration with Nathaniel Fried [1]. The maximum-valence

model (Section 2.3), the HL model (Section 4.1), and the HCS model (Section 4.3) were developed and simulated by Sergey Buldyrev and Nikolay Shumovskyi [2, 5, 6, 8]. The blinking-checkers lattice model (Section 2.4) was originally developed by Frédéric Caupin and Mikhail Anisimov [10]; I described the interfacial properties of this model [3]. My major contribution to the research project was the generalization of the Cahn-Hilliard theory of spinodal decomposition and the development of the generalized Cook-Binder theory of the time-evolution of the structure factor in fluids with interconversion of species (Chapter 3) [4, 5, 8]. Numerical calculations of the time evolution of the order parameter and structure factor (Section 3.3) were performed in collaboration with Salim Asadov, Nikolay Shumovskyi, and Sergey Buldyrev [5]. The simulations of the CM model (Section 4.2) were performed by Betül Uralcan, Frank H. Stillinger, and Pablo Debenedetti [7, 8].

Thomas J. Longo

April 15, 2023

## Acknowledgments

I would like to express my sincere gratitude to my research advisor, Professor Mikhail Anisimov. His constant tutelage, endless support (often working, literally, every day with me), and insightful suggestions not only benefited the success of this project, but also enabled me to grow as a researcher.

I am grateful for the collaborators that I had the privilege to work closely with, namely: Salim Asadov (University of Maryland, College Park and Azerbaijan National Academy of Sciences), Sergey Buldyrev (Boston University and Yeshiva University), Frédéric Caupin (Université Claude Bernard Lyon 1 and Institut Universitaire de France), Pablo Debenedetti (Princeton University), Nathaniel Fried (University of Maryland, College Park), Nikolay Shumovskyi (Boston University), and Betül Uralcan (Princeton University and Bogazici University). This endeavor would not be possible without their contributions.

I am also thankful to the Chemical Physics Program at the Institute for Physical Science and Technology as well as the Department of Chemical and Biomolecular Engineering for the continuous encouragements and financial support during my time at the University of Maryland, College Park.

This dissertation is a product of the research collaboration between the University of Maryland (the Lead institution), Princeton University, Boston University, and Arizona State University, supported by the National Science Foundation (NSF). I acknowledge the financial support of the

NSF (award No. CHE-1856479) as well as the partial support of the Chateaubriand Fellowship of the Office for Science & Technology of the Embassy of France in the United States.

I would be remiss if I did not mention my family, in particular, my parents, my siblings, and my fiancé. Thank you all for your endless support and encouragements throughout my studies.

# Table of Contents

<b>Preface</b>	<b>ii</b>
<b>Acknowledgements</b>	<b>iv</b>
<b>Table of Contents</b>	<b>vi</b>
<b>List of Tables</b>	<b>viii</b>
<b>List of Figures</b>	<b>ix</b>
<b>List of Abbreviations</b>	<b>xxiv</b>
<b>Chapter 1: Introduction</b>	<b>1</b>
<b>Chapter 2: Two-State Thermodynamics of Fluid Polyamorphism</b>	<b>8</b>
2.1 Interconversion of Two States . . . . .	8
2.2 Fluid-Fluid Phase Transition in High-Pressure Hydrogen . . . . .	13
2.2.1 Phase Behavior of Hydrogen . . . . .	13
2.2.2 Phase Separation Coupled with Dimerization . . . . .	15
2.3 Liquid-Liquid Phase Transition in High-Density Sulfur . . . . .	23
2.3.1 Maximum-Valence Model . . . . .	25
2.3.2 Phase Separation Coupled with Polymerization . . . . .	28
2.4 Liquid-Liquid Phase Transition in Fluids Exhibiting Water-Like Anomalies . . . . .	32
2.4.1 Blinking-Checkers Lattice Model . . . . .	33
2.4.2 Virtual Critical Line in Interconverting Mixtures . . . . .	37
2.4.3 Anomalies of Interfacial Properties . . . . .	42
2.5 Conclusion of Chapter 2 . . . . .	62
<b>Chapter 3: Phase Formation Affected by Species Interconversion</b>	<b>63</b>
3.1 Generalizing Cahn-Hilliard Theory . . . . .	63
3.1.1 Conserved and Nonconserved Order-Parameter Dynamics . . . . .	64
3.1.2 Phase Amplification vs. Microphase Separation . . . . .	73
3.2 Temporal Evolution of the Structure Factor . . . . .	78
3.2.1 Generalized Cook-Binder Theory . . . . .	78
3.2.2 Characteristic Length Scales . . . . .	81
3.3 Temporal Evolution of the Order Parameter . . . . .	85
3.4 Effects of Heat and Volume Change of Interconversion . . . . .	89

3.5	Effects of Critical Order-Parameter Fluctuations . . . . .	93
3.6	Conclusion of Chapter 3 . . . . .	97
<b>Chapter 4:</b>	<b>Application of Theory to Microscopic Models</b>	<b>99</b>
4.1	Hybrid Ising / Binary Lattice (HL Model) . . . . .	99
4.1.1	HL Model Description . . . . .	101
4.1.2	Phase Amplification in the HL Model . . . . .	103
4.1.3	Nonequilibrium Spatially-Modulated Stripes . . . . .	115
4.2	Chiral-Mixture of Interconverting Enantiomers (CM Model) . . . . .	122
4.2.1	CM Model Description . . . . .	123
4.2.2	Phase Amplification in the CM Model . . . . .	127
4.2.3	Formation of Dissipative Structures . . . . .	130
4.2.4	Characteristic Time Scales in the CM Model . . . . .	137
4.2.5	Finite-Size Restrictions in the CM Model . . . . .	139
4.3	Coarse-Grained Hard-Core-Shoulder Model (HCS Model) . . . . .	144
4.3.1	HCS Model Description . . . . .	144
4.3.2	Nonequilibrium Bicontinuous Microemulsions . . . . .	147
4.4	Sources of Microphase Separation . . . . .	150
4.4.1	Comparison of the Microscopic Models . . . . .	150
4.4.2	Onset and Termination of Microphase Separation . . . . .	152
4.5	Conclusion of Chapter 4 . . . . .	156
<b>Chapter 5:</b>	<b>Overall Conclusion</b>	<b>158</b>
<b>Appendix A:</b>	<b>Comparison of Exact Solution with Phenomenological Ansatzes</b>	<b>160</b>
<b>Bibliography</b>		<b>165</b>

## List of Tables

2.1	The suggested locations of the FFCP and the SFF-TP in hydrogen. . . . .	15
2.2	Liquid-vapor critical points of interconverting systems, referred to as “actual” critical points, for the seven systems considered in this section (with $\varepsilon_{AA} = 1.6$ , $\varepsilon_{BB} = 2.0$ , $\hat{e} = 3$ , and $\hat{s} = 4$ ). . . . .	39
2.3	Liquid-liquid critical points (LLCP) for the three systems exhibiting liquid polyamorphism and a LLCP (with $\varepsilon_{AA} = 1.6$ , $\varepsilon_{BB} = 2.0$ , $\hat{e} = 3$ , and $\hat{s} = 4$ ). . . . .	40
2.4	Asymptotic amplitudes of the liquid-liquid interfacial tension and liquid-liquid correlation length of concentration fluctuations for the three systems exhibiting liquid polyamorphism and a liquid-liquid critical point. The asymptotic mean-field behavior is illustrated in Fig. 2.21. . . . .	58
2.5	The surface tension $\sigma$ , normalized interfacial thickness $\hat{\zeta} = \zeta/\ell$ , and normalized shift $\hat{\delta} = \delta/\ell$ for the three coexisting phases (liquid A, liquid B, and vapor) for the system with $\varepsilon_{BA} = 1.00$ at the triple point temperature ( $T = 0.6843$ ). . . . .	58
3.1	Limiting cases of the interplay between diffusion, natural interconversion, and forced interconversion. . . . .	74
3.2	Conditions for phase amplification and microphase separation as illustrated in Fig. 3.1. The left column corresponds to the solid lines and the right column corresponds to the dashed lines. . . . .	75
4.1	Fit parameters of the theoretical prediction in Fig. 4.8a (top, $p_r = 1/32$ ) and Fig. 4.8b (bottom, $p_r = 1/256$ ) of the inverse steady-state domain size, $q_-$ . . . . .	118
4.2	Parameters for the CM model in real and reduced units . . . . .	124
4.3	Fit parameters used for the theoretical predictions in Fig. 4.14a of the inverse steady-state domain size, $q_-$ . The mobility is given by the Stokes-Einstein relation with amplitude $b_0$ and characteristic temperature $T_0 = 1.2$ . Two additional parameters, the amplitude, $A$ , and the characteristic size of the inhomogeneities ( $q_0 \sim 1/R_0$ ) are included. . . . .	134
4.4	Fit parameters used for the theoretical prediction illustrated in Fig. 4.25a for the HL model, with $p_r = 1/128$ . . . . .	155
A.1	The degree of asymmetry for each profile of the system with $\varepsilon_{BA} = 1.04$ at $T = 0.6943$ , determined from the symmetric ansatz (sym), the Fisher-Wortis ansatz (FW), or the exact solution as calculated from Eq. (A.3). . . . .	163

## List of Figures

- 1.1 Hypothesized global pressure-temperature phase diagram for water. The black curves indicate the solid-solid and solid-liquid-gas phase transitions experimentally reported for water [11], while the blue curve indicates the hypothesized liquid-liquid phase transition. The dotted black curve represents the line of spontaneous ice nucleation [12]. The red circle is the liquid-vapor critical point (LVCP) and the red star is the hypothesized liquid-liquid critical point (LLCP) around 220 K and 60 MPa as suggested in Ref. [13]. . . . . 2
- 2.1 A symmetric binary mixture is quenched along the critical molecular fraction (where the order parameter is  $\varphi = 0$ ) from a point,  $\hat{T}_1$  in the one phase region to a point,  $\hat{T}_2$  below the critical temperature of demixing in the unstable region. The solid curve indicates the liquid-liquid coexistence (binodal), while the dashed curve indicates the limit of stability (spinodal). . . . . 9
- 2.2 The global pressure-temperature phase diagram for hydrogen. (a) The full range from low to extreme pressures in logarithmic scale. The crosses indicate the experimental data for the solid-liquid melting transition presented in Diatschenko *et al.* [14] (blue), Datchi *et al.* [15] (cyan), Gregoryanz *et al.* [16] (pink), and Zha *et al.* [17] (purple). The solid black curves at low pressure ( $P \leq 0.1$  GPa) are the liquid-gas-solid phase transitions [18], while the solid black curve at high pressure ( $P > 0.1$  GPa) is the Kechin equation [19] as reported in ref. [17]. The black dashed curve is the predicted continuation of the melting line based on experimental and computational evidence [17, 20, 21], while the dotted lines represent the highly-debated prediction [22–28] of the domain of solid metallic hydrogen [22, 23, 28–33]. The red line is the first-order fluid-fluid phase transition adopted in this section. (b) The phase diagram of hydrogen at extreme conditions, in the area of the box in (a). The open circles are experimental data presented in Zaghoo *et al.* [34–36] (dark brown), McWilliams *et al.* [37] (light brown), and Ohta *et al.* [38] (orange). Simulation results [21, 39–46] are spread within the grey area and shown in detail in Fig. 2.3. The fluid-fluid phase transition (solid red) and Widom line (dotted red) are represented by Eq. (2.18). The red star is the location of the fluid-fluid critical point (FFCP) as adopted in this section. . . . 14

2.3	<p>Unifying the different simulation results with experimental data of hydrogen by the generalized law of corresponding states. (a) Experimental and simulation results for the fluid-fluid phase transition (FFPT). (b) Unified representation of the FFPT by reducing pressure, <math>\hat{P} = P/P_c</math>, temperature, <math>\hat{T} = T/T_c</math>, and the critical value of the entropy, <math>\hat{S} = S/S_c</math>. In (a) and (b), the open circles are the experimental data of Zaghoo <i>et al.</i> [34–36] (dark brown), McWilliams <i>et al.</i> [37] (light brown), and Ohta <i>et al.</i> [38] (orange). The computational results are indicated by the triangles: blue tints correspond to the Density Functional Theory (DFT) simulations of Bonev <i>et al.</i> [47] (dark blue), Morales <i>et al.</i> [48] (blue), Hinz <i>et al.</i> [44] (sky blue), and Karasiev <i>et al.</i> [45] (light blue). Meanwhile, green tints correspond to the Quantum Monte Carlo (QMC) simulations of Morales <i>et al.</i> [48] (dark sea green), Lorenzen <i>et al.</i> [39] (green), Perlioni <i>et al.</i> [41] (dark green), Mozzola <i>et al.</i> [42] (lime green), and Tirelli <i>et al.</i> [46] (yellow green). The colored stars correspond to the reported (or adopted in this section) critical points for each data set. The solid black curve is the solid-fluid phase transition line as discussed in Fig. 2.2, and the red solid line is the FFPT predicted in this section. . . . .</p>	17
2.4	<p>The components of the Gibbs energy (per atom) for hydrogen in the vicinity of the fluid-fluid phase transition. (a) The Gibbs energy of reaction, <math>G_{BA}</math>, as given by Eq. (2.9). The isotherms are <math>T = 0.5T_c</math> (orange), <math>T = 0.75T_c</math> (blue), <math>T = T_c</math> (green), <math>T = 1.25T_c</math> (red), and <math>T = 1.5T_c</math> (purple). (b) The Gibbs energy of mixing, <math>G_{mix}</math>, as given by Eq. (2.15). <math>G_{mix}</math> is shown as a function of the fraction of hydrogen atoms in the diatomic state, <math>x</math>, for isotherms <math>T = 0.5T_c</math> (blue), <math>T = 0.75T_c</math> (green), and <math>T = T_c</math> (red) at <math>P = P_c</math>. The solid curve corresponds to the fluid-fluid coexistence. . . . .</p>	19
2.5	<p>Equilibrium fraction of hydrogen atoms in the diatomic state, <math>x_e</math>. (a) Equilibrium fraction-pressure diagram for <math>T = 0.5T_c</math> (orange), <math>T = 0.75T_c</math> (blue), <math>T = T_c</math> (green), and <math>T = 1.25T_c</math> (red). (b) Equilibrium fraction-temperature diagram for <math>P = 0.75P_c</math> (blue), <math>P = P_c</math> (green), <math>P = 1.25P_c</math> (red), <math>P = 1.5P_c</math> (purple). The solid and dashed black curves are, respectively, the fluid-fluid coexistence and the limit of thermodynamic stability (spinodal). . . . .</p>	20
2.6	<p>The pressure-density phase diagram of hydrogen based on the equation of state developed in this section. The open circles correspond to the QMC simulations of Tirelli <i>et al.</i> [46]. Isotherms are <math>\hat{T} = 0.67</math> (orange), <math>\hat{T} = 0.73</math> (red), <math>\hat{T} = 0.8</math> (brown), <math>\hat{T} = 0.87</math> (purple), <math>\hat{T} = 0.93</math> (green), and <math>\hat{T} = 1.0</math> (blue). The fluid-fluid coexistence is shown by the solid black curve. The red star is the FFPT adopted in this section. . . . .</p>	22
2.7	<p>A schematic representation of the phase diagram of sulfur. The solid black curves represent the solid-liquid-gas phase transition in sulfur [49–51], while the blue curve represents the experimentally verified liquid-liquid phase transition [51]. The dashed black line is the predicted continuation of the melting line based on experimental evidence [49]. The black circles are the solid-liquid-liquid triple point (TP-SLL) and the solid-liquid-gas triple point (TP-SLG), while the red circle is the liquid-gas critical point (LGCP) and the red star is the liquid-liquid critical point (LLCP). . . . .</p>	24

2.8	Reactions and interactions in the maximum-valence model. (a) The three types of covalent bond-forming reversible chemical reactions that may occur in the system. If two atoms without bonds ( $S_0$ ) collide with each other, they may form a bond and become $S_1$ atoms. If a $S_0$ and $S_1$ atom collide, they may form a bond and become $S_1$ and $S_2$ atoms, respectively. If two $S_1$ atoms collide with each other, they form an additional bond and become $S_2$ atoms. (b-d) The three major interactions between atoms, in which each atom is composed of a core and shell, both with a radius $\sigma$ and mass $m$ . $U(r)$ is the pair potential energy and $r$ is the distance from the center of an atom. (b) The cores of each atom interact with an attractive square well of depth $\epsilon = 1$ and width $w = 0.4$ . (c) The shells may react to form covalent bonds that consist of a narrow well with depth $\epsilon_b = 1$ and width $w_b = 0.02$ . (d) Phase segregation is coupled to polymerization via the additional attractive interactions between atoms in state $S_2$ , described by a square well of depth $\epsilon_{22} = 0.5$ and width $w_{22} = 0.3$ . . . . .	27
2.9	Phase diagrams for the maximum-valence model (with $\epsilon_{22} = 0.5$ and $\epsilon_b = 1.0$ ) obtained in an NVT ensemble after $t = 10^6$ time units. (a) The isotherms in the $P$ - $\rho$ plane are $T = 0.96 - 1.20$ (red-purple) in steps $\Delta T = 0.02$ . (b) The liquid-gas and liquid-liquid critical isochores in the $P$ - $T$ plane are $\rho_c^{LG} = 0.35$ and $\rho_c^{LL} = 0.81$ as indicated by the lower and upper dashed lines, respectively. In both figures, the liquid-gas and liquid-liquid coexistence curves are calculated via the Maxwell construction and indicated by the solid curves. The liquid-gas ( $T_c^{LG} = 1.023$ , $P_c^{LG} = 0.0922$ , $\rho_c^{LG} = 0.35$ ) and liquid-liquid ( $T_c^{LL} = 1.187$ , $P_c^{LL} = 2.28$ , $\rho_c^{LL} = 0.81$ ) critical points are indicated by the red open circles, while the triple point ( $P^{TP} = 0.0738$ , $T^{TP} = 0.995$ ) is indicated by the black open circles. . . . .	29
2.10	(a) $T$ - $\rho$ phase diagram for the maximum-valence model (with $\epsilon_{22} = 0.5$ and $\epsilon_b = 1.0$ ) obtained in an NVT ensemble after $t = 10^6$ time units. The temperature dependence of the fraction of atoms with two bonds, $x_2$ , (b) and the average chain-length, $\langle n \rangle$ , (c) in two coexisting liquid phases. The simulation data in (b) is fit to a second order polynomial. . . . .	30
2.11	(a) The density correlation function $g(r)$ and (b) the structure factor $S(q)$ across the liquid-liquid transition at $T = 1.00$ for densities of $\rho = 0.65$ (blue), $\rho = 0.70$ (orange), $\rho = 0.75$ (green), $\rho = 0.80$ (red), $\rho = 0.85$ (purple), and $\rho = 0.90$ (black). In (a), the sharp peak, around $r = 1$ (in units of $\sigma$ ), corresponds to the length of the covalent bond, which increases upon increasing density. Simultaneously, in (b), the maximum of the structure factor (the first peak) shifts to larger wavenumbers upon increasing density, while the second peak acquires a characteristic bump, similar to what was recently observed in sulfur [51]. The divergence of the structure factor at $q = 0$ indicates the divergence of the isothermal compressibility in the vicinity of the LLCP. The insets (dashed boxes) highlight the behavior of the maximum of the correlation function and second peak of the structure factor. . . . .	31

2.12	Density-temperature and pressure-temperature phase diagrams for the blinking-checkers model with $\varepsilon_{AA} = 1.6$ , $\varepsilon_{BB} = 2.0$ , $\varepsilon_{AB} = 1.08$ , $\hat{e} = 3$ , and $\hat{s} = 4$ . The liquid-vapor coexistence (blue curves) terminates at the liquid-vapor critical point, LVCP. The liquid-liquid coexistence (red curves) terminates at the liquid-liquid critical point, LLCP. The limits of thermodynamic stability (spinodals) are given by the dashed curves. In (a,b), the dotted line corresponds to the condition, $x = 1/2$ , which qualitatively separates the regions enriched either by species A (at low temperatures and low densities) or species B (at high temperatures and high densities).	35
2.13	Liquid-vapor (a,b) and liquid-liquid (c,d) coexistence curves for the seven systems with $\varepsilon_{AA} = 1.6$ , $\varepsilon_{BB} = 2.0$ , $e = 3$ , $s = 4$ , and with various values of $\varepsilon_{BA}$ : $\varepsilon_{BA} = 1.00$ (blue), $\varepsilon_{BA} = 1.04$ (orange), $\varepsilon_{BA} = 1.08$ (green), $\varepsilon_{BA} = 1.12$ (red), $\varepsilon_{BA} = 1.16$ (purple), $\varepsilon_{BA} = 1.20$ (pink), and $\varepsilon_{BA} = 1.24$ (gray). The critical points, indicated by the stars in (a,b) and open circles in (c,d), are the unique liquid-vapor (LVCP) or liquid-liquid (LLCP) critical points in the interconverting system, referred to as “actual” critical points. As also indicated in Fig. 2.12, species A is enriched in the low-density, low-temperature region, while species B is enriched in the high-density, high-temperature region. For the system with $\varepsilon_{BA} = 1.00$ , the dashed blue curves in (c,d) indicate the liquid-vapor coexistence, while in (a-d), the dotted blue line indicates the discontinuity at the triple point.	38
2.14	Illustration of the thermodynamic path selected by the interconversion reaction for $\hat{e} = 3$ and $\hat{s} = 4$ at constant volume, $V$ , and at constant number of occupied lattice sites, $N_1 + N_2$ , represented through (a) the liquid branch of the liquid-vapor temperature-concentration coexistence (see Fig. 2.13b), and (b) the activity, $a = 1/[1 + e^{-G_{BA}/\hat{T}}]$ , for the systems with different interaction parameters: $\varepsilon_{BA} = 1.00$ (blue), $\varepsilon_{BA} = 1.04$ (orange), $\varepsilon_{BA} = 1.08$ (green), $\varepsilon_{BA} = 1.12$ (red), $\varepsilon_{BA} = 1.16$ (purple), $\varepsilon_{BA} = 1.20$ (pink), and $\varepsilon_{BA} = 1.24$ (gray). For each system, the liquid-vapor critical line (LVCL) is shown by the dashed curves, while the collapsed coexistence, in (a), is illustrated by the black curve. The insets show the LV critical points for each scenario. Note that for the system with $\varepsilon_{BA} = 1.00$ , the thermodynamic path crosses through the triple point, indicated by the dotted line in (a).	41
2.15	Liquid-vapor (a,b) and liquid-liquid (c,d) diameters of the density, Eq. (2.60), and the concentration, Eq. (2.61), as a function of the distance to the virtual LVCL (or LLCL) along the thermodynamic path selected by interconversion for systems with $\varepsilon_{AA} = 1.6$ , $\varepsilon_{BB} = 2.0$ , $\hat{e} = 3$ , $\hat{s} = 4$ , and with various values of $\varepsilon_{BA}$ : $\varepsilon_{BA} = 1.00$ (blue), $\varepsilon_{BA} = 1.04$ (orange), $\varepsilon_{BA} = 1.08$ (green), $\varepsilon_{BA} = 1.12$ (red), $\varepsilon_{BA} = 1.16$ (purple), $\varepsilon_{BA} = 1.20$ (pink), and $\varepsilon_{BA} = 1.24$ (gray). In (a-d), the dotted blue lines indicate the discontinuity for the system with $\varepsilon_{BA} = 1.00$ at the triple point.	47

- 2.16 The liquid-vapor interfacial tension as a function of temperature (a), and also presented in reduced units (b), for the system with  $\varepsilon_{BA} = 1.00$  (blue),  $\varepsilon_{BA} = 1.04$  (orange),  $\varepsilon_{BA} = 1.08$  (green),  $\varepsilon_{BA} = 1.12$  (red),  $\varepsilon_{BA} = 1.16$  (purple),  $\varepsilon_{BA} = 1.20$  (pink), and  $\varepsilon_{BA} = 1.24$  (gray). In (b), the critical temperature is given by the “virtual” critical point (for the non-reactive binary mixture) for each concentration along the thermodynamic path selected by the interconversion reaction. The blue arrows indicate the direction of warming. (c) The reduced interfacial thickness,  $\hat{\zeta} = \zeta/\ell$ , and (d) the reduced relative distance between the concentration and density profiles,  $\hat{\delta} = \delta/\ell$ . In (a-d), the dotted lines indicate the discontinuity of the interfacial properties for the system with  $\varepsilon_{BA} = 1.00$  at the triple point, shown by the vertical bars in (c,d). . . . . 51
- 2.17 (a) The behavior of the liquid-vapor interfacial tension follows the power law,  $\sigma = \sigma_0|\Delta\hat{T}|^{3/2}$ , where the amplitude was found to be  $\sigma_0 = 0.71$ , asymptotically close to the actual liquid-vapor critical temperature (see Table 2.2). (b) The behavior of the reduced liquid-vapor interfacial thickness,  $\hat{\zeta} = \zeta/\ell$ , follows the power law,  $\hat{\zeta} = \hat{\zeta}_0|\Delta\hat{T}|^{-0.38}$ , where the amplitude was found to be  $\hat{\zeta}_0 = 1.50$  asymptotically close to the actual critical point. . . . . 52
- 2.18 Asymptotic behavior of the liquid vapor coexistence for systems with  $\varepsilon_{AA} = 1.6$ ,  $\varepsilon_{BB} = 2.0$ ,  $\hat{e} = 3$ ,  $\hat{s} = 4$ , and with various values of  $\varepsilon_{BA}$ :  $\varepsilon_{BA} = 1.00$  (blue),  $\varepsilon_{BA} = 1.04$  (orange),  $\varepsilon_{BA} = 1.08$  (green),  $\varepsilon_{BA} = 1.12$  (red),  $\varepsilon_{BA} = 1.16$  (purple),  $\varepsilon_{BA} = 1.20$  (pink), and  $\varepsilon_{BA} = 1.24$  (gray). (a) The temperature-density LV coexistence follows the meanfield power law,  $\Delta\hat{T} \sim |\Delta\hat{\rho}|^2$ , where  $\Delta\hat{T}_{act} = 1 - T/T_c^{act}$  and  $T_c^{act}$  is the actual critical temperature selected by the interconverting path. Likewise,  $\Delta\hat{\rho}_{act} = 1 - \rho/\rho_c^{act}$ , where  $\rho_c^{act}$  is the actual critical density. (b) The temperature-average concentration LV coexistence follows the meanfield power law,  $\Delta\hat{T} \sim |\Delta\bar{x}_{act}|^2$ , where  $\Delta\bar{x}_{act} = 1 - \bar{x}/x_c^{act}$ , in which  $\bar{x} = (x_L + x_V)/2$  and  $x_c^{act}$  is the actual critical concentration. (c,d) Illustrate, as an example, the asymptotic behavior of the system with  $\varepsilon_{BA} = 1.08$ , in which (d) shows the asymptotic behavior of each branch of the concentration coexistence. . . . . 53
- 2.19 Comparison between the liquid-liquid (dashed curves) and liquid-vapor (solid curves) interfacial tensions as a function of temperature for the system with  $\varepsilon_{BA} = 1.00$  (blue),  $\varepsilon_{BA} = 1.04$  (orange),  $\varepsilon_{BA} = 1.08$  (green),  $\varepsilon_{BA} = 1.12$  (red). The dotted blue line indicates the discontinuity in the liquid-vapor interfacial tension. . . . . 56
- 2.20 Liquid-liquid interfacial properties of the systems exhibiting liquid polyamorphism with  $\varepsilon_{AA} = 1.6$ ,  $\varepsilon_{BB} = 2.0$ ,  $\hat{e} = 3$ ,  $\hat{s} = 4$ , and with various values of  $\varepsilon_{BA}$ :  $\varepsilon_{BA} = 1.00$  (blue),  $\varepsilon_{BA} = 1.04$  (orange),  $\varepsilon_{BA} = 1.08$  (green),  $\varepsilon_{BA} = 1.12$  (red). (a) the reduced thickness,  $\hat{\zeta} = \zeta/\ell$  of the liquid-liquid interface, and (b) the reduced shift,  $\hat{\delta} = \delta/\ell$ , between the density and concentration liquid-liquid profiles. In (a,b) the thickness and shift reach a finite value (marked with a blue circle) at the triple point temperature. . . . . 56

2.21	(a) The behavior of the liquid-liquid interfacial tension follows the meanfield power law, $\sigma = \sigma_0 \Delta\hat{T} ^{3/2}$ , (dashed lines) asymptotically close to the actual liquid-liquid critical temperature (see Table 2.3). (b) The behavior of the reduced liquid-liquid interfacial thickness, $\hat{\zeta} = \zeta/\ell$ , follows the meanfield power law, $\hat{\zeta} = \hat{\zeta}_0 \Delta\hat{T} ^{-1/2}$ , (dashed lines). In (a,b) the systems exhibiting liquid polyamorphism and a liquid-liquid critical point are shown: $\varepsilon_{BA} = 1.04$ (orange), $\varepsilon_{BA} = 1.08$ (green), $\varepsilon_{BA} = 1.12$ (red), and the amplitudes of the asymptotic meanfield power laws are provided in Table 2.4. . . . .	57
2.22	Normalized density and concentration liquid-vapor profiles as a function of the coordinate perpendicular to the planar interface, $\hat{z} = z/\ell$ , given by Eqs. (2.54) and (2.55) for the system with $\varepsilon_{AA} = 1.6$ , $\varepsilon_{BB} = 2.0$ , $\varepsilon_{BA} = 1.08$ , $\hat{e} = 3$ , and $\hat{s} = 4$ at the two temperatures (a,b) that correspond to the two extrema of the liquid-vapor interfacial tension (shown in Fig. 2.16). Normalized (c) density and (d) concentration profiles for three-phase coexistence at the triple point, $T_{TP} = 0.6843$ , for the system with $\varepsilon_{AA} = 1.6$ , $\varepsilon_{BB} = 2.0$ , and $\varepsilon_{BA} = 1.00$ . . . . .	59
2.23	Interfacial profiles of species B, $\rho_B = \rho x$ , in the blinking-checkers model demonstrate surface enrichment near the TP temperature, $T_{TP} = 0.68429$ . (a) Surface enrichment of species B for the system with $\varepsilon_{BA} = 1.00$ . The colored curves indicate temperatures from $T = 0.68989$ to $T = T_{TP}$ in steps of $\Delta\hat{T} = -0.0008$ in order of purple to red. The black curves are $T = 0.68389$ (dashed) and $T = 0.68309$ (solid). (b) Surface enrichment of species B for the system with $\varepsilon_{BA} = 1.04$ . The curves are $T = 0.6882$ to $T = 0.6826$ in steps of $\Delta T = -0.0008$ (blue to pink). In (a,b), the black arrows indicate the direction of decreasing temperature. Note that while the transition of a surface enriched profile ( $T > T_{TP}$ ) to a smooth profile ( $T < T_{TP}$ ) is discontinuous in the system with $\varepsilon_{BA} = 1.00$ , it is continuous in the system with $\varepsilon_{BA} = 1.04$ . . . . .	60
3.1	The characteristic growth rate, Eq. (3.14), affected by the competition between diffusion, natural interconversion, and forced interconversion at $\Delta\hat{T} = -0.5$ . Complete phase separation (as predicted by Cahn-Hilliard's theory for $L = 0$ and $K = 0$ ) is illustrated by the red curve for $M = 100$ . Phase amplification is illustrated by the purple curves for restricted ( $M = 100$ - solid) and unrestricted ( $M = 10$ - dashed) cases, in which $L = 10$ and $K = 2$ . Microphase separation for $M = 100$ , $L = 1$ , and $K = 2$ is illustrated by the solid green curve. When the growth rate is always negative, as illustrated by the green dashed curve (for $M = 1$ , $L = 1$ , and $K = 2$ ), there is no phase domain growth corresponding to a homogeneous steady state. The green circles indicate the three characteristic wavenumbers of the amplification factor: the maximum, $q_m$ , the lower cut-off, $q_-$ , and the upper cut-off, $q_+$ . . . . .	71

3.2	Steady-state phase domain morphology for different magnitudes of forced interconversion (after $\sim 10^5$ time steps) numerically computed from the time evolution of the order parameter, Eq. (3.7), with $M = 1$ , $L = 1/127$ , $\Delta\hat{T} = -0.1$ , $\ell = 64$ , $\sigma_i = 0.1$ , and $\eta = 10^{-5}$ , as discussed in Section 3.3. Morphologies are shown for the middle slice of the three-dimensional system at (a) $K = 0$ , (b) $K = 5 \times 10^{-4}$ , (c) $K = 15 \times 10^{-4}$ , and (d) $K = 25 \times 10^{-4}$ . The red regions correspond to where the value of the normalized order parameter is $\varphi/\varphi^{\max} = 1$ , the purple regions correspond to where the value of the normalized order parameter is $\varphi/\varphi^{\max} = -1$ , and the other colors depict the interface between these two regions. The image in (a) depicts a metastable structure toward phase amplification [6], while the images in (b-d) are modulated steady-state structures with a characterize size, $1/q_-$ . . . . .	77
3.3	a) The amplification factor, $\omega(q)$ , given by Eq. (3.15) with $\kappa = 1$ , $\Delta\hat{T} = -0.1$ , $M = 1$ , $L = 1/127$ , and $K = 1.3 \times 10^{-3}$ . b) The time evolution of the structure factor, given by Eq. (3.23) in the presence of natural and forced interconversion. The black dotted line depicts the evolution of the maximum of the structure factor. Due to the external source of forced interconversion, the maximum of the structure factor is interrupted at the wavenumber $q_-$ , while for complete phase separation and phase amplification, the maximum of the structure factor will evolve to $q = 0$ for an infinite-sized system. . . . .	80
3.4	Temporal evolution of the structure factor: a) for a system undergoing diffusion dynamics ( $M = 1$ ) toward an equilibrium state in the absence of natural interconversion ( $L = 0$ ) and forced interconversion ( $K = 0$ ); b) for a system undergoing a hybrid of diffusion ( $M = 1$ ) and natural interconversion ( $L = 0.01$ ) dynamics in the presence of forced interconversion ( $K = 1.5 \times 10^{-3}$ ) toward a steady state. The structure factor, given by Eq. (3.23), exhibits a crossover from spinodal decomposition to the nucleation regime. The dashed-black curves indicate the development of the maximum of the structure factor. The characteristic crossover time is defined in Eq. (3.24) and adopted as $\tau = 100$ . In (a) the evolution of the maximum of the structure factor moves to $q = 0$ for infinite-size system and saturates at $S_m(q = 0, t \rightarrow \infty) = 1/(2\xi^2) = 5$ for $\Delta\hat{T} = -0.1$ . In contrast, in (b) the evolution of the maximum is interrupted at a characteristic cut-off wavenumber predicted by the characteristic phase domain growth rate, $q_m^s(t \rightarrow \infty) \propto q_-$ , and it saturates at $S_m(q_-, t \rightarrow \infty) = 417$ . . . . .	82
3.5	The time evolution of the wavenumber corresponding to the maximum of the structure factor, given by Eq. (3.23), during the crossover from the early stage of spinodal decomposition, $q \propto t^{1/4}$ (green - dashed), to the nucleation regime, $q \propto t^{1/3}$ (orange - dashed) for a system undergoing diffusion dynamics in the absence of natural interconversion ( $L = 0$ ) and forced interconversion ( $K = 0$ ) under conditions: $M = 1$ , $\Delta\hat{T} = -0.1$ , $\tau = 100$ . . . . .	83

3.6	The effect of increasing interconversion force on the phase domain growth rate for $M = 100$ , $L = 1$ , and $\Delta\hat{T} = -0.5$ . The red dashed line corresponds to the inverse maximum size of the phase domain on the length scale of the simulation box, $q^*$ . When $q_- > q^*$ microphase domains will form. Alternatively, when $q_- < q^*$ , the size of the simulation box will cut-off the growing phase domains. The conditions where $\omega(q) < 0$ (dashed-dot portions of the curves) corresponds to non-growing wavenumbers. As the rate of forced interconversion increases, the growth rate is shifted down from the onset of phase separation where $q_- = q^*$ (red, $K = 1$ ), to the microphase region (green, $K = 3.75$ ), to the termination point of domain growth (blue, $K = 6.5$ ) where $q_- = q_m = q_+ = q^{**}$ , and to the no growth regime for any wavenumber (orange, $K = 9.25$ ). . . . .	84
3.7	Time evolution of the structure factor computed from the Fast Fourier transform (FFT) of Eq. (3.7) for $M = 1$ , $L = 1/127$ , $\Delta\hat{T} = -0.1$ , $\ell = 64$ , $\sigma_i = 0.1$ , $\eta = 10^{-5}$ depicted at times $t = 6 \times 10^3$ (green), $t = 1.2 \times 10^4$ (blue), $t = 2.4 \times 10^4$ (orange), $t = 5 \times 10^4$ (red), $t = 1 \times 10^5$ (pink), and $t = 2 \times 10^5$ (black). The open circles in (a-d) depict the computed structure factors for the four selected magnitudes of forced interconversion averaged over $N = 100$ realizations with 95% confidence interval error bars, while the solid lines illustrate the behavior of the structure factors assuming a Gaussian distribution. The wavenumber is normalized by the size of the system, such that $q = 1$ corresponds to phase domains with a characteristic size of half the simulation box, $\ell/2$ . . . . .	86
3.8	The temporal evolution of the symmetry of phase separation. a) The time evolution of the average order parameter, calculated by first averaging over all space and second by averaging the absolute value over $N = 100$ realizations, for $M = 1$ , $L = 1/127$ , $\Delta T = -0.1$ , $\sigma_i = 0.1$ , $\eta = 1.0 \times 10^{-5}$ , and various magnitudes of forced interconversion, $K$ . b) The time evolution of the $N$ -averaged standard deviation of the averaged order parameter, calculated by first determining the standard deviation of the spatially averaged order parameter and second by averaging over $N = 100$ realizations. This method of averaging highlights the behavioral deviation from an equal concentration of species A and B, $\varphi = 0$ . . . . .	88
3.9	Three hypothesized binary mixture systems exhibiting interconversion of species and liquid-liquid phase separation quenched from high temperature to low temperature (without volume change). The black dashed curve corresponds to the liquid-liquid phase coexistence in this system without interconversion and with interaction energy, $\varepsilon = 2$ . The open circle indicates the liquid-liquid critical point (LLCP), while the crosses show the locations of $T = T_{BA}$ , the points corresponding to 50:50 interconversion for different energy change of reaction. For a system with $T_{BA} = 1.05T_c$ (green), no liquid-liquid phase transition will be observed upon quenching. For a system with $T_{BA} = T_c$ (red), the quenching process passes through the critical point. For a system with $T_{BA} = 0.95T_c$ (purple), there are two equilibrium solutions for the fraction of interconversion, such that upon quenching to the cross, phase amplification occurs with equal probability of forming an A-rich or B-rich phase. . . . .	90

3.10	The phase diagram (suggested in ref. [13]) for supercooled water that exhibits a liquid-liquid phase transition (global phase diagram illustrated in Fig. 1.1). A hypothesized quenching process by compression for supercooled water is shown from the one phase region at $P_1 = 20$ MPa (orange) to the two phase region at $P_2 = 120$ MPa (green) along the Widom line (dashed black) which corresponds to a line of constant fraction of interconversion, $\ln \mathcal{K} = 0$ . Two additional isobars are shown for reference at $P = 40$ MPa (blue) and $P = 80$ MPa (purple) along with the liquid-liquid coexistence (black). Phase amplification would only be possible in a system where the number of molecules changes to compensate the volume change of the interconversion reaction. . . . .	92
3.11	a) Characteristic phase domain growth rate in the vicinity of the critical point ( $\Delta\hat{T} = -0.001$ ) for $M_0 = 1$ , $L = 0.002$ , and $K = 2.25 \times 10^{-5}$ calculated through Eq. (3.13), red curve, with use of the diverging molecular mobility, Eq. (3.27), and scaling inverse susceptibility in the first order epsilon expansion, $\hat{\chi}_{q=0}^{-1} \sim  \Delta\hat{T} ^{-\gamma}$ with $\gamma = 1 + \epsilon/6$ ( $\epsilon = 4 - d$ ). The meanfield approximation is shown by the green curve, Eq. (3.13). b) The onset, red solid curves, Eq. (3.28), and termination, red dashed curves, Eq. (3.29), of microphase separation affected by critical fluctuations for $M = 1$ , $L = 0.01$ , $\ell = 100$ , $\nu = 1/2 + \epsilon/12$ . The meanfield approximation is shown by the green curves. . . . .	96
4.1	The spontaneous equilibrium order parameter ( $\varphi = \varphi_0$ ) in the lattice gas / lattice binary mixture along the liquid-vapor phase coexistence (red domain). One of the two alternative magnetizations ( $\varphi_0 > 0$ and $\varphi_0 < 0$ ) in the Ising ferromagnet in zero field are shown in the red domain with blue arrows. The solid curve is the crossover from meanfield behavior (dashed) to the asymptotic scaling power law $\varphi \propto \Delta T^\beta$ with $\beta = 0.326$ [52, 53], while the crosses correspond to simulation results of the HL model. . . . .	100
4.2	Phase amplification in the HL model for systems with $T = 4.0$ , $\ell = 100$ , and interconversion probabilities $p_r$ : (a) 100%, (b) 10%, (c) $10^{-4}\%$ , and (d) $10^{-7}\%$ . The inset in (d) shows $10^{-7}\%$ interconversion probability at a shorter time scale. Each curve represents one of the 100 different realizations of the MC simulations, while the solid zero line depicts the behavior of a system with 0% interconversion. The simulation snapshots in (a,d) correspond to the end of the simulation time. . . . .	104
4.3	The evolution of the order parameter during phase amplification. (a) The RMS of the distribution of the growth rates for different probabilities captured at the same time, $t = 300$ . The solid curve is the crossover between $\sigma \propto \sqrt{p_r}$ and $\sigma \propto p_r$ , approximated as $\sigma = a\sqrt{p_r}(1 + bp_r)/(1 + \sqrt{p_r})$ . (b-d) The growth of the order parameter for different (b) probabilities at $\Delta\hat{T} = -0.11$ and $\ell = 100$ , (c) system sizes at $p_r = 1.0$ and $\Delta\hat{T} = -0.11$ , and (d) distances to the critical point at $p_r = 1.0$ and $\ell = 100$ ; The inset shows the power law for the initial growth of the reduced order parameter, $\varphi/\varphi_0 \propto t^{3/4}$ . . . . .	106

4.4	Scaling properties of the growth of the reduced order parameter, $\hat{\varphi} = \langle \varphi \rangle / \varphi_0$ . (a) The order parameter growth with time rescaled by system size. The size dependence of the rescaling parameter, $\tau(\ell)$ , is shown in the inset; in the log-log scale with a slope of 1. The colors are the same as in Fig. 4.3c. (b) The order parameter growth with time rescaled by probability; the rescaling parameter $\tau_0(p_r)$ , inversely proportional to the probability, is shown in the inset. The colors are the same as in Fig. 4.3b. . . . .	109
4.5	Topological characteristics of the time dependence of phase amplification. (a) For spherical domains, the reduced deviation from the equilibrium order parameter, $\Delta\hat{\varphi} = 1 - \varphi/\varphi_0$ scales as $t^{3/2}$ . This is shown for temperatures, $\Delta\hat{T}$ , as: $-0.11$ (cyan), $-0.025$ (purple), $-0.014$ (orange), and $-0.009$ (brown). The inset shows the effect for a cylindrical domain at $\Delta\hat{T} = -0.11$ . (b) A zero curvature Schwarz-P interface is initially formed by simulating a system with Kawasaki dynamics ( $p_r = 0$ ) for a long time. At $t - t_0 = 0$ , the system obtains Glauber dynamics ( $p_r = 1$ ) and the collapse of one of the phases is shown. Amplification transitions from random-walk behavior, $\sqrt{t}$ , at short times (see inset) to exponential behavior before saturation shown by the straight line. . . . .	110
4.6	The time evolution of the concentration for the HL model with pure Ising dynamics ( $p_r = 1$ ), given by Eq. (4.5) with the time-dependent susceptibility in the form of Eq. (4.4). For $\Delta\hat{T} = -0.32$ (green), $\tau = 0.2$ , $\varphi_\infty = 0.91$ , $a = 1.9$ and $b = 0.3$ , and for $\Delta\hat{T} = -0.11$ (blue) $\tau = 0.2$ , $\varphi_\infty = 0.73$ , $a = 4.6$ , and $b = 0.4$ . The open circles are the computational data presented in Fig. 4.3d. . . . .	113
4.7	Effect of forced interconversion on domain size, $R$ , normalized by the system size, $\ell$ , in the HL model. (a) The time dependence of the domain growth for energy source $E = 5$ and interconversion probability $p_r = 1/128$ at $T/T_c = 0.24$ (green), $T/T_c = 0.27$ (blue), and $T/T_c = 0.40$ (red), where $T_c = 4.511$ [54]. The horizontal dashed line indicates the size of the simulation box, $R = \ell$ . (b) Temperature dependence of the steady-state domain size for $E = 5$ and $p_r = 1/128$ . The vertical dashed line indicates the onset temperature, $T^*/T_c$ . (c) Dependence of the steady-state domain size on the energy of forced interconversion for $p_r = 1/256$ and $T/T_c = 0.31$ . The vertical dashed line denotes the onset source energy, $E^*$ . In (a-c), the system is simulated on a 3-dimensional lattice of size $\ell = 100$ . The open circles are the results of MC simulations, the images are snapshots of the system for selected conditions, and the curves are the theoretical predictions. In (a-c), black denotes up-spins and white denotes down-spins. . . .	116
4.8	Domain size as a function of temperature in the HL model. (a) $p_r = 1/32$ and (b) $p_r = 1/256$ , for a system of size $\ell = 100$ and energies: $E = 1$ (orange), $E = 2$ (green), $E = 3$ (red), $E = 4$ (purple), $E = 5$ (brown), $E = 6$ (pink), $E = 7$ (gray), $E = 8$ (yellow), $E = 9$ (cyan), and $E = 10$ (dark blue). The solid curves are the theoretical predictions of $q_-$ , the inverse steady-state domain size, where the fit parameters are provided in Table 4.1. . . . .	118

4.9	<p>a) Steady-state structure factors computed for the HL (open circles) and the prediction given by Eq. (4.7) (solid lines) for selected external energy sources (<math>E</math>) at <math>\Delta\hat{T} = -0.4</math>, <math>M = 1</math>, <math>L = 1/127</math>, <math>\ell = 100</math>, and averaged over <math>N = 60</math> realizations with 95% confidence interval error bars. The insets show steady-state (<math>t \sim 3 \times 10^5</math>) domain morphologies observed in the HL model for the selected energies. b) The dependence of forced interconversion on the wavenumber corresponding to the maximum of the structure factor, <math>q_m^s</math>, in the steady-state limit. The open circles are numerical computations of structure factors determined from FFTs of the time evolution of the order parameter, given by Eq. (3.7), in the steady-state limit (<math>t \sim 10^5</math>) for <math>M = 1</math>, <math>L = 1/127</math>, <math>\sigma_i = 0.1</math>, and <math>\eta = 10^{-5}</math>, averaged over <math>N = 100</math> realizations. The triangles correspond to the predictions of <math>K</math> determined from fits of Eq. (4.7) to the structure factor for the HL model, like those presented in (a). The curves illustrate the theoretical prediction <math>q_m(t \rightarrow \infty) \propto q_-</math>, given by the full expression for <math>q_-</math>, found from evaluating <math>\omega(q, 0) = 0</math> using Eq. (3.15). The colors correspond to temperatures: <math>\Delta\hat{T} = -0.1</math> (blue), <math>\Delta\hat{T} = -0.2</math> (green), <math>\Delta\hat{T} = -0.3</math> (red), and <math>\Delta\hat{T} = -0.4</math> (purple). The inset shows the relationship between <math>K</math> and <math>E</math>. . . . .</p>	121
4.10	<p>Molecular representation and geometrical features of tetramer molecules. L-enantiomers (green), D-enantiomers (blue) and achiral transition states (cis- or trans-, red) are shown. . . . .</p>	125
4.11	<p>Time dependence of the instantaneous dihedral angle of a typical tetramer in a racemic mixture at <math>P = 0.1</math> for the conservative formulation of the CM model, at several values of <math>T</math> and <math>k_d</math>. a) <math>T = 0.6</math>, b) <math>T = 1.7</math>, and c) <math>T = 2.3</math>, with <math>k_d = 5</math> (green), <math>k_d = 9.86</math> (orange) and <math>k_d = 19.86</math> (purple). d) Behavior of the dihedral angle at a very low value of the dihedral constant, <math>k_d = 0.001</math>. . . . .</p>	128
4.12	<p>The phase diagram showing phase amplification in the CM model with conservative intermolecular forces, heterochiral bias parameter <math>\lambda = 0.5</math>, and rigidity spring constant <math>k_d = 0.001</math>. The circles on the solid curve are the computational data for the critical temperature of equilibrium phase separation and the curve is the fit of Eq. (4.12). The snapshots depict the equilibrium states for the pressures <math>P = 0.1</math>, <math>P = 1</math>, <math>P = 5</math>, and <math>P = 10</math> below the critical temperature and at <math>P = 1</math> above the critical temperature. The triangles show the prediction of the critical temperature from the extrapolation of the CM model with dissipative intermolecular forces to the limit <math>k_d \rightarrow \infty</math>. . . . .</p>	129
4.13	<p>The change of compositional heterogeneity with chiral interconversion kinetics at <math>T = 1.7</math> and <math>P = 0.1</math> in the dissipative-force formulation. a) Steady-state snapshots of chiral liquid systems at various dihedral force constants (<math>k_d</math>). b) The steady-state domain size as a function of interconversion rate, <math>1/\tau_{\text{INC}}</math>. The solid line is the approximation given by <math>1/\tau_{\text{INC}} = a_1/R_\infty^2 + a_2/R_\infty^4</math>, which follows from Eq. (4.15), where <math>a_1 = 4.6 \times 10^{-3}</math> and <math>a_2 = 3.8 \times 10^{-4}</math>. The inset shows the linear correlation between <math>R_\infty</math> and <math>k_d</math>. The colored points highlight the results corresponding to the three dihedral force constants for which the domain growth is shown in Fig. 4.15. . . . .</p>	131

4.14	Steady-state domain size, $R$ , normalized by the size of the system, $\ell$ , in the CM model. (a) The time evolution of the domain size for different interconversion rates, tuned by the rigidity parameter, $k_d$ , as $k_d = 3$ (purple), $k_d = 5$ (green), and $k_d = 9.86$ (red) at the reduced pressure $P = 0.1$ and $T/T_c = 0.35$ , where $T_c(P = 0.1) = 2.32$ , as indicated on Fig. 4.12. (b) The normalized steady-state domain size as a function of temperature at $P = 0.1$ and $k_d = 5$ . The vertical dashed line indicates the onset temperature, $T^*/T_c$ . In (a) and (b), the open circles correspond to simulation results, the curves correspond to the theoretical predictions (see Table 4.3), and the images show snapshots of the system simulated at the indicated conditions. In (a-b), dark/clear spheres correspond to the L-/D-configuration of a chiral tetramer (spheres are located a tetramer's center of mass). . . . .	133
4.15	Phase domain growth for the dissipative-force formulation of the CM model. The open circles represent computational data [7], and the curves illustrates predictions of the time evolution of the domain size, $R(t) = 1/q_m^s$ , from Eq. (3.23) for dihedral force constants: $k_d = 5$ (green), $k_d = 9.86$ (red), $k_d = 19.86$ (blue), and $k_d \rightarrow \infty$ (black) for $T = 1.8$ , $T_c = 2.3$ , $\tau = 2$ , and $M = 0.0022$ . The domain size is normalized by the size of the computational box, $\ell$ . The dashed curves represent the predictions of the domain growth if it is not restricted by the finite size. . . . .	135
4.16	The mutual diffusion coefficient affected by interconversion, given by Eq. (4.17), as a function of the normalized steady-state domain size $R_\infty$ , Eq. (4.18) in the CM model. The open circles are computational data for the dissipative-force formulation of the CM model at three different dihedral force constants: $k_d = 5$ (green), $k_d = 9.86$ (red), and $k_d = 19.86$ (blue) [7]. The molecular mobility in the limit $k_d \rightarrow \infty$ is approximated as $M = b_0 T / \eta$ , where $b_0 = 0.94$ and $\eta$ is the viscosity approximated by the Arrhenius equation $\eta \sim e^{T_0/T}$ . The characteristic temperature $T_0$ is 3.5. . . . .	136
4.17	Temperature dependence of the characteristic time scales in the dissipative-force formulation of the CM model for dihedral force constants: $k_d = 5$ (green), $k_d = 9.86$ (orange), and $k_d = 19.86$ (purple) at $P = 0.1$ . a) Characteristic time for liquid-liquid phase separation at the length scale of the simulation box, $q = q^*$ . The curves are $\tau_{\text{LLPS}} \propto 1/\tilde{\omega}(q^*)$ where $\tilde{\omega}(q)$ is given by Eq. (4.16) where it was found that $q^* = 0.15$ and $T_c = 2.35$ . The condition $\tau_{\text{LLPS}} \rightarrow \infty$ corresponds to $T = T^*$ . b) Characteristic times for chiral interconversion. $\tau_{\text{INC}} \propto 1/L$ , and the curves are given by Eq. (4.13). c) Characteristic self-diffusion times, where the curves are given by Eq. (4.19). . . . .	138

4.18	Dihedral force constant dependence of the onset temperature of phase separation on the length scale of the simulation box in the dissipative-force formulation CM model for $P = 1.0$ (red circles), $P = 0.5$ (blue circles), and $P = 0.1$ (black circles). The curves are numerically calculated from the first solution of $\tilde{\omega} = 0$ , given by Eq. (4.16), when $q_- = q^* = 0.11 \approx 1/R_{\max} \sim 1/\ell$ , $T = T^*$ , and $T_c(P = 1.0) = 3.45$ , $T_c(P = 0.5) = 2.91$ , and $T_c(P = 0.1) = 2.3$ for different pressures (a) and in rescaled coordinates (b). The triangles, shown in (b), are obtained from the asymptotic limits of the time of liquid-liquid phase separation, $\tau_{\text{LLPS}} \rightarrow \infty$ , as shown in Fig. 4.17a for $q^* = 0.15$ and $T_c = 2.35$ . . . . .	141
4.19	The conditions for microphase separation at a length scale, $R_\infty = 1/q_-$ . The solid curve depicts the onset temperature of microphase separation, $T = T^*$ , at the scale of the computational box, Eq. (4.20), for $R_\infty = 1/q^* = 7.1$ and $T_c = 2.4$ . The two dashed curves depict the lines of steady-state domain size that are smaller than the size of the computational box, $R_\infty = 3.6$ (lower) and $R_\infty = 2.0$ (upper), while the dotted curve depicts the growth-termination temperature, $T = T^{**}$ , Eq. (4.21). The symbols are computational data (from the observed size of the phase domain) in the dissipative-force formulation of the CM model for pressure $P = 0.1$ . The symbols indicate the onset of phase separation (open circles), the microphase region ( $R_\infty = 1/q^*$ , closed circles), and the two phase region ( $R_\infty > 1/q^*$ , triangle). The two simulation snapshots illustrate the behavior of the system composed of A-rich (green), B-rich (blue), and intermediate (red) states of the CM model. [7] . . . . .	143
4.20	Self-diffusion (molecular mobility) of the HCS model. Simulations were conducted for a system with $b = 0$ (no interconversion, either natural or forced). The open circles indicate simulation results, while the curve is the fit of $M = 0.056\sqrt{T} + 0.015T$ . . . . .	145
4.21	Critical temperature of the HCS model. Internal energy, $\Delta U$ , of the HCS model as a function of temperature (blue) for the case $b = 0$ (no interconversion, either natural or forced). The blue circles indicate the results of simulations, while the red circles correspond to the calculated isochoric heat capacity, $C_V = \partial U / \partial T _V$ . The solid red curve is an empirical fit of $C_V$ , where the temperature corresponding to the maximum of $C_V$ is the critical temperature for the HCS model, $T_c = 3.6 \pm 0.05$ , in units of $\epsilon_0/k_B$ . . . . .	146
4.22	Steady-state domain size, $R$ , normalized by the size of the system, $\ell$ , in the HCS model. (a) The temperature-dependence of the normalized steady-state domain size for $b = 0.005$ (blue), $b = 0.050$ (black), and $b = 0.075$ (green) at $\epsilon = 10$ . (b) The normalized steady-state domain size as a function of interconversion probability, $b$ , for the energy source $\epsilon = 12$ and $T/T_c = 0.22$ . The vertical dashed line indicates the onset interconversion probability, $b^*$ . In (a) and (b), the open circles correspond to simulation of 64,000 particles, the curves correspond to the theoretical predictions, and the images show snapshots of the system simulated at the indicated conditions. . . . .	148

4.23	Structure factor, $S(q, t)$ , in the HCS model. The formation of a steady-state bi-continuous microemulsions observed in MD simulations of the HCS model for 64,000 particles at interconversion energy source $\epsilon = 12$ , $T/T_c = 0.1$ , and interconversion probability $b = 0.05$ (a) and $b = 0.15$ (b). The images show snapshots of the steady-state system simulated at the specified conditions. . . . .	149
4.24	Domain size as a function of temperature for the HCS model. (a) $\epsilon = 6$ and (b) $\epsilon = 8$ , for system size $\ell = 40\sigma$ , averaged over $N = 10$ realizations, for interconversion probabilities, $b = 0.005$ (blue), $b = 0.05$ (black), and $b = 0.075$ (green). It should be noted that for low temperatures, $T/T_c \leq 0.8$ , the simulated systems freeze, such that the characteristic domain size is always less than the predicted size (as indicated by the triangles). . . . .	150
4.25	The onset and termination of microphase separation. (a) The steady-state domain size in the HL model for $p_r = 1/128$ and different forced interconversion energies from $E = 1$ (orange) to $E = 10$ (dark blue) in steps of $\Delta E = 1$ , just as in Fig. 4.8 (Fit parameters provided in Table 4.4). For $E > E^{**} = 7$ (the termination energy), the data collapse into a single line (black), indicating that the characteristic steady-state domain size remains on the order of the microscopic length scale $R_0(T)$ , which corresponds to homogeneous steady-state systems for all temperatures. For $E \leq 7$ , the onset of microphase separation is observed at $T = T^*(E^*)$ , where $E^*$ is the onset energy. For $T < T^*$ , the steady-state domain size is equal to the size of the system, $R = \ell$ . (Caption continues on the next page.)	154
4.25	(b) The onset energy $E^*$ (black circles and curve) for the HL model as a function of temperature for $p_r = 1/128$ . Colored open circles and dashed curves correspond to steady-state domain sizes: $R = 0.143$ (blue), $R = 0.095$ (green), and $R = 0.074$ (red). (c) The inverse onset rigidity parameter $1/k_d^*$ (black circles and curve) for the CM model at $P = 0.1$ . Colored circles and dashed curves correspond to steady-state domain sizes: $R = 0.32$ (blue), $R = 0.22$ (green), and $R = 0.18$ (red). In (b) and (c), the blue area corresponds to phase separation on the scale of the simulation box, the white area corresponds to microphase separation, and the yellow area corresponds to homogeneous steady states. The images in (b) and (c) correspond to the different final states of the systems below $E^*(T^*)$ and $1/k_d^*(T^*)$ where the size of the phase domain is on the scale of the simulation box ( $q^* \sim 1/\ell$ ). In (b), phase amplification is observed since for $p_r = 1/128$ natural interconversion is relatively fast, while in (c), where natural interconversion is relatively slow for the simulated range of $k_d$ , complete two-phase separation, on the scale of the simulation box, is found. . . . .	155
A.1	Comparison between the Fisher-Wortis (FW) and an alternative symmetric ansatz (sym). obtained for the liquid-vapor coexistence, for two systems with $\epsilon_{BA} = 1.04$ (a) and $\epsilon_{BA} = 1.12$ (b) with $\epsilon_{AA} = 1.6$ , $\epsilon_{BB} = 2.0$ , $\hat{e} = 3$ , and $\hat{s} = 4$ . (c) The relative deviation between the symmetric and FW ansatzes. . . . .	161
A.2	Numerical calculations of the liquid-vapor surface tension for three temperatures in the system with $\epsilon_{BA} = 1.04$ , $\epsilon_{AA} = 1.60$ , $\epsilon_{BB} = 2.00$ , $\hat{e} = 3$ , and $\hat{s} = 4$ . The FW ansatz is given at iteration 0. The temperatures were chosen based on surface tensions with similar values, as predicted by the FW ansatz. . . . .	162

A.3 Comparison of the liquid-vapor density (a) and concentration (b) interfacial profiles, as obtained from numerical calculations after eight iterations,  $\rho_{V4}$  and  $x_{V4}$ , and for the FW ansatz,  $\rho_{V0}$  and  $x_{V0}$ , for the system with  $\varepsilon_{BA} = 1.04$ ,  $\varepsilon_{AA} = 1.60$ ,  $\varepsilon_{BB} = 2.00$ ,  $\hat{e} = 3$ , and  $\hat{s} = 4$  at temperature,  $T = 0.6943$  (red curve in Fig. A.2). (c,d) The difference between the exact solution for the density and concentration profiles and the FW and symmetric ansatzes. In (a-d), the different profiles were aligned along their Gibbs dividing surface, such that the excess density is zero for all profiles. . . . . 164

## List of Abbreviations and Key Notations

### Acronyms

FFCP	Fluid-fluid critical point
FFPT	Fluid-fluid phase transition
FFT	Fast Fourier transform
FW	Fisher-Wortis
HDL	High-density liquid
INC	Characteristic interconversion
LDL	Low-density liquid
LLCP	Liquid-liquid critical point
LLPS	Liquid-liquid phase separation
LLPT	Liquid-liquid phase transition
LVCL	Liquid-vapor critical line
LVCP	Liquid-vapor critical point
MC	Monte Carlo
MD	Molecular dynamics
DMD	Discrete molecular dynamics
QMC	Quantum Monte Carlo
RG	Renormalization Group
RMS	Root mean square
SFF-TP	Solid-fluid-fluid triple point
SLL-TP	Solid-liquid-liquid triple point
SLG-TP	Solid-liquid-gas triple point
TP	Triple point

### Simulated Models

HL	Hybrid Ising / binary lattice
CM	Chiral mixture of interconverting enantiomers
HCS	Coarse-grained hard-core-shoulder

### Key Notation

$b$	Interconversion probability in the HCS model
$\varepsilon$	Non-ideality interaction parameter
$\ell$	Size of a system
$F_t$	Total free energy (Helmholtz energy)
$f = F_t/N$	Free energy per molecule (or per lattice site)
$G_t$	Total Gibbs energy

$G = G_t/N$	Gibbs energy per molecule (or per lattice site)
$G_{\text{mix}}$	Gibbs energy of mixing
$G_{\text{BA}}$	Gibbs energy of reaction
$\kappa$	The square of the range of molecular interactions
$k_B$	Boltzmann's constant
$k_d$	Force constant of dihedral motion in the CM model
$K$	Kinetic coefficient of forced interconversion
$L$	Kinetic coefficient of natural interconversion
$M$	Kinetic coefficient of diffusion (Mobility)
$\mu$	Chemical potential
$\mu_{\text{th}}$	Thermodynamic "bulk" part of the chemical potential
$N$	Number of molecules (or lattice sites)
$P$	Pressure
$p_r$	Probability (rate) of interconversion in the HL model
$\varphi$	Order parameter
$R$	Phase domain size
$R_{\text{id}}$	Ideal gas constant
$\rho$	Density
$S$	Structure Factor
$T$	Temperature
$q$	Wavenumber
$q_m$	Wavenumber corresponding to the maximum of the amplification factor
$q_m^s$	Wavenumber corresponding to the maximum of the structure factor
$q_-$	Wavenumber corresponding to the first root of the amplification factor
$q^*$	Wavenumber corresponding to the onset of microphase separation
$q^{**}$	Wavenumber corresponding to the termination of microphase separation
$\omega$	Amplification factor (phase domain growth rate)
$\Omega_t$	Total grand thermodynamic potential
$\Omega = \Omega_t/N$	Grand thermodynamic potential per lattice site
$x$	Molecular fraction
$\xi$	Correlation length of order-parameter fluctuations

## Chapter 1: Introduction

Typically, pure substances may be found with only one gaseous or liquid state, while their solid state may exist in various polymorphic crystalline states. The existence of multiple distinct liquid forms in a single component substance is more unusual since liquids lack the long-range order common to crystals. Yet, the existence of multiple amorphous liquid states in a single component substance, a phenomenon known as “liquid polyamorphism,” [9, 55, 56] has been observed or predicted in a wide variety of substances, such as superfluid helium [57, 58], high-pressure hydrogen [1, 35, 37, 38, 59], high-density sulfur [2, 51], phosphorous [60, 61], carbon [62], silicon [63–66], silica [67, 68], selenium and tellurium [69, 70], and cerium [71]. Liquid polyamorphism is also highly plausible in deeply supercooled liquid water [9, 13, 55, 56, 72–80].

A substance may be found to be polyamorphic by experimentally or computationally detecting a liquid-liquid phase transition (LLPT), which terminates at a liquid-liquid critical point (LLCP). For example, liquid polyamorphism, via the existence of two alternative supramolecular structures, has been hypothesized to explain the remarkable anomalies in the thermodynamic properties of supercooled water, namely a maximum in the temperature dependence of its density and its isothermal compressibility [81, 82], a maximum in the isobaric heat capacity [83], and an inflection point in its surface tension [84–87]. Simulations of water-like models [74–77, 79, 88–91], apparently supported by experiment [92, 93], have demonstrated the hy-

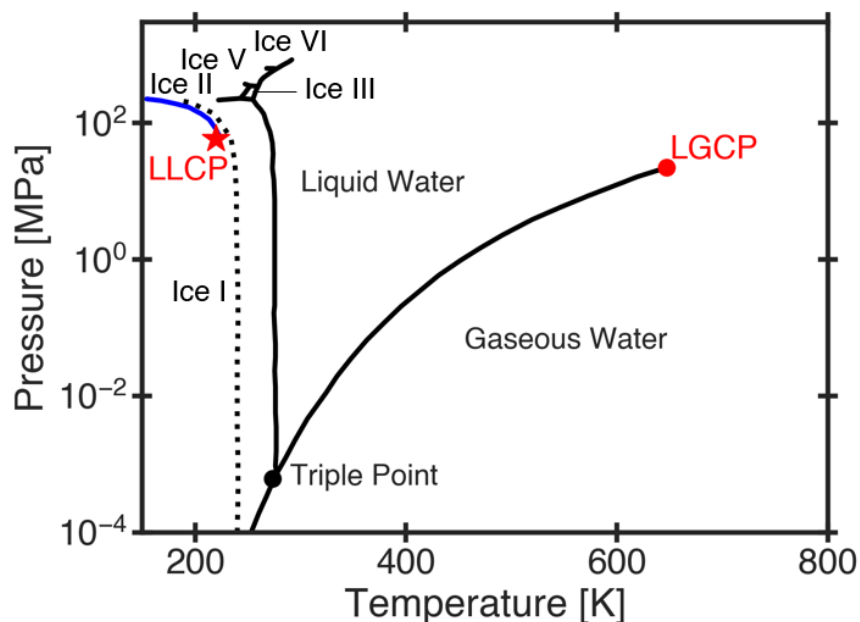


Figure 1.1: Hypothesized global pressure-temperature phase diagram for water. The black curves indicate the solid-solid and solid-liquid-gas phase transitions experimentally reported for water [11], while the blue curve indicates the hypothesized liquid-liquid phase transition. The dotted black curve represents the line of spontaneous ice nucleation [12]. The red circle is the liquid-vapor critical point (LVCP) and the red star is the hypothesized liquid-liquid critical point (LLCP) around 220 K and 60 MPa as suggested in Ref. [13].

pothesized LLPT in supercooled water, see Fig. 1.1.

Fluid polyamorphism ultimately originates from the complex interactions between molecules or supramolecular structures. However, it may be phenomenologically modeled through the reversible interconversion of two alternative molecular or supramolecular states [4, 9, 10]. The application of this “two-state” approach to the variety of polyamorphic substances could be just as a useful phenomenology or it may reflect the true microscopic origin of fluid polyamorphism. Indeed, there are a few substances, such as hydrogen, sulfur, phosphorous, and carbon, where the existence of alternative liquid or dense-fluid states is explicitly induced by a reversible chemical reaction: dimerization in hydrogen [1] or polymerization in sulfur, phosphorus, and carbon [2]. While equilibrium phase transitions in simple fluids have been well-studied, the descrip-

tion of phase transformations in the presence of interconversion between alternative molecular or supramolecular states, and in fluids far from equilibrium, is much less investigated [94–96].

The interconversion of two-states significantly effects both the thermodynamics and dynamics of fluid mixtures. In particular, molecular interconversion imposes an additional thermodynamic constraint, the chemical-reaction equilibrium condition, which reduces the number of thermodynamic degrees of freedom. In this case, the concentration of a binary mixture is no longer an independent variable, being a function of temperature and pressure. Consequently, a binary mixture with interconversion of species follows the Gibbs phase rule for a single-component substance. In the absence of interconversion, the binary mixture exhibits a critical point for each concentration. Collectively, these critical points make up a critical locus. The interconversion of species selects a single path through the planes of phase coexistence at fixed concentration, crossing the critical locus of the binary mixture at a unique point. Moreover, this path could cross the critical line, the line of triple points, or any other unique line on the phase diagram more than once. The resulting phase diagram can be viewed as the phase diagram of a polyamorphic single-component fluid with multiple fluid-fluid critical points.

The thermodynamic properties, being state functions, under interconversion equilibrium conditions are the same as those in the non-reacting binary mixture at the corresponding equilibrium temperature, pressure, and overall concentration. Therefore, at any point along the thermodynamic path selected by interconversion, the properties are affected by the proximity to the critical line of the non-reacting binary mixture. It should be noted that the evolution of the thermodynamic properties along the path (where the equilibrium concentration changes) is generally very different from the evolution of the same property at constant composition, which would typically be studied in non-reacting binary mixtures. This line in the interconverting mixture is

referred to as the “virtual critical line,” which may be used to describe the anomalous behavior of the thermodynamic properties along this path.

The interconversion of species also effects the dynamics of phase formation. Generally, a mixture of two liquids will phase separate if their interactions are not favorable for mutual mixing. The most recognizable example is almost complete separation of water and oil. Another example is a possible demixing of structural isomers, such as enantiomers with opposite molecular chirality [7, 97–99]. In contrast, solid ferromagnetic (such as iron) or ferroelectric (such as barium titanate) materials, in the absence of a magnetic or electric field, do not establish equilibrium coexistence between phases with alternative magnetizations or polarizations [94, 100, 101]. However, if liquids exhibit interconversion of species, similar to the flipping of magnetic spins or electric dipoles, the thermodynamics and dynamics of phase separation will dramatically change.

In this thesis, it is shown that molecular interconversion may destroy or restrict liquid-liquid phase separation. After a binary mixture, initially containing equal amounts of the alternative molecules, is quenched from the one-phase homogeneous region at a high temperature into the unstable region below the critical temperature of demixing at constant pressure, the species will separate through a process known as spinodal decomposition [102]. However, if the two species with the same density may rapidly interconvert (like in a mixture of enantiomers [7]), then to avoid the formation of an energetically unfavorable interface, the phases will compete with each other until one of them is eliminated [6]. This is the phenomenon of phase amplification, the result of the competition between the diffusive dynamics of phase separation and the “flipping” dynamics of interconversion. In magnetic and ferroelectric materials, away from the Curie temperature and in the absence of a magnetic or electric field, the phenomenon of phase amplification occurs naturally. In such materials, there is no restriction on the direction of magnetization or

polarization, meaning that there is no conservation of the number of magnetic spins or electric dipoles with a particular orientation. Similarly, in fluids with fast molecular interconversion, the conservation of the number of alternative molecules is broken and phase amplification could occur.

In interconverting fluids, the growth of one phase at the expense of another stable phase occurs to avoid the formation of an energetically unfavorable interface, and consequently, the coexistence of the alternative phases is destroyed [6]. Since the interface is crucial to phase amplification, in macroscopic systems where the interfacial energy is much smaller than the bulk energy, the system may enter a metastable state in which the energetic benefit of phase amplification is negligible [4]. Thus, the size of the system plays a crucial role in phase amplification. As discussed in Chapter 3, it is also shown that, in addition to smaller system sizes, a faster rate of the interconversion reaction and closer proximity to the LLC of demixing are necessary for one to observe phase amplification [4, 6].

In a nonequilibrium system, if an external force causes the alternative molecules to stay in equal numbers, the striking phenomenon of steady-state, restricted (“microphase”) separation into mesoscale domains may be observed. In equilibrium, examples of mesoscale structures are present in bicontinuous or spatially modulated microemulsions [103, 104] and microphase separation of diblock or polyelectrolyte copolymers [105, 106], where these mesoscale patterns are the result of the minimization of the equilibrium free energy [9, 107]. As discussed in Chapter 4, it is found that the structure of the phase domains formed from nonequilibrium microphase separation resembles modulated or bicontinuous microemulsion structures [9, 103–107]. However, contrary to the patterns formed in equilibrium or in metastable (“frozen”) conditions [108, 109] (like those commonly observed in glasses [110, 111]), these nonequilibrium structures persist in steady-state

due to the continuous energy supply. Thus, steady-state microphase separation is one of the simplest examples of dissipative structures in condensed matter. The characteristic length scale of this dissipative structure emerges as a result of the competition between forced interconversion and phase growth. If the source of forced interconversion is not sufficiently strong to overcome the natural interconversion of alternative species, then the phenomenon of phase amplification, the growth of one stable phase at the expense of another phase, is observed [4, 6, 112]. An external racemizing energy source can be achieved in physical systems through the interactions of energy-carrying particles, such as photons, that may break intramolecular bonds [111]. It can also be seen in biological cells through a flux of energy produced by ATP [113, 114] or it could be achieved chemically through an external flux of matter or heat [115–117].

The size of the system, rate of forced interconversion, and proximity to the LLCP are also important to observe microphase separation. In this thesis, it is found that there are two key conditions for microphase separation to be observed. First, if the characteristic size of the mesoscopic steady-state microphase domains is comparable to half the size of the system, then the system will produce the same two alternative phases that would be observed without interconversion [4, 5, 8]. As a result, the size of the system may “cut off” the system’s ability to phase separate into microdomains. Second, if the rate of forced interconversion is much faster than the natural interconversion or diffusion rate, then the external force dominates the systems’ kinetics and no phase formation is possible. Consequently, it is shown that the size of the system and the rate of the forced interconversion reaction are crucial components to observe microphase separation [4, 5, 8].

This thesis is organized as follows: In Chapter 2, the two-state thermodynamic approach to model fluid polyamorphism is discussed. The application of this approach is considered for

fluid-fluid transitions in hydrogen, sulfur, and substances exhibiting water-like anomalies. In Chapter 3, the Cahn-Hilliard model of spinodal decomposition (phase separation process that occurs after a binary mixture is quenched into the unstable region), is generalized to include equilibrium (natural) and nonequilibrium (forced) interconversion of species. In Chapter 4, the generalized Cahn-Hilliard theory is applied to describe the behavior of microscopic models of mixtures, simulated through molecular dynamics (MD) or Monte Carlo (MC) methods, which exhibit both natural and forced molecular interconversion. General concluding remarks and suggestions for future research are presented in Chapter 5.

## Chapter 2: Two-State Thermodynamics of Fluid Polyamorphism

In this chapter, the two-state thermodynamic approach for fluid polyamorphism is introduced (Sec. 2.1). The approach is applied to describe the fluid-fluid transition in high-pressure hydrogen (Sec. 2.2), high-density sulfur (Sec. 2.3), and fluids exhibiting water-like anomalies (Sec. 2.4). In addition to the phase behavior of these substances, the approach is also used to describe the anomalies in the interfacial properties of fluids exhibiting interconversion between species.

### 2.1 Interconversion of Two States

Consider a symmetric binary mixture of two species A and B with molecular fractions,  $x_B = x$  and  $x_A = 1 - x$ . Initially, it may be assumed that both species have the same densities ( $\rho = 1$ ), viscosities, and molecular weights. This system can be described by a Landau-Ginzburg free-energy functional with a single order parameter uniquely linked to the fraction of species B as,  $\varphi = x/x_c - 1$ , where  $x_c$  is the critical fraction. This functional reads as

$$F[\{\varphi\}] = \frac{1}{\rho} \int_V \left( \hat{G}(\varphi, T, P) + \frac{1}{2} \kappa |\nabla \varphi|^2 \right) dV \quad (2.1)$$

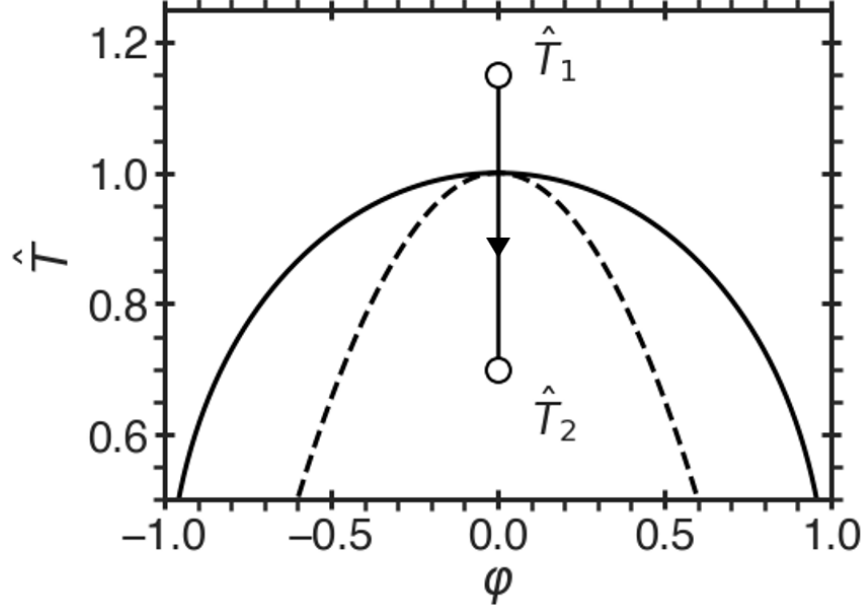


Figure 2.1: A symmetric binary mixture is quenched along the critical molecular fraction (where the order parameter is  $\varphi = 0$ ) from a point,  $\hat{T}_1$  in the one phase region to a point,  $\hat{T}_2$  below the critical temperature of demixing in the unstable region. The solid curve indicates the liquid-liquid coexistence (binodal), while the dashed curve indicates the limit of stability (spinodal).

where the first term represents the thermodynamic “bulk” free energy and the second term is included to describe the contribution to the free energy due to inhomogeneities within the system. For an isotropic system, the coefficient  $\kappa$  is the square of the range of intermolecular interactions, on the order of the square of the molecular size.

The bulk free energy density for the system,  $\hat{G}$ , is the reduced Gibbs energy,  $\hat{G} = G/k_B T_c$ , where  $k_B$  is Boltzmann’s constant and the critical temperature for liquid-liquid phase separation is  $T_c$ . The bulk free energy density may be expressed in the general form,

$$\hat{G} = \hat{G}_A + x\hat{G}_{BA} + \hat{G}_{\text{mix}} \quad (2.2)$$

where  $\hat{G}_{BA} = \hat{\mu}_B^0 - \hat{\mu}_A^0$  is the reduced difference between the Gibbs energies (chemical potentials) of pure species A and B, referred to as the Gibbs energy change of reaction. For the symmetric

binary-lattice (“regular solution”) model,  $\hat{G}_{\text{mix}}$  is formulated through the order parameter,  $\varphi$ , and in the meanfield approximation, it reads as

$$\hat{G}_{\text{mix}} = \hat{T} \left[ \left( \frac{1+\varphi}{2} \right) \ln \left( \frac{1+\varphi}{2} \right) + \left( \frac{1-\varphi}{2} \right) \ln \left( \frac{1-\varphi}{2} \right) \right] + \frac{\varepsilon}{4}(1-\varphi^2) \quad (2.3)$$

where  $\hat{T} = T/T_c$  is the reduced temperature and  $\varepsilon$  is a non-ideality interaction parameter, which generally depends on temperature and pressure. The conditions for liquid-liquid phase equilibrium is

$$\left. \frac{\partial \hat{G}_{\text{mix}}}{\partial \varphi} \right|_{T,P} = \frac{\hat{T}}{2} \ln \left( \frac{1+\varphi}{1-\varphi} \right) - \frac{\varepsilon}{2} \varphi = 0 \quad (2.4)$$

The critical molecular fraction,  $x_c$ , and critical temperature,  $T_c$ , are obtained from the thermodynamic stability conditions

$$\left. \frac{\partial^2 \hat{G}}{\partial \varphi^2} \right|_{T,P} = 0 \quad \text{and} \quad \left. \frac{\partial^3 \hat{G}}{\partial \varphi^3} \right|_{T,P} = 0 \quad (2.5)$$

as

$$x_c = 0.5 \quad \text{and} \quad T_c = \varepsilon/(2k_B) \quad (2.6)$$

Consider the interconversion between molecular states A and B through a reversible chemical reaction of the form



where  $k_1$  and  $k_2$  are the forward and reverse reaction rates, respectively. Since, for this system, the chemical reaction coordinate is the order parameter, the chemical reaction equilibrium condition

reads

$$\left. \frac{\partial \hat{G}}{\partial \varphi} \right|_{T,P} = \left. \frac{\partial \hat{G}_{\text{mix}}}{\partial \varphi} \right|_{T,P} - \hat{G}_{\text{BA}} = 0 \quad (2.8)$$

The reaction-equilibrium condition constrains the number of thermodynamic degrees of freedom for the system. Consequently, the fraction of interconversion, given through the order parameter  $\varphi$ , is no longer an independent thermodynamic variable, but instead, becomes a function of temperature and pressure. The reduced Gibbs energy change of the reaction,  $\hat{G}_{\text{BA}}$ , can be expressed through the reaction equilibrium constant,  $\mathcal{K}(\hat{T}, \hat{P}) = k_1/k_2$ , and is given, up to second-order in temperature and pressure, as

$$\hat{G}_{\text{BA}} = -\hat{T} \ln \mathcal{K}(\hat{T}, \hat{P}) = \hat{e} - \hat{s}\hat{T} + \hat{v}\hat{P} + \gamma\hat{T}\hat{P} + \frac{1}{2}\delta\hat{T}^2 - \frac{1}{2}\kappa\hat{P}^2 \quad (2.9)$$

where  $\hat{e} = e/(k_{\text{B}}T_c)$ ,  $\hat{s} = s/k_{\text{B}}$ , and  $\hat{v} = v/(k_{\text{B}}T_c)$  are the reduced energy, entropy, and volume changes of the reaction, while  $\gamma$ ,  $\delta$ , and  $\kappa$  are proportional to the volumetric expansivity, isobaric heat capacity, and isothermal compressibility changes of the reaction, respectively [9, 10].

The reduced chemical potential for such a system undergoing spinodal decomposition towards both chemical-reaction and phase equilibrium,  $\hat{\mu} = \mu/k_{\text{B}}T_c$ , is the reduced deviation of the chemical-potential difference in solution ( $\mu = \mu_{\text{A}} - \mu_{\text{B}}$ ) from its equilibrium value,  $\mu = 0$ . The reduced time-dependent chemical potential is found from the functional derivative of Eq. (2.1) as

$$\hat{\mu} = \hat{\mu}_{\text{th}} - \kappa \nabla^2 \varphi \quad (2.10)$$

where the order parameter depends on space and time,  $\varphi = \varphi(\mathbf{r}, t)$ . In this form, the chemical potential is comprised of a thermodynamic potential as  $\hat{\mu}_{\text{th}} = \partial \hat{G} / \partial \varphi|_{T,P}$ , and a spatial-dependent

part,  $\kappa \nabla^2 \varphi$ . The thermodynamic component [118] is

$$\hat{\mu}_{\text{th}} = \frac{\hat{T}}{2} \ln \left( \frac{1 + \varphi}{1 - \varphi} \right) - \frac{\varepsilon}{2} \varphi - \hat{G}_{\text{BA}} \quad (2.11)$$

Expanding the logarithmic term to first order in  $\varphi$  via a Taylor series around  $\varphi = 0$  (the value of the order parameter at the initial time  $t = 0$ ), gives  $\partial \hat{G} / \partial \varphi \approx \hat{\chi}_{q=0}^{-1} \varphi$ , where the inverse thermodynamic susceptibility in the limit of zero wavenumber is  $\hat{\chi}_{q=0}^{-1} = \partial^2 \hat{G} / \partial \varphi^2$ . In the meanfield regular-solution model, the inverse susceptibility scales as  $\hat{\chi}_{q=0}^{-1} \sim \Delta \hat{T}$ , where  $\Delta \hat{T} = T / T_c - 1$  is the reduced distance to the critical temperature. Therefore, the chemical potential defined in Eq. (2.10) in the first-order approximation becomes

$$\hat{\mu} \approx \Delta \hat{T} \varphi - \hat{G}_{\text{BA}} - \kappa \nabla^2 \varphi \quad (2.12)$$

It should be emphasized that the reduced chemical potential, given by Eq. (2.12), when the term related to interconversion is absent, is the same as obtained in the classical Cahn-Hilliard theory [102].

In addition to the chemical potential, the density and entropy are obtained from derivatives of the Gibbs energy, Eq. (2.2), as

$$\hat{\rho}(\hat{P}, \hat{T}) = \left( \frac{\partial \hat{G}}{\partial \hat{P}} \right)_{\varphi, \hat{T}}^{-1} = \left[ \frac{1}{\hat{\rho}_A} + x_e \frac{\partial \hat{G}_{\text{BA}}}{\partial \hat{P}} \Big|_{\varphi, \hat{T}} + \frac{\partial \hat{G}_{\text{mix}}}{\partial \hat{P}} \Big|_{\varphi, \hat{T}} \right]^{-1} \quad (2.13)$$

$$S(\hat{P}, \hat{T}) = - \frac{\partial \hat{G}}{\partial \hat{T}} \Big|_{\varphi, \hat{P}} = S_A - x_e \frac{\partial \hat{G}_{\text{BA}}}{\partial \hat{T}} \Big|_{\varphi, \hat{P}} - \frac{\partial \hat{G}_{\text{mix}}}{\partial \hat{T}} \Big|_{\varphi, \hat{P}} \quad (2.14)$$

where  $\hat{\rho}_A = \hat{\rho}_A(P, T)$  and  $S_A = S_A(P, T)$  are the density and entropy (per molecule) of state A

and  $x_e = x(\hat{P}, \hat{T})$  is the equilibrium fraction of species. Thus, from the appropriate specification of state A and the equilibrium reaction constant,  $\mathcal{K}$ , one may obtain all other thermodynamic properties, such as the isothermal compressibility and heat capacity, as well as the global phase diagram that includes both the vapor-liquid and the liquid-liquid transitions. In the next section, this is demonstrated by applying the two-state approach to the fluid-fluid phase transition in high-pressure hydrogen.

## 2.2 Fluid-Fluid Phase Transition in High-Pressure Hydrogen

Experiments and simulations have discovered that at extremely high pressures, highly-dense fluid (dimeric) hydrogen dissociates into atomistic fluid hydrogen [21, 34–45, 48, 59, 119–123]. In this section<sup>1</sup>, the two-state thermodynamic approach (Sec. 2.1) and the generalized law of corresponding states (obtained from reducing the temperature, pressure, and entropy by their critical values), in combination with the available experimental data and with the results of computations [21, 39–46, 48, 124], are utilized to predict the equation of state of hydrogen near the fluid-fluid phase transition (FFPT).

### 2.2.1 Phase Behavior of Hydrogen

The suggested global phase diagram of hydrogen, based only on the available experimental evidence for the fluid-fluid phase transition [34–38], the solid-liquid melting transition [14–17, 125–127], and the location of solid-metallic hydrogen [22, 29–33], which is supported by the most recent computational studies [21, 39–45, 47, 48, 124, 128–130], is shown in Fig. 2.2a. It

---

<sup>1</sup>This section was reproduced from Nathaniel R. Fried, Thomas J. Longo, and Mikhail A. Anisimov, *J. Chem. Phys.*, **157**, 101101 (2022); <https://doi.org/10.1063/5.0107043>, with the permission of AIP Publishing.

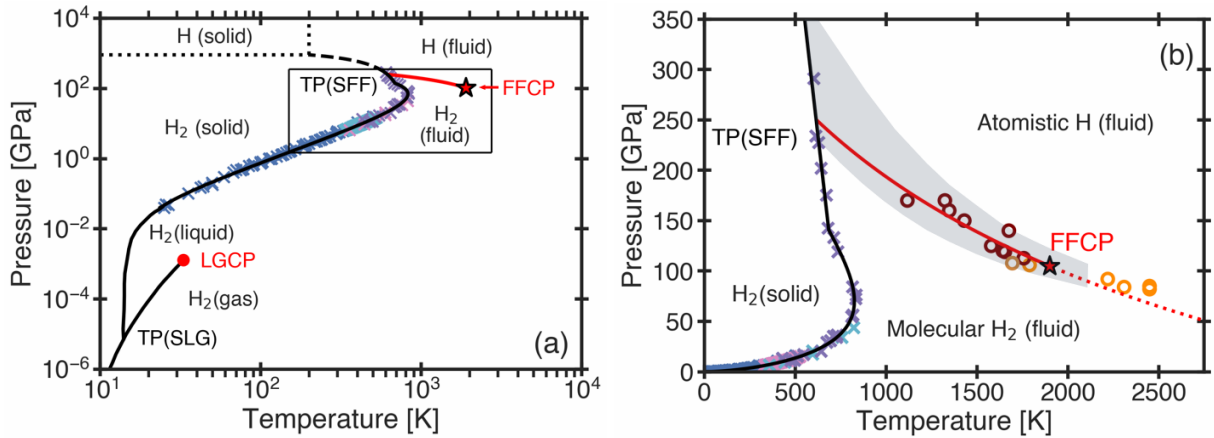


Figure 2.2: The global pressure-temperature phase diagram for hydrogen. (a) The full range from low to extreme pressures in logarithmic scale. The crosses indicate the experimental data for the solid-liquid melting transition presented in Diatschenko *et al.* [14] (blue), Datchi *et al.* [15] (cyan), Gregoryanz *et al.* [16] (pink), and Zha *et al.* [17] (purple). The solid black curves at low pressure ( $P \leq 0.1$  GPa) are the liquid-gas-solid phase transitions [18], while the solid black curve at high pressure ( $P > 0.1$  GPa) is the Kechin equation [19] as reported in ref. [17]. The black dashed curve is the predicted continuation of the melting line based on experimental and computational evidence [17,20,21], while the dotted lines represent the highly-debated prediction [22–28] of the domain of solid metallic hydrogen [22, 23, 28–33]. The red line is the first-order fluid-fluid phase transition adopted in this section. (b) The phase diagram of hydrogen at extreme conditions, in the area of the box in (a). The open circles are experimental data presented in Zaghoo *et al.* [34–36] (dark brown), McWilliams *et al.* [37] (light brown), and Ohta *et al.* [38] (orange). Simulation results [21, 39–46] are spread within the grey area and shown in detail in Fig. 2.3. The fluid-fluid phase transition (solid red) and Widom line (dotted red) are represented by Eq. (2.18). The red star is the location of the fluid-fluid critical point (FFCP) as adopted in this section.

illustrates the fact that a huge pressure gap separates the liquid-gas [18] and fluid-fluid phase transitions in hydrogen.

The adopted locations of the FFCP and the solid-fluid-fluid triple point (SFF-TP) in this section are based on the available experimental data [34–38] and on discussions present in the literature [42–44] (Table 2.1). It should be noted that the exact location of the FFCP is uncertain, as the interpretation of both the Zaghoo *et al.* [35] and Ohta *et al.* [38] experimental data have been highly debated [43, 131–133]. Most authors suggest that the experimental data of Ohta *et al.* [38], on the anomalies of the heating efficiency, are obtained in the supercritical region [43].

Table 2.1: The suggested locations of the FFCP and the SFF-TP in hydrogen.

	$P$ [GPa]	$T$ [K]	$\rho$ [g/cm <sup>3</sup> ]
FFCP	105	1900	0.8
SFF-TP	250	600	-

The results observed by Ohta *et al.* [38] have been interpreted [1] as being the anomalies of the heating efficiency along the “Widom line”, the line corresponding to the maximum of the fluctuations of the order parameter, which emanates from the critical point [9, 78, 134].

The significant discrepancy between the results of different computational models makes it impossible to utilize these results for a single equation of state. However, presenting the same results in reduced variables, as suggested by the law of corresponding states, allows the computational results to be used along with the experimental data for thermodynamic modeling. In Fig. 2.3, all of the available computational and experimental data on the fluid-fluid phase transition are presented in real units of pressure and temperature (Fig. 2.3a) and in reduced variables (Fig. 2.3b),  $\hat{P} = P/P_c$  and  $\hat{T} = T/T_c$ , where  $P_c$  and  $T_c$  are the critical pressures and temperatures obtained (or adopted) from different works. It has been found that the simulation data based on the Quantum Monte Carlo (QMC) approach could also be collapsed into the universal phase diagram by reducing the entropy by its critical value,  $\hat{S} = S/S_c$  [1]. In classical thermodynamics, the reference value for the entropy is arbitrary. Commonly, the value,  $S_c$ , is adopted as  $S_c = d\hat{P}/d\hat{T}|_{T=T_c}$  [135–138], which was found to be  $S_c = 0.8$  for all QMC simulations.

### 2.2.2 Phase Separation Coupled with Dimerization

Thermodynamically, the fluid-fluid transition in hydrogen can be modeled through the two-state approach (Sec. 2.1), in which state A represents the free atoms of hydrogen and state B

represents dimerized hydrogen atoms. The total Gibbs energy per hydrogen atom (reduced by  $R_{\text{id}}T_c$ , where  $R_{\text{id}}$  is the ideal-gas constant) is given by Eq. (2.2), where  $\hat{\mu}_A^\circ$  and  $\hat{\mu}_B^\circ$  are the Gibbs energies of hydrogen in the monatomic or diatomic states, respectively, and  $x$  is the fraction of hydrogen atoms in the diatomic state. Unlike the symmetric system considered in Sec. 2.1, the mixing of free hydrogen atoms and diatomic hydrogen is not symmetric, and thus,  $\hat{G}_{\text{mix}}$  may be modeled as

$$\hat{G}_{\text{mix}}(x) = \hat{T} \left[ \left(\frac{x}{2}\right) \ln \left(\frac{x}{2}\right) + (1-x) \ln(1-x) \right] + \varepsilon(\hat{T}, \hat{P}) x(1-x) \quad (2.15)$$

The dimensionless non-ideality parameter,  $\varepsilon = \varepsilon(\hat{T}, \hat{P})$ , may be approximated up to first order in  $\Delta\hat{T}$  and  $\Delta\hat{P}$ , as

$$\varepsilon(T, P) = \varepsilon_0 - \varepsilon_T \Delta\hat{T} + \varepsilon_P \Delta\hat{P} \quad (2.16)$$

where  $\Delta\hat{T} = \hat{T} - 1$  and  $\Delta\hat{P} = \hat{P} - 1$ .

The FFCP parameters are determined from the thermodynamic stability criteria (Eq. 2.5), such that the critical fraction and critical temperature of hydrogen atoms is given by

$$x_c = \sqrt{2} - 1 \quad \text{and} \quad T_c = 2(2 - \sqrt{2})^2 \varepsilon_0 \quad (2.17)$$

It should be noted that the first study to apply the two-state thermodynamic approach to high-pressure hydrogen was presented by Cheng *et al.* [21]. While the predictions of Cheng *et al.* for the FFPT are not in agreement with the results of all other simulations and experimental studies [45], their study provides a reasonable idea for how the non-ideality parameter,  $\varepsilon$ , might depend on pressure and temperature. Based on the suggested trend,  $\varepsilon_T$  and  $\varepsilon_P$  are optimized to

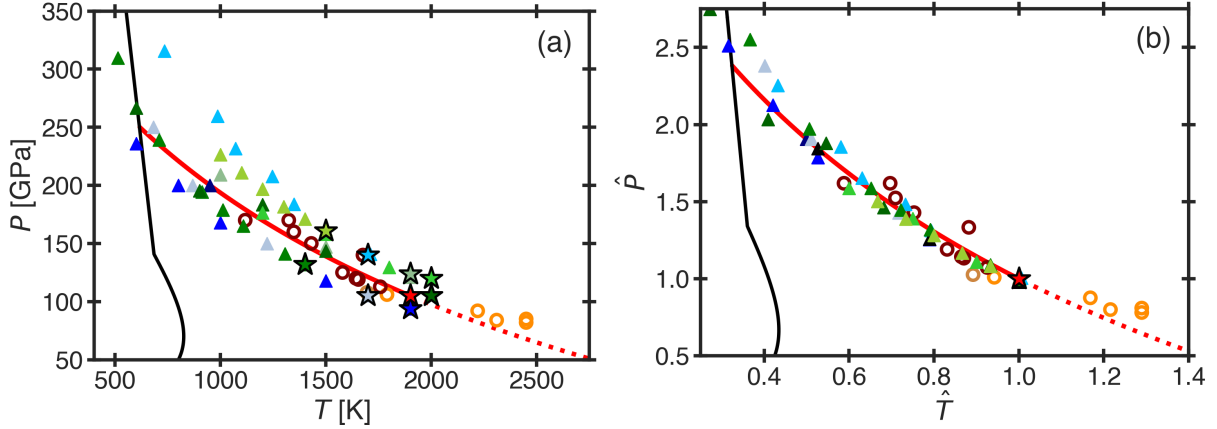


Figure 2.3: Unifying the different simulation results with experimental data of hydrogen by the generalized law of corresponding states. (a) Experimental and simulation results for the fluid-fluid phase transition (FFPT). (b) Unified representation of the FFPT by reducing pressure,  $\hat{P} = P/P_c$ , temperature,  $\hat{T} = T/T_c$ , and the critical value of the entropy,  $\hat{S} = S/S_c$ . In (a) and (b), the open circles are the experimental data of Zaghoo *et al.* [34–36] (dark brown), McWilliams *et al.* [37] (light brown), and Ohta *et al.* [38] (orange). The computational results are indicated by the triangles: blue tints correspond to the Density Functional Theory (DFT) simulations of Bonev *et al.* [47] (dark blue), Morales *et al.* [48] (blue), Hinz *et al.* [44] (sky blue), and Karasiev *et al.* [45] (light blue). Meanwhile, green tints correspond to the Quantum Monte Carlo (QMC) simulations of Morales *et al.* [48] (dark sea green), Lorenzen *et al.* [39] (green), Perlioni *et al.* [41] (dark green), Mozzola *et al.* [42] (lime green), and Tirelli *et al.* [46] (yellow green). The colored stars correspond to the reported (or adopted in this section) critical points for each data set. The solid black curve is the solid-fluid phase transition line as discussed in Fig. 2.2, and the red solid line is the FFPT predicted in this section.

agree with the behavior of hydrogen from the available computational data [41–44, 46, 48], and consequently, these parameters were adopted as  $\varepsilon_T = 2.062$  and  $\varepsilon_P = -0.175$ . The asymmetric Gibbs energy of mixing is illustrated in Fig. 2.4a along with the fluid-fluid coexistence, calculated via the common tangent method, and the limit of absolute stability (spinodal), calculated via the thermodynamic stability conditions.

The condition for chemical-reaction equilibrium is given by  $\partial\hat{G}/\partial x|_{T,P} = 0$ , resulting in the balance of the Gibbs energy of reaction,  $\hat{G}_{BA}$ , and the exchange chemical potential of mixing,

$\hat{\mu}_{\text{mix}} = \partial \hat{G}_{\text{mix}} / \partial x |_{\hat{T}, \hat{P}}$ , such that thermodynamic equilibrium follows from

$$\hat{G}_{\text{BA}} = -\hat{\mu}_{\text{mix}} \quad (2.18)$$

The Gibbs energy of reaction,  $\hat{G}_{\text{BA}} = \hat{G}_{\text{BA}}(\hat{T}, \hat{P})$ , may be approximated up to second order in  $\hat{T}$  and  $\hat{P}$ , as in Eq. (2.9). To balance the Gibbs energy of reaction, Eq. (2.9), with the derivative of the Gibbs energy of mixing,  $\hat{G}_{\text{BA}}$  is expressed as an expansion in  $\Delta \hat{T}$  and  $\Delta \hat{P}$  as

$$\hat{G}_{\text{BA}} = u - a\Delta \hat{T} + b\Delta \hat{P} + g\Delta \hat{T}\Delta \hat{P} + \frac{d}{2}(\Delta \hat{T})^2 - \frac{k}{2}(\Delta \hat{P})^2 \quad (2.19)$$

where the modified coefficients of the thermodynamic balance, Eq. (2.19), are related to the coefficients of reaction, Eq. (2.9), as:

$$\begin{aligned} \hat{e} &= u + a - b + g + \frac{d}{2} - \frac{k}{2} \\ \hat{s} &= a + g + d \\ \hat{v} &= b - g + k \end{aligned} \quad (2.20)$$

along with  $\gamma = g$ ,  $\delta = d$ , and  $\kappa = k$ .

If the Gibbs energy of mixing,  $\hat{G}_{\text{mix}}$ , would be symmetric with respect to  $x$ , then  $\hat{G}_{\text{BA}} = -\hat{\mu}_{\text{mix}} = 0$ , could describe the conditions for both reaction equilibrium and fluid-fluid phase equilibrium [9]. However, since the monatomic and diatomic mixing is asymmetric, the condition for the balance of phase and reaction equilibrium, Eq. (2.18), is given through

$$\frac{\hat{\mu}_{\text{mix}}}{\hat{T}} = a_2 \left( \frac{\varepsilon(T, P)}{\hat{T}} - \varepsilon_0 \right)^2 + a_1 \left( \frac{\varepsilon(T, P)}{\hat{T}} - \varepsilon_0 \right) + a_0 \quad (2.21)$$

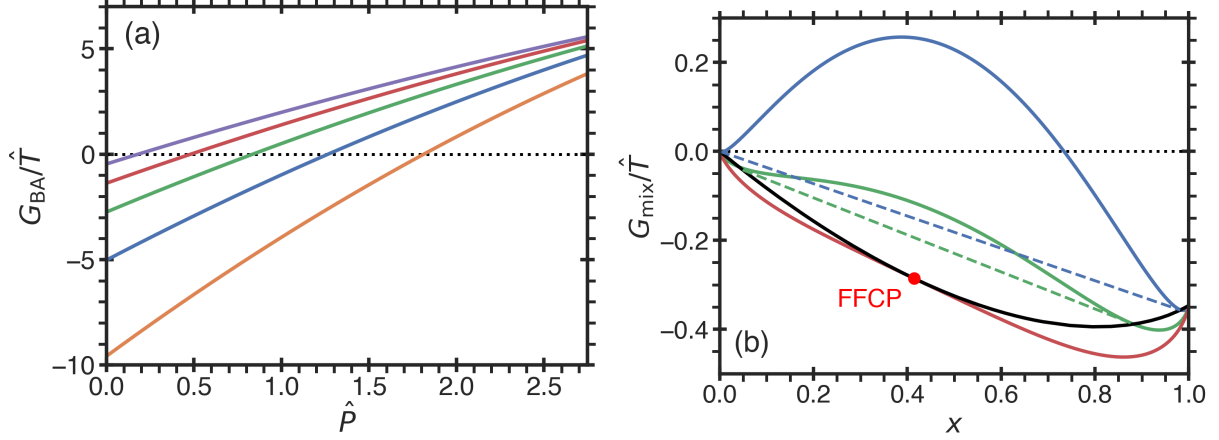


Figure 2.4: The components of the Gibbs energy (per atom) for hydrogen in the vicinity of the fluid-fluid phase transition. (a) The Gibbs energy of reaction,  $G_{BA}$ , as given by Eq. (2.9). The isotherms are  $T = 0.5T_c$  (orange),  $T = 0.75T_c$  (blue),  $T = T_c$  (green),  $T = 1.25T_c$  (red), and  $T = 1.5T_c$  (purple). (b) The Gibbs energy of mixing,  $G_{mix}$ , as given by Eq. (2.15).  $G_{mix}$  is shown as a function of the fraction of hydrogen atoms in the diatomic state,  $x$ , for isotherms  $T = 0.5T_c$  (blue),  $T = 0.75T_c$  (green), and  $T = T_c$  (red) at  $P = P_c$ . The solid curve corresponds to the fluid-fluid coexistence.

where the coefficients  $a_0 = -0.502$ ,  $a_1 = 0.166$ , and  $a_2 = -0.071$ .

The developed equation of state is formulated through the Gibbs energy for the system as a function of temperature and pressure. Due to the interconverting nature, the two-states of hydrogen are thermodynamically equivalent to a single component system. Consequently, this produces an equation of state in terms of the equilibrium fraction of dimerized atoms,  $x_e = x_e(T, P)$ , and the density of the system,  $\rho = \rho(T, P)$ . The equation of state presented in this section contains seven adjustable parameters: five from the Gibbs energy of reaction,  $G_{BA}$ , ( $u$ ,  $a$ ,  $b$ ,  $g$ , and  $k$ ), Eq. (2.9) and two from the non-ideality parameter in the Gibbs energy of mixing ( $\varepsilon_T$  and  $\varepsilon_P$ ), Eq. (2.16). The number of adjustable parameters are reduced from the following analysis of the available computational data on hydrogen in the vicinity of the fluid-fluid critical point.

From the computational heat capacity data presented by Karasiev *et al.* [45], the heat-

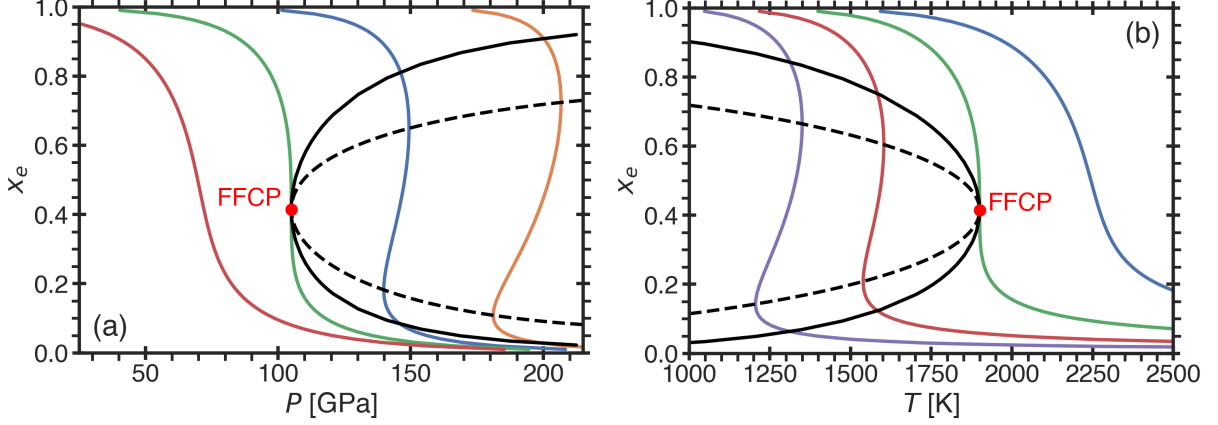


Figure 2.5: Equilibrium fraction of hydrogen atoms in the diatomic state,  $x_e$ . (a) Equilibrium fraction-pressure diagram for  $T = 0.5T_c$  (orange),  $T = 0.75T_c$  (blue),  $T = T_c$  (green), and  $T = 1.25T_c$  (red). (b) Equilibrium fraction-temperature diagram for  $P = 0.75P_c$  (blue),  $P = P_c$  (green),  $P = 1.25P_c$  (red),  $P = 1.5P_c$  (purple). The solid and dashed black curves are, respectively, the fluid-fluid coexistence and the limit of thermodynamic stability (spinodal).

capacity change of reaction is approximated to be  $\delta \approx 0$ , and from the computational isothermal-compressibility data presented in the supplemental material of Pierleoni *et al.* [41], it is approximated that  $\kappa \approx 0.625$  [ $\text{mm}^3/\text{GPa} \cdot \text{mol}$ ]. Additionally,  $e = -108$  [ $\text{kJ}/\text{mol}$ ] is adopted based on the known value of the bond dissociation energy of  $\text{H}_2$  [139]. As discussed above,  $\varepsilon_T$  and  $\varepsilon_P$  are assigned as  $\varepsilon_T = 2.062$  and  $\varepsilon_P = -0.175$ .

From these findings, the number of free parameters have been reduced to three:  $a$ ,  $b$ , and  $g$ . The values of the remaining free parameters are determined as  $a = -4.95$ ,  $b = 0.044$ , and  $g = 0.0124$  from the computational and experimental data utilizing the generalized law of corresponding states (Fig. 2.3). Using the relations between these parameters and the physical parameters in Eq. (2.9), the following parameters are estimated: the entropy change of the reaction as  $s = -34.0$  [ $\text{J}/\text{K} \cdot \text{mol}$ ], the volume change of the reaction as  $v = 393$  [ $\text{mm}^3/\text{mol}$ ], and the volume-expansivity change of the reaction as  $\gamma = 0.0677$  [ $\text{mm}^3/\text{K} \cdot \text{mol}$ ]. The Gibbs energy change of reaction is shown in Fig. 2.4b. It demonstrates that the pressure is the major factor in

the behavior of  $G_{\text{BA}}$ .

Using the Gibbs energy of mixing, Eq. (2.15), the Gibbs energy of reaction, Eq. (2.9), and the variables determined from the universal phase diagram, the equilibrium fraction of hydrogen atoms in the dimerized state,  $x_e$ , is determined from Eq. (2.18). The corresponding equilibrium-fraction phase diagrams are presented in Fig. 2.5(a,b). At higher temperatures and lower pressures, the equilibrium composition changes from the dimeric state  $x_e = 1$  to the monomeric state  $x_e = 0$ .

The density of species is expressed through the equilibrium fraction via Eq. (2.13), and with use of Eq. (2.15) for  $\hat{G}_{\text{mix}}$  is given in the form [9]

$$\hat{\rho}(\hat{P}, \hat{T}) = \left( \frac{\partial \hat{G}}{\partial \hat{P}} \right)_{\hat{T}}^{-1} = \left[ \frac{1}{\hat{\rho}_A} + x_e \frac{\partial \hat{G}_{\text{BA}}}{\partial \hat{P}} + \frac{\partial \varepsilon}{\partial \hat{P}} x_e (1 - x_e) \right]^{-1} \quad (2.22)$$

where  $\hat{\rho}_A = \hat{\rho}_A(\hat{P}, \hat{T})$  is the volume of the monatomic hydrogen state, and may be expressed up to second-order in  $\Delta \hat{T}$  and  $\Delta \hat{P}$  as

$$\hat{\rho}_A = \hat{\rho}_c - \hat{\rho}_0 \Delta \hat{T} + \hat{\rho}_1 \Delta \hat{P} + \hat{\rho}_2 \Delta \hat{T} \Delta \hat{P} - \hat{\rho}_3 (\Delta \hat{P})^2 + \hat{\rho}_4 (\Delta \hat{T})^2 \quad (2.23)$$

Using the most recent QMC simulations presented in Tirelli *et al.* [46],  $\hat{\rho}_A$  is estimated by Eq. (2.23) with coefficients:  $\hat{\rho}_c = 1.01$ ,  $\hat{\rho}_0 = 0.25$ ,  $\hat{\rho}_1 = 0.56$ ,  $\hat{\rho}_2 = 0.56$ ,  $\hat{\rho}_3 = 0.21$ , and  $\hat{\rho}_4 = 0.12$ . The corresponding pressure-density phase diagram is presented in Fig. 2.6, and demonstrates a good agreement with the computational data in the vicinity of the FFCP.

It is noted that the properties observed in experimental studies (*e.g.* conductivity, reflectivity, thermal efficiency, etc.) could be indirectly related to the order parameter for the FFPT in

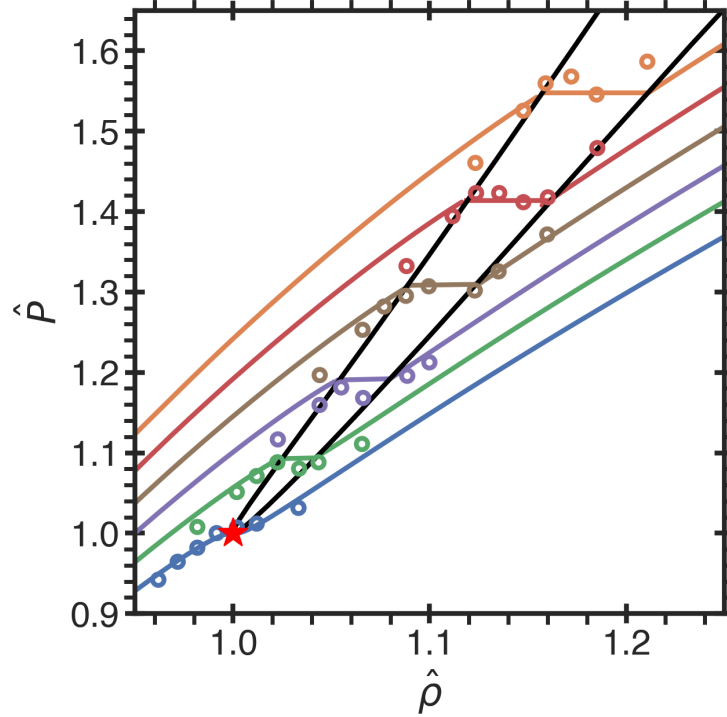


Figure 2.6: The pressure-density phase diagram of hydrogen based on the equation of state developed in this section. The open circles correspond to the QMC simulations of Tirelli *et al.* [46]. Isotherms are  $\hat{T} = 0.67$  (orange),  $\hat{T} = 0.73$  (red),  $\hat{T} = 0.8$  (brown),  $\hat{T} = 0.87$  (purple),  $\hat{T} = 0.93$  (green), and  $\hat{T} = 1.0$  (blue). The fluid-fluid coexistence is shown by the solid black curve. The red star is the FFCP adopted in this section.

hydrogen,  $\varphi = x/x_c - 1$ . The measurable quantities (such as density or conductivity) are coupled to the order parameter.

There is a remarkable analogy between the challenges in thermodynamic modeling of fluid polyamorphism in hydrogen and that in supercooled water. In both cases, there is a reasonable agreement among the scientific community on the shape and location of the first-order transition line, while the position of the corresponding FFCP and LLCP are highly uncertain and subjects of current debate in the literature [13, 34–36, 43, 78, 131–133]. This uncertainty, in both hydrogen and water, is due to the extreme conditions of the phenomena. In supercooled water, the liquid-liquid transition is hidden below the temperature of spontaneous ice formation [75, 78],

while in hydrogen, the fluid-fluid transition occurs at immensely high pressures (millions of atm) [43]. Consequently, it is not surprising that the available computational or experimental data are scarce [40, 43, 44]. In this section, it has been shown that despite the uncertainty in determining the location of the FFCP in hydrogen, thermodynamic modeling provides a principle direction to predict the equation of state for the system. Remarkably, the law of corresponding states can be utilized to reconcile the different computational models of hydrogen and experiment [21, 34–45, 48, 124] into a unified equation of state. An additional parameter has been included to generalize the law of corresponding states, the entropy at the critical point ( $S_c$ ), which provides the opportunity for further studies of hydrogen, both experimental and computational, to be unified under the general approach presented in this section.

### 2.3 Liquid-Liquid Phase Transition in High-Density Sulfur

While the fluid-fluid phase transition in hydrogen was induced by the dimerization reaction, a fluid-fluid phase transition may also be induced by more complex chemical reactions or interactions, such as polymerization or gelation. An example of polymerization induced fluid polyamorphism was recently discovered in high-density sulfur [51]. A polymerized state of sulfur exists above 433 K [140–144]). It has been experimentally demonstrated that well above the liquid-gas critical pressure (in the range from 0.5 to 2.0 GPa around 1000 K), sulfur exhibits a LLPT indicated by a discontinuity in density from a low-density-liquid (LDL) monomer-rich phase to a high-density-liquid (HDL) polymer-rich phase [51]. However, with further increase of temperature, as the system approaches the liquid-gas phase transition (LGPT), the polymer chains gradually dissociate. A schematic representation of the phase diagram in sulfur is illustrated in

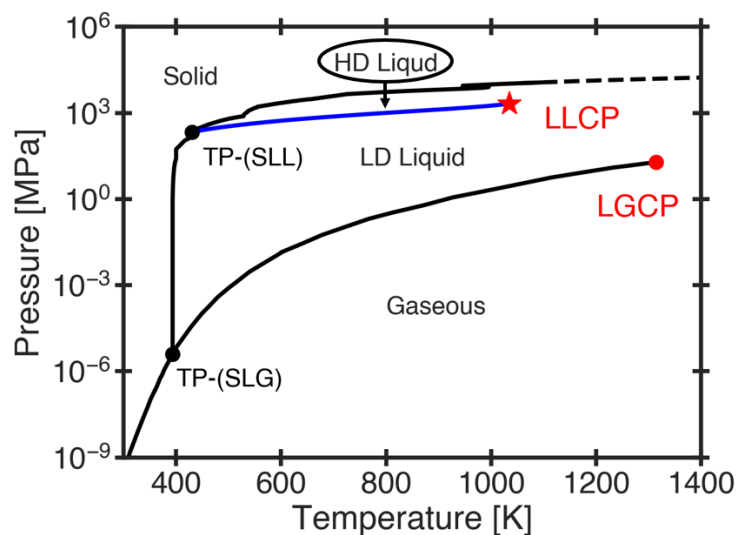


Figure 2.7: A schematic representation of the phase diagram of sulfur. The solid black curves represent the solid-liquid-gas phase transition in sulfur [49–51], while the blue curve represents the experimentally verified liquid-liquid phase transition [51]. The dashed black line is the predicted continuation of the melting line based on experimental evidence [49]. The black circles are the solid-liquid-liquid triple point (TP-SLL) and the solid-liquid-gas triple point (TP-SLG), while the red circle is the liquid-gas critical point (LGCP) and the red star is the liquid-liquid critical point (LLCP).

Fig. 2.7.

In this section<sup>2</sup>, the liquid-liquid phase transition in high-density sulfur is considered via a simple model that may describe liquid polyamorphism in a variety of chemically-reacting fluids. This model is referred to as the “maximum-valence model,” as it combines the ideas of two-state thermodynamics [9] with the maximum-valence approach [145–147], in which atoms may form covalent bonds via a reversible reaction, changing their state according to their bond number. By mimicking the valence structure and maximum bond number,  $z$ , the maximum-valence model predicts the LLPT in systems with dimerization ( $z = 1$ ), polymerization ( $z = 2$ ), and gelation ( $z > 2$ ). The maximum-valence model, simulated via Molecular dynamics (MD) methods, is

<sup>2</sup>This section was reproduced from Nikolay A. Shumovskyi, Thomas J. Longo, Sergey V. Buldyrev, and Mikhail A. Anisimov, *Phys. Rev. E*, **106**, 015305 (2022); <https://doi.org/10.1103/PhysRevE.106.015305>, with the permission of APS Publishing.

utilized to model the liquid-liquid phase transition in high-density sulfur. In particular, it will be demonstrated that when the bonded atoms attract each other stronger than to the unbonded atoms, phase separation is coupled to polymerization generating the LLPT in sulfur.

### 2.3.1 Maximum-Valence Model

The polymerization of a sulfur-like system ( $z = 2$ ) is modeled by characterizing each atom by its coordination number, the number of bonds it has with other atoms. Depending on the coordination number, each atom is assigned to distinguished states:  $S_0$  (with zero bonds),  $S_1$  (with one bond), and  $S_2$  (with two bonds). Atoms cannot form more than two bonds and, consequently, will polymerize into a linear polymer. All of the atoms in the system may change their state by forming or breaking a covalent bond via a reversible reaction. Fig. 2.8a depicts the three types of reversible reactions that may occur in the system. In this section, it is demonstrated that the minimum ingredients required to produce a LLPT are the following: i) the van der Waals interactions between atoms, which produce a LGPT; ii) covalent bonds between atoms, which induce polymerization; and iii), as hypothesized here, additional van der Waals interactions between atoms with maximum valency (having two bonds), which couple phase segregation to polymerization. These three ingredients are illustrated by square-well potentials in Figs. 2.8(b-d).

Physically, the additional attraction between atoms in neighboring chains may stem from the fact that in real polymers the covalent bond is shorter than the diameter of the unbonded (“free”) atoms, such that the attractive wells of bonded atoms in neighboring chains overlap with each other [148–153]. This effectively creates an additional zone of attraction between polymer chains, which is a common attribute that produces LLPTs in soft-core potentials [150, 151].

In these models, the atoms which penetrate the soft-core, can be regarded as bonded, which generate an additional “effective” attractive well due to the fact that such “bonded” atoms have more neighbors in their attractive range [154]. However, the explicit shortening of the covalent bonds between atoms would require the development of a microscopic Hamiltonian for this phenomenon, which would be most desirable for a future study. Therefore, for simplicity, instead of shortening the length of the covalent bonds, this effect is accounted for in the model through the additional “effective” square-well attraction (iii). Without this potential, with characteristic energy  $\epsilon_{22}$ , and consequently, in the absence of polymerized atoms, no LLPT will occur. It is noted that this simplification is in the spirit of common semi-phenomenological models of non-ideal binary mixtures, such as the Flory-Huggins theory of polymer solutions [155–158] or a regular-solution model [159].

The three ingredients of interactions were implemented in the maximum-valence model via an event-driven MD technique [160, 161]; in particular, a discrete MD package (DMD) is utilized that only includes particles interacting through spherically-symmetric step-wise potentials, which may form bonds via reversible reactions [162]. Simulations are performed in an NVT ensemble of  $N = 1000$  atoms in a cubic box with periodic boundaries at various constant densities and temperatures. The temperature is controlled by a Berendsen thermostat [163]. The van der Waals and covalent-bonding interactions are implemented by separating each atom into two overlapping hard spheres (a core and a shell), with the same diameter  $\sigma$  and mass  $m$ , see Figs. 2.8(b-d). The connection between the core and its shell is represented by an infinite square-well potential of width  $d \ll \sigma$ . The cores and shells of different atoms do not interact with each other. The core represents the atom without its valence electrons. It interacts with other cores via a wide potential well with depth  $\epsilon$  and width  $w = 0.4\sigma$  (the parameters are chosen as an example, Fig. 2.8b), which

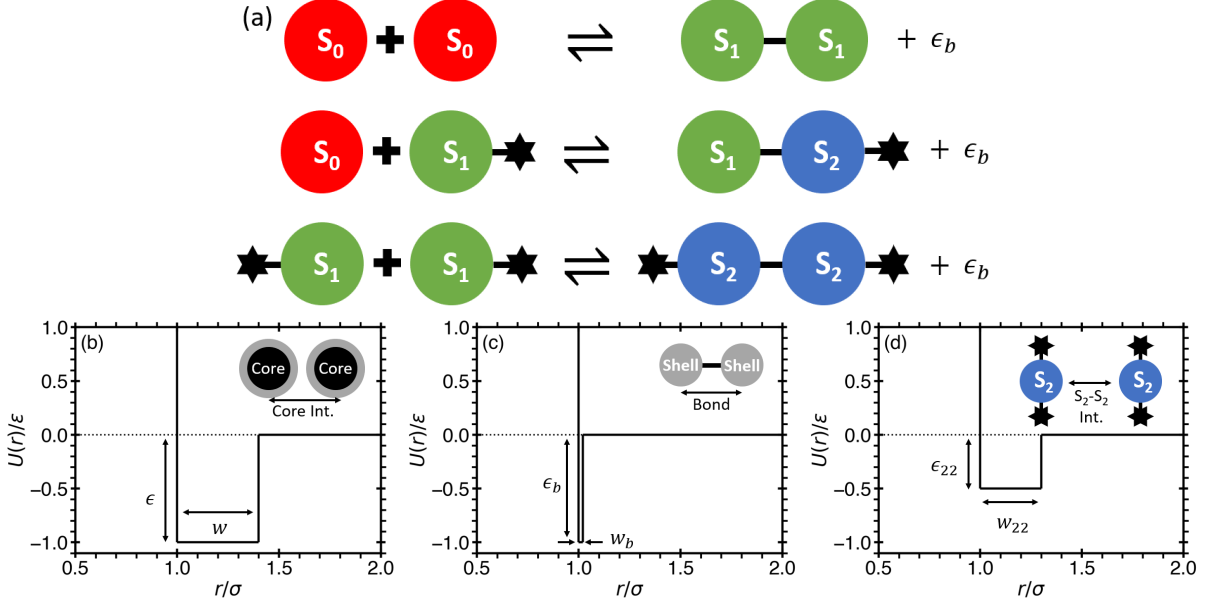


Figure 2.8: Reactions and interactions in the maximum-valence model. (a) The three types of covalent bond-forming reversible chemical reactions that may occur in the system. If two atoms without bonds ( $S_0$ ) collide with each other, they may form a bond and become  $S_1$  atoms. If a  $S_0$  and  $S_1$  atom collide, they may form a bond and become  $S_1$  and  $S_2$  atoms, respectively. If two  $S_1$  atoms collide with each other, they form an additional bond and become  $S_2$  atoms. (b-d) The three major interactions between atoms, in which each atom is composed of a core and shell, both with a radius  $\sigma$  and mass  $m$ .  $U(r)$  is the pair potential energy and  $r$  is the distance from the center of an atom. (b) The cores of each atom interact with an attractive square well of depth  $\epsilon = 1$  and width  $w = 0.4$ . (c) The shells may react to form covalent bonds that consist of a narrow well with depth  $\epsilon_b = 1$  and width  $w_b = 0.02$ . (d) Phase segregation is coupled to polymerization via the additional attractive interactions between atoms in state  $S_2$ , described by a square well of depth  $\epsilon_{22} = 0.5$  and width  $w_{22} = 0.3$ .

models the van der Waals interactions in the system. Meanwhile, the shell represents the outer valence electron cloud. It interacts with other shells via a narrow potential well with depth  $\epsilon_b = \epsilon$  and width  $w_b = 0.02\sigma$  (Fig. 2.8c), which models the breaking and forming of covalent bonds.

In the absence of the shell, this system has a liquid-gas critical point (LGCP) at  $\rho_c^{\text{LG}} = N/V = 0.35 \pm 0.05$ ,  $T_c^{\text{LG}} = 1.04 \pm 0.01$ , and  $P_c^{\text{LG}} = 0.094 \pm 0.005$  [153], well above the equilibrium crystallization line, which was forced to be at low temperature by selecting the appropriate width,  $w$ , of the potential. It is noted that all physical parameters are normalized by the appropriate combination of mass  $m$ , length  $\sigma$ , and energy  $\epsilon$  units, as used in Ref. [153]. When the

shell interactions are included and the system may form covalent bonds, the location of the LGCP changes, but not significantly. In addition to the wide and narrow wells, an additional attractive potential well is introduced (with depth  $\epsilon_{22} = 0.5\epsilon$  and width  $w_{22} = 0.3\sigma$ , Fig. 2.8d) for the van der Waals interaction between the shells of the atoms with two bonds (both in the state  $S_2$ ), which are not chemically bonded to each other.

It should be noted that during either the formation or breaking of a bond, the new state of the reacting particles may modify the potential energy of the interactions with their non-bonded neighboring particles [162]. In the maximum-valence model, this occurs when particles in the state  $S_1$  convert to the state  $S_2$  (or vice versa). To maintain the conservation of energy, the change of the total potential energy,  $\Delta U$ , is calculated due to the change of the state of the reacting particles and subtracted from the kinetic energy of the reacting pair. As a consequence, the equations for computing the new velocities [162] may not have real solutions. In this case, the bond will not form or break, and the reacting particles will conserve their states through an elastic collision.

### 2.3.2 Phase Separation Coupled with Polymerization

Figure 2.9a illustrates isotherms on a pressure-density ( $P$ - $\rho$ ) plane, which exhibit two sets of van der Waals loops. The loops correspond to the LGCP, located at low density and pressure, and the LLCP, located at a higher density and pressure. Fig. 2.9b illustrates the LG and LL coexistence on a  $P$ - $T$  plane along with the critical isochores. At the triple point (TP), the gaseous, LDL, and HDL phases coexist. In contrast to the ST2 model for water [74], but in agreement with spherically symmetric models [151, 164], the  $P$ - $T$  line of the LL coexistence has a positive slope.

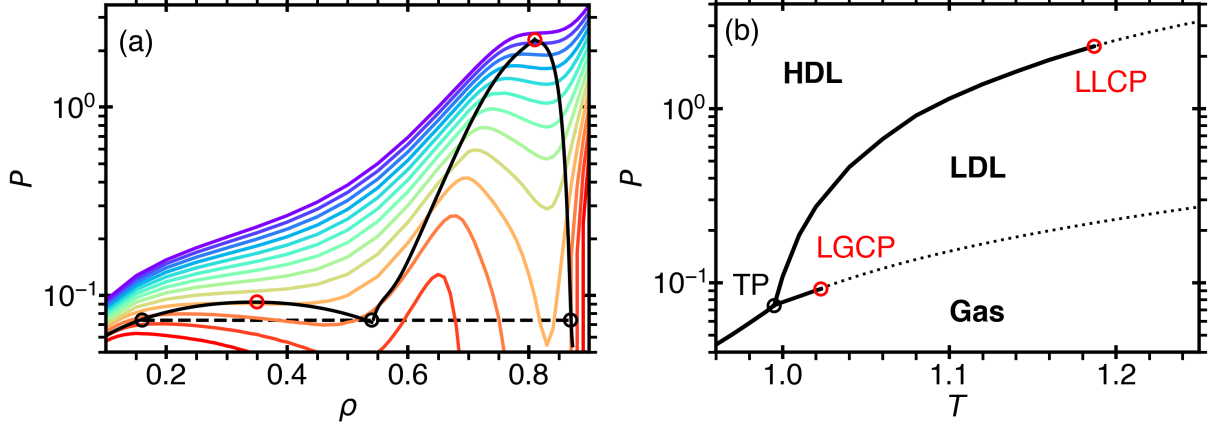


Figure 2.9: Phase diagrams for the maximum-valence model (with  $\epsilon_{22} = 0.5$  and  $\epsilon_b = 1.0$ ) obtained in an NVT ensemble after  $t = 10^6$  time units. (a) The isotherms in the  $P$ - $\rho$  plane are  $T = 0.96 - 1.20$  (red-purple) in steps  $\Delta T = 0.02$ . (b) The liquid-gas and liquid-liquid critical isochores in the  $P$ - $T$  plane are  $\rho_c^{\text{LG}} = 0.35$  and  $\rho_c^{\text{LL}} = 0.81$  as indicated by the lower and upper dashed lines, respectively. In both figures, the liquid-gas and liquid-liquid coexistence curves are calculated via the Maxwell construction and indicated by the solid curves. The liquid-gas ( $T_c^{\text{LG}} = 1.023$ ,  $P_c^{\text{LG}} = 0.0922$ ,  $\rho_c^{\text{LG}} = 0.35$ ) and liquid-liquid ( $T_c^{\text{LL}} = 1.187$ ,  $P_c^{\text{LL}} = 2.28$ ,  $\rho_c^{\text{LL}} = 0.81$ ) critical points are indicated by the red open circles, while the triple point ( $P^{\text{TP}} = 0.0738$ ,  $T^{\text{TP}} = 0.995$ ) is indicated by the black open circles.

Figure 2.10a presents the LG and LL coexistence curves on a  $T$ - $\rho$  phase diagram. Although there is a distribution of polymer chains with varying lengths, a simple way to characterize the degree of polymerization is to find the fractions  $x_0$ ,  $x_1$  and  $x_2$  of atoms in states  $S_0$ ,  $S_1$  and  $S_2$ . Due to the conservation of the number of atoms,  $x_0 + x_1 + x_2 = 1$ . The fraction  $x_2$  was computed based on the asymmetric LL coexistence curve (Fig. 2.10a). Remarkably,  $x_2$  was found to be symmetric and centered around  $x_2 = 0.5$  as shown in Fig. 2.10b. Consequently, the sum  $x_0 + x_1 = 1 - x_2$  has the same symmetry. This feature suggests that  $1 - x_2$  may be viewed as the appropriate order parameter for the LLPT coupled with polymerization. In contrast, the density,  $\rho - \rho_c^{\text{LG}}$ , is the order parameter for the LGPT, as commonly accepted. The symmetric nature of  $x_2$ , and the fact that  $S_1$  atoms are the intermediate states in the formation of polymer chains, enables a two-state thermodynamic approach [9] by reducing this model to two alternative states, with fractions  $x_2$

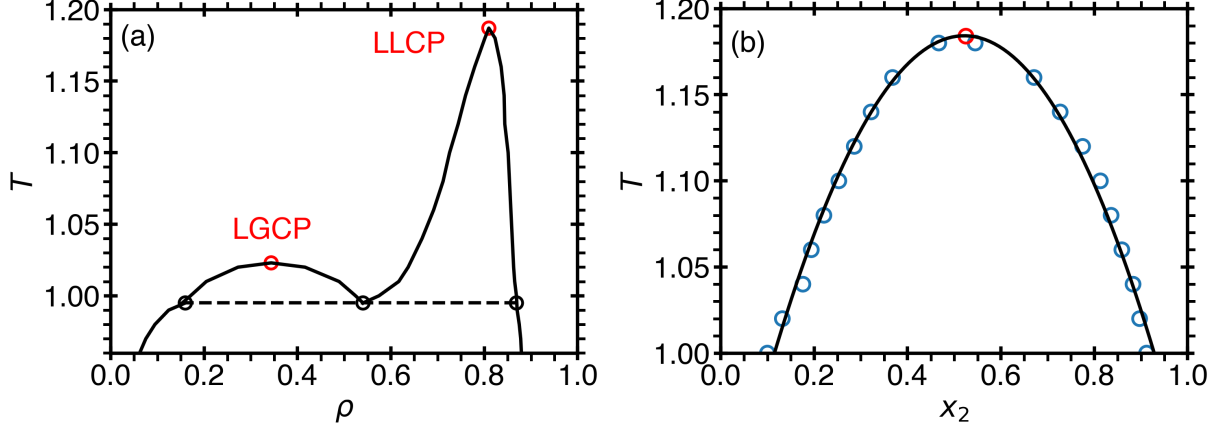


Figure 2.10: (a)  $T$ - $\rho$  phase diagram for the maximum-valence model (with  $\epsilon_{22} = 0.5$  and  $\epsilon_b = 1.0$ ) obtained in an NVT ensemble after  $t = 10^6$  time units. The temperature dependence of the fraction of atoms with two bonds,  $x_2$ , (b) and the average chain-length,  $\langle n \rangle$ , (c) in two coexisting liquid phases. The simulation data in (b) is fit to a second order polynomial.

and  $x_0 + x_1$ .

Qualitatively, the phase diagram of sulfur matches that of the maximum-valence model with a specific set of interaction parameters. In sulfur, the LGCP is located at  $T_c^{\text{LG}} = 1314$  K,  $P_c^{\text{LG}} = 20.7$  MPa, and  $\rho_c^{\text{LG}} = 563$  kg/m<sup>3</sup> [165], while the LLCP is located at  $T_c^{\text{LL}} = 1035$  K,  $P_c^{\text{LL}} = 2.15$  GPa, and  $\rho_c^{\text{LL}} \approx 2000$  kg/m<sup>3</sup> [51], such that the ratio of the LL to LG critical parameters qualitatively matches the predictions of the maximum-valence model. It is noted that the behavior of sulfur is more complicated away from the LLPT since liquid sulfur contains octamers that (above the lambda transition [140–144]) are to be broken down upon heating before polymerization can occur [143]. Since in the considered formulation of the maximum-valence model, it is approximated that atoms link together to form linear polymers, which mimics the valence structure and bond formation of sulfur in the vicinity of the LLPT.

Also, the computed structure factor contains qualitative similarities with the LLPT in sulfur. In Fig. 2.11, the structural differences between the LDL and HDL phases is depicted through the density correlation function,  $g(r)$ , and the structure factor,  $S(q)$ , for several densities at con-

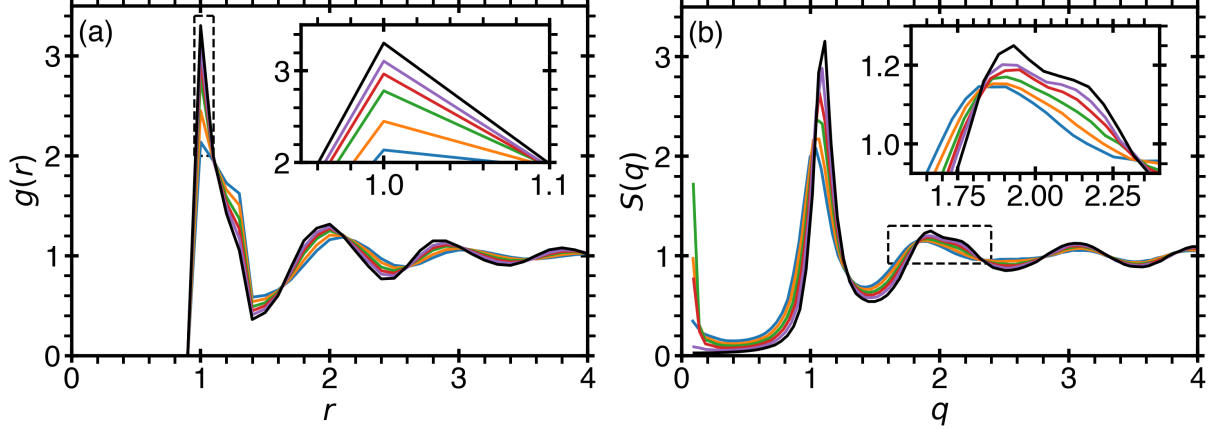


Figure 2.11: (a) The density correlation function  $g(r)$  and (b) the structure factor  $S(q)$  across the liquid-liquid transition at  $T = 1.00$  for densities of  $\rho = 0.65$  (blue),  $\rho = 0.70$  (orange),  $\rho = 0.75$  (green),  $\rho = 0.80$  (red),  $\rho = 0.85$  (purple), and  $\rho = 0.90$  (black). In (a), the sharp peak, around  $r = 1$  (in units of  $\sigma$ ), corresponds to the length of the covalent bond, which increases upon increasing density. Simultaneously, in (b), the maximum of the structure factor (the first peak) shifts to larger wavenumbers upon increasing density, while the second peak acquires a characteristic bump, similar to what was recently observed in sulfur [51]. The divergence of the structure factor at  $q = 0$  indicates the divergence of the isothermal compressibility in the vicinity of the LLC. The insets (dashed boxes) highlight the behavior of the maximum of the correlation function and second peak of the structure factor.

stant temperature near the liquid-liquid coexistence (computed for the atom cores). In Fig. 2.11a, the  $g(r)$  shows a sharp peak corresponding to the covalent bond length  $r = 1.02\sigma$ , in the HDL phase. Correspondingly, the structure factor shows a shift in the first peak to a larger wavenumber  $q$ , while the second peak changes due to polymerization. This change is similar to what was observed in a recent experiment on sulfur [51]. In addition,  $S(q)$  shows a dramatic increase as  $q \rightarrow 0$  for the points corresponding to the equilibrium between two liquid phases (see Fig. 2.11b), which is indicative of the divergence of the isothermal compressibility. It is noted that in this section, a gas-LDL-HDL triple point is found, while in the recent experimental work on sulfur [51], the solid-LDL-HDL triple point is observed. In principle, this triple point may be reproduced in the maximum-valence model by fine-tuning the parameters, which requires further investigation.

Overall, the maximum-valence model demonstrates that when bonded atoms attract each

other more strongly than to the non-bonded atoms or when the bonded and non-bonded atoms repel each other, the LLPT is generated by the coupling between phase separation and the chemical reaction. The maximum-valence model could also be used to study the LLPTs in systems with other maximum valence numbers. For instance, when  $z = 1$ , the LLPT is induced by dimerization (e.g. in hydrogen, as discussed in Sec. 2.2). For  $z \geq 3$ , the LLPT could be induced either by gelation or by molecular network formation [145]. For example, it could be used to model the phase behavior of liquid phosphorous with  $z = 3$  [60, 61] as well as silicon [66], silica [68, 166], or supercooled water with  $z > 3$  [78, 147]. Further investigation of the maximum-valence model for these coordination numbers  $z \neq 2$ , has been recently performed by Shumovskyi and Buldyrev [167].

## 2.4 Liquid-Liquid Phase Transition in Fluids Exhibiting Water-Like Anomalies

In addition to the fluid-fluid phase transitions induced by interconversion reactions, such as the dimerization in hydrogen (Sec. 2.2) and the polymerization in sulfur (Sec. 2.3), the interconversion may be induced by the structural change between two supramolecular states. For instance, it has been hypothesized that the existence of a liquid-liquid phase transition in supercooled water may be caused by the interconversion between a high-density state (five coordination number) and a low-density state (four coordination number) of water [9, 13, 55, 56, 72–80]. In this section<sup>3</sup>, a simple microscopic model is introduced and discussed. This model, which is referred to as the “blinking-checkers” lattice model, is capable of describing the anomalies in the thermodynamic properties of supercooled water and systems exhibiting similar anomalies (like silicon [63]). In

---

<sup>3</sup>This section was reproduced from Thomas J. Longo, Sergey V. Buldyrev, Mikhail A. Anisimov, and Frédéric Caupin, *J. Phys. Chem. B*, **127**, 3079 (2023); <https://doi.org/10.1021/acs.jpcc.2c08901>, with the permission of ACS Publications.

particular, this model is utilized to describe the anomalous behavior in the interfacial properties of such systems [3].

The blinking-checkers model is a compressible binary lattice, thermodynamically equivalent to the mixture of two lattice gases. In this model, “black” (state A) and “white” (state B) species interact on a lattice, while interconversion is implemented by allowing the particles to change their color by tuning the energy and entropy of interconversion. Previous lattice models, were able to reproduce the anomalous behavior of water, but required complex interactions between species [168–170]. Phenomenologically, the blinking-checkers lattice model may be applied to describe the structural interconversion of any two states, like that predicted for supercooled water. Depending on the interaction parameters between species, the blinking-checkers model is able to reproduce the three possible scenarios of polyamorphic behavior, one of which could occur in supercooled water. For instance, if the interaction between the two species is strong, no liquid-liquid transition occurs, corresponding to the “singularity-free” scenario [168]. If the interaction between two species is weak (but not too weak), then a LLPT with a LLCP occurs, which corresponds to the “second critical point” scenario [74]. However, if the interaction is very weak, then a LLPT occurs, but the LLCP disappears (as it lies in the unstable region), which corresponds to the “critical point free” scenario [171, 172].

#### 2.4.1 Blinking-Checkers Lattice Model

Consider a compressible binary-lattice of fixed total volume,  $V$ , where each of the  $N$  lattice sites can either be empty or occupied by one particle of two types (A and B). The numbers of particles of type A and B are  $N_A$  and  $N_B$ , respectively. The number density is  $\rho = (N_A + N_B)/N$

and the fraction of particles of type B in the mixture is  $x = N_B/(N_A + N_B)$ . The interactions of each particle with its neighbors is given by interaction parameters between each particle type of the form,  $\varepsilon_{AA}$ ,  $\varepsilon_{BB}$ , and  $\varepsilon_{BA}$ . There is no interaction with empty sites. The total Gibbs energy, in the form of Eq. (2.2), is adopted, in which the Gibbs energy of pure species A, the Gibbs energy change of reaction, and the Gibbs energy of mixing are given in the forms

$$\hat{\mu}_A^\circ = -2\rho\varepsilon_{AA} + \hat{T} \ln \left( \frac{\rho}{1-\rho} \right) \quad (2.24)$$

$$\hat{G}_{BA} = -\hat{T} \ln \mathcal{K} = \hat{e} - \hat{s}\hat{T} + \hat{v}\hat{P} \quad (2.25)$$

$$\hat{G}_{\text{mix}} = \hat{T} [x \ln x + (1-x) \ln(1-x)] - 2\rho\varepsilon x(1-x) \quad (2.26)$$

where  $\varepsilon = \varepsilon_{AA} + \varepsilon_{BB} - 2\varepsilon_{BA}$  and  $\hat{v}\hat{P} = 2\rho(\varepsilon_{BB} - \varepsilon_{AA})$ . In this model, all units are expressed in a dimensionless form relative to the species B - species B interaction energy,  $\varepsilon_{BB}$ . Thus, the units of energy, temperature, pressure, and surface tension are, respectively,  $\varepsilon_{BB}/2$ ,  $\varepsilon_{BB}/(2k_B)$ ,  $\varepsilon_{BB}/(2\ell^3)$ , and  $\varepsilon_{BB}/(2\ell^2)$ , in which  $\ell$  is the length of a lattice cell and  $k_B$  is adopted as  $k_B = 1$ . The temperature and pressure are reduced by the critical temperature or pressure of a pure system consisting of only species B as  $\hat{T} = T/T_c^B$  in which  $T_c^B = \varepsilon_{BB}/(2k_B)$  and  $\hat{P} = P/P_c^B$  in which  $P_c^B = \varepsilon_{BB}/(2\ell^3)$ . Note that upon comparing the Gibbs energy change, Eq. (2.25), with that of the general case, Eq. (2.9),  $\hat{G}_{BA}$  in the blinking-checkers lattice model is the simplest possible approximation of the Gibbs energy change of reaction.

In lattice models, it is often more convenient to use the Helmholtz energy instead of the Gibbs energy, since the volume of each lattice site is constant. Thus, since the Gibbs energy per lattice site,  $G = G_t/N$ , is related to the Helmholtz energy per lattice site,  $F = F_t/N$ , via a Legendre transform of the form  $G = F + PV$ , where  $PV$  is a constant, then the Helmholtz

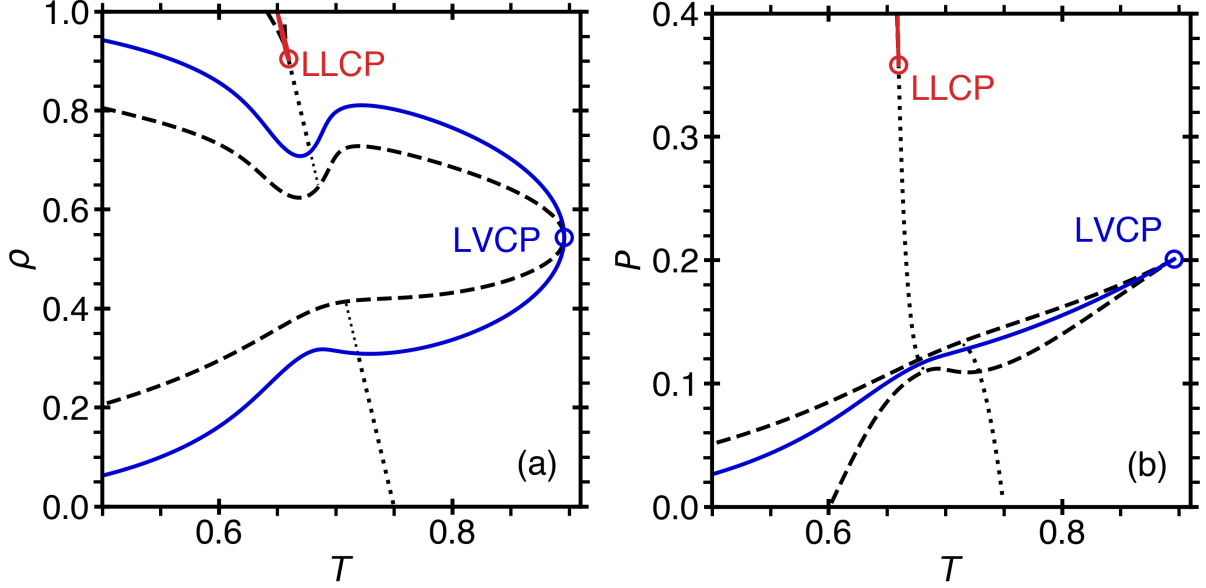


Figure 2.12: Density-temperature and pressure-temperature phase diagrams for the blinking-checkers model with  $\varepsilon_{AA} = 1.6$ ,  $\varepsilon_{BB} = 2.0$ ,  $\varepsilon_{AB} = 1.08$ ,  $\hat{e} = 3$ , and  $\hat{s} = 4$ . The liquid-vapor coexistence (blue curves) terminates at the liquid-vapor critical point, LVCP. The liquid-liquid coexistence (red curves) terminates at the liquid-liquid critical point, LLCP. The limits of thermodynamic stability (spinodals) are given by the dashed curves. In (a,b), the dotted line corresponds to the condition,  $x = 1/2$ , which qualitatively separates the regions enriched either by species A (at low temperatures and low densities) or species B (at high temperatures and high densities).

energy may be obtained from the integral of the Gibbs energy, Eqs. (2.2), with respect to density.

The reduced Helmholtz energy per lattice site,  $\hat{f} = F/(Nk_B T_c)$ , in the blinking-checkers model is given by

$$\begin{aligned} \hat{f}(T, \rho, x) = & \rho x (\hat{e} - \hat{T} \hat{s}) - \rho^2 [\varepsilon_{BB} x^2 + \varepsilon_{AA} (1-x)^2 + 2\varepsilon_{BA} x(1-x)] \\ & + \hat{T} [\rho x \ln x + \rho(1-x) \ln(1-x)] + \hat{T} [\rho \ln \rho + (1-\rho) \ln(1-\rho)] \end{aligned} \quad (2.27)$$

The three terms in square brackets in Eq. (2.27) describe the contribution to the free energy from the energy of interactions, the entropy of mixing of the two species, and the entropy of mixing of the occupied and empty sites. The condition for chemical-reaction equilibrium defines

the equilibrium concentrations (molecular fractions) of species B,  $x = x_e(T, \rho)$ , such that the interconverting binary mixture thermodynamically behaves as a single component fluid.

Figure 2.12(a) and (b) illustrates the  $\rho$ - $T$  and  $P$ - $T$  phase diagram of the blinking-checkers lattice for an example set of interaction parameters ( $\varepsilon_{AA} = 1.6$ ,  $\varepsilon_{BB} = 2.0$ , and  $\varepsilon_{AB} = 1.08$ ) and interconversion-reaction parameters ( $\hat{e} = 3$  and  $\hat{s} = 4$ ). For this choice of the energy and the entropy of reaction, we obtain a negative slope for the liquid-liquid phase transition, similar to that predicted for supercooled water. The line that qualitatively separates the region enriched by species 1, at low temperatures and low densities (referred to as “L1”), from the region enriched by species 2, at high temperatures and high densities (referred to as “L2”), is indicated by the dotted line in Fig. 2.12(a,b). Furthermore, for this set of interaction parameters, two critical points and a “bottleneck” in the liquid-vapor coexistence are observed. The  $\rho$ - $T$  and  $x$ - $T$  phase diagrams for seven systems are illustrated in Fig. 2.13(a,b). Note that for different sets of parameters, one may obtain multiple fluid-fluid critical points, representing the more complex phase behavior of polyamorphic fluids.

The Helmholtz energy of the non-reacting binary lattice model,  $\hat{f}$ , Eq. (2.27), may be expressed through the partial densities,  $\rho_B = \rho x$  and  $\rho_A = \rho(1 - x)$ , as given by

$$\begin{aligned} \hat{f}(\hat{T}, \rho_A, \rho_B) = & \rho_B \left( \hat{e} - \hat{T} \hat{s} \right) - (\rho_A + \rho_B)(\varepsilon_{AA}\rho_A + \varepsilon_{BB}\rho_B) + \varepsilon\rho_A\rho_B \\ & + \hat{T}[\rho_A \ln \rho_A + \rho_B \ln \rho_B + (1 - \rho_A - \rho_B) \ln(1 - \rho_A - \rho_B)] \end{aligned} \quad (2.28)$$

The chemical potentials of each species in solution is given by

$$\hat{\mu}_B = \left. \frac{\partial \hat{f}}{\partial \rho_B} \right|_{\rho_A, \hat{T}} = \left( \hat{e} - \hat{T} \hat{s} \right) - 2\varepsilon_{BB} \rho_B - (\varepsilon_{AA} + \varepsilon_{BB} - \varepsilon) \rho_A + \hat{T} \ln \left( \frac{\rho_B}{1 - \rho_A - \rho_B} \right) \quad (2.29)$$

$$\hat{\mu}_A = \left. \frac{\partial \hat{f}}{\partial \rho_A} \right|_{\rho_B, \hat{T}} = -(\varepsilon_{AA} + \varepsilon_{BB} - \varepsilon) \rho_B - 2\varepsilon_{AA} \rho_A + \hat{T} \ln \left( \frac{\rho_A}{1 - \rho_A - \rho_B} \right) \quad (2.30)$$

The difference between the chemical potentials,  $\hat{\mu}_{BA} = \hat{\mu}_B - \hat{\mu}_A$ , for the non-reacting binary lattice model in solution is given by

$$\hat{\mu}_{BA} = \left( \hat{e} - \hat{T} \hat{s} \right) + 2(\varepsilon_{AA} - \varepsilon_{BA}) \rho_A - 2(\varepsilon_{BB} - \varepsilon_{BA}) \rho_B + \hat{T} \ln \left( \frac{\rho_B}{\rho_A} \right) \quad (2.31)$$

The chemical-reaction equilibrium condition requires,  $\hat{\mu}_{BA} = 0$ , or equivalently  $\partial \hat{f} / \partial x|_{\hat{T}, \rho} = 0$ .

## 2.4.2 Virtual Critical Line in Interconverting Mixtures

If interconversion does not occur, the blinking-checkers model describes a compressible binary mixture, which may exhibit liquid-vapor and liquid-liquid coexistence, as well as the corresponding critical lines [10]. Consider a point on a critical line with temperature,  $T_c$ , density,  $\rho_c$ , and type A particles' molecular fraction,  $x_c$ . In a fixed volume,  $V$ , the corresponding critical isochore, at fixed composition, contains a fixed number of particles A and B, given by  $\rho_c x_c V$  and  $\rho_c (1 - x_c) V$ , respectively. At temperatures below  $T_c$ , the system will separate into two phases,  $\alpha$  and  $\beta$  (which could be liquid and vapor or liquid and liquid). For phase  $i = \alpha$  or  $\beta$ , let  $\rho_i$ ,  $x_i$ , and  $V_i$  be the density, type A fraction, and volume, respectively. At each  $T \leq T_c$ , the six values  $(\rho_i, x_i, V_i)_{i=\alpha, \beta}$  are fully determined by three conservation equations (one for volume and two for mass), and three equilibrium conditions (two for the chemical potentials and one for the pressure)

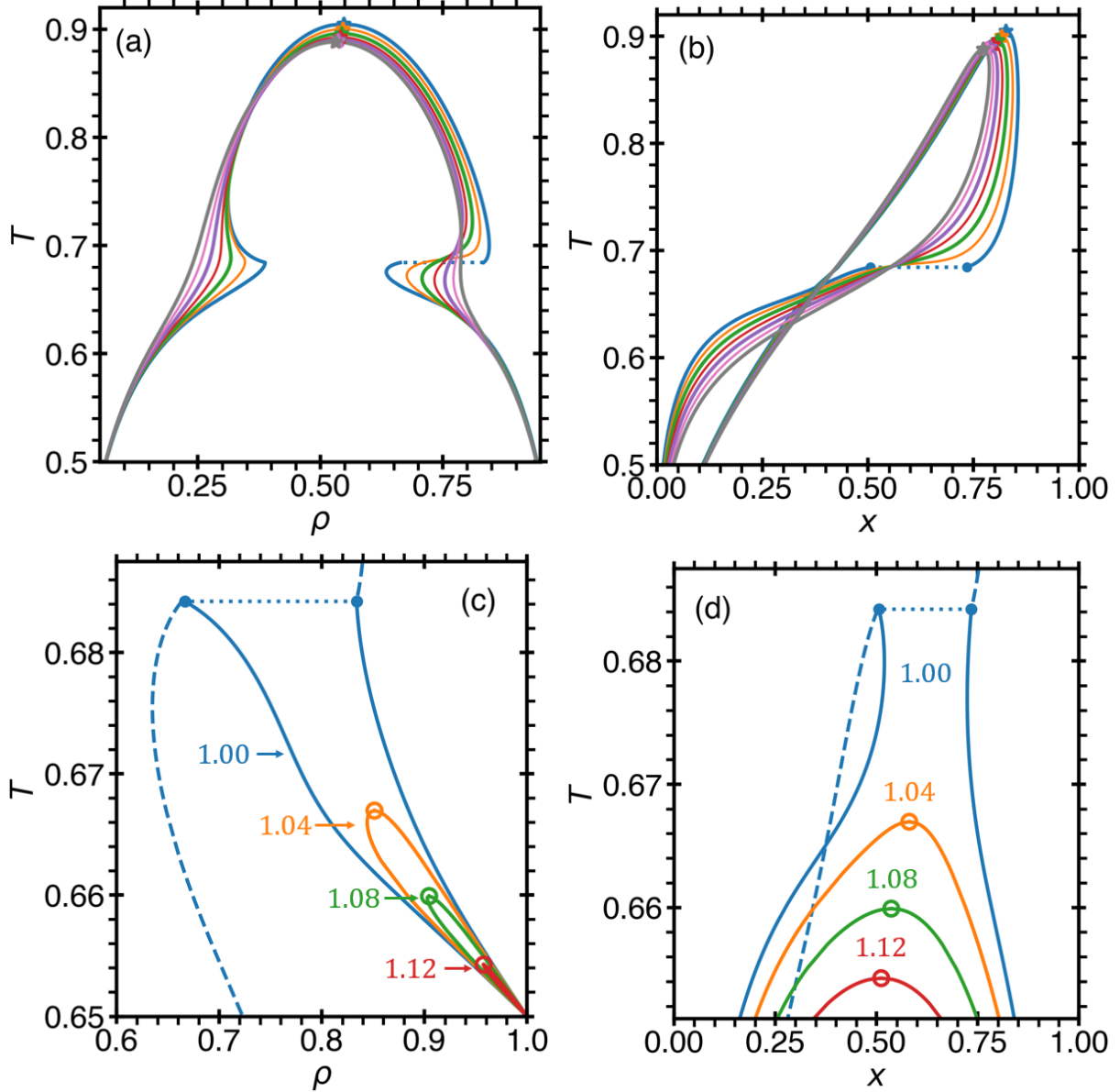


Figure 2.13: Liquid-vapor (a,b) and liquid-liquid (c,d) coexistence curves for the seven systems with  $\varepsilon_{AA} = 1.6$ ,  $\varepsilon_{BB} = 2.0$ ,  $e = 3$ ,  $s = 4$ , and with various values of  $\varepsilon_{BA}$ :  $\varepsilon_{BA} = 1.00$  (blue),  $\varepsilon_{BA} = 1.04$  (orange),  $\varepsilon_{BA} = 1.08$  (green),  $\varepsilon_{BA} = 1.12$  (red),  $\varepsilon_{BA} = 1.16$  (purple),  $\varepsilon_{BA} = 1.20$  (pink), and  $\varepsilon_{BA} = 1.24$  (gray). The critical points, indicated by the stars in (a,b) and open circles in (c,d), are the unique liquid-vapor (LVCP) or liquid-liquid (LLCP) critical points in the interconverting system, referred to as “actual” critical points. As also indicated in Fig. 2.12, species A is enriched in the low-density, low-temperature region, while species B is enriched in the high-density, high-temperature region. For the system with  $\varepsilon_{BA} = 1.00$ , the dashed blue curves in (c,d) indicate the liquid-vapor coexistence, while in (a-d), the dotted blue line indicates the discontinuity at the triple point.

Table 2.2: Liquid-vapor critical points of interconverting systems, referred to as “actual” critical points, for the seven systems considered in this section (with  $\varepsilon_{AA} = 1.6$ ,  $\varepsilon_{BB} = 2.0$ ,  $\hat{e} = 3$ , and  $\hat{s} = 4$ ).

$\varepsilon_{BA}$	$T_c^{\text{act}}$	$\rho_c^{\text{act}}$	$x_c^{\text{act}}$	$P_c^{\text{act}}$
1.00	0.905	0.548	0.174	0.208
1.04	0.900	0.546	0.183	0.204
1.08	0.896	0.544	0.193	0.201
1.12	0.893	0.541	0.202	0.198
1.16	0.890	0.538	0.211	0.195
1.20	0.889	0.534	0.219	0.192
1.24	0.888	0.531	0.227	0.189

as

$$\rho_V x_V v_V + \rho_L x_L v_L = \rho x \quad (2.32)$$

where  $\rho_V$ ,  $x_V$ ,  $\rho_L$ , and  $x_L$  are the liquid and vapor coexisting values of the density and concentration, while  $v_V$  and  $v_L$  are the volumes of the liquid (L) or vapor (V) phases. Eliminating the volumes via  $v_V + v_L = 1$  and  $\rho_V v_V + \rho_L v_L = \rho$  in Eq. (2.32), gives the overall concentration and density in terms of just the coexisting parameters as

$$x_V \rho \rho_V - x_L \rho \rho_L + x_L \rho_L \rho_V - x_V \rho_L \rho_V = x \rho (\rho_V - \rho_L) \quad (2.33)$$

Equation (2.33) defines the overall density and concentration for any set of coexisting densities and concentrations.

As discussed in Section 2.1, when interconversion takes place, the system (in terms of the Gibbs Phase Rule [173]) thermodynamically behaves as a single component fluid, following the given paths along liquid-vapor or liquid-liquid coexistence in the two phase region. It should be emphasized that after the interconverting system reaches equilibrium, the thermody-

Table 2.3: Liquid-liquid critical points (LLCP) for the three systems exhibiting liquid polyamorphism and a LLCP (with  $\varepsilon_{AA} = 1.6$ ,  $\varepsilon_{BB} = 2.0$ ,  $\hat{e} = 3$ , and  $\hat{s} = 4$ ).

$\varepsilon_{BA}$	$T_c^{\text{act}}$	$\rho_c^{\text{act}}$	$x_c^{\text{act}}$	$P_c^{\text{act}}$
1.04	0.667	0.851	0.419	0.211
1.08	0.660	0.904	0.463	0.358
1.12	0.654	0.958	0.488	0.726

dynamic properties, being state functions, are the same as a non-reacting binary mixture with the same equilibrium composition, temperature, and pressure. Therefore, for each point along the interconversion path, there is a corresponding unique critical point of the non-reacting binary mixture, which is connected to this point on the path by a critical isochore for the non-reacting mixture at fixed composition. Thus, the corresponding binary-mixture critical point is referred to as the “virtual” (*i.e.* invisible along the interconversion path) critical point, while the interconverting system’s unique liquid-vapor critical point (LVCP) is referred to as the “actual” LVCP. Similarly, for systems exhibiting interconversion, the single liquid-liquid critical point (LLCP), is referred to as the actual LLCP. It should be emphasized that not only the phase diagram of the interconverting mixture is characterized by unique fluid-fluid critical points (like that of a single-component fluid), but the response functions, being second derivatives of the free energy at  $\mu_{12} = 0$ , also exhibit the singularities characteristic of single-component fluids.

The virtual critical points are defined for the binary mixture at each overall concentration,  $x$ , and overall density,  $\rho$ , through the conservation equations, Eqs. (2.32) and (2.33). Introducing the notation,  $\hat{f}_y = \partial \hat{f} / \partial y$ , the critical line is determined from the following thermodynamic stability conditions,

$$\hat{f}_{\rho_B \rho_B} \hat{f}_{\rho_A \rho_A} - \hat{f}_{\rho_B \rho_A}^2 = 0 \quad (2.34)$$

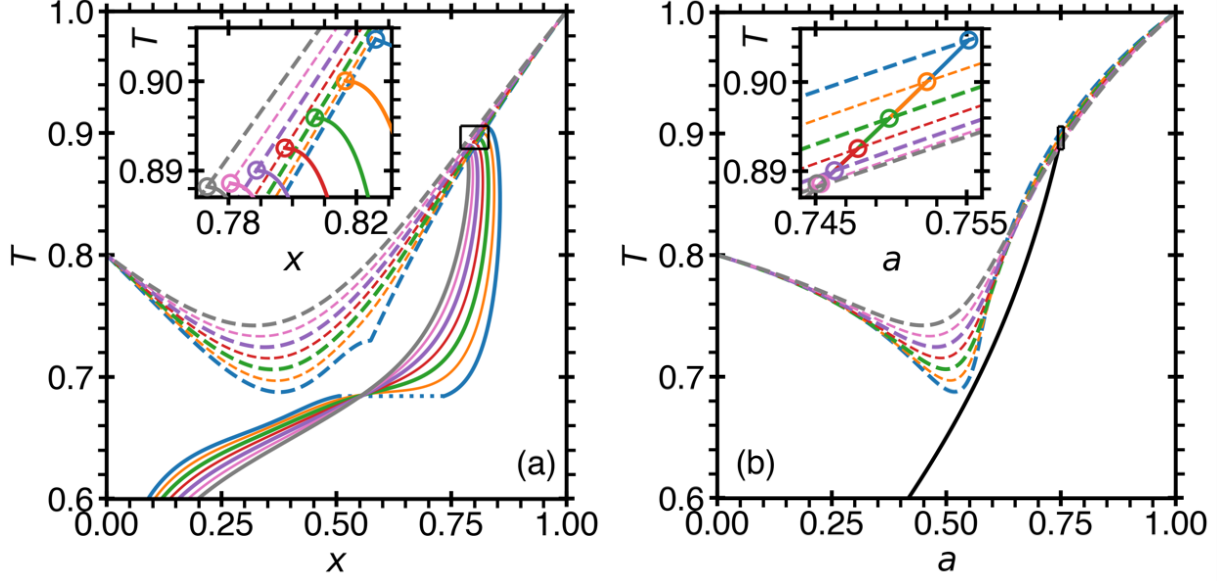


Figure 2.14: Illustration of the thermodynamic path selected by the interconversion reaction for  $\hat{\epsilon} = 3$  and  $\hat{s} = 4$  at constant volume,  $V$ , and at constant number of occupied lattice sites,  $N_1 + N_2$ , represented through (a) the liquid branch of the liquid-vapor temperature-concentration coexistence (see Fig. 2.13b), and (b) the activity,  $a = 1/[1 + e^{-G_{BA}/\hat{T}}]$ , for the systems with different interaction parameters:  $\epsilon_{BA} = 1.00$  (blue),  $\epsilon_{BA} = 1.04$  (orange),  $\epsilon_{BA} = 1.08$  (green),  $\epsilon_{BA} = 1.12$  (red),  $\epsilon_{BA} = 1.16$  (purple),  $\epsilon_{BA} = 1.20$  (pink), and  $\epsilon_{BA} = 1.24$  (gray). For each system, the liquid-vapor critical line (LVCL) is shown by the dashed curves, while the collapsed coexistence, in (a), is illustrated by the black curve. The insets show the LV critical points for each scenario. Note that for the system with  $\epsilon_{BA} = 1.00$ , the thermodynamic path crosses through the triple point, indicated by the dotted line in (a).

$$\hat{f}_{\rho_B \rho_B \rho_B} \left( \frac{\hat{f}_{\rho_B \rho_A}}{\hat{f}_{\rho_B \rho_B}} \right)^3 - 3\hat{f}_{\rho_B \rho_B \rho_A} \left( \frac{\hat{f}_{\rho_B \rho_A}}{\hat{f}_{\rho_B \rho_B}} \right)^2 + 3\hat{f}_{\rho_B \rho_A \rho_A} \left( \frac{\hat{f}_{\rho_B \rho_A}}{\hat{f}_{\rho_B \rho_B}} \right) - \hat{f}_{\rho_A \rho_A \rho_A} = 0 \quad (2.35)$$

Collectively, these critical points, realized only for the non-reacting binary system, make up the virtual critical line in the reacting system. At each point along the thermodynamic path, the behavior of the thermodynamic properties, being state functions, are connected to each unique virtual critical point by critical isochores at constant composition.

An illustration of the thermodynamic path along liquid-vapor equilibrium in the interconverting fluid for seven different sets of interaction parameters,  $\epsilon_{BA}$ , is shown in Fig. 2.14(a). In

the coexisting liquid and vapor phases, there are two branches of the density and concentration, given by  $\rho_L^{\text{exc}}(T)$ ,  $\rho_V^{\text{exc}}(T)$ ,  $x_L^{\text{exc}}(T)$ , and  $x_V^{\text{exc}}(T)$ , see Fig. 2.13(a,b) for details. For simplicity, in Fig. 2.14(a) only the liquid branch of the liquid-vapor coexistence is shown, see Fig. 2.13(b) for both branches. The liquid-vapor critical lines for the seven binary mixtures with the same interaction parameters are also shown (dashed lines). Fig. 2.14(b) displays the same, but replacing the abscissa,  $x$ , by the “activity”,  $a = 1/[1 + e^{-\hat{G}_{\text{BA}}/\hat{T}}]$ , [174–176] where  $\hat{G}_{\text{BA}}$  is given by Eq. (2.25). Thus, for each point along the thermodynamic path selected by interconversion, the activity is restricted by Eq. (2.25), such that for the seven systems considered in this section, the activities collapse into the line shown in Fig. 2.14(b), as only  $\varepsilon_{\text{BA}}$  is varied in each system.

The proximity of the virtual critical line affects the properties along coexistence in the interconverting fluid, causing, in particular, the bottlenecked shape of the  $\rho$ - $T$  liquid-vapor coexistence (Fig. 2.13). For the chosen selection of the interaction parameters, this particular effect is pronounced because the difference between  $\varepsilon_{\text{AA}}$  and  $\varepsilon_{\text{BB}}$  is significant ( $\varepsilon_{\text{AA}} = 1.6$  and  $\varepsilon_{\text{BB}} = 2.0$ ). In addition, the asymmetry of the liquid-vapor coexistence occurs due to the existence of the liquid-liquid critical point, and even occurs in the singularity-free scenario where the liquid-liquid critical point is moving to indefinite pressure.

### 2.4.3 Anomalies of Interfacial Properties

The possibility of anomalous behavior of the liquid-vapor surface tension,  $\sigma_{\text{LV}}$ , of supercooled water has been a topic of long-standing interest. In 1951, an inflection point in the temperature dependence of  $\sigma_{\text{LV}}$  was reported to occur near 0 °C [177], but later studies, showing larger uncertainties, cast doubts on the early measurements [178, 179]. Only recently, the highly

accurate studies by Hruby and coworkers became available [84–87]. Initially, in Refs. [84–86] it was concluded that no anomaly occurred in  $\sigma_{LV}(T)$  down to  $-26\text{ }^\circ\text{C}$ ; however, the results of the latest experiment [87], reaching  $-31.4\text{ }^\circ\text{C}$ , suggest that an inflection point might be possible. Theoretical studies support the existence of anomalies in liquid-vapor surface tension of supercooled water [169, 180–185]. Using two closely related microscopic models of water-like associating fluids, Feeney and Debenedetti [180] predicted either an inflection point or a maximum, depending on the details and assumptions of the approach. Hruby and Holten [169] proposed a two-state model able to generate an inflection point in the liquid-vapor surface tension of water. The inflection point has also been predicted by molecular dynamics simulations with several water potentials, such as SPC/E [181, 182], WAIL [183], and TIP4P/2005 [182, 184, 185].

To model the fluid interfaces, density gradient theory (DGT) is utilized [186–190], in which the free energy of the system is expanded in a Taylor series up to second-order in terms of derivatives of the concentration and density with respect to the coordinate perpendicular to the interface [190]. In this subsection, the anomalous behavior of the interfacial properties in the blinking-checkers lattice model is investigated. Also, the conditions for observing either an inflection point or an extrema in the liquid-vapor interfacial tensions is discussed.

### 2.4.3.1 Interfacial Properties via Density Gradient Theory

Following the ideas presented by van der Waals [191, 192], and later elaborated by Cahn and Hilliard [193], the interfacial tension of a binary fluid may be obtained [189, 194, 195] by assuming a local spatial-dependent density and concentration,  $\rho = \rho(\mathbf{r}')$  and  $x = x(\mathbf{r}')$ , where  $\mathbf{r}'$  is the spatial coordinate, and generating a Taylor series around a neighboring point  $\mathbf{r}$  to second-

order, yielding

$$\rho(\mathbf{r}') = \rho(\mathbf{r}) + (\mathbf{r}' - \mathbf{r})\nabla\rho(\mathbf{r}) + \frac{1}{2}(\mathbf{r}' - \mathbf{r})^2\nabla^2\rho(\mathbf{r}) \quad (2.36)$$

$$x(\mathbf{r}') = x(\mathbf{r}) + (\mathbf{r}' - \mathbf{r})\nabla x(\mathbf{r}) + \frac{1}{2}(\mathbf{r}' - \mathbf{r})^2\nabla^2 x(\mathbf{r}) \quad (2.37)$$

The total interaction energy,  $E$ , is defined through each of four possible species interactions by integrating over  $\mathbf{r}'$ . For the species B - species B interaction (denoted as “BB”), assuming all interaction parameters are independent of position, this gives  $E_{\text{BB}} = -\varepsilon_{\text{BB}} \int d\mathbf{r}' [(\mathbf{r}')x(\mathbf{r}')\rho(\mathbf{r}')]$ . With use of Eqs. (2.36) and (2.37), this gives the following expressions for the four interaction energies:

$$E_{\text{BB}}^{(2)} = -\varepsilon_{\text{BB}}\ell^2 \left( \nabla x \nabla \rho + \frac{1}{2} [x \nabla^2 \rho + \rho \nabla^2 x] \right) \quad (2.38)$$

$$E_{\text{BA}}^{(2)} = -\varepsilon_{\text{BA}}\ell^2 \left( -\nabla x \nabla \rho + \frac{1}{2} [(1-x)\nabla^2 \rho - \rho \nabla^2 x] \right) \quad (2.39)$$

$$E_{\text{AB}}^{(2)} = -\varepsilon_{\text{AB}}\ell^2 \left( \nabla x \nabla \rho + \frac{1}{2} [x \nabla^2 \rho + \rho \nabla^2 x] \right) \quad (2.40)$$

$$E_{\text{AA}}^{(2)} = -\varepsilon_{\text{AA}}\ell^2 \left( -\nabla x \nabla \rho + \frac{1}{2} [(1-x)\nabla^2 \rho - \rho \nabla^2 x] \right) \quad (2.41)$$

where the superscript “(2)” indicates only the contribution to the interaction energy from the second-order gradient terms, the notation “(r)” has been dropped for simplicity, and  $\ell = |\mathbf{r}' - \mathbf{r}|$  is the distance between two lattice cells. Note that all odd terms go to zero upon integration over  $\mathbf{r}'$  due to the symmetry of the lattice.

It is assumed that the gradient terms only contribute to the local internal energy per lattice site,  $u = U/N$ , and do not effect the local entropy. The internal energy per lattice site is given by

$$u = \frac{1}{2} \int d\mathbf{r} [\rho x(E_{\text{BB}} + E_{\text{BA}}) + \rho(1-x)(E_{\text{AB}} + E_{\text{AA}})] \quad (2.42)$$

Simplifying Eq. (2.42) with use of Green's first identity [196] gives the contribution from the interactions of the surface to the excess free energy. Thus, one obtains

$$\sigma = \int \left[ \Delta\Omega(x, \rho, T) + \frac{1}{2}\kappa_x(\rho)|\nabla x|^2 + \frac{1}{2}\kappa_\rho(x)|\nabla\rho|^2 + \kappa_{\rho,x}(\rho, x)\nabla\rho \cdot \nabla x \right] d\mathbf{r} \quad (2.43)$$

where  $\kappa_x$ ,  $\kappa_\rho$ , and  $\kappa_{\rho,x}$  are the microscopic ‘‘influence’’ coefficients.  $\Delta\Omega$  is the excess grand potential per lattice site, given by [189]

$$\Delta\Omega(x, \rho, T) = \hat{f}(x, \rho, T) - \rho x \hat{\mu}_{\text{B}}^{\text{cxc}} - \rho(1-x) \hat{\mu}_{\text{A}}^{\text{cxc}} + \hat{P}^{\text{cxc}} \quad (2.44)$$

where  $\hat{\mu}_{\text{A}}$ ,  $\hat{\mu}_{\text{B}}$ , and  $\hat{P}$  are the chemical potentials of species A and B per lattice site in solution and the pressure per lattice site, respectively, while the superscript ‘‘cxc’’ indicates that the quantity is evaluated along the phase coexistence. The three influence parameters are given by

$$\kappa_x(\rho) = \frac{1}{2}\ell^2\rho^2\varepsilon \quad (2.45)$$

$$\kappa_\rho(x) = \frac{1}{2}\ell^2 [\varepsilon_{\text{BB}}x^2 + 2\varepsilon_{\text{BA}}x(1-x) + \varepsilon_{\text{AA}}(1-x)^2] \quad (2.46)$$

$$\kappa_{\rho,x}(\rho, x) = \frac{1}{2}\ell^2\rho [\varepsilon_{\text{BB}}x + \varepsilon_{\text{BA}}(1-2x) - \varepsilon_{\text{AA}}(1-x)] \quad (2.47)$$

It is noted that there are three limits that may be observed for Eq. (2.43), in which the system reverts to either the lattice-gas or binary-lattice models [9]. For these three cases, the integrand

of Eq. (2.43) becomes: In the limit of pure species B ( $x = 1$ ),

$$\Delta\Omega(x = 1, \rho, T) + \frac{1}{4}\ell^2\varepsilon_{\text{BB}}|\nabla\rho|^2 \quad (2.48)$$

In the limit of pure species A ( $x = 0$ ),

$$\Delta\Omega(x = 0, \rho, T) + \frac{1}{4}\ell^2\varepsilon_{\text{AA}}|\nabla\rho|^2 \quad (2.49)$$

In the limit of very high density ( $\rho = 1$ ),

$$\Delta\Omega(x, \rho = 1, T) + \frac{1}{4}\ell^2\varepsilon|\nabla x|^2 \quad (2.50)$$

Furthermore, the equilibrium condition is found by the minimization of Eq. (2.43) with respect to density or concentration via the Euler-Lagrange derivative [192, 194, 195], which yields two expressions,

$$\frac{\partial(\Delta\Omega)}{\partial\rho} + \frac{1}{2}\frac{\partial\kappa_x}{\partial\rho}|\nabla x|^2 + \frac{1}{2}\frac{\partial\kappa_\rho}{\partial x}\nabla x\nabla\rho = \kappa_\rho\nabla^2\rho + \kappa_{x,\rho}\nabla^2x \quad (2.51)$$

$$\frac{\partial(\Delta\Omega)}{\partial x} + \frac{1}{2}\frac{\partial\kappa_\rho}{\partial x}|\nabla\rho|^2 + \frac{1}{2}\frac{\partial\kappa_x}{\partial\rho}\nabla x\nabla\rho = \kappa_{x,\rho}\nabla^2\rho + \kappa_x\nabla^2x \quad (2.52)$$

where the fact that  $\partial\kappa_{x,\rho}/\partial\rho = (1/2)\partial\kappa_\rho/\partial x$  and  $\partial\kappa_{x,\rho}/\partial x = (1/2)\partial\kappa_x/\partial\rho$  are used. Upon integration, these equations give the equilibrium condition for the interfacial tension [189, 194, 195]

$$\Delta\Omega(x, \rho, T) = \frac{1}{2}\kappa_x(\rho)|\nabla x|^2 + \frac{1}{2}\kappa_\rho(x)|\nabla\rho|^2 + \kappa_{\rho,x}(\rho, x)\nabla\rho \cdot \nabla x \quad (2.53)$$

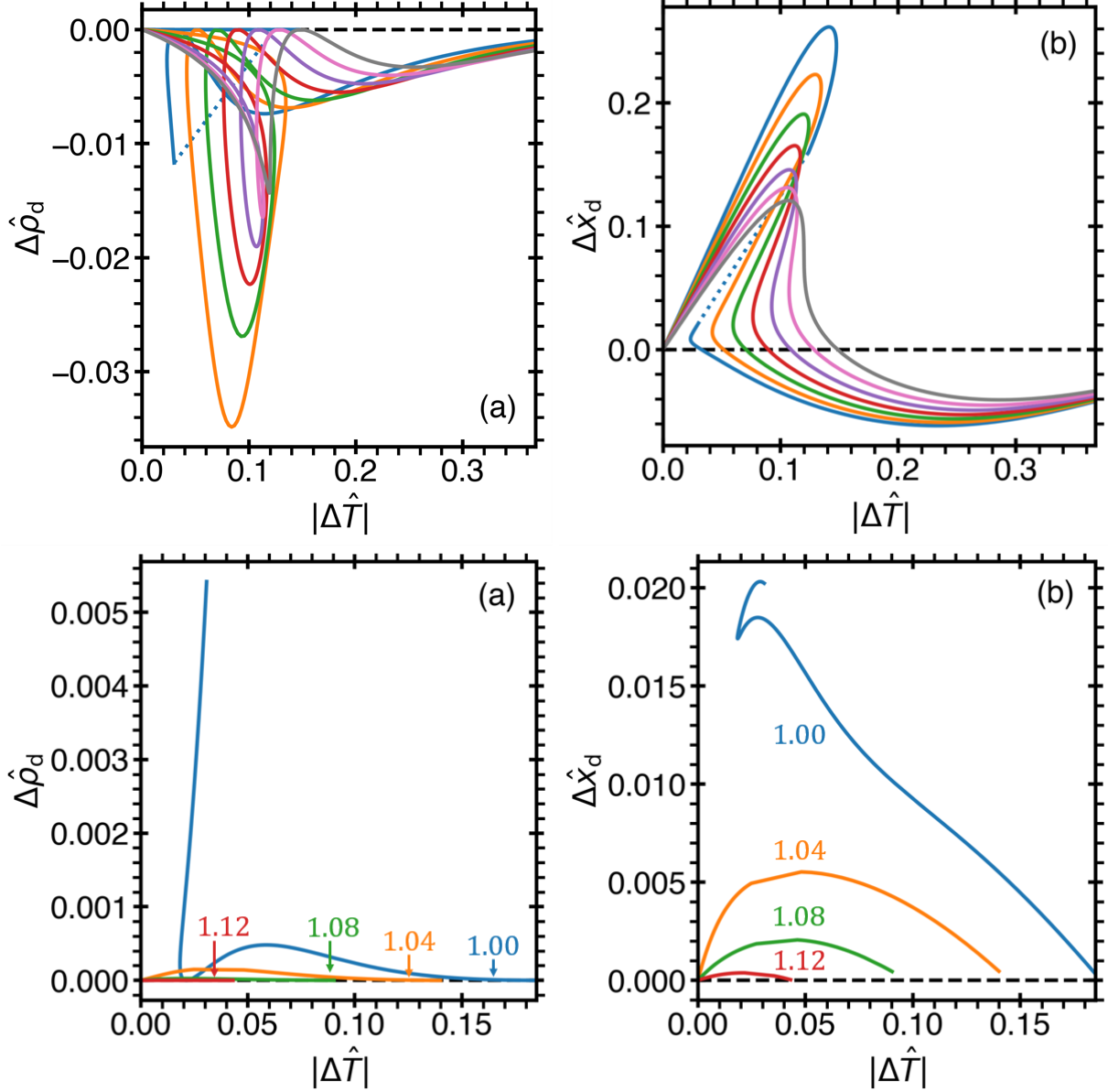


Figure 2.15: Liquid-vapor (a,b) and liquid-liquid (c,d) diameters of the density, Eq. (2.60), and the concentration, Eq. (2.61), as a function of the distance to the virtual LVCL (or LLCL) along the thermodynamic path selected by interconversion for systems with  $\varepsilon_{AA} = 1.6$ ,  $\varepsilon_{BB} = 2.0$ ,  $\hat{e} = 3$ ,  $\hat{s} = 4$ , and with various values of  $\varepsilon_{BA}$ :  $\varepsilon_{BA} = 1.00$  (blue),  $\varepsilon_{BA} = 1.04$  (orange),  $\varepsilon_{BA} = 1.08$  (green),  $\varepsilon_{BA} = 1.12$  (red),  $\varepsilon_{BA} = 1.16$  (purple),  $\varepsilon_{BA} = 1.20$  (pink), and  $\varepsilon_{BA} = 1.24$  (gray). In (a-d), the dotted blue lines indicate the discontinuity for the system with  $\varepsilon_{BA} = 1.00$  at the triple point.

To determine the interfacial profiles, a variational approach is adopted based on a family of ansatz functions, choosing the optimal one by minimizing the interfacial tension, given by Eq. (2.43).

Also, exact numerical solutions for the profiles are obtained by solving the equilibrium condition for the surface tension, Eq. (2.53). It is found that the variational approach is enough to capture the anomalous behavior of the interfacial properties with sufficient accuracy (see Appendix A for details). Throughout this subsection, the variational results are reported, based on the Fisher-Wortis profile, which accounts for the thermodynamic asymmetry between the two coexisting phases [197, 198]. A comparison with an alternative symmetric ansatz is also discussed in Appendix A. The Fisher-Wortis ansatz is given in normalized form as a combination of symmetric and asymmetric components for both the density and concentration (molecular fraction) profiles as

$$\hat{\rho}(\hat{z}) = \frac{\rho(\hat{z}) - \rho_\alpha}{\rho_\beta - \rho_\alpha} = \hat{\rho}_{\text{sym}}(\hat{z}) + \Delta\hat{\rho}_d\hat{\rho}_{\text{asym}}(\hat{z}) \quad (2.54)$$

$$\hat{x}(\hat{z}) = \frac{x(\hat{z}) - x_\alpha}{x_\beta - x_\alpha} = \hat{x}_{\text{sym}}(\hat{z}) + \Delta\hat{x}_d\hat{x}_{\text{asym}}(\hat{z}) \quad (2.55)$$

where the symmetric contributions to the profiles are given by

$$\hat{\rho}_{\text{sym}}(\hat{z}) = \frac{1}{2} \left[ \tanh\left(\frac{\hat{z}}{\hat{\zeta}}\right) + 1 \right] \quad (2.56)$$

$$\hat{x}_{\text{sym}}(\hat{z}) = \frac{1}{2} \left[ \tanh\left(\frac{\hat{z} + \hat{\delta}}{\hat{\zeta}}\right) + 1 \right] \quad (2.57)$$

and where the asymmetric contributions to the profiles are given by

$$\hat{\rho}_{\text{asym}}(\hat{z}) = \tanh^2\left(\frac{\hat{z}}{\hat{\zeta}}\right) + \frac{\ln\left[\cosh\left(\frac{\hat{z}}{\hat{\zeta}}\right)\right]}{\cosh^2\left(\frac{\hat{z}}{\hat{\zeta}}\right)} - (\rho_\beta - \rho_\alpha) \quad (2.58)$$

$$\hat{x}_{\text{asym}}(\hat{z}) = \tanh^2\left(\frac{\hat{z} + \hat{\delta}}{\hat{\zeta}}\right) + \frac{\ln\left[\cosh\left(\frac{\hat{z} + \hat{\delta}}{\hat{\zeta}}\right)\right]}{\cosh^2\left(\frac{\hat{z} + \hat{\delta}}{\hat{\zeta}}\right)} - (x_\beta - x_\alpha) \quad (2.59)$$

in which  $\hat{z} = z/\ell$  is the normalized coordinate perpendicular to the planar interface, the subscripts “ $\alpha$ ” and “ $\beta$ ” indicate the coexisting phases,  $\hat{\zeta} = \zeta/\ell$  is the normalized interfacial thickness, and  $\hat{\delta} = \delta/\ell$  is the normalized shift between the concentration and density profiles. The coefficient of the asymmetric terms in Eqs. (2.54) and (2.55) is the reduced diameter for the density and concentration, given by

$$\Delta\hat{\rho}_d = \frac{\rho_\beta + \rho_\alpha}{2\rho_c} - 1 \quad (2.60)$$

$$\Delta\hat{x}_d = \frac{x_\beta + x_\alpha}{2x_c} - 1 \quad (2.61)$$

where  $\rho_c$  and  $x_c$  are the critical points determined from the non-reacting blinking-checkers model, referred to as virtual critical points, see Sec. 2.4.2. The diameters with respect to the virtual critical points are illustrated in Fig. 2.15 for each system investigated. Relative to the liquid-vapor coexistence, for the liquid-liquid coexistence, the diameters are small, such that the asymmetric contribution to the liquid-liquid interfacial profiles is also minimal.

Due to the lack of a theory to account for the interfacial profile asymmetry in compressible binary fluids, the Fisher-Wortis ansatz is adopted, even though it was originally developed for a single component substance [197, 198]. This ansatz contains only two free parameters,  $\hat{\zeta}$  and  $\hat{\delta}$ ,

less than the symmetric ansatz, and it partially reproduces the asymmetry of the exact solution (see details in Appendix A).

### 2.4.3.2 Liquid-Vapor Interfacial Tensions

Using the Fisher-Wortis ansatz, the liquid-vapor interfacial tension along the thermodynamic path (selected by interconversion) as a function of temperature is presented in Fig. 2.16(a) for seven systems. It is found that all scenarios exhibit either an inflection point or two extrema. Of the two scenarios that exhibited an inflection point, but not extrema, ( $\varepsilon_{BA} = 1.20$  and  $\varepsilon_{BA} = 1.24$ ) both were “singularity free scenarios” (exhibiting no liquid-liquid phase transition) [10] whose thermodynamic path was relatively far away from the liquid-vapor critical line, see Fig. 2.14. Each of the remaining scenarios exhibit a maximum and minimum depending on the proximity of the selected thermodynamic path to the liquid-vapor critical line, including the singularity-free system with  $\varepsilon_{BA} = 1.16$ . The scenarios for which the liquid-vapor coexistence was interrupted by the triple point ( $\varepsilon_{BA} = 1.00$ ) exhibit a discontinuity of the liquid-vapor surface tension at this point.

The reduced interfacial tension, expressed through the distance to the virtual LV critical temperature  $\Delta\hat{T} = 1 - T/[T_c(x)]$ , is illustrated in Fig. 2.16(b). Systems exhibiting two extrema in their interfacial tension demonstrate a “looping” pattern as the thermodynamic path approaches and then deviates from the virtual LVCL. As the interconverting systems approach their actual LV critical points, the surface tension asymptotically follows the meanfield power law  $\sigma \sim |\Delta\hat{T}|^{3/2}$ , as presented in Fig. 2.17(a).

In the region where the surface tension reaches a minimum, the interfacial thickness, pre-

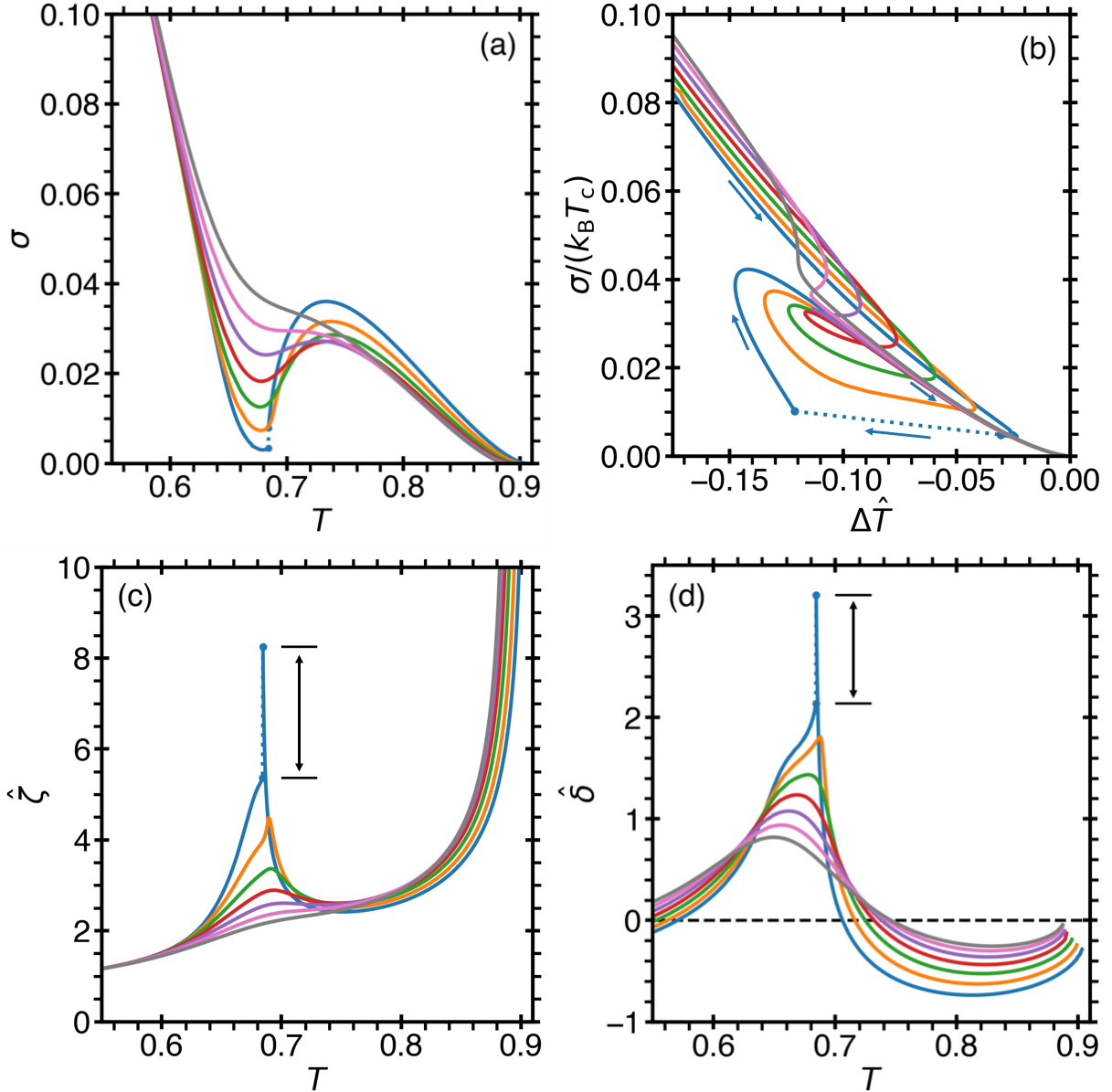


Figure 2.16: The liquid-vapor interfacial tension as a function of temperature (a), and also presented in reduced units (b), for the system with  $\varepsilon_{BA} = 1.00$  (blue),  $\varepsilon_{BA} = 1.04$  (orange),  $\varepsilon_{BA} = 1.08$  (green),  $\varepsilon_{BA} = 1.12$  (red),  $\varepsilon_{BA} = 1.16$  (purple),  $\varepsilon_{BA} = 1.20$  (pink), and  $\varepsilon_{BA} = 1.24$  (gray). In (b), the critical temperature is given by the “virtual” critical point (for the non-reactive binary mixture) for each concentration along the thermodynamic path selected by the interconversion reaction. The blue arrows indicate the direction of warming. (c) The reduced interfacial thickness,  $\hat{\zeta} = \zeta/\ell$ , and (d) the reduced relative distance between the concentration and density profiles,  $\hat{\delta} = \delta/\ell$ . In (a-d), the dotted lines indicate the discontinuity of the interfacial properties for the system with  $\varepsilon_{BA} = 1.00$  at the triple point, shown by the vertical bars in (c,d).

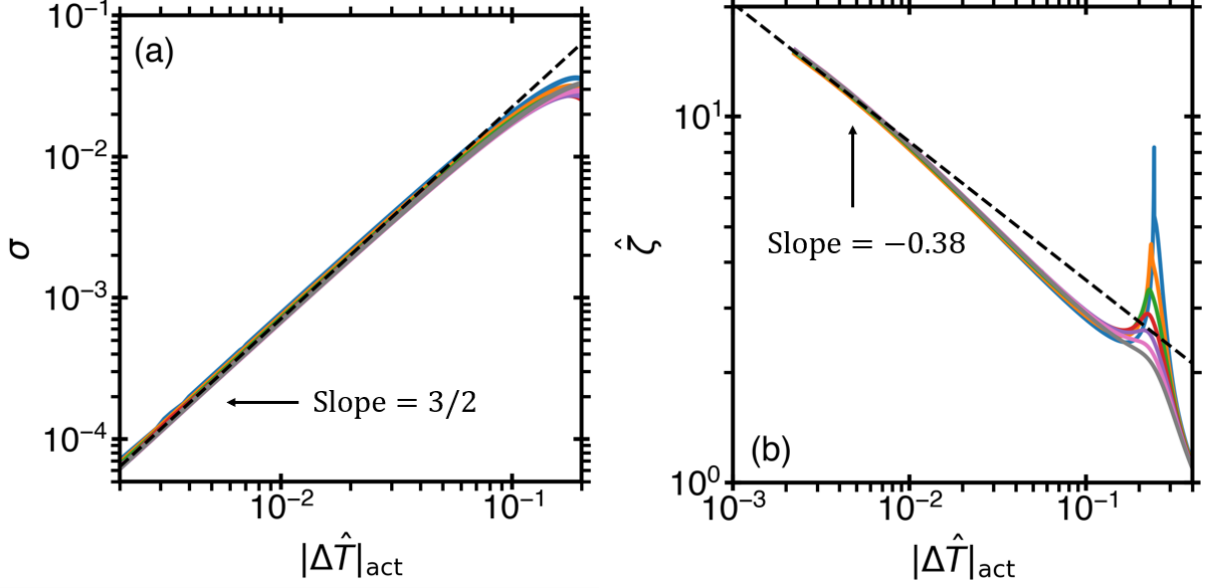


Figure 2.17: (a) The behavior of the liquid-vapor interfacial tension follows the power law,  $\sigma = \sigma_0 |\Delta \hat{T}|^{3/2}$ , where the amplitude was found to be  $\sigma_0 = 0.71$ , asymptotically close to the actual liquid-vapor critical temperature (see Table 2.2). (b) The behavior of the reduced liquid-vapor interfacial thickness,  $\hat{\zeta} = \zeta/\ell$ , follows the power law,  $\hat{\zeta} = \hat{\zeta}_0 |\Delta \hat{T}|^{-0.38}$ , where the amplitude was found to be  $\hat{\zeta}_0 = 1.50$  asymptotically close to the actual critical point.

sented in Fig. 2.16(c), correspondingly reaches a maximum. This phenomenon occurs since the thermodynamic path approaches the virtual LVCL. A DGT treatment of the liquid-vapor interface of real water [199] reported the possibility of a minimum in the temperature dependence of the interfacial thickness (as observed in several cases here), depending on the equation of state used to describe metastable water. Also, it should be noted that, in particular, for the system with  $\varepsilon_{BA} = 1.00$ , the interfacial thickness exhibits a discontinuity at the triple point temperature (see Table 2.5). It is estimated that the DGT approximation breaks down when the interface becomes sharp. In this limit, the contribution to the free energy from the liquid-vapor interface is given through Eq. (2.48), as  $(1/4)\ell^2 \varepsilon_{BB} |\nabla \rho|^2$ , which upon integration over the volume of space gives,  $\sigma_{LV,shp} \approx \varepsilon_{BB}/8 = 0.2$ . This limit is reached around  $T = 0.5$ , where the interfacial thickness becomes proportional to the size of the lattice cell,  $\hat{\zeta} = 1$ . For each system in the vicinity of

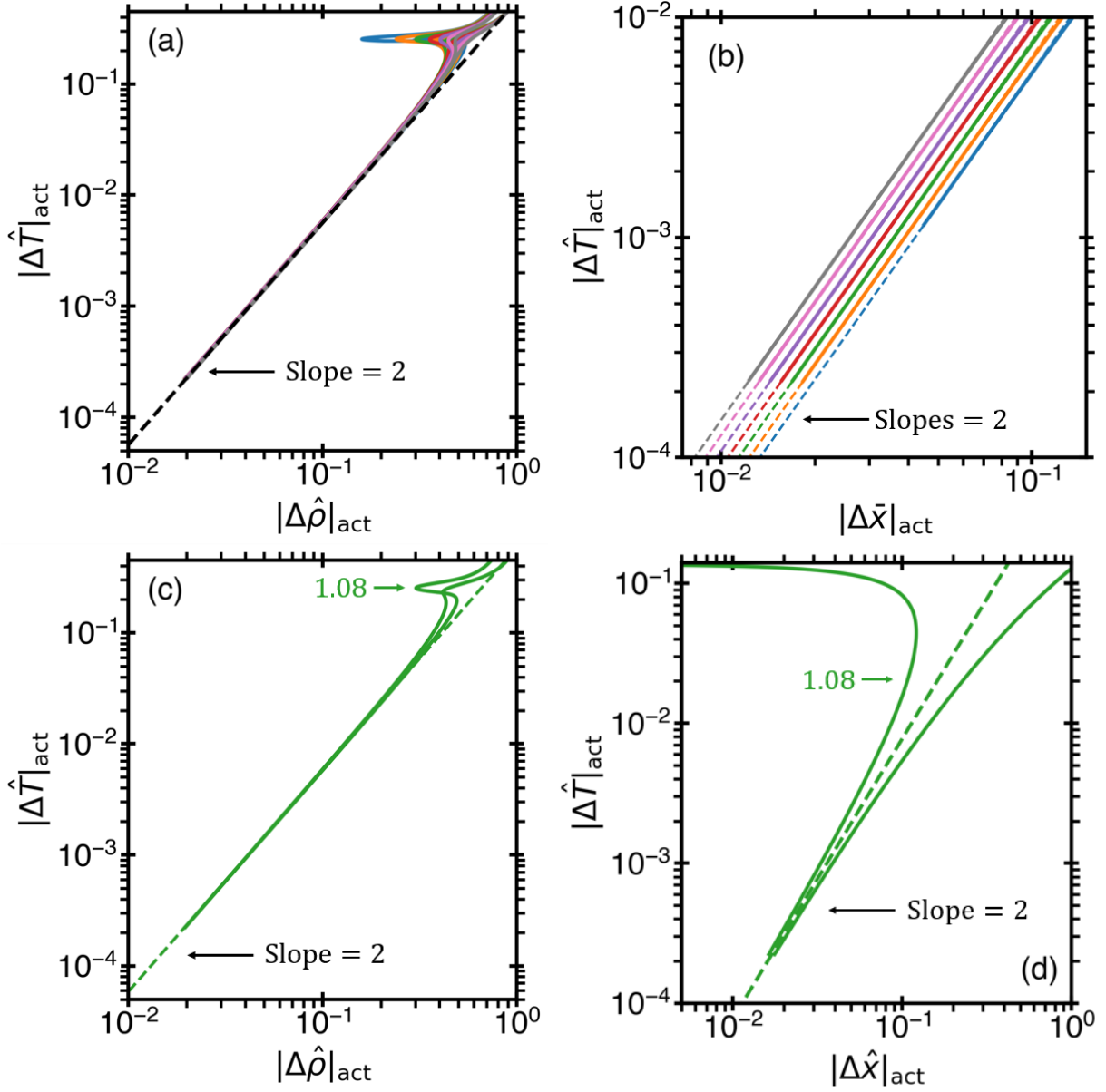


Figure 2.18: Asymptotic behavior of the liquid vapor coexistence for systems with  $\epsilon_{\text{AA}} = 1.6$ ,  $\epsilon_{\text{BB}} = 2.0$ ,  $\hat{e} = 3$ ,  $\hat{s} = 4$ , and with various values of  $\epsilon_{\text{BA}}$ :  $\epsilon_{\text{BA}} = 1.00$  (blue),  $\epsilon_{\text{BA}} = 1.04$  (orange),  $\epsilon_{\text{BA}} = 1.08$  (green),  $\epsilon_{\text{BA}} = 1.12$  (red),  $\epsilon_{\text{BA}} = 1.16$  (purple),  $\epsilon_{\text{BA}} = 1.20$  (pink), and  $\epsilon_{\text{BA}} = 1.24$  (gray). (a) The temperature-density LV coexistence follows the meanfield power law,  $\Delta \hat{T} \sim |\Delta \hat{\rho}|^2$ , where  $\Delta \hat{T}_{\text{act}} = 1 - T/T_c^{\text{act}}$  and  $T_c^{\text{act}}$  is the actual critical temperature selected by the interconverting path. Likewise,  $\Delta \hat{\rho}_{\text{act}} = 1 - \rho/\rho_c^{\text{act}}$ , where  $\rho_c^{\text{act}}$  is the actual critical density. (b) The temperature-average concentration LV coexistence follows the meanfield power law,  $\Delta \hat{T} \sim |\Delta \bar{x}_{\text{act}}|^2$ , where  $\Delta \bar{x}_{\text{act}} = 1 - \bar{x}/x_c^{\text{act}}$ , in which  $\bar{x} = (x_L + x_V)/2$  and  $x_c^{\text{act}}$  is the actual critical concentration. (c,d) Illustrate, as an example, the asymptotic behavior of the system with  $\epsilon_{\text{BA}} = 1.08$ , in which (d) shows the asymptotic behavior of each branch of the concentration coexistence.

the liquid-vapor critical point, it was found that the interfacial thickness followed an asymptotic power law of the form  $\hat{\zeta} \sim |\Delta\hat{T}|^{-0.38}$ , which deviates from the van der Waals meanfield asymptotic power law [192],  $\hat{\zeta} \sim |\Delta\hat{T}|^{-0.5}$ , for the thickness of the order-parameter interface, Fig. 2.17(b). As predicted by the complete scaling theory [136, 137, 200], the order parameter for the compressible binary mixture is a nonlinear combination of  $\rho$  and  $x$ . Thus, the discrepancy in the asymptotic behavior of the interfacial thickness may be attributed to the assumption that the thickness for the density and concentration profiles is the same as for the order parameter in the Fisher-Wortis ansatz, see Eqs. (2.54) and (2.55).

The inflection points of the concentration and density profiles are related through the shift  $\delta$ , which was included in the concentration profile ansatz, Eq. (2.55). In the first-order approximation,  $\delta$  can be separated into symmetric and asymmetric contributions as,  $\delta = \delta_{\text{sym}} + \delta_{\text{asym}}$ . The symmetric contribution is proportional to the difference in the centers of each profile,  $\delta_{\text{sym}} \sim x[\hat{z} = 0] - \rho[\hat{z} = 0]$ , while the asymmetric contribution is proportional to the difference in diameters,  $\delta \sim \Delta\hat{x}_d - \Delta\hat{\rho}_d$ . The effects of asymmetry on near-critical interfacial profiles in the scaling theory of inhomogeneous fluids was considered in Ref. [201] In the region of the anomalous behavior of the surface tension, this shift reaches a maximum as illustrated in Fig. 2.16(d). Similarly to the interfacial thickness, the shift is also discontinuous at the triple point temperature (see Table 2.5). Meanwhile, at the actual LV critical temperature  $\delta$  approaches a finite value, as both the density and concentration profiles become infinitely smooth and the numerical calculation become uncertain due to the large fluctuations.

### 2.4.3.3 Liquid-Liquid Interfacial Tensions

The liquid-liquid interfacial tensions were calculated for the four systems exhibiting liquid polyamorphism ( $\varepsilon_{BA} = 1.00$ ,  $\varepsilon_{BA} = 1.04$ ,  $\varepsilon_{BA} = 1.08$ , and  $\varepsilon_{BA} = 1.12$ ) with use of the Fisher-Wortis ansatzes for the density and concentration profiles, Eqs. (2.54) and (2.55), and are illustrated in comparison with the liquid-vapor interfacial tension in Fig. 2.19. It was found that for three systems: ( $\varepsilon_{BA} = 1.00$ ,  $\varepsilon_{BA} = 1.04$ , and  $\varepsilon_{BA} = 1.08$ ), the liquid-liquid interfacial tension crosses that of the liquid-vapor, being larger for lower temperatures [180]. This is different from the conclusion of Feeney and Debenedetti [180] that  $\sigma_{LL}$  is fundamentally lower than  $\sigma_{LV}$  at the same temperature. Indeed, this behavior is observed when the bottleneck in the liquid-vapor coexistence is absent, as in the case of Ref. [180], or not very deep, as in the blinking-checkers model for the system with  $\varepsilon_{BA} = 1.12$ . Depending on the choice of parameters in the blinking-checkers model,  $\sigma_{LL}$  may be large away from the LLCPC; however, as the LLCPC is approached, the ratio  $\sigma_{LL}/\sigma_{LV}$  must vanish.

It should be noted that, for the liquid-liquid interfacial tension, the DGT is a good approximation everywhere as the liquid-liquid coexistence approaches infinite pressures before forming a sharp interface between the two liquid phases. In the limit of a sharp liquid-liquid interface, the contribution to the free energy from the liquid-liquid interfacial tension,  $\sigma_{LL}$ , is given through Eq. (2.50), as  $(1/4)\ell^2\varepsilon|\nabla\rho|^2$ , which when integrated over space, gives  $\sigma_{LL,shp} \approx \varepsilon/8$ . It is estimated that a sharp interface forms where  $\sigma_{shp} \approx \varepsilon/8$ , which goes from  $\sigma_{shp} \approx 0.2$  for the system with  $\varepsilon_{BA} = 1.00$  to  $\sigma_{shp} \approx 0.17$  for the system with  $\varepsilon_{BA} = 1.12$ , which is larger than any of the liquid-liquid interfacial tensions observed in the model. For the system with  $\varepsilon_{BA} = 1.00$ , the liquid-liquid interfacial tension is smaller than both the liquid A - vapor or the liquid B - vapor

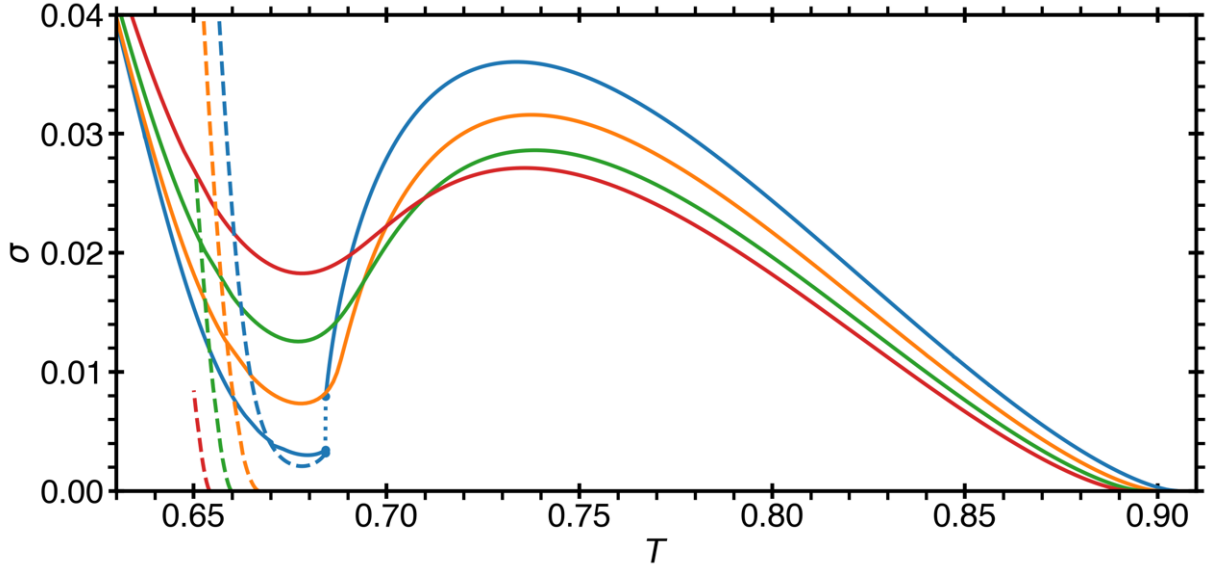


Figure 2.19: Comparison between the liquid-liquid (dashed curves) and liquid-vapor (solid curves) interfacial tensions as a function of temperature for the system with  $\varepsilon_{BA} = 1.00$  (blue),  $\varepsilon_{BA} = 1.04$  (orange),  $\varepsilon_{BA} = 1.08$  (green),  $\varepsilon_{BA} = 1.12$  (red). The dotted blue line indicates the discontinuity in the liquid-vapor interfacial tension.

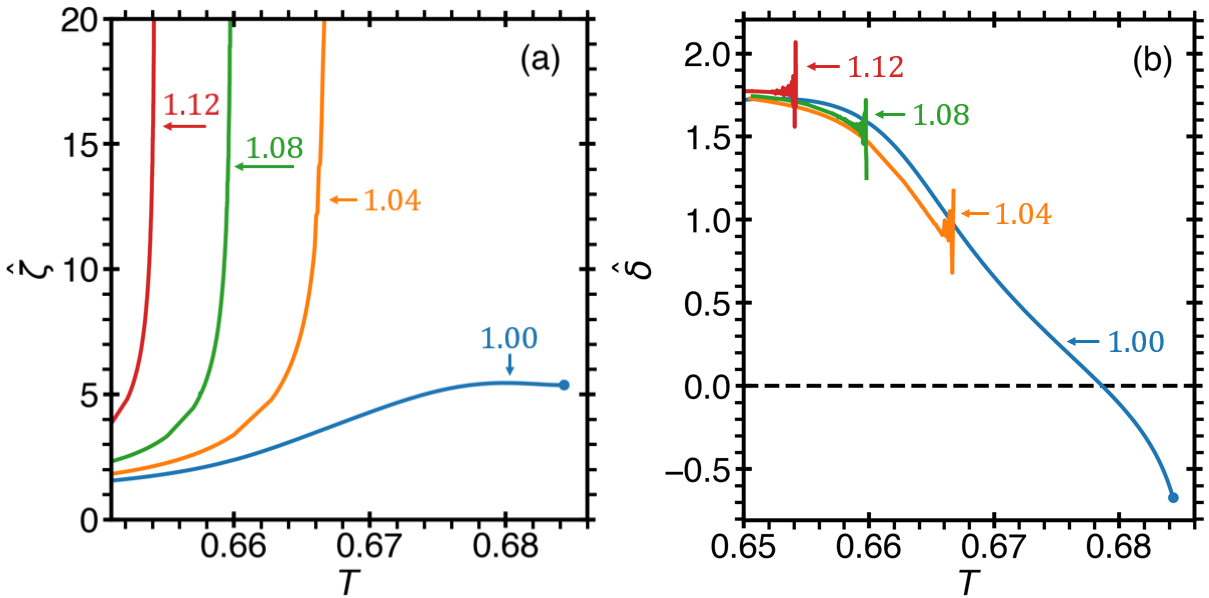


Figure 2.20: Liquid-liquid interfacial properties of the systems exhibiting liquid polyamorphism with  $\varepsilon_{AA} = 1.6$ ,  $\varepsilon_{BB} = 2.0$ ,  $\hat{e} = 3$ ,  $\hat{s} = 4$ , and with various values of  $\varepsilon_{BA}$ :  $\varepsilon_{BA} = 1.00$  (blue),  $\varepsilon_{BA} = 1.04$  (orange),  $\varepsilon_{BA} = 1.08$  (green),  $\varepsilon_{BA} = 1.12$  (red). (a) the reduced thickness,  $\hat{\zeta} = \zeta/\ell$  of the liquid-liquid interface, and (b) the reduced shift,  $\hat{\delta} = \delta/\ell$ , between the density and concentration liquid-liquid profiles. In (a,b) the thickness and shift reach a finite value (marked with a blue circle) at the triple point temperature.

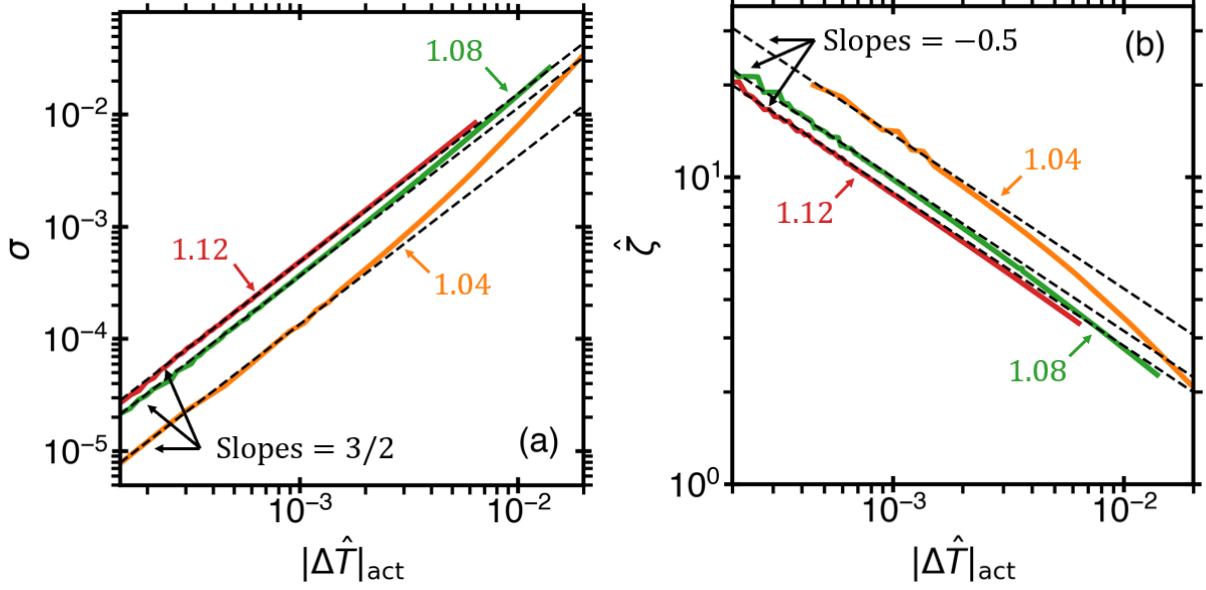


Figure 2.21: (a) The behavior of the liquid-liquid interfacial tension follows the meanfield power law,  $\sigma = \sigma_0 |\Delta \hat{T}|^{3/2}$ , (dashed lines) asymptotically close to the actual liquid-liquid critical temperature (see Table 2.3). (b) The behavior of the reduced liquid-liquid interfacial thickness,  $\hat{\zeta} = \zeta/\ell$ , follows the meanfield power law,  $\hat{\zeta} = \hat{\zeta}_0 |\Delta \hat{T}|^{-1/2}$ , (dashed lines). In (a,b) the systems exhibiting liquid polyamorphism and a liquid-liquid critical point are shown:  $\varepsilon_{\text{BA}} = 1.04$  (orange),  $\varepsilon_{\text{BA}} = 1.08$  (green),  $\varepsilon_{\text{BA}} = 1.12$  (red), and the amplitudes of the asymptotic meanfield power laws are provided in Table 2.4.

interfacial tensions (see Table 2.5 for details). The reduced interfacial thicknesses,  $\hat{\zeta}$ , and the reduced shifts between the concentration and density profiles,  $\hat{\delta}$ , are illustrated in Fig. 2.20. In particular, it is noted that, for the systems that reach a liquid-liquid critical point: ( $\varepsilon_{\text{BA}} = 1.04$ ,  $\varepsilon_{\text{BA}} = 1.08$ , and  $\varepsilon_{\text{BA}} = 1.12$ ), the liquid-liquid interfacial tension does not demonstrate any anomalous behavior. Furthermore, the interfacial tensions and interfacial thicknesses follow the predicted meanfield asymptotic power laws, see Fig. 2.21. Moreover, in the system with  $\varepsilon_{\text{BA}} = 1.00$ , the liquid-liquid interfacial tension exhibits a minimum prior to the triple point temperature.

Table 2.4: Asymptotic amplitudes of the liquid-liquid interfacial tension and liquid-liquid correlation length of concentration fluctuations for the three systems exhibiting liquid polyamorphism and a liquid-liquid critical point. The asymptotic meanfield behavior is illustrated in Fig. 2.21.

$\varepsilon_{\text{BA}}$	$\sigma_0$	$\hat{\zeta}_0$
1.04	4.26	0.433
1.08	11.48	0.315
1.12	15.35	0.282

#### 2.4.3.4 Interfacial Profiles

In this subsection, the interfacial profiles for density and concentration. Figure 2.22(a) and (b) show the interfacial profiles predicted from the Fisher-Wortis ansatzes, Eqs. (2.54) and (2.55), for the system with  $\varepsilon_{\text{BA}} = 1.08$  at the temperatures that correspond to the maximum and minimum of the LV interfacial tension. It is found that at the minimum, the interfacial profiles are relatively symmetric, while at the maximum, the concentration profile contains a large asymmetric contribution. The large asymmetry predicted by the Fisher-Wortis concentration ansatz occurs since the diameter of the concentration,  $\Delta\hat{x}_d$ , reaches a maximum at this temperature, see Fig. 2.15.

For the system with  $\varepsilon_{\text{BA}} = 1.00$ , at the triple point temperature,  $T_{\text{TP}} = 0.6843$ , all of the interfacial properties exhibit a discontinuity (see Table 2.5). Since the interfacial tension of the LB-V (low-density-liquid - vapor) interface is much larger than the other two interfacial

Table 2.5: The surface tension  $\sigma$ , normalized interfacial thickness  $\hat{\zeta} = \zeta/\ell$ , and normalized shift  $\hat{\delta} = \delta/\ell$  for the three coexisting phases (liquid A, liquid B, and vapor) for the system with  $\varepsilon_{\text{BA}} = 1.00$  at the triple point temperature ( $T = 0.6843$ ).

	$\sigma$	$\hat{\zeta}$	$\hat{\delta}$
LB-V	0.00793	8.242	3.203
LA-V	0.00334	5.372	2.145
LA-LB	0.00321	6.040	0.983

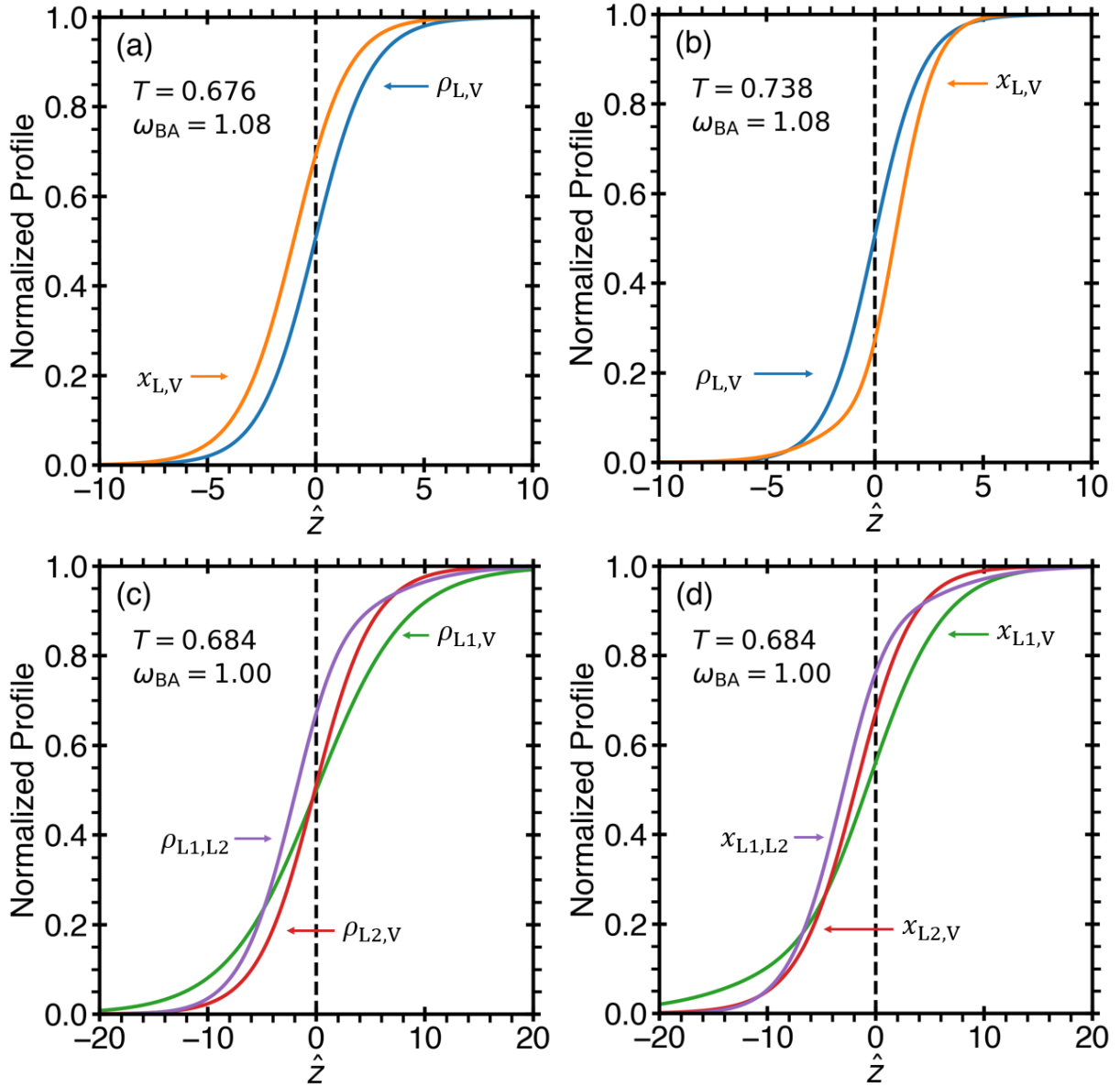


Figure 2.22: Normalized density and concentration liquid-vapor profiles as a function of the coordinate perpendicular to the planar interface,  $\hat{z} = z/\ell$ , given by Eqs. (2.54) and (2.55) for the system with  $\varepsilon_{AA} = 1.6$ ,  $\varepsilon_{BB} = 2.0$ ,  $\varepsilon_{BA} = 1.08$ ,  $\hat{e} = 3$ , and  $\hat{s} = 4$  at the two temperatures (a,b) that correspond to the two extrema of the liquid-vapor interfacial tension (shown in Fig. 2.16). Normalized (c) density and (d) concentration profiles for three-phase coexistence at the triple point,  $T_{TP} = 0.6843$ , for the system with  $\varepsilon_{AA} = 1.6$ ,  $\varepsilon_{BB} = 2.0$ , and  $\varepsilon_{BA} = 1.00$ .

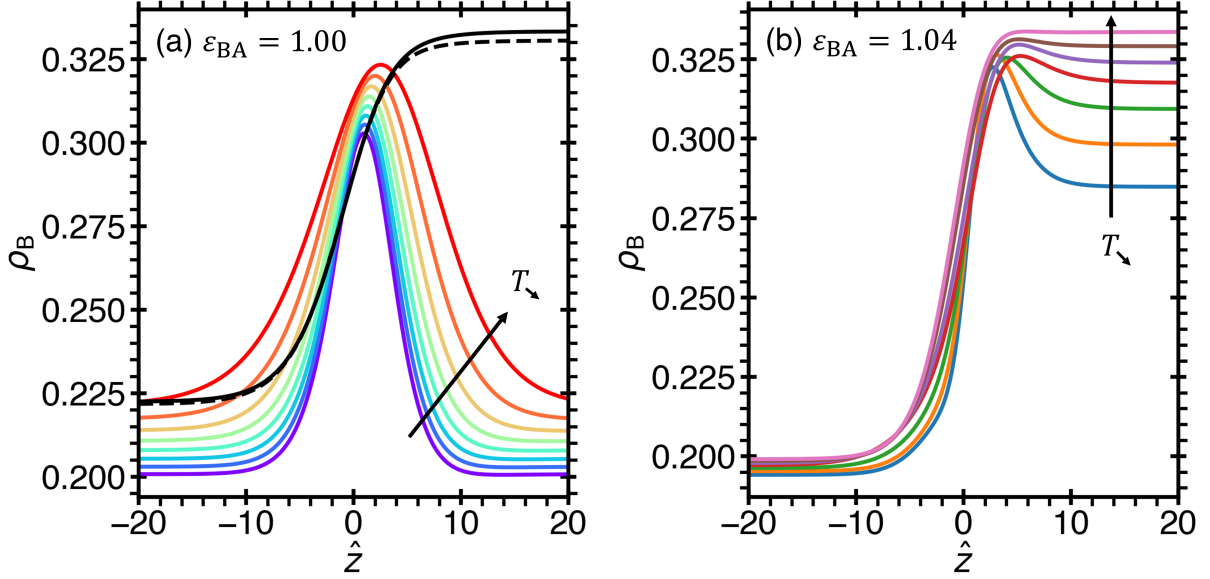


Figure 2.23: Interfacial profiles of species B,  $\rho_B = \rho x$ , in the blinking-checkers model demonstrate surface enrichment near the TP temperature,  $T_{TP} = 0.68429$ . (a) Surface enrichment of species B for the system with  $\varepsilon_{BA} = 1.00$ . The colored curves indicate temperatures from  $T = 0.68989$  to  $T = T_{TP}$  in steps of  $\Delta\hat{T} = -0.0008$  in order of purple to red. The black curves are  $T = 0.68389$  (dashed) and  $T = 0.68309$  (solid). (b) Surface enrichment of species B for the system with  $\varepsilon_{BA} = 1.04$ . The curves are  $T = 0.6882$  to  $T = 0.6826$  in steps of  $\Delta T = -0.0008$  (blue to pink). In (a,b), the black arrows indicate the direction of decreasing temperature. Note that while the transition of a surface enriched profile ( $T > T_{TP}$ ) to a smooth profile ( $T < T_{TP}$ ) is discontinuous in the system with  $\varepsilon_{BA} = 1.00$ , it is continuous in the system with  $\varepsilon_{BA} = 1.04$ .

tensions, then in accordance with Antonov's rule [192],  $\sigma_{LA,V} + \sigma_{LA,LB} < \sigma_{LB,V}$ , it is predicted that the LB-V interface will be enriched (wetted) by the LA (high-density-liquid) phase to reduce the energetically unfavorable LB-V interface. This indicates that the non-monotonic behavior of the liquid-vapor interfacial tension may be caused by the surface enrichment of the LB-V coexistence by species A (see Fig. 2.23). Notwithstanding this complete wetting phenomenon, it is displayed in Fig. 2.22(c) and (d) that the interfacial profiles for the density and concentration of the three coexisting phases at the triple point.

### 2.4.3.5 Conditions for Anomalous Interfacial Behavior

It should be noted that, based on the findings presented in the previous subsections, no general conclusion about the absence of a liquid-liquid transition can be drawn from the existence of an inflection point in the liquid-vapor interfacial tension. For instance, on one hand, in the present description, the inflection point is observed only for singularity free scenarios; on the other hand, the TIP4P/2005 model of water exhibits an inflection point [182, 184, 185], while it is thought to possess a liquid-liquid transition terminated by a critical point [91, 202, 203]. It is emphasized that the anomaly in the temperature dependence of the interfacial tension is linked to the anomaly in the liquid-vapor coexistence along the thermodynamic path selected by interconversion, and originates in the region where the equilibrium fraction of species,  $x_e$ , most dramatically changes, a concept that was first suggested by Hruby and Holten [169]. It follows from the results discussed in the previous subsections that the shape of the LV coexistence is affected by two factors: the proximity to the virtual LVCL and the existence of the liquid-liquid phase transition. The anomalies in supercooled water can be interpreted as the results of the interconversion of two supramolecular structures. This interconversion occurs only at low temperatures, extremely far away from the liquid-vapor critical point. Therefore, the LV coexistence in supercooled water, because of the maximum of the liquid density at 4 °C, exhibits a valley only in its liquid branch [78]. Consequently, the LV surface tension may exhibit a maximum or an inflection point depending on the depth of the valley [180].

## 2.5 Conclusion of Chapter 2

It has been found that the fluid-phase behavior is significantly affected by molecular interconversion. The two-state thermodynamic approach provides a general framework to describe fluid-fluid phase transitions in a variety of polyamorphic fluids. This approach considers the interconversion of two species or two supramolecular structures to be generic cause of fluid polyamorphism, for example: the dimerization in hydrogen (Sec. 2.2), the polymerization in sulfur (Sec. 2.3), the folding-unfolding of proteins, or the structural transition in polyamorphic supercooled water (Sec. 2.4). It should be emphasized that even without an explicit chemical reaction between two species, like that in supercooled water, polyamorphism may be modeled through the framework of two-state thermodynamics.

## Chapter 3: Phase Formation Affected by Species Interconversion

In this chapter<sup>1</sup>, based on the ideas of the Cahn-Hilliard theory of spinodal decomposition [193], a phenomenological theory to describe the nonequilibrium dynamics of phase formation in interconverting mixtures is introduced. This approach is referred to as the “generalized Cahn-Hilliard theory.” The developed approach goes beyond Cahn-Hilliard’s theory by not only including the interconversion of species, but also by describing the time-evolution of the system into the coarsening and the nucleation regimes. Polyamorphic systems, with non-zero energy and volume of reactions, as well as the effects of fluctuations of the order parameter in the critical region are also investigated.

### 3.1 Generalizing Cahn-Hilliard Theory

In this section, the Cahn–Hilliard theory of spinodal decomposition is generalized to include the effects of two types of molecular interconversion: natural, in which the interconversion of species mirrors the equilibrium “flipping” of spins in the Ising model, and forced, in which an external force causes the alternative molecules to stay in equal amounts. This behavior is captured by the spatial and temporal evolution of the order parameter, given through the continuity

---

<sup>1</sup>This chapter was reproduced from Thomas J. Longo and Mikhail A. Anisimov, *J. Chem. Phys.*, **156**, 084502 (2022); <https://doi.org/10.1063/5.0081180> and from Thomas J. Longo, Nikolay A. Shumovskyi, Salim M. Asadov, Sergey V. Buldyrev, and Mikhail A. Anisimov, *J. Non-Cryst. Solids: X*, **13**, 100082 (2022); <https://doi.org/10.1016/j.nocx.2022.100082> with the permission of AIP Publishing and Elsevier, respectfully.

equation. Also, the experimental and computational conditions required to observe the two major predictions of the theory, phase amplification (under equilibrium conditions) and microphase separation (under nonequilibrium conditions), are discussed.

### 3.1.1 Conserved and Nonconserved Order-Parameter Dynamics

The continuity equation for an incompressible binary mixture is given in the general form [94, 107, 117, 118, 204–207],

$$\frac{\partial \varphi}{\partial t} + \nabla \cdot \mathbf{J}_C = J_{NC} \quad (3.1)$$

where  $\mathbf{J}_C$  is the mutual diffusion flux associated with the conserved component of the order parameter, and it is related to the gradient of the chemical potential by  $\mathbf{J}_C = -M\nabla\hat{\mu}$ , in which  $M$  is the molecular mobility and  $\hat{\mu}$  is the chemical potential given by Eq. (2.10). Similarly, the flux associated with the nonconserved component of the order parameter is  $J_{NC}$ , which (for reaction-diffusion systems) is expressed through the reaction rate [118, 206, 207].

In Cahn-Hilliard's theory of spinodal decomposition, when there is only mutual diffusion (no interconversion of any form), the number of molecules of a particular species is conserved such that  $J_{NC} = 0$  and Eq. (3.1) reduces to the classical Cahn-Hilliard equation [102]

$$\frac{\partial \varphi}{\partial t} = M\nabla^2 \hat{\mu} \quad (3.2)$$

This equations describes the dynamics of a system that will evolve toward phase separation when quenched into the unstable region (under the spinodal). This equation can be analytically solved with use of Fourier analysis to determine the phase domain growth rate (also, referred to as the

“amplification factor”) [102], which, in the Cahn-Hilliard theory, is given by

$$\omega(q) = -Dq^2(1 - \xi^2q^2) \quad (3.3)$$

where  $\xi$  is the correlation length of concentration fluctuations and  $D$  is the mutual diffusion coefficient; in the meanfield approximation,  $\xi^2 = \kappa/|\hat{\chi}_{q=0}^{-1}|$  and  $D = M\hat{\chi}_{q=0}^{-1}$ . In the unstable region (under the spinodal), the susceptibility is negative, the correlation length by definition is positive, and, consequently, the mutual diffusion coefficient is negative. Hence, mutual diffusion is the driving force for phase separation through spinodal decomposition [102, 208, 209].

The flux, associated with the nonconserved component of the order parameter, in the continuity equation, Eq. (3.1), originates due to the two types of interconversion reactions present in the system, and consequently,  $J_{\text{NC}}$ , may be expressed through two terms [100],

$$J_{\text{NC}} = -L\hat{\mu} + \pi \quad (3.4)$$

where the first term,  $-L\hat{\mu}$ , with an interconversion kinetic coefficient  $L$ , represents the rate of natural interconversion, in which the chemical potential is given by Eq. (2.12). The second term,  $\pi$ , denotes a nonequilibrium source of forced interconversion that requires the alternative species to remain in equal amounts and is analogous to the external magnetic or electric field in ferromagnetic or ferroelectric systems [100].

Initially, consider the simplest chemical reaction in which the interconversion equilibrium constant  $\mathcal{K} = k_1/k_2 = 1$ , which does not depend on temperature or pressure, such that  $\ln \mathcal{K} = 0$ . Therefore, the Gibbs energy change of reaction, given by Eq. (2.9), is  $\hat{G}_{BA} = 0$  [210], (the more

general case, when  $\mathcal{K} = \mathcal{K}(T, P)$ , will be considered in Section 3.4). In this approximation, the interconversion between species A and B mirrors the flipping of spins in the Ising model, in which there is no heat or volume change of the reaction. Thus, the  $-L\hat{\mu}$  term, corresponding to the natural interconversion, represents the nonconserved evolution of the order parameter, in which the conservation of molecules of a certain species is no longer a conserved property [211].

As for the source term,  $\pi$ , depending on the system, it can be written in a variety of forms, but typically, it characterizes the additional interactions present in a system. It may be classified as a “source” ( $\pi > 0$ ) or a “sink” ( $\pi < 0$ ) of diffusion or interconversion, and it may exist as an equilibrium source or be introduced externally, producing a nonequilibrium system. For example, the internal source can be found in systems of diblock copolymers, where the finite size of the block competes with phase segregation, leading to the formation of equilibrium microphase domains [212, 213]. Another example of this type of source is in ferromagnetic or ferroelectric systems and dipolar fluids, in which the long-ranged Coulombic interactions may produce equilibrium microphase separation [107]. A diffusion-promoting source could also be introduced externally through radiation to enhance or inhibit phase separation [214].

Alternatively, an external interconversion source could be achieved via the interactions of energy-carrying particles, such as photons, that may break intramolecular bonds [215] or it could be seen in biological cells through a flux of energy produced by ATP [113, 114]. Likewise, the source could promote interconversion through the flux of matter, such as in a system constrained to an adsorbing-desorbing layer [116]. Lastly, an internal interconversion source originating from a disbalance of intermolecular forces could produce a nonequilibrium system with steady-state microphase domains. This effect was observed by Uralcan *et al.* [7] in a dissipative chiral-mixture model, which is referred to as the “CM model.” This case is considered in Section 4.2.

In this chapter, a source of forced interconversion that is independent of the chemical potential in the equilibrium state is considered; one that will drive the system towards a “completely interconverted state” - a spatially homogeneous state with equal amounts of interconverting species - by allowing the alternative species to interconvert against the equilibrium conditions via a simple interconversion reaction, Eq. (2.7). Thus, forced interconversion may be viewed as a local chemical reaction for which the chemical potential difference depends only on the bulk concentration [207]. For this reason, such a source is referred to as a “forced interconversion source.”

If the effect of forced interconversion on a system with conserved order-parameter dynamics ( $L = 0$ ) is considered, then this scenario corresponds to the model originally introduced by Glotzer *et al.* [216, 217] where in the first-order approximation (valid only near thermodynamic equilibrium [207]) the forced interconversion term in Eq. (3.4) has the form of  $\pi = k_2 x_B - k_1 x_A$ . Rearranging this reaction rate using the fact that the total number of particles in the system is conserved,  $x_A + x_B = 1$  and  $K = k_1 = k_2$ , then the source of forced interconversion may be written in terms of the order parameter ( $\varphi$ ) as  $\pi = -K\varphi(\mathbf{r}, t)$ . In this case, Eq. (3.1) is given in the form

$$\frac{\partial \varphi}{\partial t} = M \nabla^2 \hat{\mu} - K \varphi \quad (3.5)$$

The corresponding growth rate for this system is  $\omega(q) = -K - Dq^2(1 - \xi^2 q^2)$ . Glotzer *et al.* found that the addition of such a specific type of forced interconversion source causes the system to phase separate into microphase domains with a characteristic length scale less than the size of the simulation box - the phenomenon of nonequilibrium microphase separation. They show that the growth rate is restricted at a wavenumber,  $q_- = \sqrt{-K/D}$ , corresponding to the first root of  $\omega(q) = 0$ . Glotzer *et al.*'s model predicts the formation of microphase domains only in

a nonequilibrium steady-state in the presence of a forced interconversion source [117, 207, 218]. It is noted that this phenomenon could be conceptually compared to the common “household” example of stirring a mixture of water and oil. Obviously, there is no chemical interconversion between water and oil molecules. However, the water and oil will separate into phase domains, whose size depends on the stirring rate,  $K$ .

It is important to note that, in the first-order approximation, the form of the source of forced interconversion is similar to the thermodynamic part of the chemical potential,  $\hat{\mu}_{\text{th}}$ , being linearly proportional to  $\varphi$ , Eq. (2.12). However, as shown by Eq. (2.12),  $\hat{\mu}$  in the meanfield approximation is linearly dependent on the distance to the critical temperature, while the source only depends on the order parameter,  $\varphi$  and the reaction rate  $K$ .

Combining Eq. (3.4) for  $J_{\text{NC}}$  and choosing the source of forced interconversion considered by Glotzer *et al.*,  $\pi = -K\varphi$ , the continuity equation, Eq. (3.1), may be expressed in the generalized form

$$\frac{\partial \varphi}{\partial t} = M\nabla^2 \hat{\mu} - L\hat{\mu} - K\varphi \quad (3.6)$$

In which the three terms with kinetic coefficients,  $M$ ,  $L$ , and  $K$  represent mutual diffusion, natural interconversion, and forced interconversion dynamics, which typically depend on temperature, pressure, and (for  $L$  and  $K$ ) the interconversion rate.

Equation (3.6) may be generalized by expressing the source term,  $\pi$ , through a nonequilibrium (“unbalanced”) chemical potential,  $\tilde{\mu}$ . This unbalanced chemical potential competes with the “balanced” chemical potential,  $\hat{\mu}$ , given by Eq. (2.12). In the first-order approximation,  $\tilde{\mu}$  is a non-local (spatially-independent) chemical potential that scales linearly with the order parameter as  $\tilde{\mu} \sim -\varphi$ . Thus, in this form, the general continuity equation, involving all three dynamical

processes, is given by [4,5]

$$\frac{\partial \varphi}{\partial t} = M \nabla^2 \hat{\mu} - L \hat{\mu} + K \tilde{\mu} \quad (3.7)$$

Note that in the lowest-order approximation of Eq. (2.12), the natural interconversion dynamics scales as  $-L \hat{\mu} \sim -L \Delta \hat{T} \varphi$ , which is positive for  $T < T_c$ , while in the same approximation, the forced interconversion dynamics scales as  $K \tilde{\mu} \sim -K \varphi$ , which is negative, indicating that the two are always in opposition. Consequently, the difference between the unbalanced and balanced chemical potentials,  $\Delta \tilde{\mu} = \hat{\mu} - \tilde{\mu}$ , provides the net driving force on the system.

By rearranging Eq. (3.7) to explicitly include this driving force, the dynamics of the natural and forced interconversions may be combined into a single term with a kinetic coefficient,  $L$ . Redefining the unbalanced chemical potentials as  $\tilde{\mu}' = (K/L) \tilde{\mu}$ , a simplified continuity equation may be expressed through two dynamic processes in the form [4,8]

$$\frac{\partial \varphi}{\partial t} = M \nabla^2 \hat{\mu} - L \Delta \tilde{\mu}' \quad (3.8)$$

where  $\Delta \tilde{\mu}'$  is the difference between the balanced and (redefined) unbalanced chemical potential,  $\Delta \tilde{\mu}' = \hat{\mu} - \tilde{\mu}'$ , such that the second term describes the coupled natural-forced interconversion dynamics in the system. In this form, Eq. (3.8) is similar to the continuity equations used to describe the dynamic behavior in active matter systems [107, 219–221]. However, it should be noted that the derivation presented in this section is different from other studies of active matter systems as this derivation explicitly considers the evolution of the system toward equilibrium and the behavior at equilibrium. For instance, in the developed approach, both the natural interconversion and diffusion dynamics depend on the local (spatially-dependent) part of the chemical

potential,  $\hat{\mu}$ .

It can be shown that the reduced entropy production,  $\hat{\sigma}_s = \sigma_s/k_B$ , obtained using the derivation from Groot and Mazur [204] as well as by Mauri [206], has the form  $\hat{\sigma}_s = -\mathbf{J}_C \cdot \nabla \hat{\mu} + J_{NC} \hat{\mu}_{th}$ . Using the mutual diffusion flux,  $\mathbf{J}_C$ , from the discussion of Eq. (3.1) and the interconversion flux,  $J_{NC}$ , from Eq. (3.4) with the unbalanced chemical potential  $\tilde{\mu}$ , the entropy production may be written in the simplified form

$$\hat{\sigma}_s = M|\nabla \hat{\mu}|^2 + L\hat{\mu}_{th}\hat{\mu} + K\hat{\mu}_{th}\tilde{\mu} \quad (3.9)$$

or, equivalently, through the difference in balanced and unbalanced chemical potentials as

$$\hat{\sigma}_s = M|\nabla \hat{\mu}|^2 + L\hat{\mu}_{th}\Delta\tilde{\mu}' \quad (3.10)$$

where it can be seen that  $\hat{\sigma}_s > 0$  always, and specifically, in the equilibrium limit when,  $\hat{\mu} = 0$ , the entropy production remains  $\hat{\sigma}_s > 0$  due to the presence of the external source of forced interconversion.

Using the chemical potential described by Eq. (2.12) with  $\hat{G}_{BA} = 0$  for the simple interconversion reaction, Eq. (3.7) may be expressed in the expanded form

$$\frac{\partial \varphi}{\partial t} = -(K + L\hat{\chi}_{q=0}^{-1})\varphi + (M\hat{\chi}_{q=0}^{-1} + L\kappa)\nabla^2\varphi - M\kappa\nabla^4\varphi \quad (3.11)$$

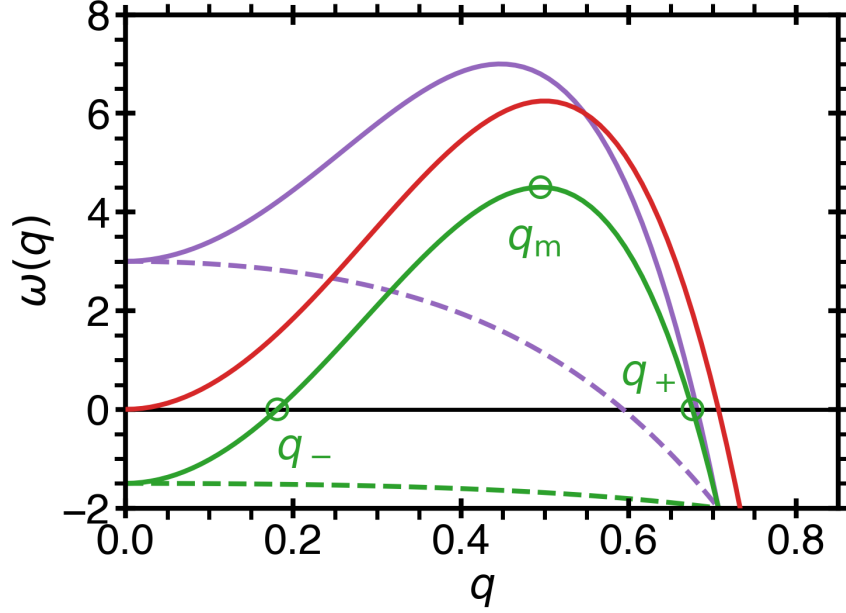


Figure 3.1: The characteristic growth rate, Eq. (3.14), affected by the competition between diffusion, natural interconversion, and forced interconversion at  $\Delta\hat{T} = -0.5$ . Complete phase separation (as predicted by Cahn-Hilliard's theory for  $L = 0$  and  $K = 0$ ) is illustrated by the red curve for  $M = 100$ . Phase amplification is illustrated by the purple curves for restricted ( $M = 100$  - solid) and unrestricted ( $M = 10$  - dashed) cases, in which  $L = 10$  and  $K = 2$ . Microphase separation for  $M = 100$ ,  $L = 1$ , and  $K = 2$  is illustrated by the solid green curve. When the growth rate is always negative, as illustrated by the green dashed curve (for  $M = 1$ ,  $L = 1$ , and  $K = 2$ ), there is no phase domain growth corresponding to a homogeneous steady state. The green circles indicate the three characteristic wavenumbers of the amplification factor: the maximum,  $q_m$ , the lower cut-off,  $q_-$ , and the upper cut-off,  $q_+$

This differential equation has the following solution:

$$\varphi = \varphi_0 + \sum_i \varphi_\infty e^{\omega(q_i)t} \cos(\mathbf{q}_i \cdot \mathbf{r}) \quad (3.12)$$

where  $\varphi_0$  and  $\varphi_\infty$  are constants determined by the initial ( $t = 0$ ) and steady-state ( $t \rightarrow \infty$ ) conditions of the order parameter, respectively, while  $\omega(q)$  is the generalized growth rate, defined as

$$\omega(q) = -(L\hat{\chi}_{q=0}^{-1} + K) - (M\hat{\chi}_{q=0}^{-1} + \kappa L)q^2 - M\kappa q^4 \quad (3.13)$$

It is noted that a conceptually similar equation for the growth rate in a system with an auto-catalytic reaction [115] was also obtained by Lefever *et al.* [117]. Eq. (3.13) can also be expressed through the susceptibility,  $\hat{\chi}_{q=0}$ , and the correlation length,  $\xi$ , as

$$\omega(q) = -K - \hat{\chi}_{q=0}^{-1}(Mq^2 + L\kappa)(1 - \xi^2 q^2) \quad (3.14)$$

Alternatively, Eq. (3.14) may be symmetrized and expressed in the form

$$\omega(q, t) = M\kappa q_m^2(t)[q_m^2(t) - 2q_-^2] - M\kappa[q^2 - q_m^2(t)]^2 \quad (3.15)$$

where the two characteristic wavenumbers,  $q_m$  and  $q_-$ , are the maximum and the lower cut-off of the amplification factor, respectively (see Fig. 3.1). Using a first order approximation, they have the form

$$q_m^2 = -\frac{(M\hat{\chi}_{q=0}^{-1}(t) + L\kappa)}{2M\kappa} \quad \text{and} \quad q_-^2 = -\frac{(K + L\Delta\hat{T})}{M\Delta\hat{T} + L\kappa} \quad (3.16)$$

It should be noted that the maximum of the amplification factor,  $q_m = q_m(t)$  is time dependent, while  $q_-$  is time independent. The time dependence of  $q_m(t)$  is given through the higher order terms of the chemical potential, Eq. (2.11), and is introduced into the time-dependent inverse susceptibility,  $\hat{\chi}_{q=0}^{-1}(t) = \partial\hat{\mu}/\partial\varphi(t)$ . The origin of this temporal evolution is due to the change in concentration at constant temperature from the unstable ( $\varphi = 0$ ) to the stable ( $\varphi > 0$ ) regime; as such, in the second order approximation,  $\hat{\chi}_{q=0}^{-1}(t) \simeq \Delta\hat{T} + (1 + \Delta\hat{T})\varphi(t)$  [4, 5, 222, 223]. In contrast,  $q_-$  is an intrinsic property of the system, and since  $q_-$  determines the cut-off for the smallest possible growing domain modes, then the steady-state limit of the time evolution of the maximum wavenumber will also be cut-off by  $q_-$  as  $q_m(t \rightarrow \infty) \propto q_-$ . To verify this prediction,

$q_m$  was numerically computed from the wavenumber corresponding to the maximum of the structure factor,  $q_m^s$  (Section 3.3), and compared with the steady-state domain modes obtained from simulations of a nonequilibrium hybrid model (Section 4.1).

### 3.1.2 Phase Amplification vs. Microphase Separation

In this section, the key differences between phase amplification, microphase separation, and phase separation without interconversion, which is referred to as “complete phase separation” is presented. First, it should be emphasized that the phase transition through phase amplification is fundamentally different from phase separation. Phase amplification occurs to avoid the formation of an energetically unfavorable interface between alternative stable phase domains. This phenomenon is only possible due to the nonconserved nature of the order parameter. In contrast, in a phase separating binary mixture the formation of an interface is required due to the conserved nature of the order parameter. However, it is noted that in macroscopic systems where the interfacial energy is much smaller than the bulk energy, a system with a nonconserved order parameter may enter a metastable state in which an interface forms between phases [6, 224, 225]. An example of such a metastable state is depicted in Fig. 3.2a. Thus, the size of the system plays a crucial role in phase amplification. With increasing system size, the energy of the surface decreases when compared to the bulk energy, the conformational energy of the metastable interface becomes less unfavorable, and the possibility that the system will form an interface drastically increases.

Second, similar to phase amplification, the size of the system and the rate of forced interconversion are crucial for microphase separation to occur. It has been found that there are

Table 3.1: Limiting cases of the interplay between diffusion, natural interconversion, and forced interconversion.

Conditions	Phenomenon
Only Diffusion ( $L = 0$ & $K = 0$ )	Complete Phase Separation
Only Natural Interconversion ( $M = 0$ & $K = 0$ )	Unrestricted Phase Amplification
Only Forced Interconversion ( $M = 0$ & $L = 0$ )	Homogeneous Steady State

two key conditions required to observe microphase separation: 1) if the characteristic size of the mesoscopic steady-state microphase domains are comparable to half the size of the system, then the system will produce the same two alternative phases that would be observed without interconversion. As a result, the size of the system may “cut off” the system’s ability to phase separate into microdomains. 2) if the rate of forced interconversion is much faster than the natural interconversion or diffusion rate ( $Dq^2$ ), then the external force dominates the systems’ kinetics and no phase formation is possible. Consequently, the characteristic length scale of the microphase emerges as a result of the competition between forced interconversion and diffusion.

Whether phase amplification or microphase separation will occur depends on the interplay of the three dynamics in the system: diffusion, natural interconversion, and forced interconversion, as given through the characteristic growth rate, Eq. (3.14). In the limiting cases when one of the rates dominates the system, complete phase separation, unrestricted phase amplification, or a homogeneous steady state will be observed. The results of these observations are summarized in Table 3.1.

Table 3.2: Conditions for phase amplification and microphase separation as illustrated in Fig. 3.1. The left column corresponds to the solid lines and the right column corresponds to the dashed lines.

	$M \hat{\chi}_{q=0}^{-1}  > L\kappa$	$M \hat{\chi}_{q=0}^{-1}  < L\kappa$
$L \hat{\chi}_{q=0}^{-1}  > K$	Restricted (Slow) Phase Amplification	Unrestricted (Fast) Phase Amplification
$L \hat{\chi}_{q=0}^{-1}  < K$	Microphase Separation	Homogeneous Steady State

In a system with mixed dynamics where diffusion, natural interconversion, and forced interconversion are present, the interplay between these three rates produces either phase amplification, microphase separation, or a homogeneous steady state with no domain growth. The resultant effect on the system may be determined through the shape and intercepts of the characteristic growth rate (amplification factor). For instance, the competition between natural interconversion ( $L\hat{\chi}_{q=0}^{-1}$ ) and forced interconversion ( $K$ ), as follows from Eq. (3.13), shifts the intercept of  $\omega(q = 0)$  up or down producing either phase amplification or microphase separation depending on their magnitude. Meanwhile, the competition between diffusion ( $M\hat{\chi}_{q=0}^{-1}$ ) and natural interconversion ( $L\kappa$ ) dynamics is described by the concavity or convexity of the growth rate around  $q = 0$ , which when combined with the position of the intercept determines whether restricted or unrestricted phase amplification will be observed or if the system will remain homogeneous instead of phase separating into microphase domains. Characteristic growth rates for various relationships between  $M$ ,  $L$ , and  $K$  are shown in Fig. 3.1 and summarized in Table 3.2. Examples of the phase domains formed in a system exhibiting microphase separation are depicted in Figs. 3.2(b-d).

To achieve phase amplification, the forced interconversion rate must be slower than the

natural interconversion rate,  $K < L|\hat{\chi}_{q=0}^{-1}|$ , such that the growth rate is shifted up. Alternatively, microphase separation occurs when the forced interconversion rate and the diffusion rate is faster than the natural interconversion rate, such that  $K > L|\hat{\chi}_{q=0}^{-1}|$  and  $M|\hat{\chi}_{q=0}^{-1}| > \kappa L$ , respectively. It is noted that in the case when forced interconversion is faster than natural interconversion (while the diffusion rate is slower than the interconversion rate) the system will be in a homogeneous state as the growth rate is negative for all wavenumbers.

The conditions for whether the system will achieve complete macro-phase separation, undergo microphase separation, or experience phase amplification can be determined from the characteristic wavenumbers of the growth rate, Eq. (3.14), found from its two roots and maximum. These wavenumbers are defined as:  $q_m$ , the wavenumber corresponding to the fastest growing inhomogeneities;  $q_-$ , the first root of  $\omega(q)$ ; and  $q_+$ , the second root of  $\omega(q)$ . These three characteristic wavenumbers are related through  $q_-^2 = 2q_m^2 - q_+^2$ . The existence of a non-zero  $q_-$  indicates steady-state microphase separation; such that, after infinite time, the size of the steady-state phase domain,  $R_\infty$ , will be described by  $R_\infty \sim 1/q_-$ , where  $q_-$  is given by Eq. (3.16). Thus, it is predicted that the steady-state domain size may be expressed through an “effective” mutual diffusion coefficient, modified by interconversion kinetics,  $D_{\text{eff}} = -\hat{\chi}_{q=0}^{-1}(M - L\xi^2)$ , such that Eq. (3.16) may be expressed in the form

$$q_-^2 = \frac{K - L\hat{\chi}_{q=0}^{-1}}{D_{\text{eff}}} \quad (3.17)$$

Additionally, solving Eq. (3.14) for  $q_m$ , gives

$$(q_m)^2 = \frac{1}{2\xi^2} \left( 1 - \frac{L}{M}\xi^2 \right) \quad (3.18)$$

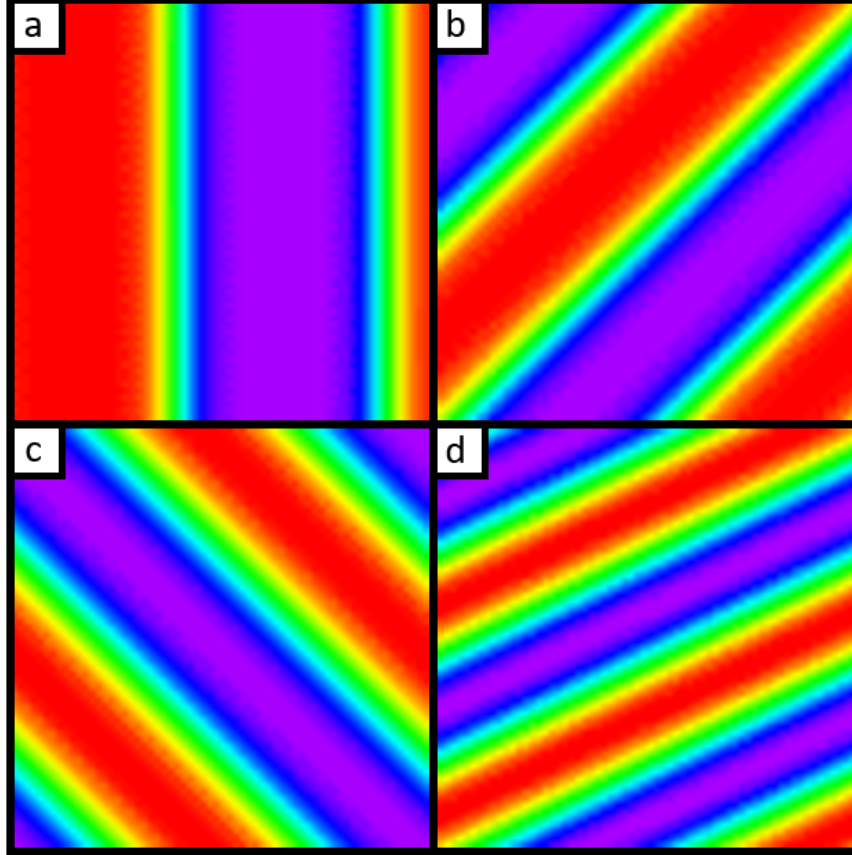


Figure 3.2: Steady-state phase domain morphology for different magnitudes of forced interconversion (after  $\sim 10^5$  time steps) numerically computed from the time evolution of the order parameter, Eq. (3.7), with  $M = 1$ ,  $L = 1/127$ ,  $\Delta\hat{T} = -0.1$ ,  $\ell = 64$ ,  $\sigma_i = 0.1$ , and  $\eta = 10^{-5}$ , as discussed in Section 3.3. Morphologies are shown for the middle slice of the three-dimensional system at (a)  $K = 0$ , (b)  $K = 5 \times 10^{-4}$ , (c)  $K = 15 \times 10^{-4}$ , and (d)  $K = 25 \times 10^{-4}$ . The red regions correspond to where the value of the normalized order parameter is  $\varphi/\varphi^{\max} = 1$ , the purple regions correspond to where the value of the normalized order parameter is  $\varphi/\varphi^{\max} = -1$ , and the other colors depict the interface between these two regions. The image in (a) depicts a metastable structure toward phase amplification [6], while the images in (b-d) are modulated steady-state structures with a characterize size,  $1/q_-$ .

Thus, the maximum of the growth rate is shifted in comparison to Cahn-Hilliard theory,  $q_m = 1/(\sqrt{2}\xi)$  [102], as shown in Fig. 3.1. This shift is independent of the strength of the source of forced interconversion.

## 3.2 Temporal Evolution of the Structure Factor

In this section, following the ideas of Cook [226], a phenomenological theory to describe the temporal evolution of the structure factor of a system of interconverting fluids is presented. Based on the suggestions of Binder *et al.* [227], a simple crossover function to account for the transition from spinodal decomposition (at early times) to nucleation and coarsening (at long times) is incorporated. This theory is referred to as the “generalized Cook-Binder theory.”

### 3.2.1 Generalized Cook-Binder Theory

Defining the order parameter fluctuation variable as  $\delta\hat{c}(\mathbf{r}, t)$ , the structure factor is given through the correlation function for the concentration fluctuations [228], such that

$$S(q, t) = \int d\mathbf{r} \langle \delta\hat{c}(\mathbf{r}, t) \delta\hat{c}(\mathbf{r}_0, t) \rangle e^{i\mathbf{q}\cdot\mathbf{r}} \quad (3.19)$$

As shown by Cook [226] and Langer *et al.* [229], the equation of motion for  $S(q, t)$  is found by introducing order-parameter fluctuations into the time evolution of the order parameter, Eq. (3.7), with  $\delta\hat{c}(\mathbf{r})$  as the fluctuation variable and spatially integrating  $\langle |\delta\hat{c}|^2 \rangle$ . Following this procedure, one obtains the first-order solution for mixed diffusion-interconversion dynamics as

$$\frac{\partial S(q, t)}{\partial t} = 2\omega(q, t)S(q, t) + 2(Mq^2 + L\kappa) \quad (3.20)$$

where  $\omega(q, t)$  is given by Eq. (3.15) [213, 230, 231]. It is noted that in the absence of interconversion and forced racemization, this equation reduces to the result presented by Cook [226].

Solving this differential equation for the structure factor, assuming a linear approximation [222],  $\partial\omega/\partial t \ll \omega(q, t)$ , gives [223, 227, 232, 233]

$$S(q, t) = S_\infty(q) + [S_0(q) - S_\infty(q)] e^{2\omega(q, t)t} \quad (3.21)$$

where  $S_0(q) \equiv S(q, t = 0)$  and  $S(q, t)$  represents the modified Cahn-Hilliard-Cook structure factor, which now includes natural and forced interconversion. In the limit of infinite time, when  $\partial S(q, t)/\partial t = 0$ , the steady-state structure factor,  $S_\infty(q)$ , is given by

$$S(q, t \rightarrow \infty) \equiv S_\infty(q) = \frac{Mq^2 + L\kappa}{-\omega(q, t \rightarrow \infty)} \quad (3.22)$$

It can be seen that when either  $L = 0$  or  $M = 0$ , then this equation under equilibrium conditions ( $K = 0$ ) reduces to the Ornstein-Zernike structure factor -  $S_{OZ} = \xi^2/(1 + \xi^2q^2)$ .

The time-dependent structure factor, Eq. (3.21), can be simplified by applying the condition that at  $t = 0$ , the system is quenched from a sufficiently high temperature where  $S_0(q) = 0$ . Therefore, Eq. (3.21) may be written as

$$S(q, t) = S_\infty(q) (1 - e^{2\omega(q, t)t}) \quad (3.23)$$

which is valid from the initial stages of spinodal decomposition to the coarsening regime [232, 234]. Evaluating  $\partial S_\infty/\partial q = 0$  to determine the wavenumber corresponding to the maximum of the structure factor gives,  $q_m^s = 2^{1/4}q_-$  in the steady-state limit. The time evolution of the structure factor is illustrated in Fig. 3.3b. As suggested by Binder *et al.* [227], to account for the

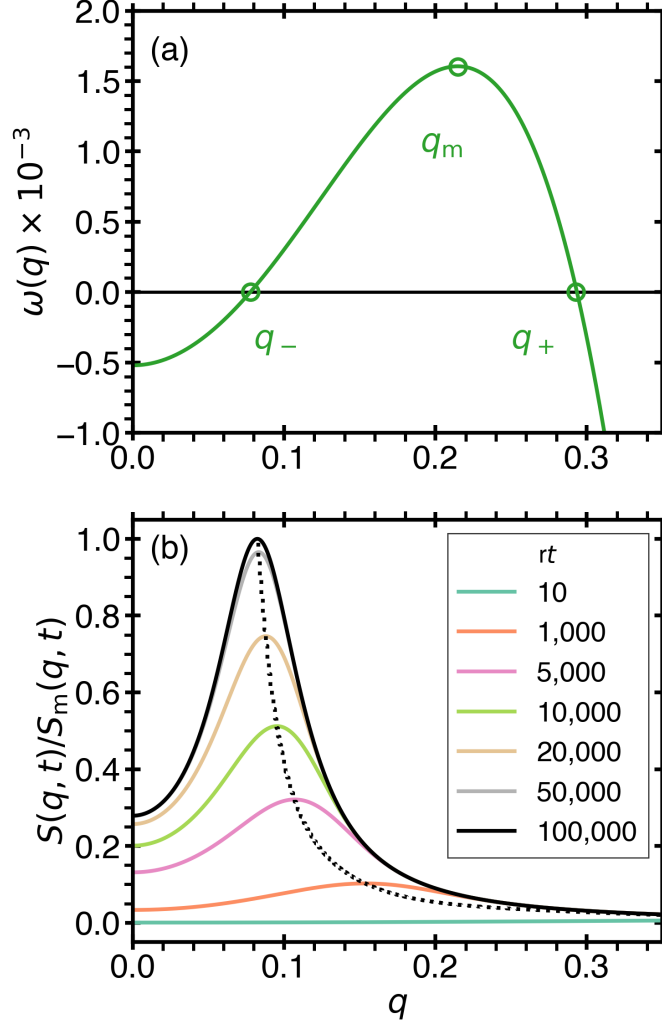


Figure 3.3: a) The amplification factor,  $\omega(q)$ , given by Eq. (3.15) with  $\kappa = 1$ ,  $\Delta\hat{T} = -0.1$ ,  $M = 1$ ,  $L = 1/127$ , and  $K = 1.3 \times 10^{-3}$ . b) The time evolution of the structure factor, given by Eq. (3.23) in the presence of natural and forced interconversion. The black dotted line depicts the evolution of the maximum of the structure factor. Due to the external source of forced interconversion, the maximum of the structure factor is interrupted at the wavenumber  $q_-$ , while for complete phase separation and phase amplification, the maximum of the structure factor will evolve to  $q = 0$  for an infinite-sized system.

time dependence of  $q_m(t)$ , a simple approximation of the transition is assumed in the form

$$q_m(t) = q_m(t=0)e^{-t/\tau} + q_- (1 - e^{-t/\tau}) \quad (3.24)$$

based on the limiting values of  $q_m$  at  $t = 0$  and  $t \rightarrow \infty$ , where  $\tau = 100$ , is a system dependent

parameter that controls the crossover from spinodal decomposition to the coarsening regime. As shown in Fig. 3.3, the wavenumber corresponding to the maximum of the steady-state structure factor,  $q_m^s$ , aligns with the prediction of  $q_-$  from the theory. To accurately match the predictions from the theory with the computational results presented in the following section, the characteristic wavenumbers from the theory are scaled by the size of the system.

### 3.2.2 Characteristic Length Scales

Using Eq. (3.23), the evolution of a system that only exhibits diffusion dynamics (toward equilibrium) is compared to a system that exhibits diffusion dynamics in the presence of a source of forced interconversion (toward steady state). The behavior of these systems through all three regimes: namely, spinodal decomposition, coarsening, and nucleation is shown in Figs. 3.4(a,b). It is observed that the introduction of a forced interconversion source causes the growth of the structure factor to be interrupted at the lower cut-off wavenumber,  $q_-$ . In the first order approximation, the wavenumber corresponding to the maximum of structure factor,  $q_m^s$ , in the steady-state limit of  $q_m^s(t \rightarrow \infty)$  determined from  $\partial S(q, t \rightarrow \infty)/\partial q = 0$  is given by

$$q_m^s(t \rightarrow \infty) = 2^{1/4} q_- \propto \sqrt{\frac{K}{-D_{\text{eff}}}} \quad (3.25)$$

It should be noted that the general scaling law  $q_m^s \propto K^{1/2}$  was observed in simulations of a chiral model [7] and a hybrid Ising/lattice-gas model [5] as will be discussed in detail in Sections 4.1 and 4.2. This behavior differs from studies of the microphase domain formation in block copolymers where it was found that  $q_m^s \propto K^{1/4}$  [213, 235]. The difference in this behavior between the systems considered in this section (as well as those in Chapter 4) and the block copolymers might

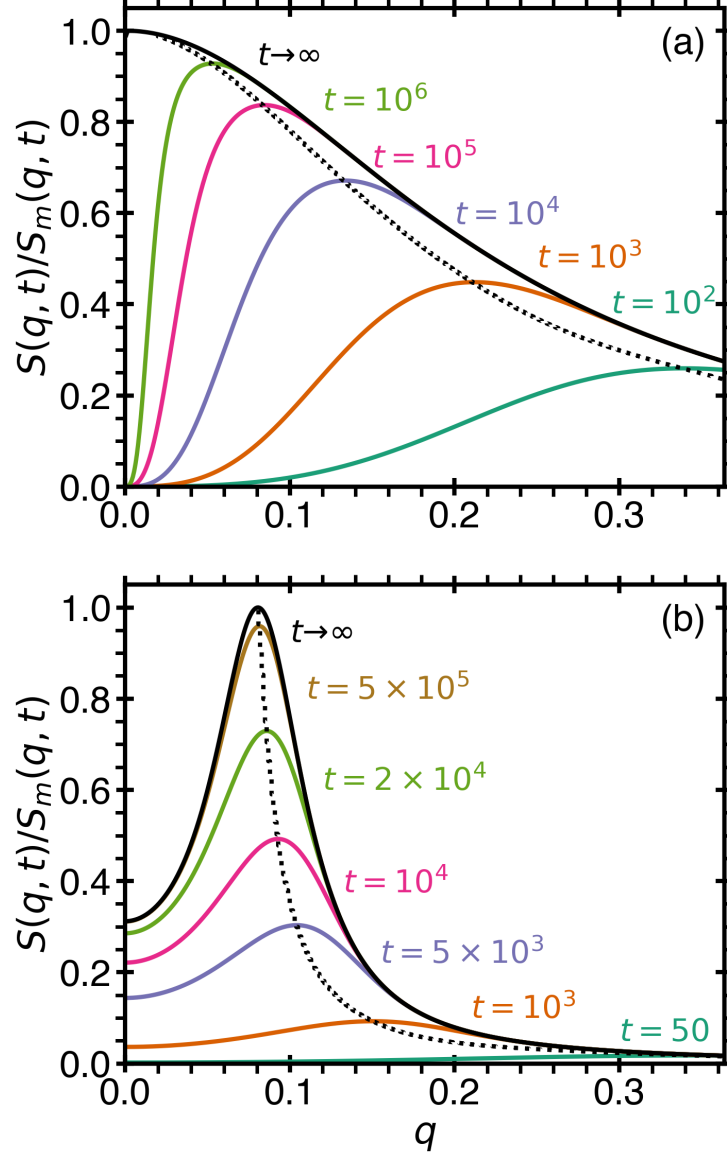


Figure 3.4: Temporal evolution of the structure factor: a) for a system undergoing diffusion dynamics ( $M = 1$ ) toward an equilibrium state in the absence of natural interconversion ( $L = 0$ ) and forced interconversion ( $K = 0$ ); b) for a system undergoing a hybrid of diffusion ( $M = 1$ ) and natural interconversion ( $L = 0.01$ ) dynamics in the presence of forced interconversion ( $K = 1.5 \times 10^{-3}$ ) toward a steady state. The structure factor, given by Eq. (3.23), exhibits a crossover from spinodal decomposition to the nucleation regime. The dashed-black curves indicate the development of the maximum of the structure factor. The characteristic crossover time is defined in Eq. (3.24) and adopted as  $\tau = 100$ . In (a) the evolution of the maximum of the structure factor moves to  $q = 0$  for infinite-size system and saturates at  $S_m(q = 0, t \rightarrow \infty) = 1/(2\xi^2) = 5$  for  $\Delta\hat{T} = -0.1$ . In contrast, in (b) the evolution of the maximum is interrupted at a characteristic cut-off wavenumber predicted by the characteristic phase domain growth rate,  $q_m^s(t \rightarrow \infty) \propto q_-$ , and it saturates at  $S_m(q_-, t \rightarrow \infty) = 417$ .

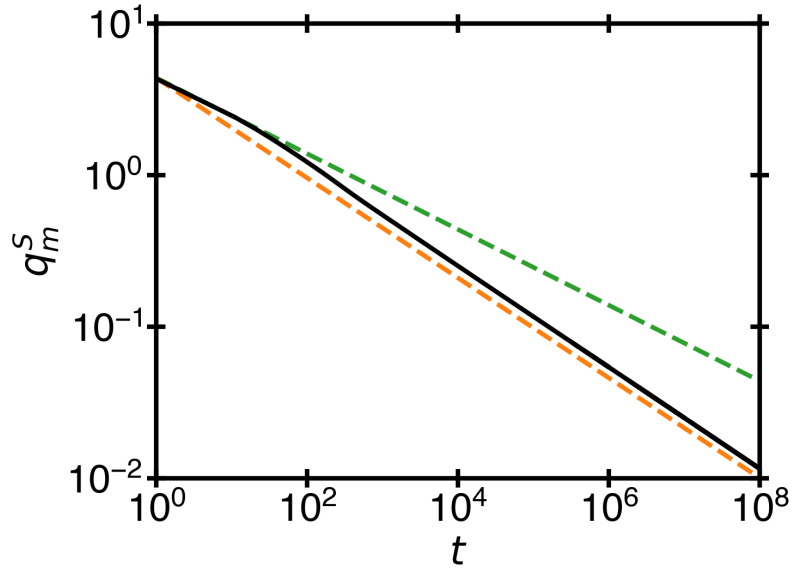


Figure 3.5: The time evolution of the wavenumber corresponding to the maximum of the structure factor, given by Eq. (3.23), during the crossover from the early stage of spinodal decomposition,  $q \propto t^{1/4}$  (green - dashed), to the nucleation regime,  $q \propto t^{1/3}$  (orange - dashed) for a system undergoing diffusion dynamics in the absence of natural interconversion ( $L = 0$ ) and forced interconversion ( $K = 0$ ) under conditions:  $M = 1$ ,  $\Delta\hat{T} = -0.1$ ,  $\tau = 100$ .

be attributed to the difference in the nature of the order parameters - the systems considered in this section being described by a single-component order parameter and the block copolymers being described by an  $n$ -component order parameter.

The crossover behavior for the transition between spinodal decomposition and nucleation in a system with diffusion dynamics toward equilibrium is shown in Fig. 3.5. The wavenumber corresponding to the maximum of the structure factor, given by Eq. (3.23), evolves according to  $q \propto t^{1/4}$  (short times, spinodal decomposition regime) and  $q \propto t^{1/3}$  (long times, nucleation regime). The crossover from one regime to the other is illustrated by the crossing of the orange and green dashed lines in Fig. 3.5.

Within systems that exhibit microphase separation, the generalized Cahn-Hilliard theory predicts that there are two characteristic length scales that restrict phase formation. First, in sim-

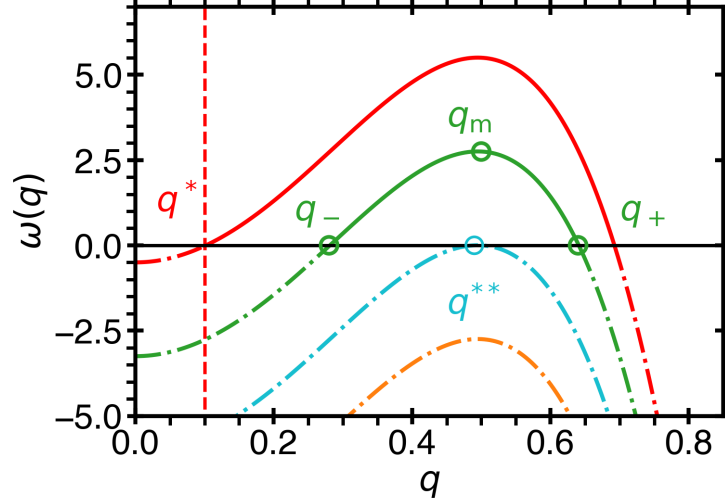


Figure 3.6: The effect of increasing interconversion force on the phase domain growth rate for  $M = 100$ ,  $L = 1$ , and  $\Delta\hat{T} = -0.5$ . The red dashed line corresponds to the inverse maximum size of the phase domain on the length scale of the simulation box,  $q^*$ . When  $q_- > q^*$  microphase domains will form. Alternatively, when  $q_- < q^*$ , the size of the simulation box will cut-off the growing phase domains. The conditions where  $\omega(q) < 0$  (dashed-dot portions of the curves) corresponds to non-growing wavenumbers. As the rate of forced interconversion increases, the growth rate is shifted down from the onset of phase separation where  $q_- = q^*$  (red,  $K = 1$ ), to the microphase region (green,  $K = 3.75$ ), to the termination point of domain growth (blue,  $K = 6.5$ ) where  $q_- = q_m = q_+ = q^{**}$ , and to the no growth regime for any wavenumber (orange,  $K = 9.25$ ).

ulation or experiment, the phase domain is restricted by the finite size of the system,  $\ell$ . The event where the domain size reaches the size of the system is defined as “complete” phase separation, and is denoted as  $\ell \sim 1/q^*$ . This event is referred to as the “onset” of microphase separation, and it is characterized by a magnitude of forced interconversion,  $K = K^*$ , and temperature  $T = T^*$ . Second, when the size of the microphase domains become proportional to the correlation length of order-parameter fluctuations ( $\xi \sim 1/q^{**}$ ), the formation of microphase domains no longer become energetically favorable. The event when fluctuations become so great as to destroy the phase domain is referred to as the “termination” of microphase separation. At this event, the system is in a “homogeneous steady state,” and is characterized by a magnitude of forced interconversion  $K = K^{**}$  at a temperature  $T = T^{**}$ . These phenomena are illustrated by

the amplification factor, Eq. (3.14), in Fig. 3.6.

### 3.3 Temporal Evolution of the Order Parameter

In this section, the finite difference method [236] is utilized, with a spatial step  $\Delta x = 1$  and a time step  $\Delta t = 0.015$ , to numerically calculate the temporal evolution of the order parameter, given by Eq. (3.7) with a chemical potential with the higher-order terms given by Eq. (2.10) for the simple interconversion reaction with  $\hat{G}_{\text{BA}} = 0$ . The structure factor, numerically calculated via a Fast Fourier Transform (FFT) of the order parameter throughout the system [236] is compared to the structure factor predicted by the generalized Cook-Binder theory. It is observed that for time steps  $\Delta t > 0.015$ , the solution diverges [5, 236]. A random force term,  $\eta$ , is included to account for the thermal motion of the particles [226, 232]. The system is initialized on an  $\ell \times \ell \times \ell$  cubic lattice with positions varied with initial random, Gaussian noise,  $\sigma_i$ .

It has been confirmed that the presence of a source of forced interconversion causes the system to phase separate into steady-state microphase domains as presented in Figs. 3.2(a-d). Due to the periodic boundary conditions imposed in the continuum finite-difference method used to compute Eq. (3.7), it has been found that the stripe morphologies will form at any angle with respect to the simulation box. The characteristic size of the stripe-like domains decreases with increasing forced interconversion source strength,  $K$ . It is noted that a condition for microphase separation is that  $K$  must be sufficiently “strong” as to overcome the natural interconversion. If the magnitude of  $K$  is not strong enough, then (depending on the rate of natural interconversion) the system will either undergo phase amplification or complete phase separation. For instance, for  $M = 1$ ,  $L = 1/127$ ,  $\Delta\hat{T} = -0.1$ , and  $K \leq 4 \times 10^{-4}$ , then microphase separation is not

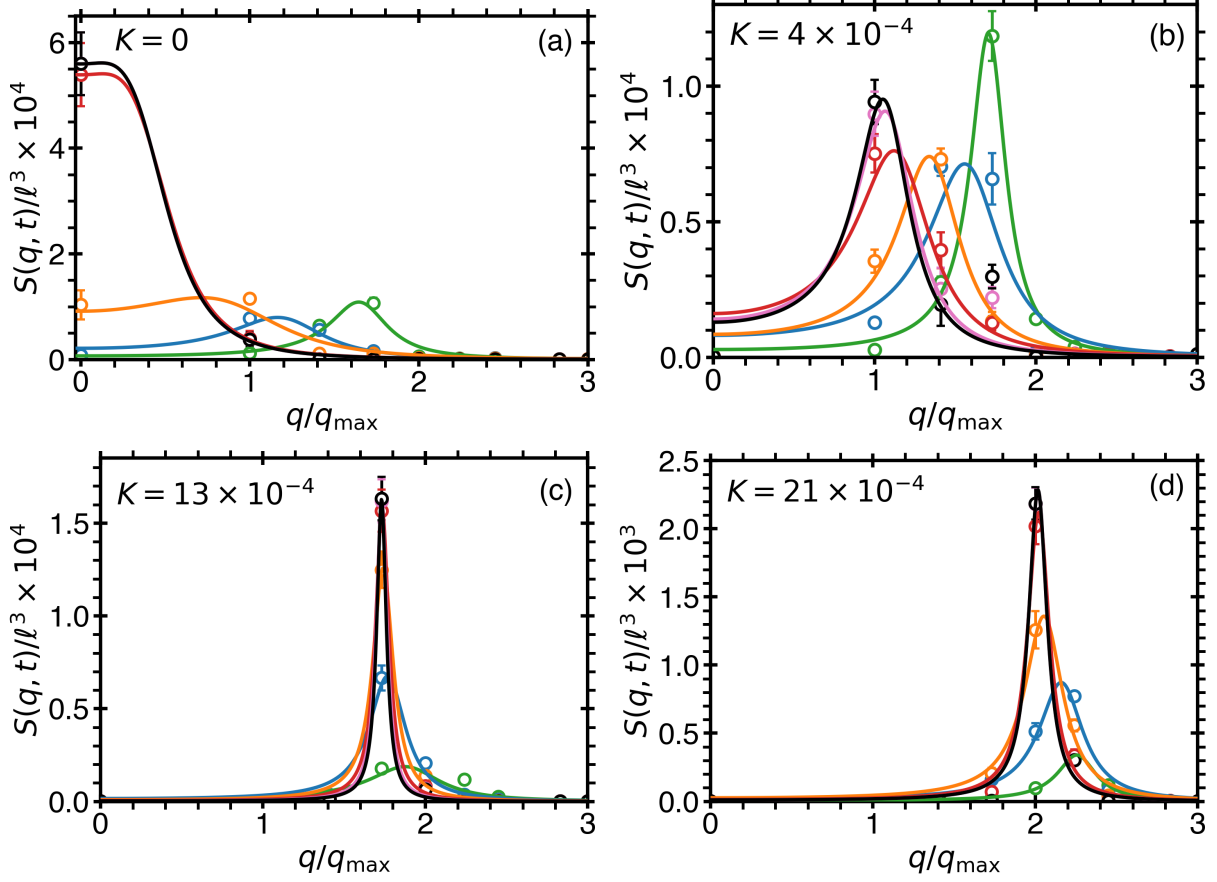


Figure 3.7: Time evolution of the structure factor computed from the Fast Fourier transform (FFT) of Eq. (3.7) for  $M = 1$ ,  $L = 1/127$ ,  $\Delta\hat{T} = -0.1$ ,  $\ell = 64$ ,  $\sigma_i = 0.1$ ,  $\eta = 10^{-5}$  depicted at times  $t = 6 \times 10^3$  (green),  $t = 1.2 \times 10^4$  (blue),  $t = 2.4 \times 10^4$  (orange),  $t = 5 \times 10^4$  (red),  $t = 1 \times 10^5$  (pink), and  $t = 2 \times 10^5$  (black). The open circles in (a-d) depict the computed structure factors for the four selected magnitudes of forced interconversion averaged over  $N = 100$  realizations with 95% confidence interval error bars, while the solid lines illustrate the behavior of the structure factors assuming a Gaussian distribution. The wavenumber is normalized by the size of the system, such that  $q = 1$  corresponds to phase domains with a characteristic size of half the simulation box,  $\ell/2$ .

observed. Since  $L = 1/127$ , the interconversion rate is relatively slow, and thus, the system has a higher probability of forming an interface between phases as shown in Fig. 3.2a. However, for a system with natural interconversion this state is metastable, and eventually, the interface between phases will break down and phase amplification will occur [4–6].

The time-dependent structure factors, which produce the stripe-like morphology illustrated

in Figs. 3.2(a-d), are presented in Figs. 3.7(a-d). It is observed that the time evolution of the maximum of the structure factor in Fig. 3.7a is interrupted at the wavenumber  $q = 0$ , which corresponds to a system undergoing phase amplification. For  $K = 4 \times 10^{-4}$  (Fig. 3.7b), the maximum of the time evolution of the structure factor is interrupted at  $q/q_{\max} = 1$ , indicating complete phase separation where the phase domains have a characteristic size of half the simulation box,  $\ell/2$ . In Figs. 3.7(c,d), the time evolution of the maximum of the structure factor is interrupted at higher wavenumbers, depending on  $K$ . These wavenumbers correspond to the characteristic size of the stripe-like phase domains and are independent of the size of the system. It is also observed that the structure factor at the maximum wavenumber ( $q_m$ ) contains the largest uncertainty, with respect to the other wavenumbers. The non-monotonic temporal evolution of the structure factor observed in Figs. 3.7b can be attributed to  $\tau \approx 1.5 \times 10^3$ , a large characteristic crossover time scale between spinodal decomposition and coarsening. This observation suggests that the crossover time scale,  $\tau = \tau(K)$ , may depend on forced interconversion.

The average value of the order parameter, calculated by first averaging over all space and second averaging the absolute value over  $N = 100$  realizations, is presented in Fig. 3.8a. This method of averaging highlights the behavioral deviation from  $\varphi = 0$ , when the molecular fraction of species A is equivalent to species B; therefore, this figure represents the temporal evolution of the symmetry of phase separation. It is observed that the initial value  $\langle |\varphi| \rangle$  is determined by  $\sigma_i$ , the random initial configuration, whereas the steady-state behavior of  $\langle |\varphi| \rangle$  is determined by  $\eta$ , the thermal noise to be included in Eq. (3.7). It is found that  $\langle |\varphi| \rangle$  develops a peak during the formation of the stripe-like patterns. As the phase domains coarsen, the averaged order parameter reaches a steady-state value,  $\langle |\varphi(t \rightarrow \infty)| \rangle = \varphi_0$  indicating the stable formation of the stripe-like domains.

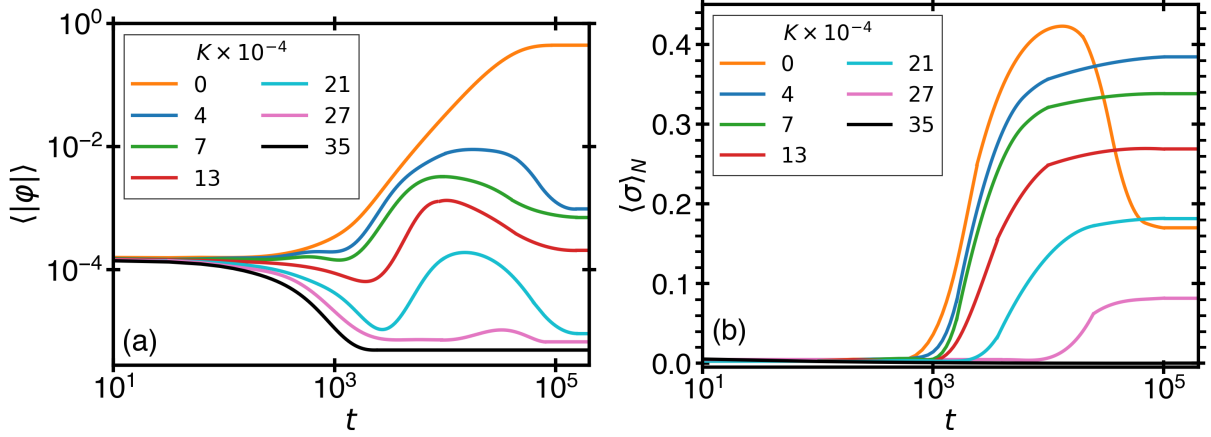


Figure 3.8: The temporal evolution of the symmetry of phase separation. a) The time evolution of the average order parameter, calculated by first averaging over all space and second by averaging the absolute value over  $N = 100$  realizations, for  $M = 1$ ,  $L = 1/127$ ,  $\Delta T = -0.1$ ,  $\sigma_i = 0.1$ ,  $\eta = 1.0 \times 10^{-5}$ , and various magnitudes of forced interconversion,  $K$ . b) The time evolution of the  $N$ -averaged standard deviation of the averaged order parameter, calculated by first determining the standard deviation of the spatially averaged order parameter and second by averaging over  $N = 100$  realizations. This method of averaging highlights the behavioral deviation from an equal concentration of species A and B,  $\varphi = 0$ .

In Fig. 3.8b, it is shown the temporal evolution of the standard deviation of the averaged order parameter, calculated by first determining the standard deviation over all space and second by averaging over  $N = 100$  realizations. It is observed that the  $N$ -averaged standard deviation,  $\langle \sigma \rangle_N$ , was constant through the early stages of spinodal decomposition, but dramatically increased during the formation of the stripe-like patterns. It is noted that in the  $K = 0$  case, due to phase amplification,  $\langle \sigma \rangle_N$  rapidly increases as the domains coarsen, but then decreases when one phase grows at the expense of the other. In this case, the constant steady-state limit of the averaged standard deviation,  $\langle \sigma(t \rightarrow \infty) \rangle_N = \sigma_0$ , indicates that the order parameter has reached its equilibrium value,  $|\varphi| = \varphi_0$ , which depends on the distance to the critical temperature.

### 3.4 Effects of Heat and Volume Change of Interconversion

So far in this chapter, the dynamics of simple systems have been considered, in which the Gibbs energy change of the reaction,  $\hat{G}_{\text{BA}}$ , does not depend on pressure or temperature; thus, the forward and reverse equilibrium reaction rates are always equivalent ( $\mathcal{K} = 1$ ). Since, in this case, the enthalpy of reaction is zero, as given through the Gibbs-Helmholtz relation,  $\Delta\hat{H}_{\text{BA}} = \hat{T}^2\partial(\ln \mathcal{K})/\partial\hat{T} = 0$  [210], then, in the one phase region, the equilibrium interconversion between states A and B remains always equivalent, being independent of temperature and pressure. However, as discussed in Chapter 2, most polyamorphic substances have a non-zero enthalpy and volume change of the reaction, such that the equilibrium fraction of interconversion depends on temperature and pressure,  $\mathcal{K} = \mathcal{K}(T, P)$  [9]. This effect may be incorporated into the time evolution of the order parameter using Eq. (2.12) for the reduced chemical potential. In this case, the solution of Eq. (3.7) becomes

$$\varphi = \frac{L\hat{G}_{\text{BA}}}{2(K + L\hat{\chi}_{q=0}^{-1})} + \sum_i \varphi_\infty e^{\omega(q_i)t} \cos(\mathbf{q}_i \cdot \mathbf{r}) \quad (3.26)$$

where only the infinite time solution of the order parameter is effected by the Gibbs energy of reaction. The phase domain growth rate,  $\omega(q)$ , remains unaffected and is described by Eq. (3.14). It should be noted that the introduction of the temperature and pressure dependence into the equilibrium interconversion fraction is different from considering the symmetric binary mixture quenched with at a higher concentration of species A (or B). In this case, phase amplification will proceed with a higher probability of forming an A-rich (or B-rich) phase.

For the remainder of this section, the effects of temperature and pressure on the equilibrium

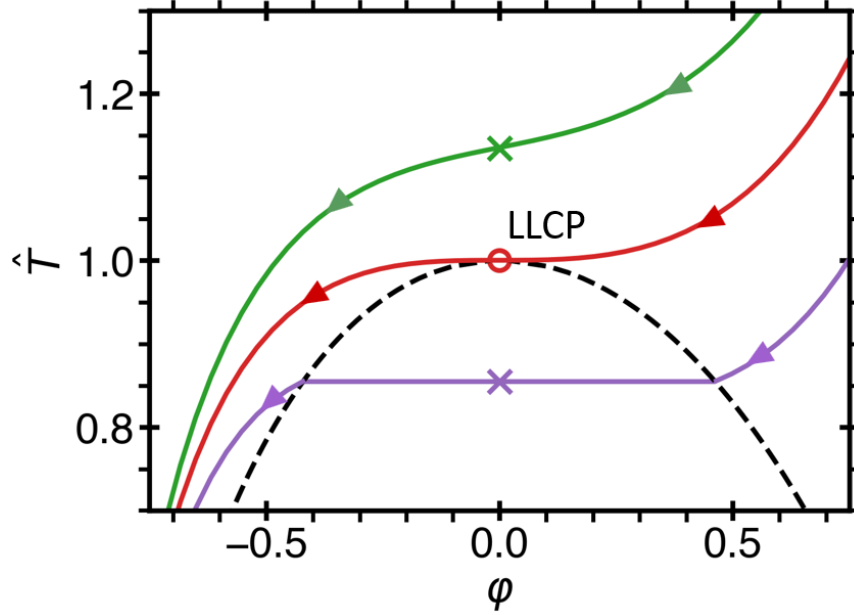


Figure 3.9: Three hypothesized binary mixture systems exhibiting interconversion of species and liquid-liquid phase separation quenched from high temperature to low temperature (without volume change). The black dashed curve corresponds to the liquid-liquid phase coexistence in this system without interconversion and with interaction energy,  $\varepsilon = 2$ . The open circle indicates the liquid-liquid critical point (LLCP), while the crosses show the locations of  $T = T_{BA}$ , the points corresponding to 50:50 interconversion for different energy change of reaction. For a system with  $T_{BA} = 1.05T_c$  (green), no liquid-liquid phase transition will be observed upon quenching. For a system with  $T_{BA} = T_c$  (red), the quenching process passes through the critical point. For a system with  $T_{BA} = 0.95T_c$  (purple), there are two equilibrium solutions for the fraction of interconversion, such that upon quenching to the cross, phase amplification occurs with equal probability of forming an A-rich or B-rich phase.

interconversion fraction,  $\mathcal{K}$  will be discussed, and, in particular, how they could affect the possibility of phase amplification. To do so, the hypothesized phase diagram of supercooled water that exhibits a liquid-liquid phase transition, see Fig. 3.10, is utilized to illustrate a real system. Also, predictions about how phase amplifications could be observed in such a system are made.

To start, a discussion of the effect of temperature on the equilibrium fraction,  $\mathcal{K}$ , in three different hypothesized polyamorphic systems, characterized by three different heat of reactions,  $\Delta\hat{H}_{BA}$ , are presented, in which the two alternative phases are assumed to have the same density. In this formulation, there are two characteristic energies,  $\hat{e}$  and  $\varepsilon$ . Consider the heat of reac-

tion,  $\Delta\hat{H}_{\text{BA}} = \hat{e}$ , which defines the temperature dependence of the equilibrium interconversion fraction, and the heat of mixing  $\Delta\hat{H}_{\text{mix}} \propto \varepsilon$ , given by Eq. (2.3), which defines the critical temperature of liquid-liquid demixing. Suppose that the  $\hat{e} > 0$  such that cooling favors the formation of species B. Depending on the relation between the reference temperature of interconversion  $T_{\text{BA}}$ , at which  $\ln \mathcal{K} = 0$  (corresponding to 50:50 interconversion), and the critical temperature of demixing one can observe different scenarios upon quenching below  $T_c \propto \varepsilon$ , as shown in Fig. 3.9. In a system with  $T_{\text{BA}} > T_c$ , the liquid-liquid phase transition will not be observed. If the system has  $T_{\text{BA}} = T_c$ , the system follows the interconversion fraction to the phase enriched with B without phase coexistence. In a system with  $T_{\text{BA}} < T_c$ , the system crosses the first-order liquid-liquid phase transition at the point where the interconversion fraction of B is smaller than 50%. Depending on the final location of the quenching point, phase amplification will occur with a preference to the formation of a single A-rich or B-rich phase. When the final location of the quench is at  $\varphi = 0$  (corresponding to a 50:50 interconversion rate) as shown in Fig. 3.9, phase amplification will occur randomly without a preference to an alternative phase [4, 6]. However, due to the difference between bulk energies of species A and B, it is predicted that for one stable phase to grow at the expense of another phase, energy must be supplied or removed from the system. Therefore, either experimentally or computationally, this process must be conducted in a heat reservoir and the thermal conductivity of the system must be faster than the interconversion rate.

Next, consider a system in which the two alternative species have different molecular volumes and the equilibrium interconversion fraction depends on pressure. In this case, the volume change of the interconversion reaction is not zero. For example, consider the hypothesized phase diagram of supercooled water suggested by Caupin and Anisimov [13] as shown

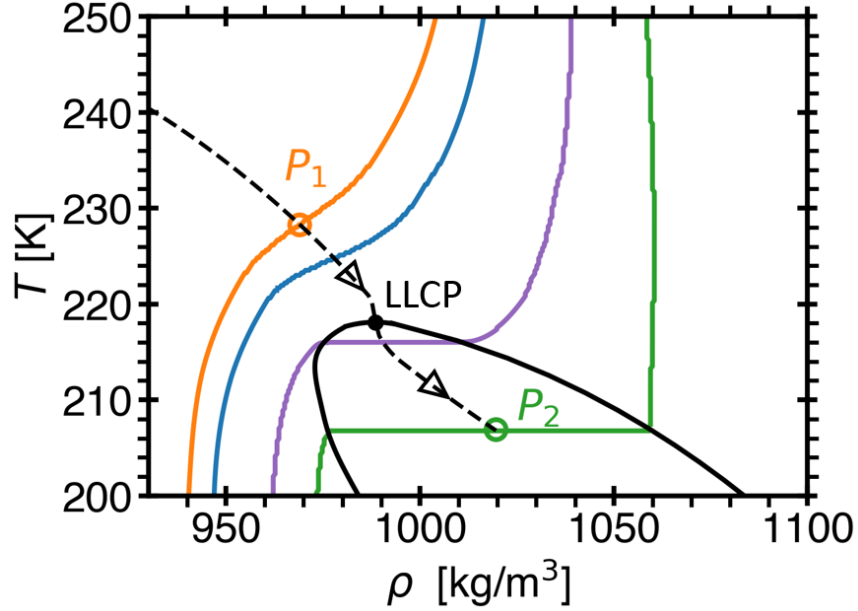


Figure 3.10: The phase diagram (suggested in ref. [13]) for supercooled water that exhibits a liquid-liquid phase transition (global phase diagram illustrated in Fig. 1.1). A hypothesized quenching process by compression for supercooled water is shown from the one phase region at  $P_1 = 20$  MPa (orange) to the two phase region at  $P_2 = 120$  MPa (green) along the Widom line (dashed black) which corresponds to a line of constant fraction of interconversion,  $\ln \mathcal{K} = 0$ . Two additional isobars are shown for reference at  $P = 40$  MPa (blue) and  $P = 80$  MPa (purple) along with the liquid-liquid coexistence (black). Phase amplification would only be possible in a system where the number of molecules changes to compensate the volume change of the interconversion reaction.

in Fig. 3.10. It has been suggested the liquid-liquid phase separation in supercooled water is caused by the interconversion between two alternative supramolecular structures [13, 76, 80]. Here, a quench by compression is illustrated from  $P_1 = 20$  MPa in the one phase region to  $P_2 = 120$  MPa below the critical temperature of demixing along the Widom line for water, where  $\ln \mathcal{K} = 0$  [9, 13, 77, 79, 237]. This condition is preserved along this path because the change in the temperature is compensated by the corresponding change in the pressure as predicted by Eq. (2.9). In this case, it is predicted that phase amplification may only occur in the presence of a specific “barostat” that supplies or removes molecules to compensate the volume change of the interconversion reaction. Without such a barostat, phase amplification would not

be possible.

It is noted that even though phase amplification may be predicted to occur if there is no volume change of interconversion, there are a variety of factors (like the size of the system, distance from the critical temperature, and the rate of interconversion) that may increase the probability of a metastable interface to form between phases [6]. The effect of possible phase amplification has not been discussed in previous simulations of models for polyamorphic substances, but it could be a factor effecting the possibility of equilibrium phase separation to be observed in both experiment and simulations.

Since the order parameter in polyamorphic systems is a hybrid containing both conserved and nonconserved components, the coupling between these two components affects the phase domain growth in both nucleation and spinodal decomposition regimes [238]. This important feature of the dynamics of liquid polyamorphism could also be elaborated within the framework of interconversion of molecular or supramolecular species.

### 3.5 Effects of Critical Order-Parameter Fluctuations

In 1952, Lee and Yang showed that the Ising model for an anisotropic ferromagnet and the lattice gas model for a fluid are mathematically equivalent [239]. This was a paradigm shift in the physics of condensed matter, making a profound effect on the modern theory of phase transitions and critical phenomena. It was later proven that all fluids exhibiting phase separation, whether simple or complex, belong to the same class of critical-point universality in thermodynamics as the Ising model [240]. Within the same universality class, the systems demonstrate the same critical singularities and the same critical equation of state, provided that the appropriately defined

order parameters,  $\varphi$ , have the same symmetry. The one-component-vector order parameter ( $\varphi$ , the magnetization) in the Ising model and the scalar order parameter ( $\varphi = 1 - 2\rho$ , where  $\rho$  is the density) in the lattice gas possess the same symmetry,  $\mathcal{Z}_2$  up-down symmetry [241, 242].

According to Halperin and Hohenberg [100], the Ising and lattice-gas models belong to the different dynamic universality classes, A and H, respectively. The relaxation of the conserved order-parameter (density) in the lattice-gas model is controlled by diffusion, while the relaxation of the non-conserved order-parameter (the fraction of spins pointing up or down) in the Ising model is controlled by the flipping of spins (spin “interconversion”). In addition, the mobility,  $M$ , in fluids diverges near the critical point as described by the mode-coupling theory [243], while the interconversion kinetic coefficient,  $L$ , is constant [100].

The meanfield approximation does not properly incorporate the effects of diverging fluctuations in the critical region. This part of the phase diagram is roughly defined by the region where the correlation length of the order-parameter fluctuations is significantly larger than the distance between molecules (the Ginzburg criterion [173]). In practice, the region where physical properties of fluids are significantly modified by fluctuations can roughly be estimated as  $\Delta\hat{T} \leq 0.1$  [244]. Fluctuation-induced effects are described by the renormalization group (RG) theory and the scaling theory of critical phenomena [100, 240, 245, 246]. A comprehensive theory of phase transitions in the presence of molecular interconversion in the vicinity of the critical point has not yet been developed. In this section, simple scaling arguments on the behavior of such systems in the approximation of the first-order epsilon expansion of the RG theory in powers of  $\epsilon = 4 - d$ , where  $d$  is the system dimensionality, are presented. In this approximation, the Landau-Ginzburg free energy functional in the form of Eq. (2.1), used in the description of spinodal decomposition, corresponds to the Ornstein-Zernike correlation function, in which the

susceptibility is proportional to the square of the correlation length,  $\hat{\chi}_{q=0} = \xi^2/\kappa$  [210].

As the system approaches the critical point, the susceptibility,  $\hat{\chi}_{q=0} \sim (\partial^2 f_0/\partial\varphi^2)^{-1}$ , diverges as  $|\Delta T|^{-\gamma}$  and the correlation length diverges as  $\xi \sim |\Delta\hat{T}|^{-\nu}$ , where in the first-order RG epsilon expansion for the 3d Ising-model universality class  $\gamma = 1 + \epsilon/6 = 7/6$  and  $\nu = \gamma/2 = 1/2 + \epsilon/12 = 7/12$  [247]. The actual theoretical and most accurate experimental values for the critical exponents differ from those given by the lowest approximation of the RG theory, such that  $\gamma = 1.24$  and  $\nu = 0.63$  [248, 249]. The difference between  $\gamma$  and  $2\nu$  appears only in the second order epsilon expansion, in which  $\gamma = \nu(2 - \epsilon^2/54)$  [247]. However, these differences only marginally change the behavior of the phase domain growth rate (amplification factor), presented in Fig. 3.11a.

There is another effect, the fluctuation induced divergence of the mobility, which is only relevant for the dynamic universality class H. In the vicinity of the critical point, the mode-coupling theory, strongly supported by accurate experimental studies, predicts the divergence of the molecular mobility [250]

$$M = M_0 \xi^{1-z_\eta} K(q\xi) \left[ 1 + \left( \frac{q\xi}{2} \right) \right]^{z_\eta/2} \quad (3.27)$$

where  $M_0 = k_B T / (6\pi\eta_0\kappa)$  is the non-diverging mobility in the meanfield approximation;  $\eta_0$  is the amplitude of the dynamic viscosity, which weakly diverges as  $\eta = \eta_0 \xi^{z_\eta}$  ( $z_\eta = 1/19$  in the first RG epsilon expansion [251–253], and  $K(q\xi) \equiv K(y) = [3/(4y^2)](1 + y^2 + [y^3 - y^{-1}] \arctan y)$  is the Kawasaki function [254]. The net effect is that the mutual diffusion coefficient asymptotically close to the critical point in the limit  $q \rightarrow 0$  vanishes as  $D = M \hat{\chi}_{q=0}^{-1} \sim |\Delta T|^{\nu-z_\eta}$  [101, 255]. Therefore, the phase domain growth rate given through Eq. (3.13) incorpo-

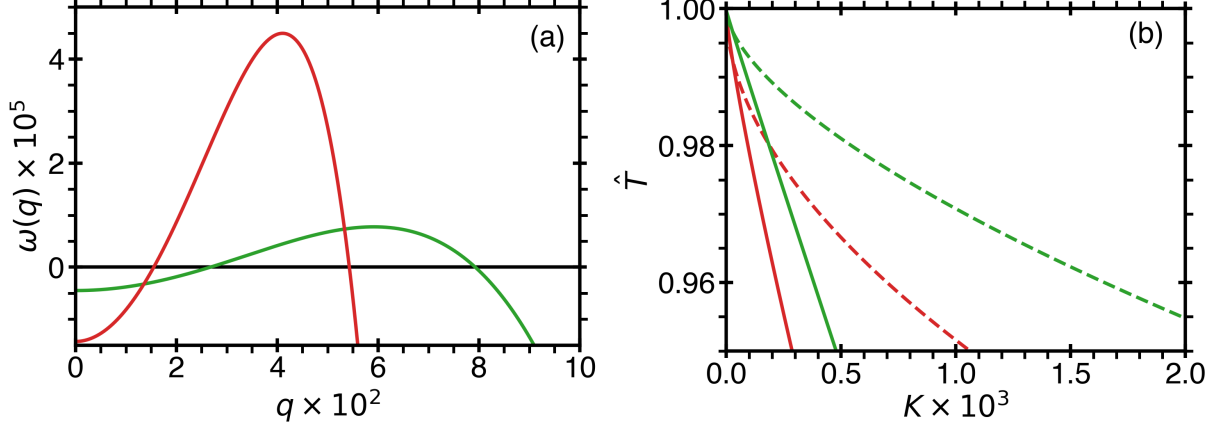


Figure 3.11: a) Characteristic phase domain growth rate in the vicinity of the critical point ( $\Delta\hat{T} = -0.001$ ) for  $M_0 = 1$ ,  $L = 0.002$ , and  $K = 2.25 \times 10^{-5}$  calculated through Eq. (3.13), red curve, with use of the diverging molecular mobility, Eq. (3.27), and scaling inverse susceptibility in the first order epsilon expansion,  $\hat{\chi}_{q=0}^{-1} \sim |\Delta\hat{T}|^{-\gamma}$  with  $\gamma = 1 + \epsilon/6$  ( $\epsilon = 4 - d$ ). The meanfield approximation is shown by the green curve, Eq. (3.13). b) The onset, red solid curves, Eq. (3.28), and termination, red dashed curves, Eq. (3.29), of microphase separation affected by critical fluctuations for  $M = 1$ ,  $L = 0.01$ ,  $\ell = 100$ ,  $\nu = 1/2 + \epsilon/12$ . The meanfield approximation is shown by the green curves.

rates the form of  $\hat{\chi}_{q=0}^{-1}$  from scaling theory and  $M$  from mode coupling theory, Eq. (3.27).

The comparison between the prediction for the growth rate, Eq. (3.13), in the meanfield approximation and in scaling theory is shown in Fig. 3.11a. This figure depicts a significant effect of critical fluctuations on the growth rate. The wavenumber corresponding to the steady-state domain size is shifted toward smaller wavenumbers and the maximum of the growth rate is much stronger, indicating that the domain size growth into steady-state microphase domains will be faster and result in larger domain sizes in the steady-state regime. The structure factor in the scaling regime is given by Eq. (3.23) with use of the scaling growth rate.

In addition, both the onset and termination of microphase separation are affected by critical fluctuations. In particular, from the growth rate,  $\omega(q)$ , it can be shown from Eq. (3.13) that

$$K^*(\hat{T} = \hat{T}^*) = L\hat{\chi}_{q=0}^{-1} - (M\hat{\chi}_{q=0}^{-1} + L\kappa)(q^*)^2 - M\kappa(q^*)^4 \quad (3.28)$$

where  $\hat{T}^* = T^*/T_c$  is the reduced temperature at the onset. Therefore, the magnitude of forced interconversion at the onset of microphase separation scales with proximity to the critical point as  $K^* \propto L\hat{\chi}_{q=0}^{-1} \sim |\Delta\hat{T}^*|^{2\nu}$ . In contrast, in the meanfield approximation,  $K^* \propto |\Delta\hat{T}^*|$ . In addition, the magnitude of forced interconversion at the termination of microphase separation,  $\omega(q_m) = 0$ , is given by

$$K^{**}(\hat{T} = \hat{T}^{**}) = \frac{(-M\hat{\chi}_{q=0}^{-1} + L\kappa)^2}{4M\kappa} \quad (3.29)$$

where  $\hat{T}^{**} = T^{**}/T_c$  is the reduced temperature at the termination point, and thus,  $K^{**} \propto D\hat{\chi}_{q=0}^{-1} \sim |\Delta\hat{T}^{**}|^{3\nu}$ , while in the meanfield approximation,  $K^{**} \propto |\Delta\hat{T}^{**}|^2$ . As shown in Fig. 3.11b, the effect of critical fluctuations lowers the amplitude of the onset and termination lines. Away from the critical point, these lines should converge with their meanfield predictions.

### 3.6 Conclusion of Chapter 3

A phenomenology describing phase formation affected by both natural (equilibrium) and forced (nonequilibrium) molecular interconversion has been presented. This theory is applicable to systems where the order parameter possesses both conserved and non-conserved dynamics. It has been shown that a source of forced interconversion may cause microphase separation, while in the absence of forced interconversion, the competition between diffusion and natural interconversion dynamics results in the phenomenon of phase amplification, where one phase grows at the expense of another stable phase. Phase amplification occurs to avoid the formation of an energetically unfavorable interface between alternative stable phase domains. In macroscopic systems, where the interfacial energy is much smaller than the bulk energy, the formation of a metastable interface becomes less unfavorable, and the possibility that the system would form an

interface significantly increases [4]. Meanwhile, in the phenomenon of microphase separation, the presence of an external energy source compensates the energy penalty of forming an interface, such that the formation of additional interfaces becomes favorable.

It should be emphasized that the possibility of observing phase amplification depends on the simulation or experimental conditions. In real systems, the volume change of the interconversion reaction may not be zero. Thus, in an  $NVT$  ensemble, phase amplification is restricted by the conservation of matter, such that complete phase separation would be observed. However, in an  $NPT$  or  $\mu VT$  ensemble, where the size of the simulation box or the number of particles in the system are allowed to fluctuate, then phase amplification could be observed (depending on the size of the system, temperature, and interconversion rate). The possibility of phase amplification has not been discussed in previous studies of polyamorphic substances. For example, the possibility of phase amplification in high-pressure hydrogen (Section 2.2) and in polyamorphic supercooled water could be a primary challenge of observing a FFPT in simulations or experiment [1].

## Chapter 4: Application of Theory to Microscopic Models

In this chapter, a quantitative agreement is obtained between the developed approach, the generalized Cahn-Hilliard theory and the Cook-Binder theory, and simulations of three microscopic models as well as through a comparison with the behavior of Glotzer *et al.*'s nonequilibrium binary-mixture model [207, 213, 216, 217, 235, 256, 257]. It is shown that the interplay between phase separation, natural interconversion, and forced interconversion may generate dissipative structures – a nonequilibrium bicontinuous microemulsion, revealed by molecular dynamics (MD), or a nonequilibrium spatially modulated state, as observed in Monte Carlo (MC) studies. It is also shown that under certain conditions the three models with different origins of interconversion and the model of Glotzer *et al.* [207, 213, 216, 217, 235, 256, 257] may exhibit identical behavior.

### 4.1 Hybrid Ising / Binary Lattice (HL Model)

As emphasized in Section 3.5, the Ising and lattice-gas models are equivalent in thermodynamics, but fundamentally different in dynamics. As a result, in zero ordering field, the average order parameter,  $\langle \varphi \rangle$ , is zero for the lattice gas ( $\rho = 1/2$ ) and non-zero for the Ising model. The density or concentration relaxes to equilibrium by spatial-dependent diffusion, while the relaxation of the magnetization in the lowest approximation is not spatial dependent. An important

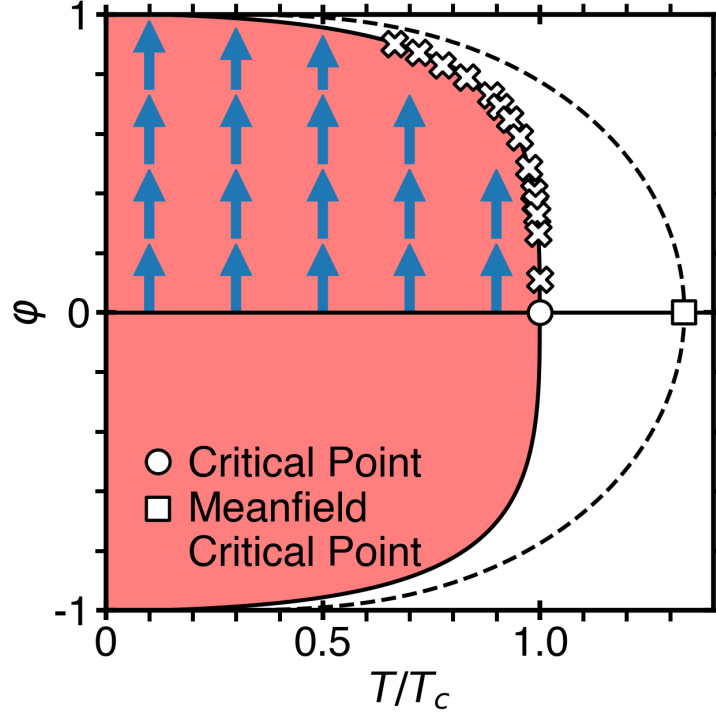


Figure 4.1: The spontaneous equilibrium order parameter ( $\varphi = \varphi_0$ ) in the lattice gas / lattice binary mixture along the liquid-vapor phase coexistence (red domain). One of the two alternative magnetizations ( $\varphi_0 > 0$  and  $\varphi_0 < 0$ ) in the Ising ferromagnet in zero field are shown in the red domain with blue arrows. The solid curve is the crossover from meanfield behavior (dashed) to the asymptotic scaling power law  $\varphi \propto \Delta T^\beta$  with  $\beta = 0.326$  [52, 53], while the crosses correspond to simulation results of the HL model.

consequence of the difference in dynamics of the conserved and non-conserved order parameters is the difference of their equilibrium states, as illustrated in Fig. 4.1. To model diffusion and interconversion dynamics in a binary system, a simple lattice model where the particles of different types are represented by spins of different orientations is considered. Diffusion is simulated by “swapping” a pair of randomly selected neighboring spins and interconversion is simulated by “flipping” a spin at a randomly selected lattice site. At each MC step, the probability that a random spin will attempt to flip is  $p_r$ , while swapping a randomly selected pair of nearest neighbor spins will be attempted with probability  $1 - p_r$ . This step is accepted according to the standard Metropolis criterion [258].

### 4.1.1 HL Model Description

<sup>1</sup> Consider an “Ising-like” lattice model where diffusion is modeled by “swapping” the position of two neighboring species and interconversion is modeled by “flipping” one species type to another [6]. The diffusion and interconversion dynamics are simulated using a hybrid of Kawasaki and Glauber Monte Carlo (MC) methods [228, 259, 260], respectively. The species are arranged on an  $\ell \times \ell \times \ell$  cubic lattice with a coordination number of 6. Using the Ising model Hamiltonian [261]

$$H = -\frac{\varepsilon}{2} \sum_{i=1}^{\ell^3} \sum_{j \in \Omega(i)} s_i s_j \quad (4.1)$$

where  $s_i, s_j = \pm 1$  are spins,  $\Omega(i)$  is the set of 6 nearest neighbors of spin  $i$ , and  $\varepsilon$  is the interaction energy. The critical temperature of this system is  $T_c = 4.5115(1)\varepsilon/k_B$  [54]. Realizations are initialized with a random spin configuration in which  $\ell^3/2$  are positive and the other  $\ell^3/2$  are negative. In addition, it is assumed that at each MC step the probability of a random spin flip (a Glauber step) is  $p_r$ , while the probability of swapping a randomly selected pair of nearest neighbor spins (a Kawasaki step) is  $1 - p_r$ .

In each Glauber step, a random spin is selected and has a chance to flip according to the standard Metropolis criterion [258]. In each Kawasaki step, a pair of spins is randomly selected out of the list of opposite pairs and this pair has a chance to be swapped according to the Metropolis criterion. After each successful flip or swap, the list of opposite pairs is updated.

---

<sup>1</sup>This subsection was reproduced from Nikolay A. Shumovskyi, Thomas J. Longo, Sergey V. Buldyrev, and Mikhail A. Anisimov, *Phys. Rev. E Lett.*, **103**, L060101 (2021); <https://doi.org/10.1103/PhysRevE.103.L060101> with the permission of APS Publications, from Thomas J. Longo, Nikolay A. Shumovskyi, Salim M. Asadov, Sergey V. Buldyrev, and Mikhail A. Anisimov, *J. Non-Cryst. Solids: X*, **13**, 100082 (2022); <https://doi.org/10.1016/j.nocx.2022.100082> with the permission of Elsevier, and from Thomas J. Longo, Nikolay A. Shumovskyi, Betül Uralcan, Sergey V. Buldyrev, Mikhail A. Anisimov, and Pablo G. Debenedetti, *Proc. Natl. Acad. Sci.*, **120**, e2215012120 (2022), <https://doi.org/10.1073/pnas.2215012120> with the permission of NAS Publications.

A size-independent MC time is introduced as  $t = n/\ell^3$ , so that in each time unit, each spin in the system has a chance  $p_r$  to flip, or each spin can swap with a neighboring spin,  $1 - p_r$ . The frequency of spin flipping is absorbed into the time step,  $\delta t$ , so the Onsager coefficients,  $L$  and  $M$  (and consequently  $p_r$ ), do not depend on temperature.

The equilibrium formulation, described above and detailed in Ref. [6], is converted to nonequilibrium via the introduction of an additional energy,  $E$ , incorporated into the Boltzmann factor for the probability that a spin flip will be accepted as  $p \sim \exp[-(\Delta U - E)/k_B T]$ , in which  $\Delta U$  is the difference in internal energy of the system for this step [258]. Thus, the effect of the energy source only affects the interconversion dynamics of the system. The diffusion dynamics, determined in each Kawasaki step, occur with a probability that two spins will swap according to the Metropolis criterion without any additional energy source.

In the nonequilibrium formulation of the HL model, an additional energy,  $E$ , due to the external source of forced interconversion is incorporated into the Boltzmann factor for the Metropolis criterion of a spin flip as  $p \sim \exp\{[-(\Delta U - E)/k_B T]\}$ , where  $\Delta U$  is the difference in internal energy of the system for this step. When  $E = 0$ , the system evolves according to the equilibrium formulation detailed above, which leads to phase amplification. If  $E > 0$  and is large enough to overcome natural interconversion (and, consequently, phase amplification), then steady-state microphase separation occurs. The energy source,  $E$ , reduces the thermodynamic energy barrier between inhomogeneous and phase separated states. Thus, it promotes interconversion to an equal composition of species in opposition to natural interconversion where, in general, the relative population of interconverting species varies with thermodynamic conditions. For energy  $E \geq 12$ , the external source of forced interconversion is always greater than  $\Delta U$  (cubic lattice in three dimensions), such that spin interconversion occurs with probability,  $p_r$ , and the Metropolis

criterion is always accepted ( $p \sim 1$ ). This scenario makes this model equivalent to the model of Glotzer *et al.* [213, 216, 217, 256]. For  $E < 12$ , the local environment of the selected species influences the probability of the interconversion reaction occurring ( $p < 1$ ). Thus, whether a spin-flip will be accepted at each MC step is determined by both the spin-flip probability,  $p_r$ , and the Metropolis criterion,  $p$ . For the diffusion dynamics, the spin-swap step is performed according to the standard Metropolis criterion without any additional energy source, such that diffusion is the same in both the equilibrium and nonequilibrium formulations of this model.

The dynamic structure factor is calculated using the method described in Kumar *et al.* [262]. It is noted that this method differed from the FFT method, used in Section 3.3, since the maximum of the structure factor (after normalizing by  $\ell^3$ ) differed by a factor of  $\pi$ . Additionally, using the FFT method, the time evolution of the structure factor was interrupted at the wavenumber  $q/q_{\max} = 1$  (indicating that the size of the two phase domains were half the size of the simulation box,  $\ell/2$ ), while using the method presented in Kumar *et al.*, the maximum of the structure factor was interrupted at a larger wavenumber. To correct for this difference, in this section, the wavenumbers are scaled such that complete phase separation occurs at  $q/q_{\max} = 1$ .

#### 4.1.2 Phase Amplification in the HL Model

In this section, the rate of phase amplification in the HL model is characterized through the interconversion probability, system size, and distance to the critical temperature. Scaling arguments are provided for the topological behavior of the resultant structures that occur during phase amplification. Through comparison with the generalized Cahn-Hilliard theory, a qualitative comparison is obtained between the predictions of the theory and simulations of the HL model.

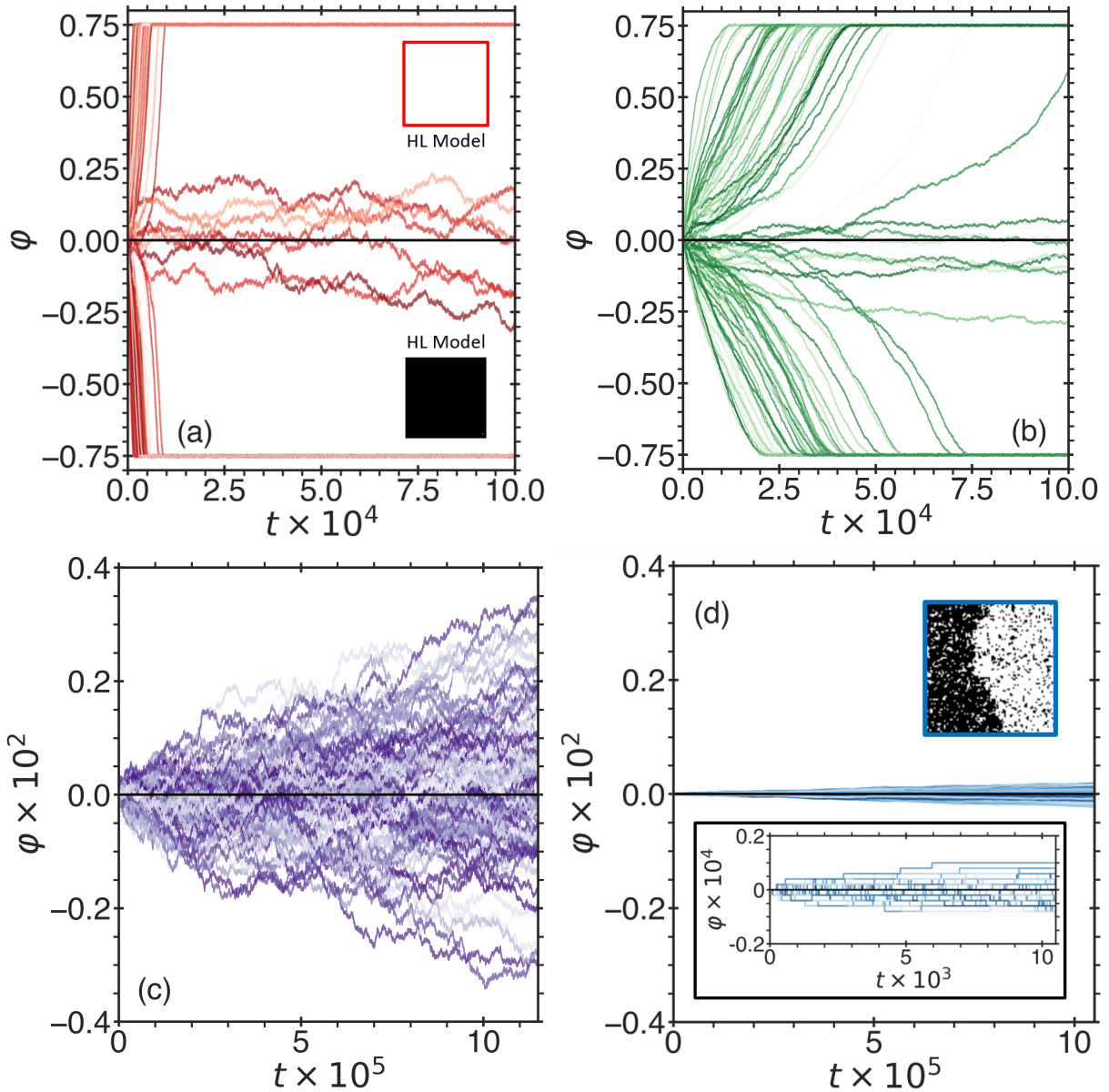


Figure 4.2: Phase amplification in the HL model for systems with  $T = 4.0$ ,  $\ell = 100$ , and interconversion probabilities  $p_r$ : (a) 100%, (b) 10%, (c)  $10^{-4}\%$ , and (d)  $10^{-7}\%$ . The inset in (d) shows  $10^{-7}\%$  interconversion probability at a shorter time scale. Each curve represents one of the 100 different realizations of the MC simulations, while the solid zero line depicts the behavior of a system with 0% interconversion. The simulation snapshots in (a,d) correspond to the end of the simulation time.

### 4.1.2.1 Temporal Evolution of the Order Parameter in the HL Model

<sup>2</sup>The lattice gas and Ising models both generate phase domains, for  $T < T_c$ , that will either grow or collapse according to the growth rate law, Eq. (3.14), see Fig. 3.1. The competition between the two types of dynamics of the order parameter results in phase amplification. However, the rate of phase amplification depends on the probability for the system to follow Ising (non-conserved) order-parameter dynamics, see Fig. 4.2(a-d) where the phenomenon of phase amplification is shown for different probabilities from pure Ising,  $p_r = 1$ , to extremely low probability  $p_r = 1.0 \times 10^{-7}$ . For the extremely low probability, most realizations just fluctuate around  $\langle \varphi \rangle = 0$ . However, it is remarkable that even for this probability phase amplification still occurs.

One of the most evident characteristic of phase amplification is the increase in the width of the distribution of the growth rates as the Ising-dynamics probability increases. Assuming that the distribution of the rates (slopes) in Fig. 4.2 is Gaussian, in Fig. 4.3a, it is shown that the standard deviation of this distribution (calculated at the same time  $t = 300$ ) changes from  $\sigma \propto \sqrt{p_r}$  to  $\sigma \propto p_r$  as the system transitions from lattice gas to Ising behavior. As a result, by comparing arithmetic averages of the absolute value of different initial configurations, the three key parameters that describe the evolution of the order parameter are: interconversion rate (probability), system size, and distance to the critical point. As shown in Fig. 4.3(b-d), phase amplification is faster for larger  $p_r$ , smaller  $\ell$ , and closer distance to the critical point (smaller  $\Delta\hat{T}$ ).

By reducing the order parameter by its equilibrium value ( $\hat{\varphi} = \langle \varphi \rangle / \varphi_0$ ) and rescaling the

---

<sup>2</sup>This subsection was reproduced from Nikolay A. Shumovskyi, Thomas J. Longo, Sergey V. Buldyrev, and Mikhail A. Anisimov, *Phys. Rev. E Lett.*, **103**, L060101 (2021); <https://doi.org/10.1103/PhysRevE.103.L060101>, with the permission of APS Publications.

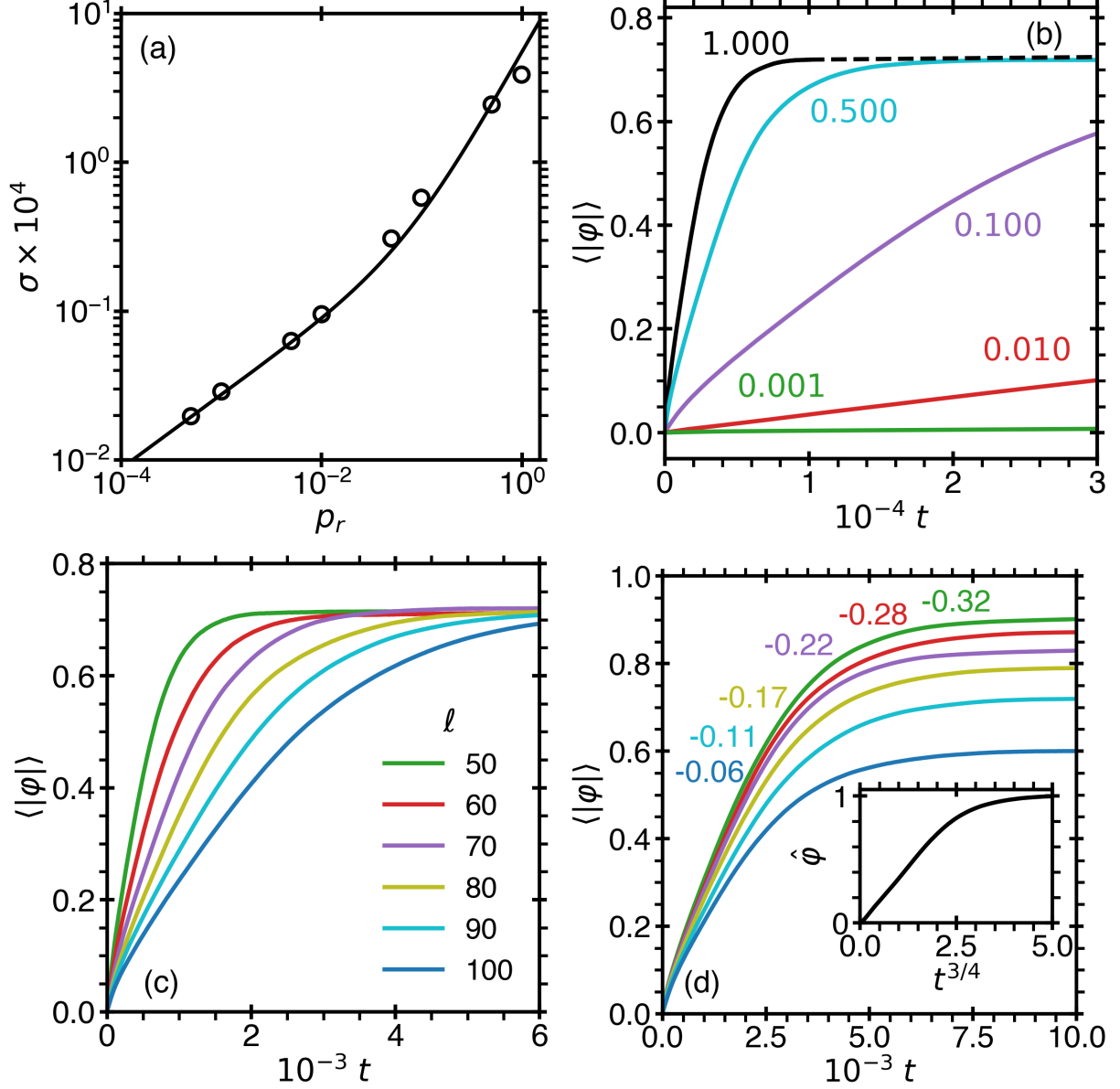


Figure 4.3: The evolution of the order parameter during phase amplification. (a) The RMS of the distribution of the growth rates for different probabilities captured at the same time,  $t = 300$ . The solid curve is the crossover between  $\sigma \propto \sqrt{p_r}$  and  $\sigma \propto p_r$ , approximated as  $\sigma = a\sqrt{p_r}(1 + bp_r)/(1 + \sqrt{p_r})$ . (b-d) The growth of the order parameter for different (b) probabilities at  $\Delta\hat{T} = -0.11$  and  $\ell = 100$ , (c) system sizes at  $p_r = 1.0$  and  $\Delta\hat{T} = -0.11$ , and (d) distances to the critical point at  $p_r = 1.0$  and  $\ell = 100$ ; The inset shows the power law for the initial growth of the reduced order parameter,  $\varphi/\varphi_0 \propto t^{3/4}$ .

time as  $t/\tau(\ell)$  the system-size and temperature dependent  $\varphi(t)$  are collapsed as shown in Fig. 4.4a, in which the characteristic time  $\tau(\ell)$  is proportional to  $\ell^2$  as shown in the inset. After

introducing another characteristic scaling time  $\tau(p_r)$ , the order parameter growth is collapsed into a set of curves which cross at the same inflection point. Except for small probability, all these curves have approximately the same slope at the inflection point, but when the probability becomes very small, the slope significantly increases and breaks the master-curve collapse. The unique case of extremely small probability will be addressed in the discussion of Fig. 4.5b. The characteristic time,  $\tau(p_r)$ , appears to be a linear function of probability as shown in the inset of Fig. 4.4b.

Simulations of the HL model also demonstrate that phase amplification occurs when one phase domain forms an interface with negative curvature against another. To highlight this effect, phase amplification for individual domains in the shape of a sphere and a cylinder are shown in Fig. 4.5a. These different topologies have different rates:  $\varphi \propto t^{3/2}$  and  $\varphi \propto t$  for the sphere and cylinder respectively.

One can notice from Fig. 4.2a, that even for systems with Ising dynamics, there is a small number of realizations that survive for a long time, but eventually, they will also be amplified rapidly. This effect is attributed to the accidental formation of zero-curvature interfaces formed during the domain growth, and hence, the emergence of two transient metastable phases. It is observed that at least two types of zero curvature interfaces are possible: a planar interface and a Schwarz-P interface [263]. The planar interfaces are stable with respect to small perturbations, while the Schwarz-P interfaces are metastable. This effect is clarified in Fig. 4.5b, by allowing the system to reach an equilibrium Schwarz-P interface under lattice-gas dynamics ( $p_r = 0$ ). The collapse of the Schwarz-P interface occurs after switching the system to Ising dynamics ( $p_r = 1$ ) at time  $t = t_0$ . The dynamics of the average order parameter during phase amplification and of individual domains with simple topological structures (spheres, cylinders, and zero-curvature

structures) may be explained through the following scaling arguments.

#### 4.1.2.2 Scaling Analysis of Phase Amplification

In this subsection<sup>3</sup>, scaling arguments are presented to describe the growth rate of phase amplification in the HL model. The number of growing phase domains in a given system is  $(\ell q)^d$ , where  $q$  is the characteristic curvature (wave number) of the domain's interface and  $d$  is the dimensionality of the space in which the domain may grow. If the interaction between different domains is neglected, then the root-mean-square (RMS) fluctuation of the density per unit volume is  $\sqrt{(\ell q)^d}/\ell^d$ . To obtain the growth rate of the average order parameter, this factor must be multiplied by the growth rate of the phase domain volume -  $v/t \propto 1/q^d t$ . Assuming the interface exhibits a random walk in which  $t \propto q^{-2}$ , then  $v/t \propto 1/q^{d-2}$ . Thus, the growth rate of the average order parameter,  $\partial\langle\varphi\rangle/\partial t \propto \ell^{-d/2} q^{-d/2+2}$ , and as a function of time this is equivalent to  $\partial\langle\varphi\rangle/\partial t \propto \ell^{-d/2} t^{d/4-1}$ . Integrating gives

$$\langle\varphi(t, \ell, T)\rangle = A\varphi_0(T) \left(\frac{t}{\tau}\right)^{d/4} \quad (4.2)$$

Where the characteristic time  $\tau = \tau_0 \ell^2$ , with  $\tau_0$  being linearly proportional to  $p_r$  (see the inset of Fig. 4.4b), and  $\varphi_0(T)$  is the equilibrium value of the order parameter. The amplitude,  $A$ , is practically independent of temperature. It can be shown from the Kelvin equation of excess pressure near a curved interface that  $A \propto \sigma\xi/\varphi_0^2$  [261], where  $\sigma$  is the interfacial tension. This combination is a constant in meanfield theory in which  $\sigma \propto \varphi_0^3$  and  $\xi \propto \varphi_0^{-1}$ , while in the

<sup>3</sup>This subsection was reproduced from Nikolay A. Shumovskiy, Thomas J. Longo, Sergey V. Buldyrev, and Mikhail A. Anisimov, *Phys. Rev. E Lett.*, **103**, L060101 (2021); <https://doi.org/10.1103/PhysRevE.103.L060101>, with the permission of APS Publications.

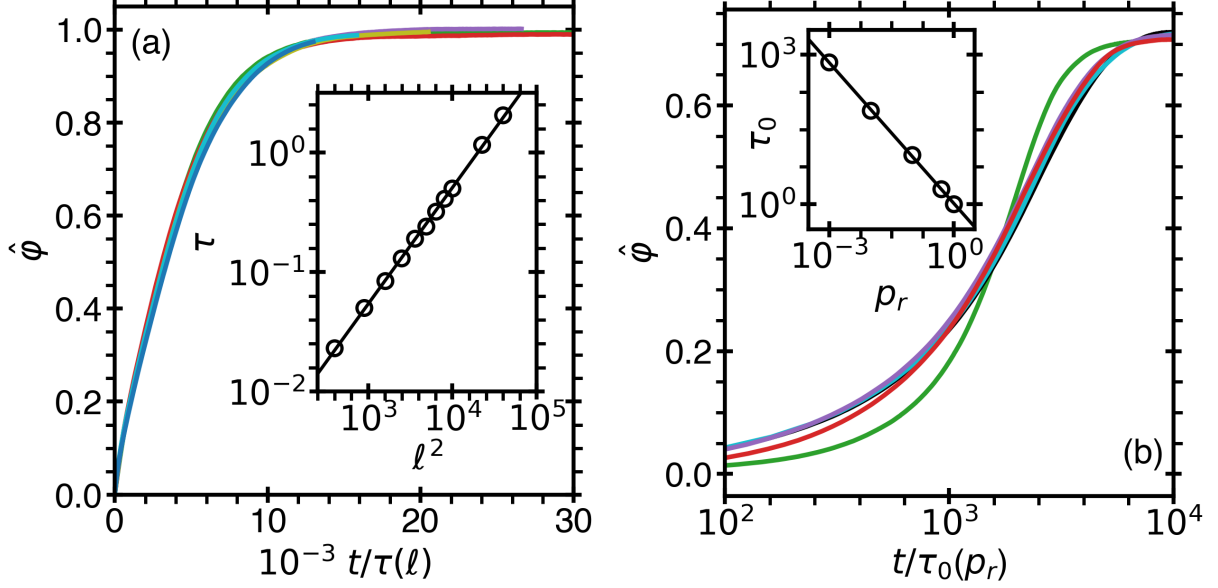


Figure 4.4: Scaling properties of the growth of the reduced order parameter,  $\hat{\varphi} = \langle \varphi \rangle / \varphi_0$ . (a) The order parameter growth with time rescaled by system size. The size dependence of the rescaling parameter,  $\tau(\ell)$ , is shown in the inset; in the log-log scale with a slope of 1. The colors are the same as in Fig. 4.3c. (b) The order parameter growth with time rescaled by probability; the rescaling parameter  $\tau_0(p_r)$ , inversely proportional to the probability, is shown in the inset. The colors are the same as in Fig. 4.3b.

Ornstein-Zernike approximation of scaling theory  $\sigma \propto \xi^{-2}$  and  $\varphi_0^2 \propto \xi^{-1}$  [198, 240]. Eq. (4.2), as demonstrated in Fig. 4.4a, is strongly supported by the simulation data. It is shown that the growth of the average order parameter, in  $d = 3$  space, closely follows the scaling law  $\langle \varphi \rangle \propto t^{3/4}$  - see the inset of Fig. 4.3d.

However, each individual phase domain within a realization of  $\varphi(t)$  evolves depending on the curvature of the interface between domains. Writing the rate of individual-domain growth in terms of time gives  $v/t \propto t^{d/2-1}$ . Integration gives the growth rate for an individual domain as  $\varphi \propto t^{d/2}$ . Using the Kelvin theory [261, 264], it is possible to show that the domain encapsulated by the convex surface with positive curvature shrinks, and eventually disappears at time  $t = t_f$ , so that the net order parameter of the system approaches its equilibrium value  $\varphi_0$  as  $\Delta \hat{\varphi} = (1 - \varphi/\varphi_0) \propto (t_f - t)^{(d^*+1)/2}$ , where  $d^* = d - 1$  is the dimension of the interface, *i.e.*  $d^* = 2$

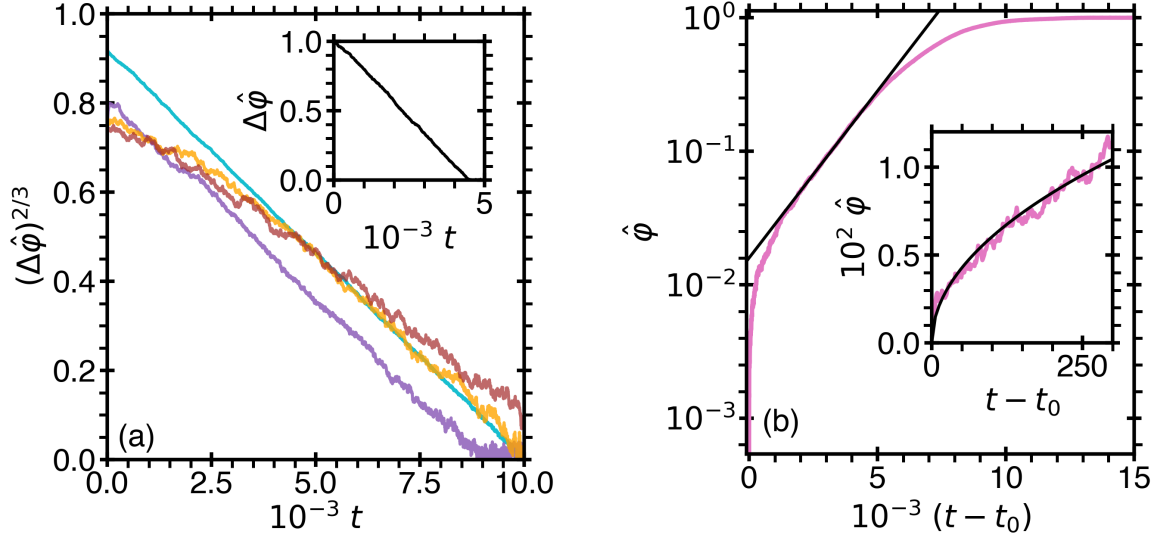


Figure 4.5: Topological characteristics of the time dependence of phase amplification. (a) For spherical domains, the reduced deviation from the equilibrium order parameter,  $\Delta\hat{\phi} = 1 - \varphi/\varphi_0$  scales as  $t^{3/2}$ . This is shown for temperatures,  $\Delta\hat{T}$ , as:  $-0.11$  (cyan),  $-0.025$  (purple),  $-0.014$  (orange), and  $-0.009$  (brown). The inset shows the effect for a cylindrical domain at  $\Delta\hat{T} = -0.11$ . (b) A zero curvature Schwarz-P interface is initially formed by simulating a system with Kawasaki dynamics ( $p_r = 0$ ) for a long time. At  $t - t_0 = 0$ , the system obtains Glauber dynamics ( $p_r = 1$ ) and the collapse of one of the phases is shown. Amplification transitions from random-walk behavior,  $\sqrt{t}$ , at short times (see inset) to exponential behavior before saturation shown by the straight line.

for a spherical domain and  $d^* = 1$  for cylindrical domain. In Fig. 4.5a, these power laws are demonstrated, by selecting two typical topologies: a cylinder, following the power law  $\varphi \propto t$ , and a sphere, following the power law  $\varphi \propto t^{3/2}$ . According to the scaling arguments presented above, it is observed that the rate of growth is independent of the distance to the critical temperature. However, as  $T \rightarrow T_c$  the fluctuations of the order parameter growth become increasingly more prominent.

Also, if a system forms an interface with zero curvature the interface could exist for a long time. The only surface corresponding to stable equilibrium against amplification is the planar interface. In this case a bump with positive curvature produced by a fluctuation shrinks,

while a cavity with negative curvature will flatten. In periodic boundary conditions this interface forms a strip with two parallel surfaces. Fluctuations will only produce random changes to the width of this strip,  $w = \ell \Delta \hat{\phi} / 2$ , corresponding to the longer lasting realizations in Fig. 4.2a. Eventually, when  $w$  becomes comparable to  $\xi$ , the domain will be punctured and a hole with the average positive curvature of the growing domain will be formed causing the strip to quickly disappear. In periodic boundary conditions, or locally, the growing domains can form other surfaces with zero curvature, for example, a Schwarz-P surface [263]. This is especially likely when  $p_r$  is small and the system has time to evolve largely according to Kawasaki dynamics. Once such an interface is formed, the amplification process is “frozen”, and the order parameter follows random walk behavior. However, such interfaces are unstable against fluctuations and will collapse when the growing phase forms an interface with negative curvature to break the phase domain of the receding phase. The average order parameter behavior in the limiting case of  $p_r \rightarrow 0$  is illustrated in Fig. 4.5b. When a zero curvature interface is first formed due to Kawasaki dynamics, then (no matter how small the Ising probability,  $p_r$ ) Glauber dynamics will proceed until, eventually, one of the phases will disappear. In this case, a renormalized time  $t_G = t p_r$  is used, which essentially counts only the Glauber steps. The sigmoidal shape of this curve shows a crossover from random, square root behavior corresponding to the initial random walk of the interface (near unstable equilibrium) to the quick exponential amplification (after a part of the interface develops non-zero curvature). This phenomenon explains the increase in the growth rate of the order parameter for the small probability of Ising dynamics in Fig. 4.4b through the transformation of  $t$  to  $t_G = t / \tau_0 \propto p_r$ . The development of negative or positive curvature on the surface of a phase domain is a result of fluctuations. The events corresponding to the collapse of the interface become increasingly more likely with smaller system size, smaller

domain width, and closer distance to the critical point where the effects of fluctuations are more pronounced. A study of phase amplification due to more complicated topologies is a subject of future work.

#### 4.1.2.3 Comparison with Generalized Cahn-Hilliard Theory

In this subsection<sup>4</sup>, the generalized Cahn-Hilliard theory is compared to simulations of phase amplification in the HL model. The growth-rate equation for the HL model is characterized by a mixture of conserved and non-conserved order-parameter dynamics. It can be characterized from Eq. (3.7), in the absence of forced interconversion ( $K = 0$ ), as

$$\omega(q) = -\hat{\chi}_{q=0}^{-1}(L\kappa + Mq^2)(1 - \xi^2q^2) \quad (4.3)$$

When  $M = 0$ , the nonconserved order parameter grows according to Ising spin-interconversion dynamics [211], while, when  $L = 0$ , the conserved order parameter grows according to lattice-gas molecular-diffusive dynamics [102]. From Eq. (4.3), the probability that the system will exhibit Ising-model spin interconversion is defined as  $p_r = L\kappa/(Mq^2 + L\kappa)$ , in which (typically)  $\kappa = 1$ . If  $p_r = 1$ , the order parameter relaxes to equilibrium through unrestricted (fast) phase amplification to one of two alternative phases with either positive or negative order parameter. If  $p_r = 0$ , the order parameter exhibits complete phase separation, and if  $0 < p_r < 1$ , the rate of phase amplification is restricted by the interconversion probability, the distance to the critical temperature, and the system size.

Applying the generalized Cahn-Hilliard theory, the evolution of the order parameter in

---

<sup>4</sup>This subsection was reproduced from Thomas J. Longo and Mikhail A. Anisimov, *J. Chem. Phys.*, **156**, 084502 (2022); <https://doi.org/10.1063/5.0081180>, with the permission of AIP Publishing.

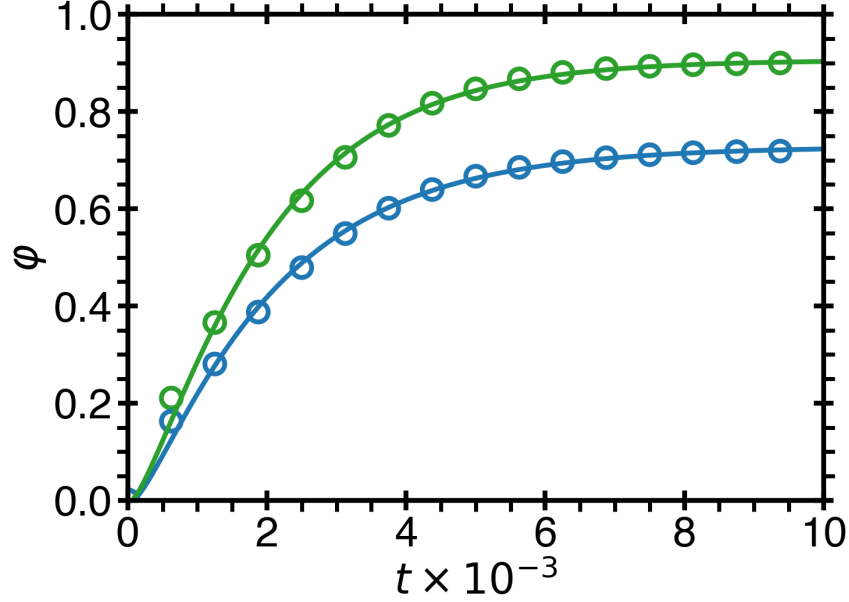


Figure 4.6: The time evolution of the concentration for the HL model with pure Ising dynamics ( $p_r = 1$ ), given by Eq. (4.5) with the time-dependent susceptibility in the form of Eq. (4.4). For  $\Delta\hat{T} = -0.32$  (green),  $\tau = 0.2$ ,  $\varphi_\infty = 0.91$ ,  $a = 1.9$  and  $b = 0.3$ , and for  $\Delta\hat{T} = -0.11$  (blue)  $\tau = 0.2$ ,  $\varphi_\infty = 0.73$ ,  $a = 4.6$ , and  $b = 0.4$ . The open circles are the computational data presented in Fig. 4.3d.

the HL model is quantified through Eq. (3.12). In a system with pure Ising dynamics ( $p_r = 1$ ), the wavenumber corresponding to the fastest growth is  $q_m = 0$ , hence the growth rate is  $\omega(q_m) = -L\hat{\chi}_{q=0}^{-1}$ . During the later stages of spinodal decomposition, as the system evolves toward nucleation, the susceptibility, at constant temperature, changes due to the time evolution of the order parameter. To account for the crossover to the nucleation regime, instead of Eq. (3.24), the time-dependent susceptibility evolving through the two limits:  $\hat{\chi}_{q=0}^{-1}(t = 0) \propto -\Delta\hat{T}$  and  $\hat{\chi}_{q=0}^{-1}(t \rightarrow \infty) \propto \Delta\hat{T}$  is considered. By interpolating between these two limits, one obtains the time-dependent susceptibility in the form

$$\hat{\chi}_{q=0}^{-1}(t) = a\hat{\chi}_{q=0}^{-1}(t = 0) \left[ 2e^{-(t/\tau)^b} - 1 \right] \quad (4.4)$$

where  $a$  is a constant depending on the temperature and  $b$  is an effective exponent, which was empirically found to change between  $b = 1/3$  to  $b = 1/2$  in the interval of  $|\Delta\hat{T}| = 0.32 - 0.06$ . The temporal evolution of the order parameter as a result of phase amplification, for  $p_r = 1$ , is obtained from Eq. (3.12) as

$$\varphi = \varphi_\infty [1 - e^{\omega(q_m)t}] \quad (4.5)$$

It should be noted that to satisfy the boundary conditions that the order parameter is  $\varphi = 0$  at  $t = 0$ , while also reaching its equilibrium value in the limit  $t \rightarrow \infty$ , then  $\varphi_\infty = -\varphi_0/\Delta\hat{T}$ , in Eq. (3.12), where  $\varphi_\infty$  denotes the equilibrium value of the order parameter. As illustrated in Fig. 4.6, the simulation results of Fig. 4.3d are in good agreement with this description.

It is emphasized that phase amplification is manifested by the growth of the average order parameter from  $\varphi = 0$  to its equilibrium value. In the case of pure diffusion dynamics,  $p_r = 0$ , the time evolution of the order parameter is described by a special form of Eq. (3.12), when the constant  $\varphi_0 = 0$ , corresponding to the Cahn-Hilliard theory:

$$\varphi = \varphi_\infty e^{\omega(q_m)t} \cos(q_m r) \quad (4.6)$$

In this case,  $q_m = 1/(\sqrt{2}\xi)$ , such that the average order parameter is given through the factor  $\langle \cos(q_m r) \rangle = 0$ . In contrast, for Ising spin-interconversion dynamics, the cosine term is evaluated at  $q_m = 0$  corresponding to  $\langle \cos(q_m = 0 \cdot r) \rangle = 1$ . Therefore, for pure diffusion dynamics ( $p_r = 0$ ), the average order parameter will remain at  $\varphi = 0$  [6], corresponding to complete phase separation into two symmetric phases of positive and negative order parameter with the same magnitude.

In a hybrid case, when both diffusion and interconversion are present ( $0 < p_r < 1$ ), the average of the general time evolution of the order parameter will no longer be zero, and phase amplification will be observed. This prediction is in agreement with the simulations presented in Section 4.1.2.1, which demonstrated that even an extremely small probability of interconversion dynamics may result in phase amplification, although the number of corresponding realizations will be exponentially small.

### 4.1.3 Nonequilibrium Spatially-Modulated Stripes

The nonequilibrium formulation of the HL model, due to an external source of interconversion, generates nonequilibrium spatially-modulated stripes. In this section, predictions of the generalized Cahn-Hilliard theory and generalized Cook-Binder theory are compared to simulations of the HL model; a qualitative agreement is obtained.

#### 4.1.3.1 Temporal Evolution of the Domain Size

<sup>5</sup>The effect of the source of forced interconversion is introduced into the HL model through a tunable imbalance in the internal energy via the energy of forced interconversion ( $E$ ), such that the source boosts the probability for two alternative species to interconvert into equal amounts. If forced interconversion is not strong enough to overcome natural interconversion (which corresponds to equilibrium conditions), then phase amplification is observed, provided that the natural interconversion probability is significant. If forced interconversion overcomes natural interconversion by a sufficient amount, it is observed that the locally phase-separated domains stop grow-

---

<sup>5</sup>This subsection was reproduced from Thomas J. Longo, Nikolay A. Shumovskyi, Betül Uralcan, Sergey V. Buldyrev, Mikhail A. Anisimov, and Pablo G. Debenedetti, *Proc. Natl. Acad. Sci.*, **120**, e2215012120 (2022), <https://doi.org/10.1073/pnas.2215012120>, with the permission of NAS Publications.

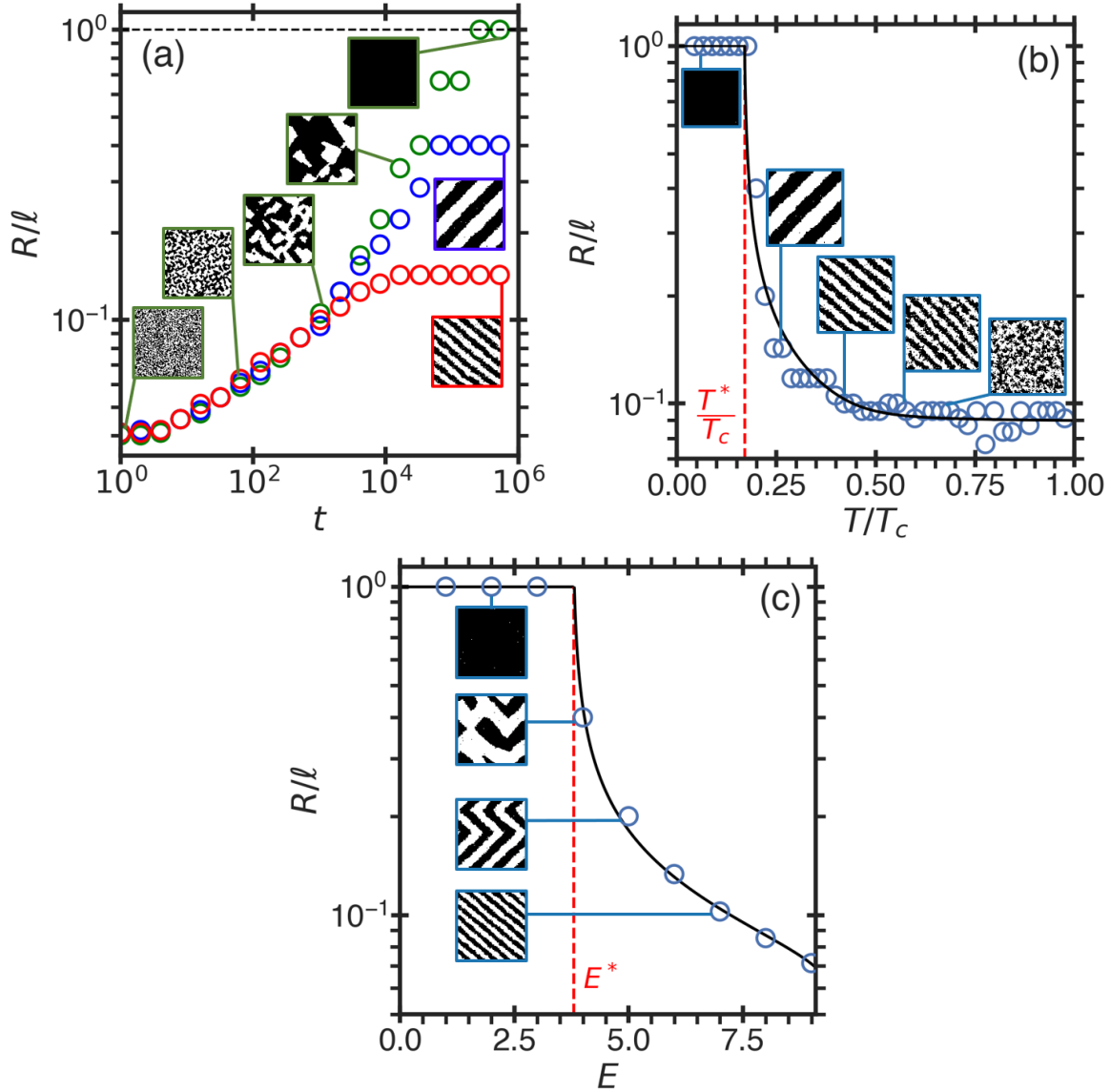


Figure 4.7: Effect of forced interconversion on domain size,  $R$ , normalized by the system size,  $\ell$ , in the HL model. (a) The time dependence of the domain growth for energy source  $E = 5$  and interconversion probability  $p_r = 1/128$  at  $T/T_c = 0.24$  (green),  $T/T_c = 0.27$  (blue), and  $T/T_c = 0.40$  (red), where  $T_c = 4.511$  [54]. The horizontal dashed line indicates the size of the simulation box,  $R = \ell$ . (b) Temperature dependence of the steady-state domain size for  $E = 5$  and  $p_r = 1/128$ . The vertical dashed line indicates the onset temperature,  $T^*/T_c$ . (c) Dependence of the steady-state domain size on the energy of forced interconversion for  $p_r = 1/256$  and  $T/T_c = 0.31$ . The vertical dashed line denotes the onset source energy,  $E^*$ . In (a-c), the system is simulated on a 3-dimensional lattice of size  $\ell = 100$ . The open circles are the results of MC simulations, the images are snapshots of the system for selected conditions, and the curves are the theoretical predictions. In (a-c), black denotes up-spins and white denotes down-spins.

ing upon reaching a characteristic size, as illustrated in Fig. 4.7a. The temperature and energy at the onset of microphase separation is defined as  $T^*$  and  $E^*$ . As shown in Figs. 4.7b and 4.7c, for temperatures and energies,  $T > T^*$  and  $E > E^*$  (for a given probability,  $p_r$ ), dissipative structures are observed and the steady-state domain size decreases as the energy of forced interconversion increases and as the temperature becomes closer to the critical demixing temperature,  $T_c$ .

It is found that the dissipative domain structure has the form of spatially-modulated stripes due to the symmetry and boundary conditions of the lattice on which the MC simulations are performed. As shown by the simulation snapshots in Fig. 4.7b, the striped pattern becomes more disordered when the domain size becomes comparable with the correlation length of concentration fluctuations. Also, it is observed that the chance of forming defects, like kinks or corners in the phase-domain structure, increases for larger-sized microphase structures (see the simulation snapshots in Fig. 4.7c). Only after an astronomically large simulation time will these kinks fully diffuse to produce the final steady-state structure. This effect is attributed to the fact that the energy penalty from forming a corner is minuscule when compared to the bulk, such that these defects would take a longer time to diffuse. Yet, for smaller microphase domains, these defects generate a larger energy penalty when compared to the bulk, and thus, are removed faster.

The theoretical curves, presented in Figs. 4.7(a-c) and Figs. 4.8(a,b) are obtained from the time-evolution of the order parameter, Eq. (3.7). The kinetic coefficients,  $M$  and  $L$ , are assigned to be independent of temperature, while the kinetic coefficient of forced interconversion is related to the energy source,  $E$ , through  $K = f(T)E^2$  (where  $f(T)$  is a function of temperature only) - verified in the next Section (4.1.3.2). With use of Eq. (3.17) for  $q_-$ , the characteristic size of the steady-state domains,  $R$ , in the HL model is given in the first-order approximation by,

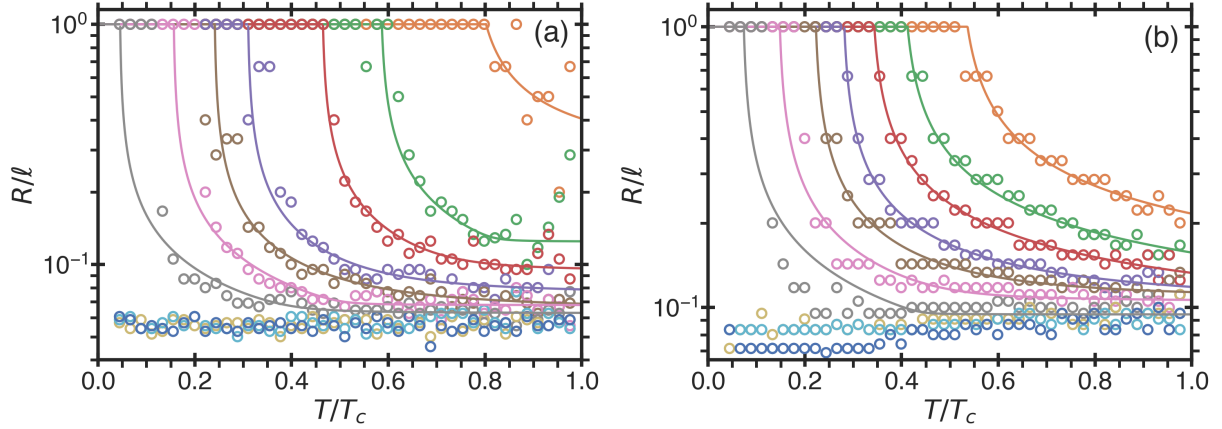


Figure 4.8: Domain size as a function of temperature in the HL model. (a)  $p_r = 1/32$  and (b)  $p_r = 1/256$ , for a system of size  $\ell = 100$  and energies:  $E = 1$  (orange),  $E = 2$  (green),  $E = 3$  (red),  $E = 4$  (purple),  $E = 5$  (brown),  $E = 6$  (pink),  $E = 7$  (gray),  $E = 8$  (yellow),  $E = 9$  (cyan), and  $E = 10$  (dark blue). The solid curves are the theoretical predictions of  $q_-$ , the inverse steady-state domain size, where the fit parameters are provided in Table 4.1.

Table 4.1: Fit parameters of the theoretical prediction in Fig. 4.8a (top,  $p_r = 1/32$ ) and Fig. 4.8b (bottom,  $p_r = 1/256$ ) of the inverse steady-state domain size,  $q_-$ .

$E$	Amp	$M$	$L$
1	13.7	0.370	0.98
2	15.6	0.360	1.06
3	19.3	0.330	1.24
4	23.8	0.276	1.28
5	26.1	0.277	1.46
6	23.6	0.292	1.57
7	25.1	0.272	1.62

$E$	Amp	$M$	$L$
1	31.3	0.050	0.46
2	31.3	0.060	0.74
3	25.8	0.109	1.00
4	18.5	0.217	1.23
5	15.9	0.268	1.42
6	15.3	0.283	1.55
7	16.4	0.285	1.67

$R^2 \sim q_-^{-2} \approx -D_{\text{eff}}^{\text{HL}}/K$ , where  $D_{\text{eff}}^{\text{HL}} = \Delta\hat{T}(M + L\xi^2)$ . The theoretical prediction of the domain size,  $R/\ell$ , in Fig. 4.7b is given by this expression with  $M = 0.26$ ,  $L = 1.33$ , and amplitude,  $A = 19.5$ , while the theoretical prediction for Fig. 4.7c is obtained with coefficients  $M = 0.16$ ,  $L = 1.21$ , and amplitude  $A = 20.9$ . Additional figures showing the steady-state domain size as a function of temperature for different source strengths,  $E$ , and interconversion probabilities,  $p_r$ , in the HL model are illustrated in Fig. 4.8. The theoretical predictions are provided in Tables 4.1 and 4.4.

#### 4.1.3.2 Temporal Evolution of the Structure Factor

<sup>6</sup>In Figs. 4.9(a,b), the generalized Cook-Binder theory (defined in Section 3.3) is compared to simulations of HL model. In Fig. 4.9a, it is shown the steady-state structure factor from simulations at three different external energy values,  $E$ , at constant temperature,  $\Delta\hat{T} = -0.4$ , averaged over  $N = 60$  realizations. Unlike the morphologies computed from Eq. (3.7) via the finite-difference method, the snapshots of the MC simulations shown in the insets of Fig. 4.9a depict stripe-like phase domains that form along the diagonal of the simulation box. Three system-dependent constants are introduced into the steady-state structure factor, when  $q_m \sim q_-$ , and use Eq. (3.22) in the form

$$S_{\infty}(q) = \frac{\tilde{S}a^2(q^2 + L_{\text{eff}})}{a^2q_-^4 + [q^2 - (1 + a)q_-^2]^2} \quad (4.7)$$

where the amplitude ratio relating the theory to the HL model is  $\tilde{S} = 46.5$  and the effective interconversion kinetic coefficient is  $L_{\text{eff}} \sim L/M = 0.0012$ . The constant  $a = 0.2$ , which

---

<sup>6</sup>This subsection was reproduced from Thomas J. Longo, Nikolay A. Shumovskyi, Salim M. Asadov, Sergey V. Buldyrev, and Mikhail A. Anisimov, *J. Non-Cryst. Solids: X*, **13**, 100082 (2022); <https://doi.org/10.1016/j.nocx.2022.100082>, with the permission of Elsevier.

describes the relationship between  $q_m(t \rightarrow \infty)$  and  $q_-$ , broadens or sharpens the scattering peak. At the maximum of the structure factor, when  $q = q_-$ , then Eq. (4.7) reduces to  $S_\infty(q_-) = \tilde{S}/(2q_-^2)$ , which is independent of  $a$ . It is noted that in this form, Eq. (4.7) resembles the scattering intensity distribution of microemulsions [265].

In Fig. 4.9b, the dependence of the wavenumber corresponding to the maximum of the structure factor,  $q_m^s$ , on the magnitude of forced interconversion,  $K$  is illustrated for the theoretical prediction (curves), computations of the time evolution of the order parameter (circles), and simulations of the HL model (triangles). The curves are determined from the full expression for the lower cut-off wavenumber,  $q_-$ , found from Eq. (3.15), when  $\omega(q, 0) = 0$ . A variable amplitude and shift are introduced to scale the theoretical prediction of  $q_-$  such that microphase separation begins at  $q = 1$ . An additional system dependent constant is introduced to describe the relationship between  $q_m(t \rightarrow \infty)$  and  $q_-$ . The numerical computations of  $q_m^s$  (averaged over  $N = 100$  realizations) from the time evolution of the order parameter, Eq. (3.7), are shown in the steady-state regime (after  $t \sim 10^5$  time steps). The magnitude of forced interconversion,  $K$ , (for different external energies,  $E$ ) was obtained for the HL model using Eq. (4.7). In the inset of Fig. 4.9b, the relationship between theory and the HL model,  $K \propto E^2$ , is illustrated.

In addition, as illustrated by Fig. 4.9b, two values of forced interconversion,  $K^*$  and  $K^{**}$  (indicated by the vertical lines), are found that bound the formation of microphase domains. Both boundaries increase with  $\Delta\hat{T}$ ; such that, for  $\Delta\hat{T} > -0.1$ ,  $K^{**}$  is located off the scale of the figure. For  $K < K^*$  phase amplification was observed, while for  $K > K^{**}$ , no striped patterns were observed; instead, only a homogeneous solution persisted, in which an apparent structure on a small scale may be attributed to the correlations between order-parameter fluctuations. In this case, the particles are forced to interconvert so rapidly that diffusion is impossible. As shown

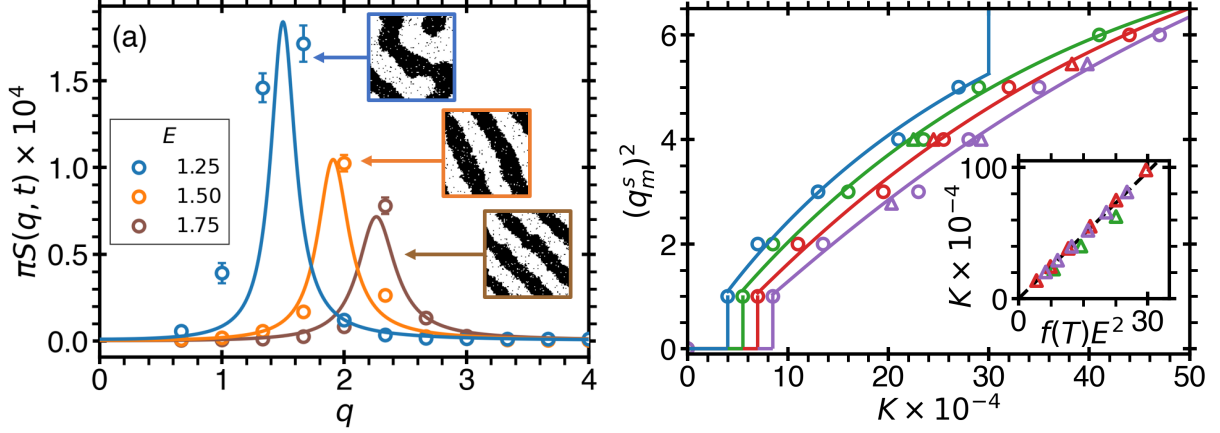


Figure 4.9: a) Steady-state structure factors computed for the HL (open circles) and the prediction given by Eq. (4.7) (solid lines) for selected external energy sources ( $E$ ) at  $\Delta\hat{T} = -0.4$ ,  $M = 1$ ,  $L = 1/127$ ,  $\ell = 100$ , and averaged over  $N = 60$  realizations with 95% confidence interval error bars. The insets show steady-state ( $t \sim 3 \times 10^5$ ) domain morphologies observed in the HL model for the selected energies. b) The dependence of forced interconversion on the wavenumber corresponding to the maximum of the structure factor,  $q_m^s$ , in the steady-state limit. The open circles are numerical computations of structure factors determined from FFTs of the time evolution of the order parameter, given by Eq. (3.7), in the steady-state limit ( $t \sim 10^5$ ) for  $M = 1$ ,  $L = 1/127$ ,  $\sigma_i = 0.1$ , and  $\eta = 10^{-5}$ , averaged over  $N = 100$  realizations. The triangles correspond to the predictions of  $K$  determined from fits of Eq. (4.7) to the structure factor for the HL model, like those presented in (a). The curves illustrate the theoretical prediction  $q_m(t \rightarrow \infty) \propto q_-$ , given by the full expression for  $q_-$ , found from evaluating  $\omega(q, 0) = 0$  using Eq. (3.15). The colors correspond to temperatures:  $\Delta\hat{T} = -0.1$  (blue),  $\Delta\hat{T} = -0.2$  (green),  $\Delta\hat{T} = -0.3$  (red), and  $\Delta\hat{T} = -0.4$  (purple). The inset shows the relationship between  $K$  and  $E$ .

in Fig. 4.9b, the lower bound,  $K^*$ , is associated with the characteristic wavenumber,  $q^* = q = 1$ , which corresponds to phase domains that form at half the size of the simulation box,  $\ell/2$ . In contrast, the characteristic wavenumber associated with the upper bound,  $q^{**}$ , is strongly dependent on temperature [4, 7].

It should be noted that for  $\Delta\hat{T} = -0.1$ , no structured microphase separation was observed in the HL model. The lack of structured domains is attributed to the increase in concentration fluctuations facilitated by the close proximity to the critical point. This effect was not observed in the time evolution of the order parameter, shown in Figs. 3.2(a-d), as the meanfield theory described in Chapter 3 is only applicable sufficiently far away from the critical point.

Lastly, as shown in Section 3.3, the wavenumber corresponding to the maximum of the structure factor,  $q_m^s$ , scales linearly with the lower cut-off wavenumber,  $q_-$ . Consequently, it is observed that the scaling law that  $q_m^s \sim \sqrt{K} \propto \sqrt{f(T)}E$ , where the temperature dependent prefactor is  $f(T) \simeq 9.71T/(T_c - T)$ . This result has also been confirmed in the CM model (Section 4.2). Interestingly, previous studies of phase separating block copolymers in the presence of forced interconversion found that  $q_m^s \sim K^{1/4}$  [213, 235]. As these previous studies considered an  $n$ -component order parameter to describe the block copolymer system (whereas, in this study, the binary mixture is described via a single-component order parameter), this implies that the effect of  $K$  on  $q_m^s$  is system dependent and could depend on the nature of the order parameter.

## 4.2 Chiral-Mixture of Interconverting Enantiomers (CM Model)

Many biological systems are chiral at different levels of organization, including the monomers that constitute proteins, nucleic acids and membranes, as well as the mesoscopic and macroscopic structures that they form, such as the DNA double helix, plant tendril helices, and human appendages [266, 267]. From a practical point of view, chirality also plays a key role in many industrial processes [268–270]. The active ingredients of many drugs are chiral molecules, and their different enantiomers can exhibit significant differences in activity, absorption, selectivity and toxicology [271–273]. Thus, molecular level insight on chiral preference and phase behavior is thus desirable for a broad range of potential applications in science and technology.

Chiral states are not static in nature, and often the individual molecules of different chiralities may interconvert. Interconversion between alternative molecular states of systems exhibiting phase separation is a ubiquitous phenomenon that has been previously found in many condensed

matter systems [117,207,213,218,256,274–282]. In this regard, such chiral systems may be considered as the simplest physical example of phase amplification. To investigate this phenomenon, the interplay between chiral interconversion kinetics and phase behavior has been investigated in the liquid phase of a three-dimensional, off-lattice, flexible tetramer model [7,98] (referred to as the CM model). This model consists of chiral tetramer molecules with a tunable interconversion rate between the two enantiomeric forms. It also includes a pair potential energy function with a tunable chiral bias parameter that can favor either locally racemic or heterochiral interactions. Two formulations of the CM model are considered - one with energy conservation and another one with energy dissipation.

#### 4.2.1 CM Model Description

<sup>7</sup>The CM model represents a series of works [7,8,97–99], inspired by the smallest known chiral molecule in nature, hydrogen peroxide [283–285], based on a 4-site flexible molecule that can adopt two non-superimposable mirror-image configurations. The model was initially introduced by Latinwo *et al.* [98] as a coarse-grained potential energy function with a force imbalance that promotes kinetically arrested liquid-liquid phase separation, and it was subsequently reformulated by Petsev *et al.* with an additional 8-body force resulting in an energy-conserving force field [99]. In this subsection, the formulation of the CM model is briefly reviewed.

A single tetramer molecule of the model is composed of 4 sites that lie along a three-bond

---

<sup>7</sup>This subsection was reproduced from Betül Uralcan, Thomas J. Longo, Mikhail A. Anisimov, Frank H. Stillinger, and Pablo G. Debenedetti, *J. Chem. Phys.*, **155**, 204502 (2021); <https://doi.org/10.1063/5.0071988>, with the permission of AIP Publishing.

Table 4.2: Parameters for the CM model in real and reduced units

Units	$k_s$ (kcal/mol Å <sup>2</sup> )	$k_b$ (kcal/mol rad <sup>2</sup> )	$k_d$ (kcal/mol)	$b$ Å	$m$ (g/mol)	$\epsilon_0$ (kcal/mol)
Real	1000	100	0.00015-4.00	1.18	72.25	0.15535
Reduced	8003	643.7	0.001-25.86	1.0583	8.5	1

backbone at  $\mathbf{r}_1$ ,  $\mathbf{r}_2$ ,  $\mathbf{r}_3$ , and  $\mathbf{r}_4$  (Fig. 4.10) with the total intramolecular potential energy function

$$\Phi^{(1)}(\{r_i\}) = \sum_{i=1}^3 \frac{k_s}{2} (r_{i,i+1} - b)^2 + \sum_{i=1}^2 \frac{k_b}{2} \left( \Theta_i - \frac{\pi}{2} \right)^2 + k_d \cos^2 \phi \quad (4.8)$$

where  $r_{i,i+1}$  is the instantaneous distance between sites  $i$  and  $i + 1$ ,  $b$  represents the equilibrium bond length,  $k_s$ ,  $k_b$ , and  $k_d$  are the force constants for bond stretching, molecular angle bending, and dihedral motion, and  $\Theta_i$  and  $\phi$  are the bond and dihedral angles, respectively. At mechanical equilibrium, the bond angles are  $\Theta_1 = \Theta_2 = \pi/2$ , and the dihedral angle is  $\phi = \pm\pi/2$ .

The intermolecular potential energy between sites  $j$  and  $k$  of tetramers  $\alpha$  and  $\gamma$  is

$$\Phi^{(2)}(\{r_i^\alpha\}, \{r_j^\gamma\}) = \sum_{i,j=1}^4 \epsilon_{tt}(\zeta^\alpha, \zeta^\gamma) v \left( \frac{|r_i^\alpha - r_j^\gamma|}{\sigma_{tt}} \right) \quad (4.9)$$

where  $\sigma_{tt}$  is the pair potential length parameter which specifies the range of the intermolecular interactions,  $v$  is the 12-6 Lennard-Jones pair potential, and  $\epsilon_{tt}$  is the strength of the interaction energy with a renormalization factor that can be tuned to favor/disfavor the homochiral and heterochiral interactions

$$\epsilon_{tt}(\zeta^\alpha, \zeta^\gamma) = \epsilon_0 \left[ 1 + \lambda \zeta(r_{i=1,2,3,4}^\alpha) \zeta(r_{i=1,2,3,4}^\gamma) \right] \quad (4.10)$$

Here,  $\zeta^\alpha$  and  $\zeta^\gamma$  are scalar chirality measures of the molecules as defined below,  $\epsilon_0$  is the LJ

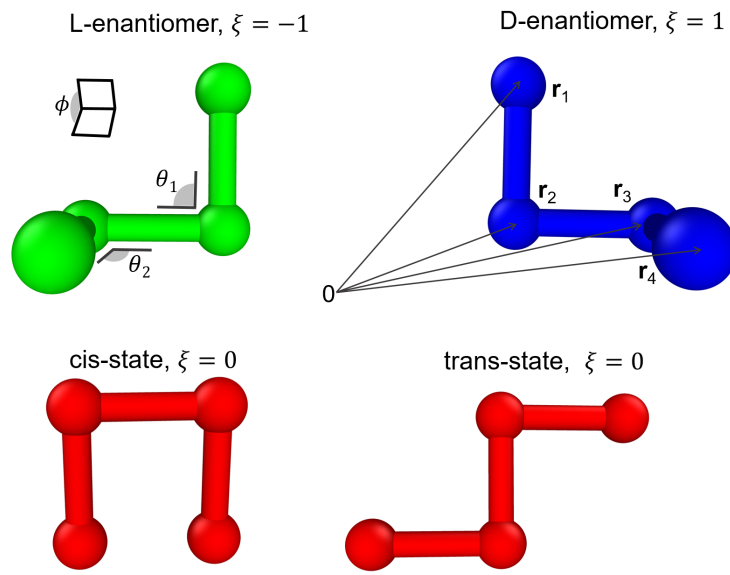


Figure 4.10: Molecular representation and geometrical features of tetramer molecules. L-enantiomers (green), D-enantiomers (blue) and achiral transition states (cis- or trans-, red) are shown.

energy of interaction in the absence of chiral bias and  $\lambda$  is the chiral bias parameter.

The sign of  $\lambda$  defines the nature of chiral bias such that,  $\lambda < 0$  favors heterochiral interactions and racemic mixtures,  $\lambda > 0$  favors homochiral interactions and enantiopure states, and  $\lambda = 0$  represents a bias-free scenario [98]. It is noted that the chirality renormalization parameter effectively represents the local binding preferences of real chiral molecules that are not captured by the LJ potential. For instance, aspartic acid and glutamic acid exhibit phase behavior in accordance with homochiral bias ( $\lambda > 0$ ) [286], while serine and histidine both display heterochiral bias ( $\lambda < 0$ ) [287]. Experimental phase separation in enantiomeric liquids [288] is modeled with  $\lambda \geq 0$ . In this study, the scalar chirality measure  $\zeta$  is defined as

$$\zeta(\mathbf{r}_1, \mathbf{r}_2, \mathbf{r}_3, \mathbf{r}_4) = \frac{\mathbf{r}_{12} \cdot (\mathbf{r}_{23} \times \mathbf{r}_{34})}{|\mathbf{r}_{12}| |\mathbf{r}_{23}| |\mathbf{r}_{34}|} \quad (4.11)$$

where, for each tetramer, the chirality of the enantiomer is determined based on the numerical sign of  $\zeta$ . In particular,  $\zeta = -1$  and  $\zeta = 1$  give L-type and D-type enantiomers, respectively. The measure varies between these extremes as the configuration of the sites change in time.

The molecular dynamics simulations of the CM model are performed using a modified version of the molecular dynamics (MD) package Large-scale Atomic / Molecular Massively Parallel Simulator (LAMMPS) [289]. The renormalization parameter is set to  $\lambda = 0.5$ . The values for the intermolecular and intramolecular interactions are summarized in Table 4.2 both in real physical units and in reduced form. The simulation system is comprised of 1000 tetramers randomly initialized in a cubic box with molecular density  $\rho = 0.27$ . The simulations are performed in the isothermal-isobaric ensemble using the Nosé-Hoover thermostat and barostat, respectively. For all systems, periodic boundary conditions are used with a potential cutoff  $4\sigma_{tt}$ , where  $\sigma_{tt} = 1.115 \text{ \AA}$  (or  $\sigma_{tt} = 1$  in reduced units). A time step of  $0.0005t^*$  is used for the velocity-Verlet integrator where  $t^*$  is the reduced time unit.

Two formulations of the CM model are considered. In the conservative formulation, all intermolecular forces are balanced by taking into account the multi-body forces arising from an explicit chirality-dependent characteristic interaction energy term, as detailed in ref. [99]. In this case, phase amplification is observed where the growth of one of the two alternative states is restricted only by system size. The dissipative formulation, on the other hand, exhibits an imbalance of intermolecular forces imposed between substituents of opposite chirality (as a result of not applying the gradient operator to the chirality dependent term in the potential energy function) [7]. The phenomenon of microphase separation is observed in the dissipative formulation of this model. It should be noted that the force constant for dihedral rotation controls the kinetics of enantiomeric interconversion, and is denoted by  $k_d$ .

## 4.2.2 Phase Amplification in the CM Model

<sup>8</sup>In Fig. 4.11, the time dependence of the dihedral angle of a single tetramer in a racemic mixture of 1000 tetramers, at different temperatures and for a range of values of the dihedral force constant, is shown for the CM model with conservative forces. It can be seen that the enantiomers do not interconvert within the simulation times sampled here, Figs. 4.11(a-c). Interconversion between the two enantiomorphs is achieved only at much lower  $k_d$  values ( $k_d = 0.001$  in Fig. 4.11d).

The CM model with conservative intermolecular forces always undergoes phase amplification below the critical demixing temperature. This is because in a system where molecules can interconvert, the number of molecules of each type (chirally distinct enantiomers in the present case) is not a conserved quantity, and hence the system minimizes its free energy by avoiding the energetic penalty associated with the formation of an interface, such that one of the two alternative phases grows at the expense of the other.

The above considerations apply strictly only at true thermodynamic equilibrium. From a numerical point of view, it is important to understand that the “stiffness” of the force constant for the dihedral angle,  $k_d$ , determines the ease with which such equilibrium can be attained. The mean frequency with which an individual molecule is able to switch its chirality varies in the opposite direction to any  $k_d$  variation. Thus, below the critical temperature for demixing, and for small enough values of  $k_d$ , interconversion occurs frequently and the system is able to attain true equilibrium, resulting in phase amplification. On the other hand, for sufficiently large

---

<sup>8</sup>This subsection was reproduced from Betül Uralcan, Thomas J. Longo, Mikhail A. Anisimov, Frank H. Stillinger, and Pablo G. Debenedetti, *J. Chem. Phys.*, **155**, 204502 (2021); <https://doi.org/10.1063/5.0071988>, with the permission of AIP Publishing.

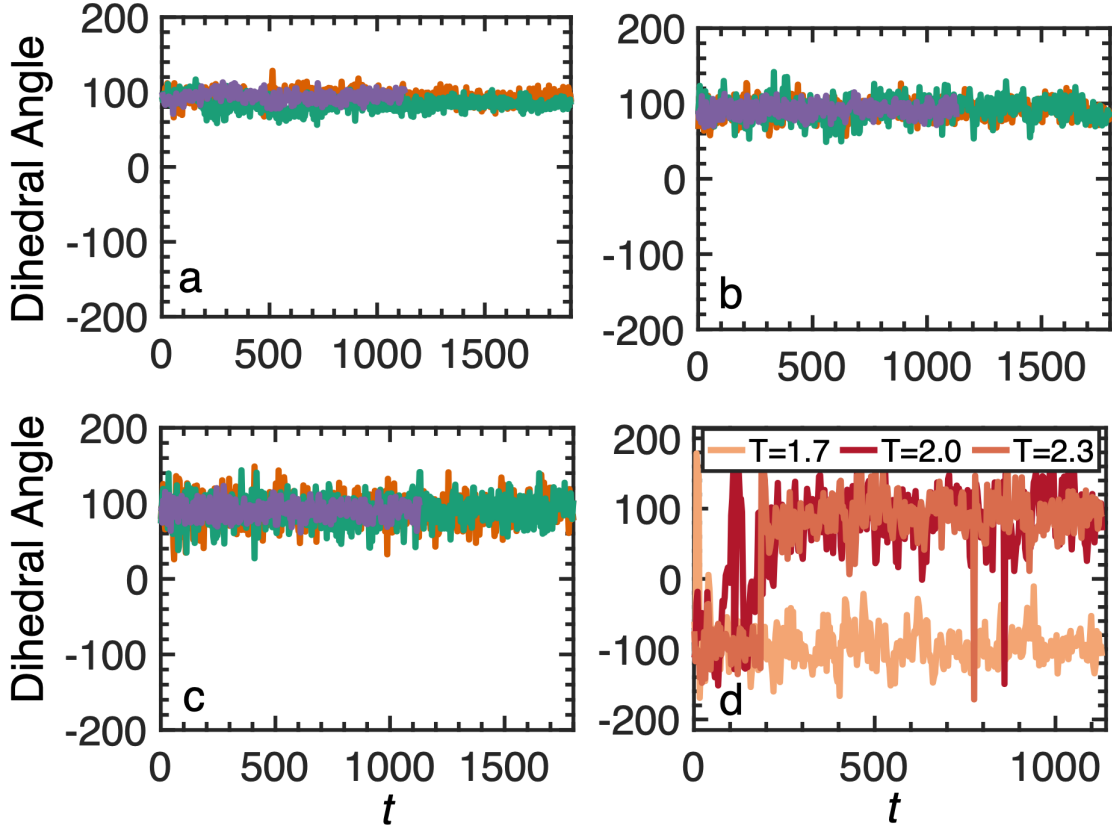


Figure 4.11: Time dependence of the instantaneous dihedral angle of a typical tetramer in a racemic mixture at  $P = 0.1$  for the conservative formulation of the CM model, at several values of  $T$  and  $k_d$ . a)  $T = 0.6$ , b)  $T = 1.7$ , and c)  $T = 2.3$ , with  $k_d = 5$  (green),  $k_d = 9.86$  (orange) and  $k_d = 19.86$  (purple). d) Behavior of the dihedral angle at a very low value of the dihedral constant,  $k_d = 0.001$ .

values of  $k_d$ , interconversion is increasingly rare, the system is under diffusive control, and phase separation, rather than amplification, occurs on practical time scales accessible to simulation, even if the system is under the action of conservative forces.

The mixed diffusion and interconversion dynamics of the CM model can be described through the generalized Cahn-Hilliard theory presented in Chapter 3. In the conservative-force formulation of the CM model, the dynamics of such a system is characterized by a growth rate given in the form of Eq. (4.3). In the CM model, the self-diffusion (mobility) coefficient is given by  $M \approx kT/6\pi\eta R_0$ , where  $\eta$  is the shear viscosity and  $R_0$  is the size of the tetramer (adopted as

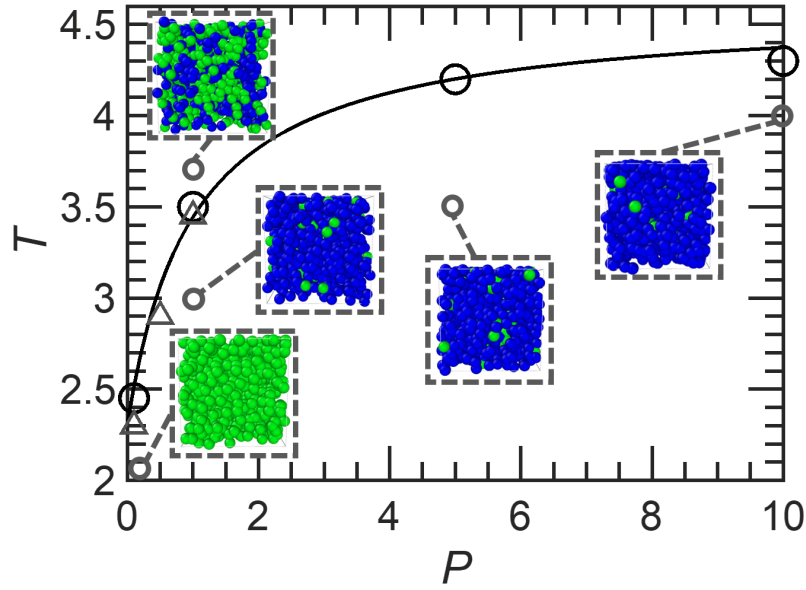


Figure 4.12: The phase diagram showing phase amplification in the CM model with conservative intermolecular forces, heterochiral bias parameter  $\lambda = 0.5$ , and rigidity spring constant  $k_d = 0.001$ . The circles on the solid curve are the computational data for the critical temperature of equilibrium phase separation and the curve is the fit of Eq. (4.12). The snapshots depict the equilibrium states for the pressures  $P = 0.1$ ,  $P = 1$ ,  $P = 5$ , and  $P = 10$  below the critical temperature and at  $P = 1$  above the critical temperature. The triangles show the prediction of the critical temperature from the extrapolation of the CM model with dissipative intermolecular forces to the limit  $k_d \rightarrow \infty$ .

$R_0 = 1$  in reduced units). The interconversion kinetic coefficient,  $L$  depends on the strength of the rigidity spring constant,  $k_d$ , such that it becomes zero in the limit when  $k_d \rightarrow \infty$  and diverges when  $k_d \rightarrow 0$ . Therefore, for large values of  $k_d$  ( $M \gg L$ ), phase separation is expected, while for very small values of  $k_d$  ( $L \gg M$ ), phase amplification is predicted.

Figure 4.12 shows the phase diagram of the CM model in the case when  $k_d = 0.001$  ( $L \gg M$ ) and interconversion dynamics control the phase behavior of the system. The pressure dependence of the critical temperature is empirically described by

$$T_c(P) = T_c(P = 0) + \frac{\alpha P}{1 + P} \quad (4.12)$$

where  $T_c(P = 0) = 2.19$  and  $\alpha = 2.43$ . It is noted that although  $k_d$  primarily determines the interconversion rate, it also affects the system's equilibrium thermodynamics. For example, the total pair interaction energy shows a small but non-zero dependence on  $k_d$  at otherwise identical thermodynamic conditions. Accordingly, one expects the critical temperature to depend on  $k_d$ . This effect is at the limit of detectability, and for numerical purposes,  $k_d$  can be considered as controlling interconversion kinetics, while having at most a modest effect on the system's thermodynamics.

As shown in Fig. 4.12, where  $\lambda = 0.5$ , above the critical temperature, a homogeneous mixture of A- and B- enantiomers is observed throughout the simulation box. The apparent mesoscopic inhomogeneities shown by the snapshot in Fig. 4.12 above the critical temperature are attributed to the growing correlation length of concentration fluctuations in the critical region. Below  $T_c$ , phase amplification occurs. Note that by quenching the racemic mixture below  $T_c$ , due to the effect of phase amplification [6], the system equilibrates arbitrarily to either A- or B-type enriched enantiomer phases as illustrated in Fig. 4.12, thereby establishing a chiral preference.

### 4.2.3 Formation of Dissipative Structures

<sup>9</sup>In the dissipative-force formulation of the CM model, the nonequilibrium condition is mimicked internally through an imbalance in intermolecular forces [7, 99]. This imbalance is introduced if the chirality-dependent characteristic energy scale is not included (as it should) when

---

<sup>9</sup>This subsection was reproduced from Betül Uralcan, Thomas J. Longo, Mikhail A. Anisimov, Frank H. Stillinger, and Pablo G. Debenedetti, *J. Chem. Phys.*, **155**, 204502 (2021); <https://doi.org/10.1063/5.0071988>, with the permission of AIP Publishing, from Thomas J. Longo and Mikhail A. Anisimov, *J. Chem. Phys.*, **156**, 084502 (2022); <https://doi.org/10.1063/5.0081180>, with the permission of AIP Publishing, and from Thomas J. Longo, Nikolay A. Shumovskyi, Betül Uralcan, Sergey V. Buldyrev, Mikhail A. Anisimov, and Pablo G. Debenedetti, *Proc. Natl. Acad. Sci.*, **120**, e2215012120 (2022), <https://doi.org/10.1073/pnas.2215012120>, with the permission of NAS Publications.

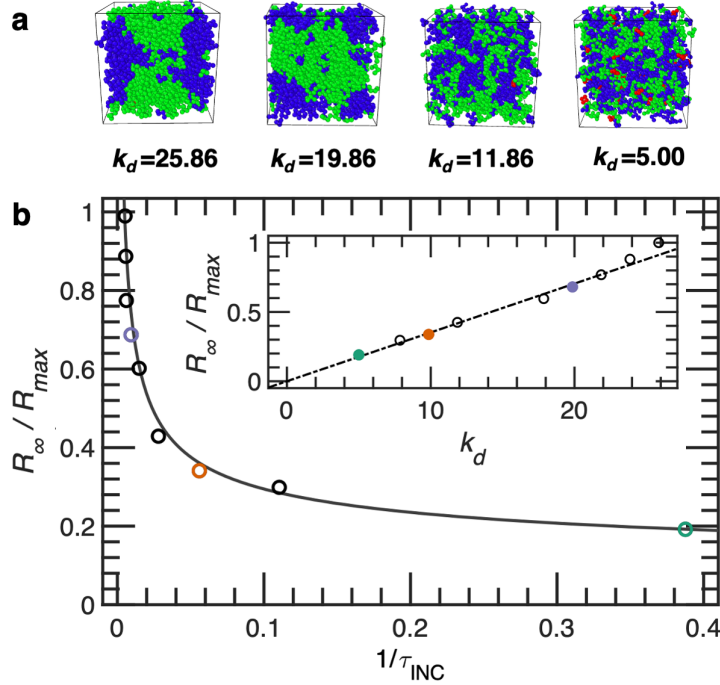


Figure 4.13: The change of compositional heterogeneity with chiral interconversion kinetics at  $T = 1.7$  and  $P = 0.1$  in the dissipative-force formulation. a) Steady-state snapshots of chiral liquid systems at various dihedral force constants ( $k_d$ ). b) The steady-state domain size as a function of interconversion rate,  $1/\tau_{\text{INC}}$ . The solid line is the approximation given by  $1/\tau_{\text{INC}} = a_1/R_\infty^2 + a_2/R_\infty^4$ , which follows from Eq. (4.15), where  $a_1 = 4.6 \times 10^{-3}$  and  $a_2 = 3.8 \times 10^{-4}$ . The inset shows the linear correlation between  $R_\infty$  and  $k_d$ . The colored points highlight the results corresponding to the three dihedral force constants for which the domain growth is shown in Fig. 4.15.

applying the gradient operator to calculate site-site forces [8]. Figure 4.13 illustrates the infinite time limit of the dependence of the steady-state domain length,  $R(t \rightarrow \infty) = R_\infty \propto k_d$ , on the dihedral force constant of the tetramer model with  $P = 0.1$  when the system is quenched from  $T = 2.6$  to  $T = 0.8$ . It is shown that below  $k_d = 25.86$ , the domain growth saturates at a certain steady-state value below  $R_{\max}$ , which is indicated by the simulation snapshots in Fig. 4.13a. The emergence of such smaller domain sizes suggests that the growth of the phase domains at these conditions is restricted by the dissipation in the intermolecular interaction forces, not by the finite length scale of the simulation box.

The characteristic time of interconversion,  $\tau_{\text{INC}}$  is inversely related to the interconversion kinetic coefficient,  $L$ , such that the simulation data can be well described by  $1/\tau_{\text{INC}} = a_1/R_\infty^2 + a_2/R_\infty^4$  (solid-line in Fig. 4.13b). Thus, the interconversion kinetic coefficient has the following dependence on the rigidity parameter,  $k_d$ ,

$$L = M \frac{T^2}{k_d^2} \left( 1 + a \frac{T^2}{k_d^2} \right) \quad (4.13)$$

where  $a$  is constant and the even power of the temperature dependence originates from the natural coupling between dihedral angle rotation and thermal energy in an equilibrium ensemble. Furthermore, the assumption  $L \propto M$  provides a good fit to simulation data and implies that enantiomer interconversion is linked to rotational mobility (the latter being proportional to translational mobility through the Stokes-Einstein and Debye-Stokes-Einstein equations.)

The prediction that the size of the microphase domains is restricted proportionally to  $k_d$  at fixed temperature and pressure is also demonstrated in Fig. 4.14a. Just like the HL model, the domain size at fixed dihedral-force constant decreases with increasing temperature as shown for  $k_d = 5$  in Fig. 4.14b. As depicted by the simulation snapshots in Fig. 4.14, the onset temperature  $T^*$  and  $k_d^*$ , correspond to the conditions where the domain size reaches the size of the simulation box.

Unlike the HL model, where the source of forced interconversion ( $E$ ) is uncoupled from the interconversion probability ( $p_r$ ), in the CM model, both of these effects are controlled by the rigidity parameter,  $k_d$ . Consequently, when  $k_d \rightarrow \infty$  (corresponding to  $p_r \rightarrow 0$  in the HL model) no interconversion, either natural or forced, occurs and the system would phase separate via Cahn-Hilliard diffusion-induced spinodal decomposition [4]. As discussed for the HL model

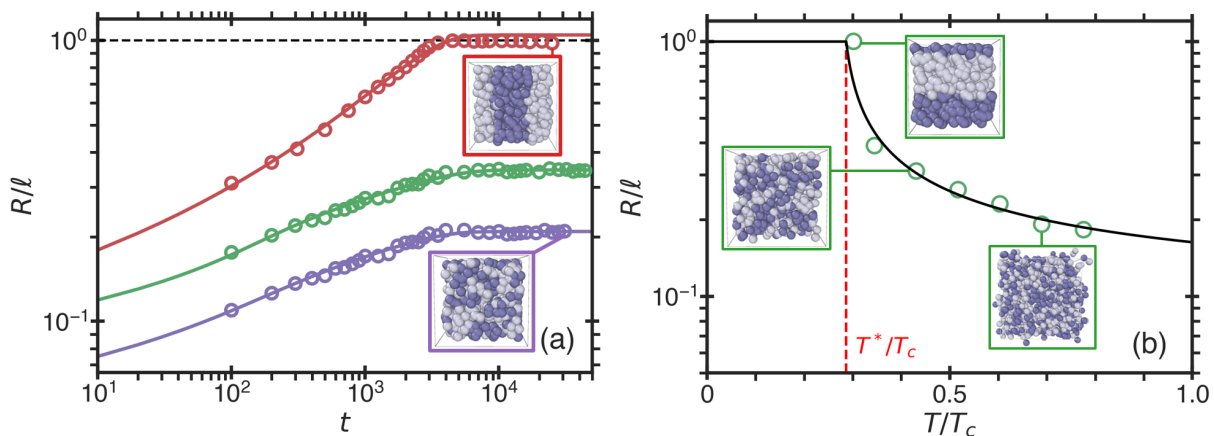


Figure 4.14: Steady-state domain size,  $R$ , normalized by the size of the system,  $\ell$ , in the CM model. (a) The time evolution of the domain size for different interconversion rates, tuned by the rigidity parameter,  $k_d$ , as  $k_d = 3$  (purple),  $k_d = 5$  (green), and  $k_d = 9.86$  (red) at the reduced pressure  $P = 0.1$  and  $T/T_c = 0.35$ , where  $T_c(P = 0.1) = 2.32$ , as indicated on Fig. 4.12. (b) The normalized steady-state domain size as a function of temperature at  $P = 0.1$  and  $k_d = 5$ . The vertical dashed line indicates the onset temperature,  $T^*/T_c$ . In (a) and (b), the open circles correspond to simulation results, the curves correspond to the theoretical predictions (see Table 4.3), and the images show snapshots of the system simulated at the indicated conditions. In (a-b), dark/clear spheres correspond to the L-/D-configuration of a chiral tetramer (spheres are located a tetramer’s center of mass).

in Section 4.1.2, for low interconversion probability, the system commonly enters a transient metastable state with an interface, rather than undergo phase amplification [6]. This phenomenon is also relevant to the CM model, where it is increasingly likely for high enough  $k_d$  that the system will enter a long-living transient state with two phases separated by an interface. This state would eventually converge to a steady-state configuration with the lowest possible interfacial energy (a single phase formed via phase amplification), for low  $T$  and high  $k_d$  (which corresponds to low  $p_r$  in the HL model). This transient dissipative structure is depicted in the simulation snapshots of Fig. 4.14, where it is observed that an interface has formed between the two phases.

Unique to the CM model, an imbalance of intermolecular forces produces an imbalance in chemical potential associated with the interconversion dynamics [99], such that the time-evolution of the order parameter is best described by Eq. (3.8), in which the difference between

Table 4.3: Fit parameters used for the theoretical predictions in Fig. 4.14a of the inverse steady-state domain size,  $q_-$ . The mobility is given by the Stokes-Einstein relation with amplitude  $b_0$  and characteristic temperature  $T_0 = 1.2$ . Two additional parameters, the amplitude,  $A$ , and the characteristic size of the inhomogeneities ( $q_0 \sim 1/R_0$ ) are included.

$k_d$	$b_0$	$A$	$q_0$
3	0.0013	4.55	0.04
5	0.0023	3.80	0.07
10	0.0022	1.55	0.06

the balanced and unbalanced chemical potentials,  $\Delta\tilde{\mu}'$ , corresponds to the compensation of the contribution from the enthalpy of mixing in the chemical potential coupled with the interconversion kinetic coefficient,  $L$ . It is noted that the first term in Eq. (2.12) could also be written through the derivatives of the reduced entropy of mixing,  $\Delta\hat{S}_{\text{mix}} = \Delta S_{\text{mix}}/\rho_c k_B T_c$ , and the reduced enthalpy of mixing,  $\Delta\hat{H}_{\text{mix}} = \Delta H_{\text{mix}}/\rho_c k_B T_c$ , as

$$\Delta\hat{T}\varphi = -T \frac{\partial(\Delta\hat{S}_{\text{mix}})}{\partial\varphi} + \frac{\partial(\Delta\hat{H}_{\text{mix}})}{\partial\varphi} \approx \hat{T}\varphi - \varphi \quad (4.14)$$

Therefore, it may be considered that the racemization of enantiomers is equivalent to forced interconversion driven only by the entropy of mixing as seen through the comparison with Eq. (4.14).

As a result,  $\Delta\tilde{\mu}'$ , in the first-order approximation is given by

$$\Delta\tilde{\mu}' \approx \hat{T}\varphi - \kappa\nabla^2\varphi \quad (4.15)$$

The characteristic phase domain growth rate for the dissipative CM model, with a chemical potential given by Eq. (4.15), reads

$$\omega(q) = -L(\hat{T} + \kappa q^2) - M\Delta\hat{T}q^2(1 - \xi^2 q^2) \quad (4.16)$$

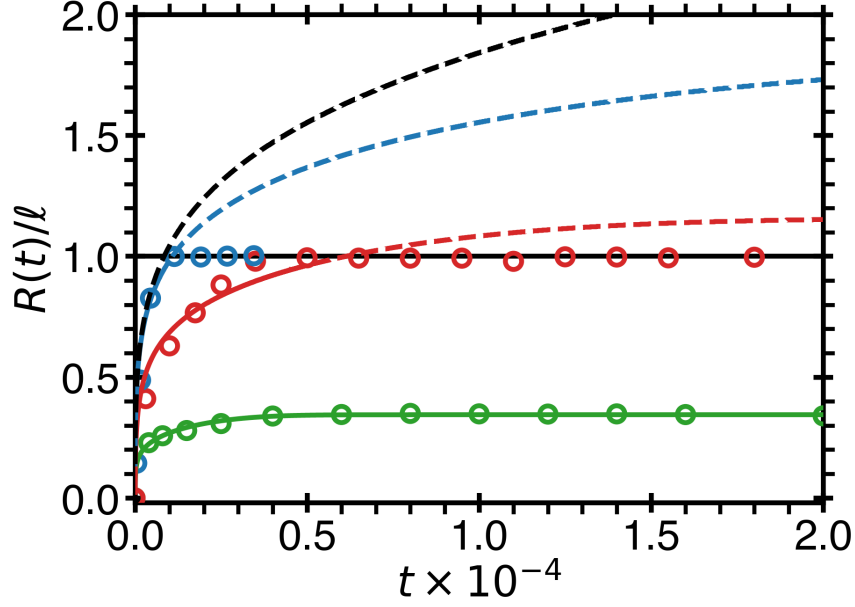


Figure 4.15: Phase domain growth for the dissipative-force formulation of the CM model. The open circles represent computational data [7], and the curves illustrates predictions of the time evolution of the domain size,  $R(t) = 1/q_m^s$ , from Eq. (3.23) for dihedral force constants:  $k_d = 5$  (green),  $k_d = 9.86$  (red),  $k_d = 19.86$  (blue), and  $k_d \rightarrow \infty$  (black) for  $T = 1.8$ ,  $T_c = 2.3$ ,  $\tau = 2$ , and  $M = 0.0022$ . The domain size is normalized by the size of the computational box,  $\ell$ . The dashed curves represent the predictions of the domain growth if it is not restricted by the finite size.

Solving Eq. (4.16) for  $\omega(q) = 0$ , the first root,  $q_-$ , is obtained, which corresponds to the minimum wavenumber below which the growth rate becomes negative and phase domain growth will not be possible. In the first approximation, Eq. (4.16) leads to the prediction of a competition between interconversion and negative diffusion as,

$$q_-^2 = \frac{L}{D_{\text{eff}}} \approx \frac{T^2}{k_d^2(-\Delta\hat{T})} \quad (4.17)$$

where the effective mutual diffusion coefficient is defined as  $D_{\text{eff}} = -(\Delta\hat{T}/\hat{T})(M + L\xi^2)$  in which  $\Delta\hat{T}/\hat{T} = (T - T_c)/T$ . The effective mutual diffusion coefficient represents the diffusion of species affected by interconversion. Remarkably, forced interconversion of species enhances

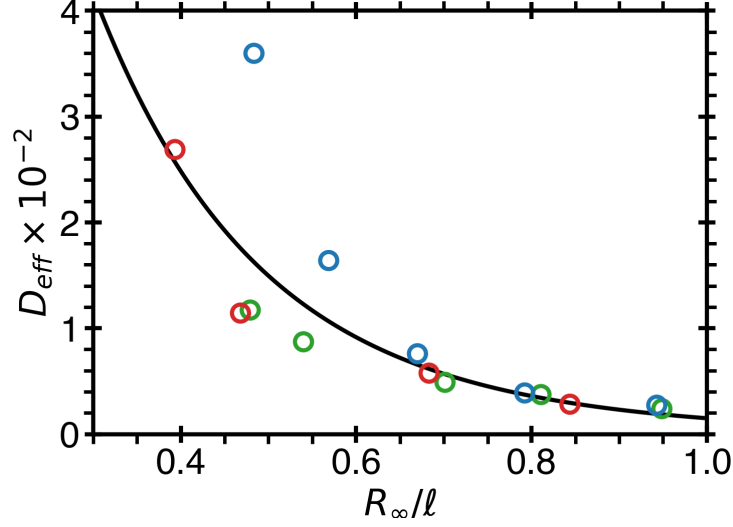


Figure 4.16: The mutual diffusion coefficient affected by interconversion, given by Eq. (4.17), as a function of the normalized steady-state domain size  $R_\infty$ , Eq. (4.18) in the CM model. The open circles are computational data for the dissipative-force formulation of the CM model at three different dihedral force constants:  $k_d = 5$  (green),  $k_d = 9.86$  (red), and  $k_d = 19.86$  (blue) [7]. The molecular mobility in the limit  $k_d \rightarrow \infty$  is approximated as  $M = b_0 T / \eta$ , where  $b_0 = 0.94$  and  $\eta$  is the viscosity approximated by the Arrhenius equation  $\eta \sim e^{T_0/T}$ . The characteristic temperature  $T_0$  is 3.5.

the translational molecular mobility  $M$ , into the effective mobility,  $M_{\text{eff}} = M + L\xi^2$ . This is a novel phenomenon that was recently discovered [7].

The characteristic size of the steady-state domains,  $R_\infty \propto 1/q_-$ , is presented in the first approximation of Eq. (4.17) by

$$R_\infty \approx \frac{k_d}{T} \sqrt{\frac{-\Delta \hat{T}}{\hat{T}}} \quad (4.18)$$

The phase domain growth in the CM model, based on the predictions from the generalized Cook-Binder theory, is illustrated in logarithmic scale in Fig. 4.14a and in normal scale in Fig. 4.15 (also depicting the predictions for  $k_d \rightarrow \infty$ ) for different dihedral force constants. The domain size is calculated from the inverse wavenumber corresponding to the maximum of the time-dependent structure factor,  $R(t) \propto 1/q_m^s$ , as given by Eq. (3.25). In Fig. 4.16, the agreement of the effect of interconversion on the effective diffusion coefficient, given by Eq. (4.17), is demonstrated

through comparisons with computational data [7].

#### 4.2.4 Characteristic Time Scales in the CM Model

<sup>10</sup>Next, in order to further elucidate the kinetics of phase separation, the correlations between the characteristic interconversion (INC) time of a tetramer  $\tau_{\text{INC}}$ , the characteristic phase separation time  $\tau_{\text{LLPS}}$ , and the characteristic molecular self-diffusion time  $\tau_{\text{D}}$  are considered, each of which are well-described by the generalized Cahn-Hilliard theory. In the fits of the simulation data, presented in Fig. 4.17, the interconversion kinetic coefficient,  $L$ , is given by Eq. (4.13), with an adjustable coefficient  $b_0$  and where the mobility,  $M$ , is given through the Stokes-Einstein relation that  $M = k_{\text{B}}T/6\pi\eta R_0$ , where the viscosity of the system is assumed to be  $\eta = e^{T_0/T}$ , in which the characteristic temperature,  $T_0$ , was also adjusted to better describe the behavior of each dihedral constant,  $k_d$ , at low temperatures.

In the two phase region, the growth rate formula, Eq. (4.16), describes the characteristic times of liquid-liquid phase separation (LLPS) on the length scale of the simulation box. As seen in Fig. 4.17a, the time of LLPS becomes infinite when the microdomain sizes reach the size of the simulation box,  $q_- = q^*$ , which is computationally observed as “complete” phase separation. Therefore, the characteristic LLPS time is found as  $\tau_{\text{LLPS}} = a_{\text{LLPS}}/\tilde{\omega}(q^*)$ , where the amplitude  $a_{\text{LLPS}} = 0.34$  and  $T_c = 2.35$ . In the fit, presented in Fig. 4.17a,  $q^*$  is adjusted such that  $\tau_{\text{LLPS}} \rightarrow \infty$  when the temperature reaches  $T = T^*$ , the onset of phase separation on the scale of the simulation box. Also, the characteristic temperature  $T_0$  was slightly different for the three different dihedral constants:  $T_0 = 2.2(k_d = 5)$ ,  $T_0 = 1.925(k_d = 9.86)$ , and  $T_0 = 1.2(k_d = 19.86)$ .

---

<sup>10</sup>This subsection was reproduced from Betül Uralcan, Thomas J. Longo, Mikhail A. Anisimov, Frank H. Stillinger, and Pablo G. Debenedetti, *J. Chem. Phys.*, **155**, 204502 (2021); <https://doi.org/10.1063/5.0071988>, with the permission of AIP Publishing.

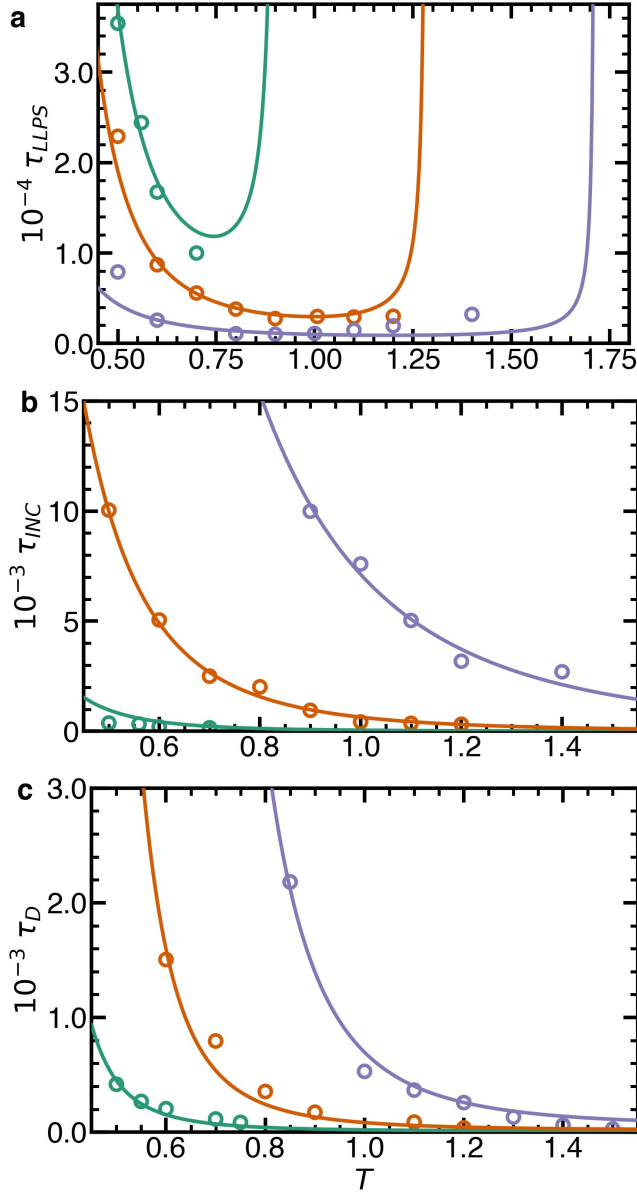


Figure 4.17: Temperature dependence of the characteristic time scales in the dissipative-force formulation of the CM model for dihedral force constants:  $k_d = 5$  (green),  $k_d = 9.86$  (orange), and  $k_d = 19.86$  (purple) at  $P = 0.1$ . a) Characteristic time for liquid-liquid phase separation at the length scale of the simulation box,  $q = q^*$ . The curves are  $\tau_{LLPS} \propto 1/\tilde{\omega}(q^*)$  where  $\tilde{\omega}(q)$  is given by Eq. (4.16) where it was found that  $q^* = 0.15$  and  $T_c = 2.35$ . The condition  $\tau_{LLPS} \rightarrow \infty$  corresponds to  $T = T^*$ . b) Characteristic times for chiral interconversion.  $\tau_{INC} \propto 1/L$ , and the curves are given by Eq. (4.13). c) Characteristic self-diffusion times, where the curves are given by Eq. (4.19).

The interconversion time in the two phase region ( $T < T^*$ ), as shown in Fig. 4.17b, is well-described by Eq. (4.13), for which the constants were found to be  $T_0 = 0.36$ ,  $b_0 = 29.4$ , and  $a = 526.6$ . The characteristic interconversion time,  $\tau_{\text{INC}}$ , of a tetramer is shown in Fig. 4.17b. The characteristic self-diffusion time is given by

$$\tau_{\text{D}} = \frac{R_0^2}{D_{\text{eff}}^{\text{CM}}} \approx \frac{R_0^2}{(M\Delta T + L)/\hat{T}} \quad (4.19)$$

where  $D_{\text{eff}}^{\text{CM}}$  is the effective ( $k_d$ -dependent) self-diffusion coefficient. As a result, the characteristic time of self-diffusion (Fig. 4.17c) is found from,  $\tau_{\text{D}} = a_{\text{D}}/D_{\text{eff}}$ , where  $a_{\text{D}}$  is an amplitude coefficient of the order  $R_0^2$ , determined from the fit to be 0.94. Also, the characteristic temperature  $T_0$  was found to be somewhat different for the three different dihedral constants:  $T_0(k_d = 5) = 3.4$ ,  $T_0(k_d = 9.86) = 4.8$ , and  $T_0(k_d = 19.86) = 7.0$ . The self-diffusion time shown in Fig. 4.17c exhibits a crossover from the inverse mobility,  $\tau_{\text{D}} \propto \hat{T}/M\Delta T$  (at large  $k_d$ ), to the interconversion time,  $\tau_{\text{D}} \propto \hat{T}/L$  (at small  $k_d$ ).

#### 4.2.5 Finite-Size Restrictions in the CM Model

<sup>11</sup>As was also observed in the HL model, in the CM model the phase domain growth is restricted by the finite size of the system,  $\ell$ . For certain temperatures (at constant  $k_d$ ), the characteristic wavelength,  $q_-$ , reaches the characteristic wavelength of the simulation box,  $q^*$  (which is related to the size of the simulation box through  $R_{\text{max}} \sim \ell \sim 1/q^*$ ), hence phase separation is observed on the length scale of the computation box. This event is referred to as “complete” phase

---

<sup>11</sup>This subsection was reproduced from Betül Uralcan, Thomas J. Longo, Mikhail A. Anisimov, Frank H. Stillinger, and Pablo G. Debenedetti, *J. Chem. Phys.*, **155**, 204502 (2021); <https://doi.org/10.1063/5.0071988> and from Thomas J. Longo and Mikhail A. Anisimov, *J. Chem. Phys.*, **156**, 084502 (2022); <https://doi.org/10.1063/5.0081180>, with the permission of AIP Publishing.

separation,  $\ell \sim 1/q^*$ , since, computationally, it would appear as if two-phase separation was occurring. Since  $q_-$  is cut-off at  $q^*$ , the temperature corresponding to the cut-off ( $T^*$ ) characterizes the onset of the observed phase separation. This phenomenon is illustrated by Fig. 4.15, where (for  $k_d = 9.86$  and  $k_d = 19.86$ ) the computational data demonstrate that the steady-state domain size stops growing when the system reaches the size of the simulation box. Dashed curves are utilized to indicate the prediction for the unrestricted domain growth.

In this case, the line separating the apparent two phase region ( $R_\infty > 1/q^*$ ) and the microphase region ( $R_\infty \leq 1/q^*$ ) is found from the first root of the phase domain growth rate - see Fig. 3.6 and Eq. (4.17). The line interpreted as the onset of microphase separation (where  $R_\infty = 1/q^* \sim \ell$ ,  $T = T^*$ ) is determined as

$$\frac{1}{k_d^2} = \frac{2}{\hat{T}^*} \left( \frac{-\Delta\hat{T}^*}{T^*} \right)^2 \left[ 1 - \sqrt{1 - \frac{(q^*)^2}{(-\Delta\hat{T}^*)^2}} \right] \quad (4.20)$$

The onset temperature as a function of dihedral angle force constant,  $k_d$ , is depicted in Fig. 4.18a. The onset temperature is numerically calculated from Eq. (4.20). As depicted in Fig. 4.18a, the onset of arrested phase separation on the scale of the simulation box also depends on pressure. Physically, this originates from the density-dependent energetic bias towards homochiral interactions, represented phenomenologically by the introduction of  $\lambda > 0$  in the model. Thermodynamically, this pressure dependence of  $T^*$  can be attributed to the underlying pressure dependence of the critical temperature of the liquid-liquid transition in the thermodynamic limit ( $T_c$ ), at infinite  $k_d$ , due to the compressibility of the tetramer model. The values for the critical temperature for three different pressures are given in the caption of Fig. 4.18a.

Rescaling the onset temperature by  $T_c(P)$  gives the universal function of  $k_d$  depicted in

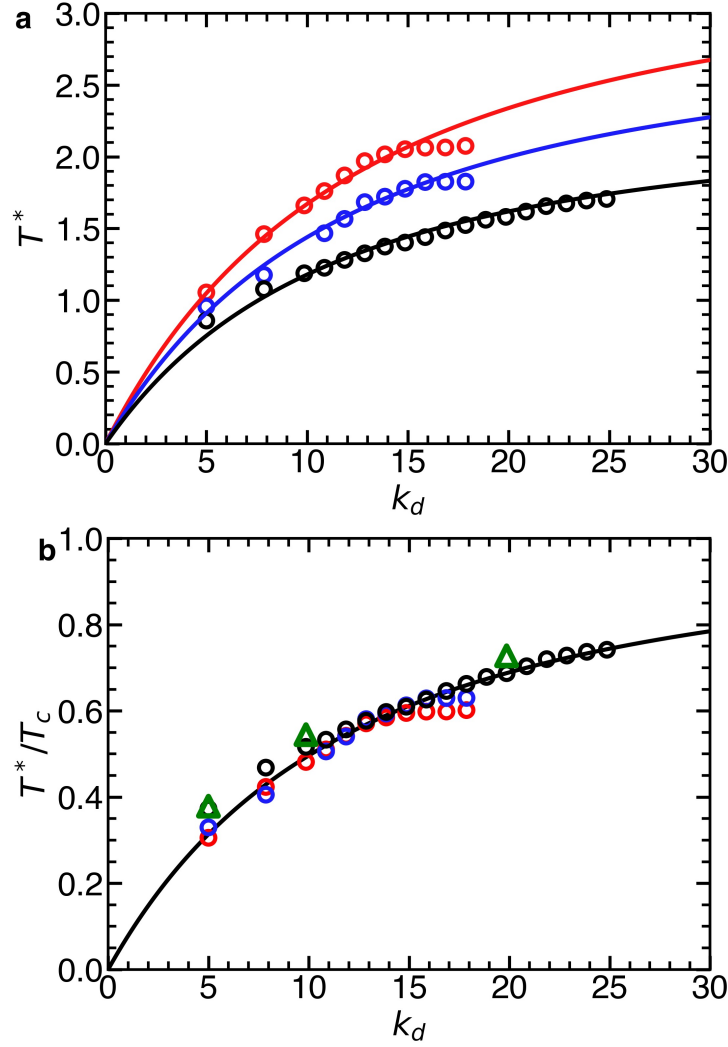


Figure 4.18: Dihedral force constant dependence of the onset temperature of phase separation on the length scale of the simulation box in the dissipative-force formulation CM model for  $P = 1.0$  (red circles),  $P = 0.5$  (blue circles), and  $P = 0.1$  (black circles). The curves are numerically calculated from the first solution of  $\tilde{\omega} = 0$ , given by Eq. (4.16), when  $q_- = q^* = 0.11 \approx 1/R_{\max} \sim 1/\ell$ ,  $T = T^*$ , and  $T_c(P = 1.0) = 3.45$ ,  $T_c(P = 0.5) = 2.91$ , and  $T_c(P = 0.1) = 2.3$  for different pressures (a) and in rescaled coordinates (b). The triangles, shown in (b), are obtained from the asymptotic limits of the time of liquid-liquid phase separation,  $\tau_{\text{LLPS}} \rightarrow \infty$ , as shown in Fig. 4.17a for  $q^* = 0.15$  and  $T_c = 2.35$ .

Fig. 4.18b. Also, in Fig. 4.18b, the predictions of  $T^*$ , obtained for three selected values of  $k_d$  through the asymptotic limits of  $\tau_{\text{LLPS}} \rightarrow \infty$  as illustrated in Fig. 4.17a, are illustrated. The predictions of  $T^*$  are just above the observed onset temperature because they correspond to slightly higher values of  $q^*$  and  $T_c$  (0.15 vs. 0.11 and 2.35 vs. 2.30 respectively). This difference can be

attributed to the uncertainty in obtaining the onset of phase separation on the scale of the simulation box. These values, however, are in good agreement with the computational  $T^*$  data obtained from the onset of phase separation.

As predicted from the growth rate factor, both the conservative and the dissipative force formulations will become identical in the limit of an infinitely rigid spring constant ( $k_d \rightarrow \infty$ ) or when the kinetic interconversion coefficient goes to zero ( $L \rightarrow 0$ ). This prediction is confirmed by extrapolating the critical temperatures shown in Fig. 4.18a to  $k_d \rightarrow \infty$  and comparing  $T_c(P)$  to the ones obtained from the conservative force formulation. Remarkably, this pressure dependence of the critical temperature for the conservative-force formulation of the CM model is fully consistent with the prediction obtained from the dissipative-force formulation as shown in Fig. 4.12. This is evidence for the consistency of the computational data of the CM model for these two alternative formulations.

In addition to the onset of microphase separation, another phenomenon takes place when the source of forced interconversion shifts the entire phase domain growth rate below zero. In this scenario, when the growth rate becomes negative for all wavenumbers, a homogeneous steady state exists, in which no phase domain growth will occur. The point at which the maximum of the growth rate crosses zero,  $\omega(q_m) = 0$ , is characterized through the termination temperature,  $T^{**}$ . At this point, the three characteristic wavenumbers merge into a single point,  $q_m = q_- = q_+ = q^{**}$ , see Fig. 3.6. For the dissipative CM model the termination probability is given in the first order approximation by

$$\frac{1}{k_d^2} = 2 \left( \frac{\Delta \hat{T}^{**}}{\hat{T}^{**}} \right)^2 \left[ \hat{T}^{**} + \frac{\Delta \hat{T}^{**}}{4} \right]^{-1} \quad (4.21)$$

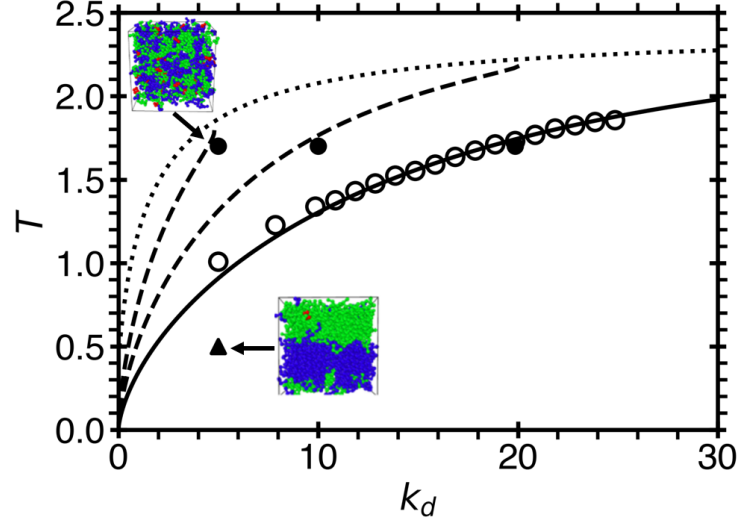


Figure 4.19: The conditions for microphase separation at a length scale,  $R_\infty = 1/q_-$ . The solid curve depicts the onset temperature of microphase separation,  $T = T^*$ , at the scale of the computational box, Eq. (4.20), for  $R_\infty = 1/q^* = 7.1$  and  $T_c = 2.4$ . The two dashed curves depict the lines of steady-state domain size that are smaller than the size of the computational box,  $R_\infty = 3.6$  (lower) and  $R_\infty = 2.0$  (upper), while the dotted curve depicts the growth-termination temperature,  $T = T^{**}$ , Eq. (4.21). The symbols are computational data (from the observed size of the phase domain) in the dissipative-force formulation of the CM model for pressure  $P = 0.1$ . The symbols indicate the onset of phase separation (open circles), the microphase region ( $R_\infty = 1/q^*$ , closed circles), and the two phase region ( $R_\infty > 1/q^*$ , triangle). The two simulation snapshots illustrate the behavior of the system composed of A-rich (green), B-rich (blue), and intermediate (red) states of the CM model. [7]

The termination line,  $T = T^{**}$  is indicated by the dotted line in Fig. 4.19. The growth-termination temperature is restricted by the correlation length such that the microphase domain is constrained between the size of the computational box and the correlation length of the order-parameter fluctuations. Figure 4.19 shows the termination line along with three lines of constant domain size (wavenumber).

### 4.3 Coarse-Grained Hard-Core-Shoulder Model (HCS Model)

<sup>12</sup>Unlike the previous examples, the HCS model, utilizes a tunable source of forced interconversion, implemented through the interactions with an external flux of energy carrying agents [8]. In biological systems, these agents can be thought of as ATP molecules, which change the conformation of a protein between two phase-segregating states. Alternatively, Each species in the HCS model represents a generic mixture of two chiral molecules (or any two chiral states), like the CM model (Section 4.2), simulated via a coarse-grained two-state approach, while the event-driven kinetics allow for an independent source of natural and forced interconversion, similar to that in the HL model (Section 4.1).

#### 4.3.1 HCS Model Description

A system initially consisting of an equal number of  $N_A = N_B = N/2 = 32,000$  identical hard spheres of type A and B with diameter  $\sigma$  are considered. While all particles repel each other as hard spheres with diameter  $\sigma$ , phase segregation is generated by the additional repulsion between A and B particles via a square shoulder potential at distance  $d = 1.3\sigma$ , with energy  $\epsilon_0$ . The interactions within the system are simulated via event-driven MD with discontinuous potentials [290, 291]. Additionally,  $N_{ag} = 10,000$  agents as an external source of energy are introduced, which collide with particles A and B at a distance  $b < \sigma$ . The agents contain an additional energy  $\epsilon$  (measured in units of  $\epsilon_0$ ), which upon collision with particles A or B boosts the probability of species interconversion ( $A \rightleftharpoons B$ ). Physically,  $\epsilon$  can be regarded as an external

---

<sup>12</sup>This section reproduced from Thomas J. Longo, Nikolay A. Shumovskyi, Betül Uralcan, Sergey V. Buldyrev, Mikhail A. Anisimov, and Pablo G. Debenedetti, *Proc. Natl. Acad. Sci.*, **120**, e2215012120 (2022), <https://doi.org/10.1073/pnas.2215012120>, with the permission of NAS Publications.

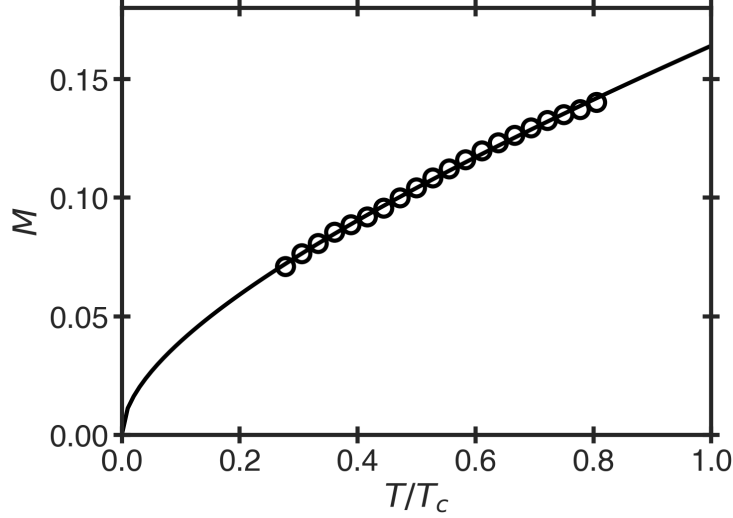


Figure 4.20: Self-diffusion (molecular mobility) of the HCS model. Simulations were conducted for a system with  $b = 0$  (no interconversion, either natural or forced). The open circles indicate simulation results, while the curve is the fit of  $M = 0.056\sqrt{T} + 0.015T$ .

energy carried by an ATP molecule or another active agent, which can compensate the effect of the heat of mixing arising from interconversion [8]. In simulations of the HCS model, this reaction occurs instantaneously, without any metastable intermediate state of either species.

The systems considered in this section are simulated in an  $\ell \times \ell \times \ell$  box of length  $\ell = 40\sigma$  with periodic boundaries at temperature  $T$ , measured in units of  $\epsilon_0/k_B$ . To regulate the temperature, a Berendsen thermostat is utilized [292]. The collision of the agents with species A or B occurs with conservation of linear and angular momentum of the pair as well as with total potential energy change,  $\Delta U$ . The total energy is composed of potential, kinetic, and external energy, in which the external energy is incorporated into the kinetic energy of the colliding particles. The equilibrium formulation occurs with conservation of energy, such that  $\epsilon = 0$ .

In the equilibrium formulation, the agents either contain no additional energy,  $\epsilon$ , or the cross-sectional area of their interaction with the species,  $b^2$ , is zero, such that the agents pass through species A or B without interacting. Physically, this corresponds to a scenario when the

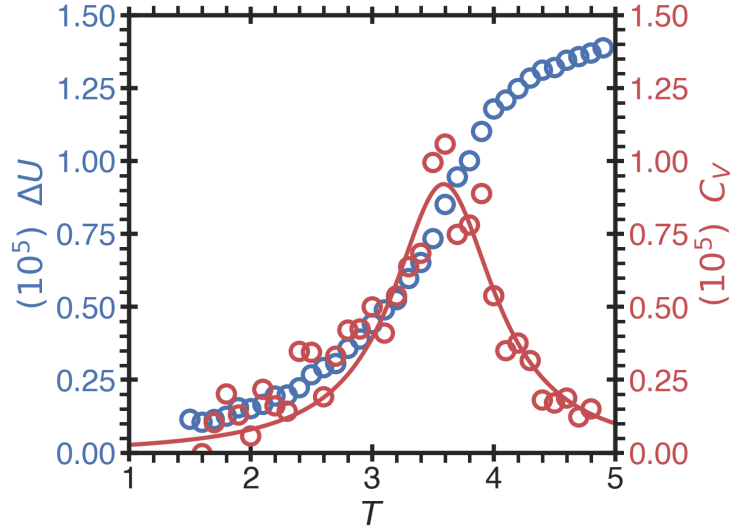


Figure 4.21: Critical temperature of the HCS model. Internal energy,  $\Delta U$ , of the HCS model as a function of temperature (blue) for the case  $b = 0$  (no interconversion, either natural or forced). The blue circles indicate the results of simulations, while the red circles correspond to the calculated isochoric heat capacity,  $C_V = \partial U / \partial T|_V$ . The solid red curve is an empirical fit of  $C_V$ , where the temperature corresponding to the maximum of  $C_V$  is the critical temperature for the HCS model,  $T_c = 3.6 \pm 0.05$ , in units of  $\epsilon_0 / k_B$ .

energy is unable to transfer from the agents to the species in the system. In the nonequilibrium formulation, the agents possess both the additional energy and cross-sectional area necessary to interact and convert species A to B and vice-versa. Without an external source of energy, an energetically costly interconversion reaction violates the conservation laws, so that the particles will recoil and interconversion will not happen. However, in the presence of an external source of energy, provided by the agents, the interconversion reaction may happen both in favorable or unfavorable conditions, just as in the HL model.

The particles (A, B, and the agents) have equal masses  $m$ , and the simulation time is measured in units of  $\sigma \sqrt{m / \epsilon_0}$ . For the HCS model, the system is modeled as a dense fluid of hard spheres with a molecular mobility found to be  $M = 0.056 \sqrt{T} + 0.015T$ , as shown in Fig. 4.20. In the kinetic theory of gases, the interconversion kinetic coefficient,  $L$ , is given by

$L \propto 4b^2 N_c \sqrt{\pi k_B T / m} / \ell^3 = \kappa b^2$ , where  $b$  is the interaction probability,  $N_c$  is the number of energy carriers in the system,  $m$  is the mass of each interacting species, and  $\ell$  is the size of the system. In the reduced form,  $\kappa = 4N_c \sqrt{\pi k_B T / m} / \ell^3$  is related to the particle interaction density and the mean-free-path per unit time (the characteristic velocity of motion), such that  $\kappa$  is proportional to  $M$ . The critical temperature for this model was determined from simulations in the limit of no interconversion ( $b = 0$ ) as  $T_c = 3.6 \pm 0.05$ . This value was found from the temperature corresponding to the maximum of the isochoric heat capacity as illustrated in Fig. 4.21.

### 4.3.2 Nonequilibrium Bicontinuous Microemulsions

In the HCS model, non-relativistic energy-carrying particles are introduced as a source of forced interconversion. They carry energy,  $\epsilon$ , and transfer this energy via molecular collisions with cross-sectional area  $b^2$ . When the additional particles carry no extra energy,  $\epsilon = 0$ , only natural interconversion, with a probability  $b$ , will occur. However, due to the external source of energy provided by the particles, forced interconversion will occur just like in the previously considered models (HL, Section 4.1, and CM, Section 4.2). Similar to those models, in the HCS model, the characteristic domain size decreases as a function of temperature and interconversion probability,  $b$ , as depicted in Fig. 4.22. In this case, when  $b = 0$ , then regardless of  $\epsilon$ , no interconversion will be possible. For conditions  $b < b^* \approx 0.02$  at  $T < T^* = 0.22T_c$  and  $\epsilon < \epsilon^* = 10$ , corresponding to the onset of microphase separation, the system enters a transient state with an interface, similar to the CM model, as illustrated by the simulation snapshots in Fig. 4.22b.

It is noted that below the onset of microphase separation, the characteristic steady-state domain size is comparable to the size of the simulation box,  $\ell \sim 1/q^*$ . Consequently, the on-

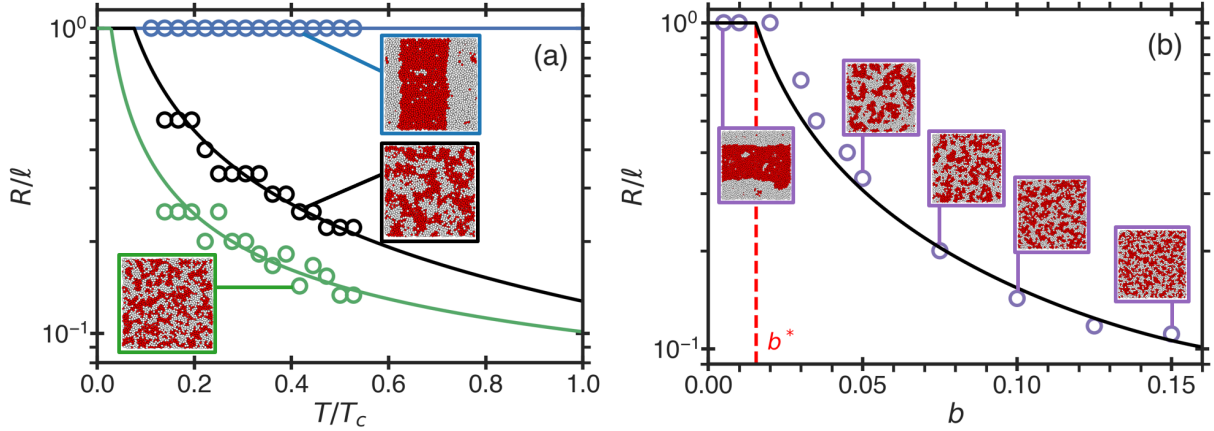


Figure 4.22: Steady-state domain size,  $R$ , normalized by the size of the system,  $l$ , in the HCS model. (a) The temperature-dependence of the normalized steady-state domain size for  $b = 0.005$  (blue),  $b = 0.050$  (black), and  $b = 0.075$  (green) at  $\epsilon = 10$ . (b) The normalized steady-state domain size as a function of interconversion probability,  $b$ , for the energy source  $\epsilon = 12$  and  $T/T_c = 0.22$ . The vertical dashed line indicates the onset interconversion probability,  $b^*$ . In (a) and (b), the open circles correspond to simulation of 64,000 particles, the curves correspond to the theoretical predictions, and the images show snapshots of the system simulated at the indicated conditions.

set conditions for all models depends on the system size. In addition, for small system sizes phase amplification occurs faster than for large systems, such that instead of entering a transient state below the onset, the system may undergo phase amplification. As observed in the HCS model, for large system sizes, in the microphase separation region, one could observe more regular structures, like the nonequilibrium spatially-modulated stripes observed in the HL model (Section 4.1.3). The snapshots, presented in Fig. 4.22 demonstrate that the off-lattice MD simulations produce nonequilibrium bicontinuous “microemulsion” structures.

The steady-state domain size is determined as the inverse of the wavenumber corresponding to the maximum of the time-dependent structure factor  $S(q, t)$  in the limit  $t \rightarrow \infty$ . The theoretical prediction for the system with  $b = 0.05$  depicted in Fig. 4.22(a) is determined from  $q_-$  with amplitude,  $A = 145$ , and mobility amplitude,  $M_0 = 0.005$ , while the prediction for the system with  $b = 0.075$  is determined from amplitude,  $A = 394$ , and mobility amplitude,  $M_0 = 0.001$ .

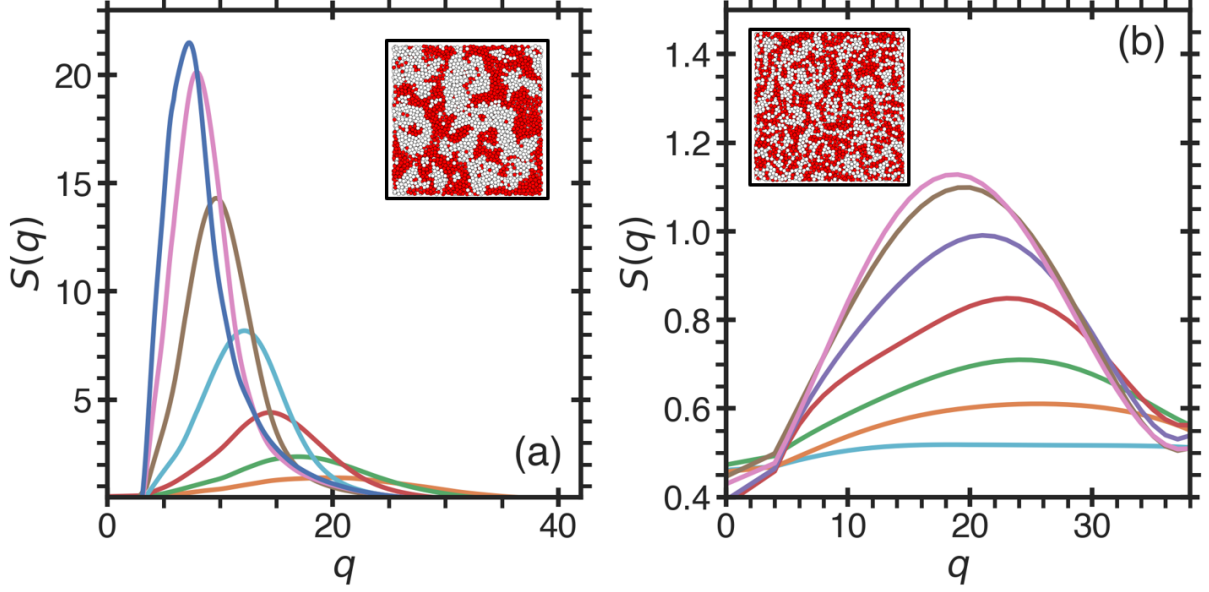


Figure 4.23: Structure factor,  $S(q, t)$ , in the HCS model. The formation of a steady-state bicontinuous microemulsions observed in MD simulations of the HCS model for 64,000 particles at interconversion energy source  $\epsilon = 12$ ,  $T/T_c = 0.1$ , and interconversion probability  $b = 0.05$  (a) and  $b = 0.15$  (b). The images show snapshots of the steady-state system simulated at the specified conditions.

The theoretical prediction for the system depicted in Fig. 4.22(b) is given by Eq. (3.17), with  $A = 88$  and  $M_0 = 0.09$ . An example of the steady-state structure factor for two different interaction cross-sections is illustrated in Figs. 4.23(a,b). Additional simulation results depicting the domain size as a function of temperature for the HCS model for different forced interconversion source strengths,  $\epsilon$ , and molecular interaction cross-sections,  $b^2$ , are shown in Figs. 4.24(a,b). It should be noted that for extremely low temperatures,  $T/T_c \leq 0.08$ , the simulated systems freeze, such that the characteristic domain size is always smaller than the predicted steady-state size. The metastable freezing is not captured by the theoretical approach. Due to this freezing effect, no phase amplification or metastable two-phase separation was observed in the HCS model at low temperatures.

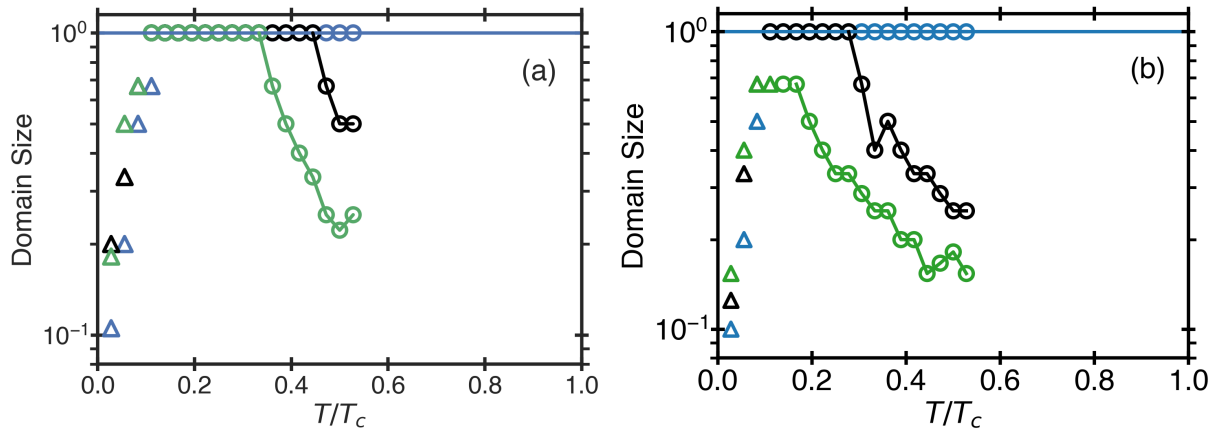


Figure 4.24: Domain size as a function of temperature for the HCS model. (a)  $\epsilon = 6$  and (b)  $\epsilon = 8$ , for system size  $\ell = 40\sigma$ , averaged over  $N = 10$  realizations, for interconversion probabilities,  $b = 0.005$  (blue),  $b = 0.05$  (black), and  $b = 0.075$  (green). It should be noted that for low temperatures,  $T/T_c \leq 0.8$ , the simulated systems freeze, such that the characteristic domain size is always less than the predicted size (as indicated by the triangles).

## 4.4 Sources of Microphase Separation

In this section<sup>13</sup>, the ubiquitous nature of the nonequilibrium behavior in interconverting binary systems are considered through comparisons of the simulated models. Also, the limiting conditions for the observation of microphase separation are discussed. It is shown that under certain constrains all three of the considered models, as well as the model of Glotzer *et al.* [207, 213, 216, 217, 235, 256, 257], would exhibit the same behavior.

### 4.4.1 Comparison of the Microscopic Models

As indicated by Eq. (3.7), there are three kinetic coefficients,  $L$ ,  $M$ , and  $K$ , whose interplay determines whether microphase separation may occur. In the HL model, the kinetic coefficients,  $L$  and  $M$  (considered to be independent of temperature and pressure), determine the probability

<sup>13</sup>This section was reproduced from Thomas J. Longo, Nikolay A. Shumovskyi, Betül Uralcan, Sergey V. Buldyrev, Mikhail A. Anisimov, and Pablo G. Debenedetti, *Proc. Natl. Acad. Sci.*, **120**, e2215012120 (2022), <https://doi.org/10.1073/pnas.2215012120>, with the permission of NAS Publications.

of natural interconversion,  $p_r$ , through  $p_r = L/(Mq^2 + L)$  [4, 6]. Thus,  $M = 0$  corresponds to fast interconversion ( $p_r = 1$ ), while  $L = 0$  corresponds to no natural interconversion ( $p_r = 0$ ). In this model, for small  $p_r$ , the source of forced interconversion is approximated as being uncoupled from natural interconversion and related it to the kinetic coefficient  $K$  as  $K \propto E^2$ , where the prefactor depends on temperature only (Section 4.1.3.2). In the limit when  $E \rightarrow E_{\max} = 12$ , the HL model becomes equivalent to the model of Glotzer *et al.* [207, 213, 216, 217, 235, 256, 257], in which there is no natural interconversion ( $p_r = 0$ ).

In the CM model, the source of forced interconversion is coupled to the natural interconversion rate through the dihedral force constant,  $k_d$ . The behavior of the system with different dihedral-force constants may be related to the behavior of the HL model system for different interconversion probabilities,  $p_r$ , by considering an interpolation between two limits as  $k_d = \sqrt{(1/p_r) - 1}$ , such that  $k_d \rightarrow 0$  ( $p_r = 1$ ) corresponds to fast natural and forced interconversion, while  $k_d \rightarrow \infty$  ( $p_r = 0$ ) corresponds to no interconversion [4]. This specific feature of the CM model, that the natural and forced interconversions are controlled by a single parameter  $k_d$ , means that without interconversion (only in the limit  $k_d \rightarrow \infty$ ), the CM system is in equilibrium and exhibits regular phase separation. This effect is utilized in the theoretical model, Eq. (3.7), when both the natural and forced interconversions are controlled by the same kinetic coefficient, such that  $L = K$ , where the dissipative intramolecular forces may be expressed, in the interconversion dynamics, through the difference between the balanced and imbalanced chemical potentials,  $\Delta\hat{\mu}$ , given by Eq. (2.10). The mobility,  $M$  is described by the Stokes-Einstein relation, while the interconversion kinetic coefficient,  $L$ , has been found to be proportional to  $M$ , such that  $L = MT^2/k_d^2$ , see Eq. (4.13).

Just like the behavior of the HL model, the source of forced interconversion in the HCS

model depends on the relation between  $L$  and  $K$ , and, in the first-order approximation, they may be assumed to be uncoupled from each other. Consequently, the behavior of the nonequilibrium HCS model may be described via a similar dynamic equation as used to describe the behavior of the HL model. However, in the nonequilibrium HCS model, while the natural interconversion rate is determined by the interaction cross-section of the molecules and energy-carrying agents,  $L \propto b^2$ , the effect of forced interconversion varies with the strength of the energy source,  $\epsilon$ . This effect is introduced into the difference between the balanced and imbalanced chemical potentials, Eq. (2.10), as a tunable parameter, such that when  $\epsilon \rightarrow 0$  the nonequilibrium chemical potential  $\tilde{\mu} \rightarrow 0$  and the system evolves according to equilibrium conditions. However, in the limiting case, when  $K$  and  $L$  are of equal magnitude, such that the enthalpic contribution to the chemical potential is completely compensated, see Eqs. (4.15) and (4.15), then the HCS model will be dynamically equivalent to the CM model.

For all of the models considered, in the first-order approximation, the domain size ( $R$ ) scales with interconversion probability as  $R \propto 1/\sqrt{p_r} \propto k_d \propto 1/b$ . The steady-state domain size also depends on the temperature. In the CM and HCS models, this temperature dependence originates from  $M$  and  $L$ , while in the HL model, this temperature dependence originates from the relationship between  $K$  and  $E$ . As shown by the solid curves on Figs. 4.7, 4.14, and 4.22, a quantitative comparison between the simulation results and the theory is obtained.

#### 4.4.2 Onset and Termination of Microphase Separation

As observed in the simulations of all three microscopic models, there are three regions in which different phenomena may be observed. They may be identified by the interplay between

diffusion, natural interconversion, and forced interconnection, which are described by the kinetic coefficients  $M$ ,  $L$ , and  $K$  in Eq. (3.7). When natural interconversion,  $L$ , is faster than the diffusion or the forced interconversion rate, then phase amplification is observed. For instance, in the HL model this occurs where  $T < T^*$  and  $E < E^*$ . When the diffusion rate,  $D \propto Mq^2$ , is faster than the natural and the forced interconversion rates, then transient (“apparent”) two-phase separation on the scale of the simulation box is observed. For instance, in the CM and HCS models, this is observed where  $T < T^*$  and  $1/k_d < 1/k_d^*$  (CM) or  $b < b^*$  (HCS). The curve that separates phase amplification or transient two-phase region from the microphase separation region is referred to as the onset. This curve may be found from Eq. (3.7), considered for the particular case, when the characteristic size of the phase domains, determined from the maximum of the growth rate equation, becomes equal to the size of the simulation box,  $q \sim 1/\ell$ .

Alternatively, when forced interconversion,  $K$ , is faster than diffusion and natural interconversion, then the alternative species will interconvert so fast that no dissipative structures may form and only a homogeneous steady state with statistically equal molecular fractions of the interconverting species will remain. In this case, the characteristic size of the domains is of the order of the molecular length scale,  $R_0 \sim \sqrt{\kappa}$ . The temperature and energy at which this occurs is defined as the “termination” of microphase separation ( $T^{**}$  and  $E^{**}$ ). For instance in the HL and HCS models, this occurs when  $E > E^{**}$  ( $\epsilon > \epsilon^{**}$ ) or  $T > T^{**}$ , while in the CM model, since the natural and forced interconversion are coupled, this region occurs when  $1/k_d > 1/k_d^{**}$  or  $T > T^{**}$ . This effect is shown in Fig. 4.25a where the characteristic size for  $E > 7$  is  $R_0$  for all temperatures. An increase in  $R_0$  with temperature could be attributed to the growing correlation length of order-parameter fluctuations upon the approach to the critical temperature. The curve that separates the microphase region from the homogeneous steady-state region is referred

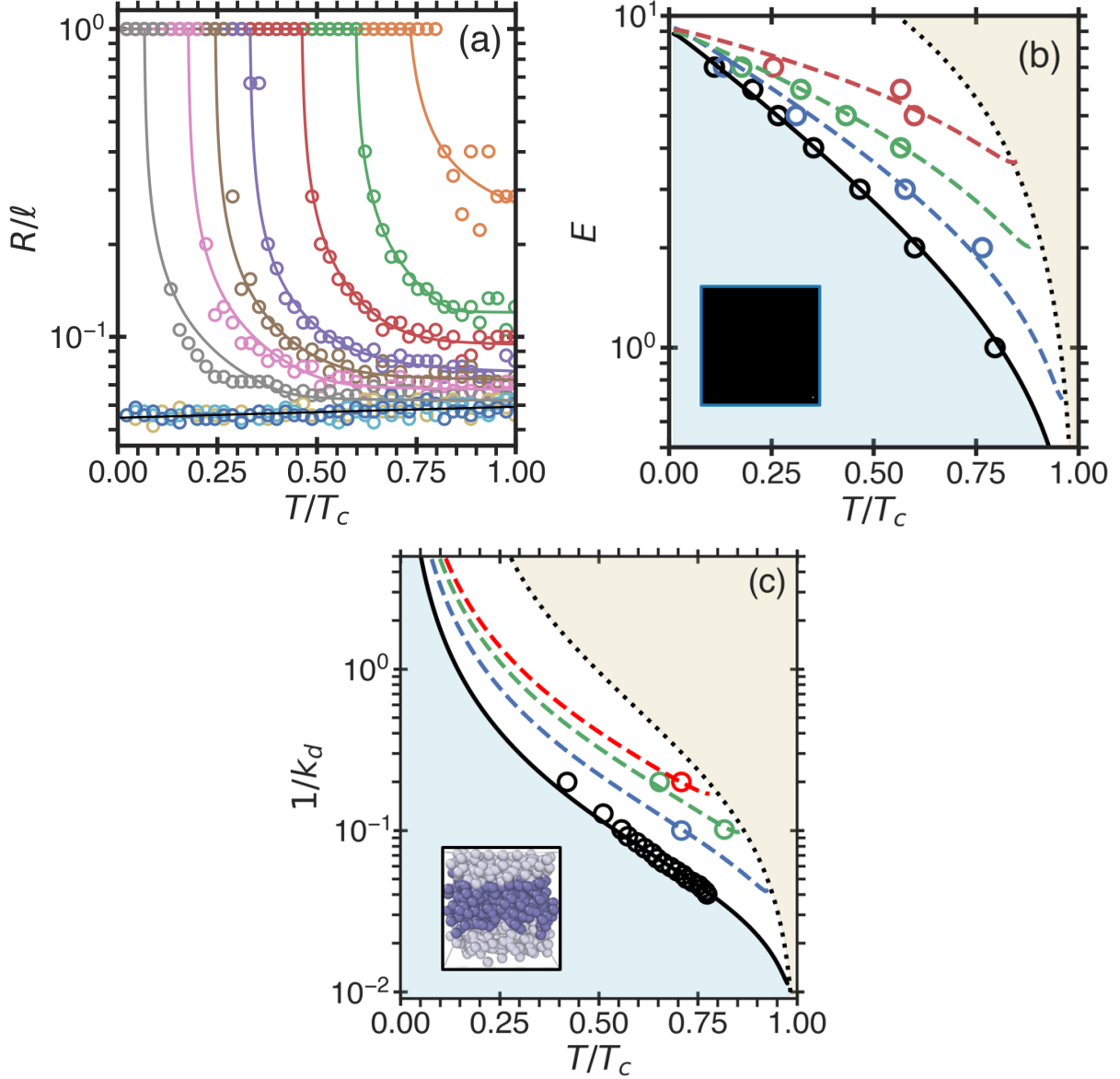


Figure 4.25: The onset and termination of microphase separation. (a) The steady-state domain size in the HL model for  $p_r = 1/128$  and different forced interconversion energies from  $E = 1$  (orange) to  $E = 10$  (dark blue) in steps of  $\Delta E = 1$ , just as in Fig. 4.8 (Fit parameters provided in Table 4.4). For  $E > E^{**} = 7$  (the termination energy), the data collapse into a single line (black), indicating that the characteristic steady-state domain size remains on the order of the microscopic length scale  $R_0(T)$ , which corresponds to homogeneous steady-state systems for all temperatures. For  $E \leq 7$ , the onset of microphase separation is observed at  $T = T^*(E^*)$ , where  $E^*$  is the onset energy. For  $T < T^*$ , the steady-state domain size is equal to the size of the system,  $R = \ell$ . (Caption continues on the next page.)

Figure 4.25: (b) The onset energy  $E^*$  (black circles and curve) for the HL model as a function of temperature for  $p_r = 1/128$ . Colored open circles and dashed curves correspond to steady-state domain sizes:  $R = 0.143$  (blue),  $R = 0.095$  (green), and  $R = 0.074$  (red). (c) The inverse onset rigidity parameter  $1/k_d^*$  (black circles and curve) for the CM model at  $P = 0.1$ . Colored circles and dashed curves correspond to steady-state domain sizes:  $R = 0.32$  (blue),  $R = 0.22$  (green), and  $R = 0.18$  (red). In (b) and (c), the blue area corresponds to phase separation on the scale of the simulation box, the white area corresponds to microphase separation, and the yellow area corresponds to homogeneous steady states. The images in (b) and (c) correspond to the different final states of the systems below  $E^*(T^*)$  and  $1/k_d^*(T^*)$  where the size of the phase domain is on the scale of the simulation box ( $q^* \sim 1/\ell$ ). In (b), phase amplification is observed since for  $p_r = 1/128$  natural interconversion is relatively fast, while in (c), where natural interconversion is relatively slow for the simulated range of  $k_d$ , complete two-phase separation, on the scale of the simulation box, is found.

Table 4.4: Fit parameters used for the theoretical prediction illustrated in Fig. 4.25a for the HL model, with  $p_r = 1/128$ .

$E$	Amp	$M$	$L$
1	11.7	0.268	0.79
2	16.0	0.374	1.10
3	19.4	0.332	1.23
4	23.4	0.294	1.32
5	23.1	0.230	1.47
6	23.5	0.300	1.61
7	25.1	0.282	1.66

to as the termination curve, and may be found in the present theory, when the maximum of the characteristic growth rate with respect to  $q$  reaches zero.

The region of the phase diagram where microphase separation occurs (between the onset and the termination lines) is where diffusion, natural interconversion, and forced interconversion are balanced, such that where steady-state dissipative structures are observed. The characteristic length scale of the microphase region is predominantly given by the interplay between diffusion and forced interconversion. The comparison between these three regions in the HL and CM models is illustrated in Figs. 4.25(b and c). As shown, the onset and termination curves behave similarly between these regions.

It has been shown that under certain limits all of the simulated models would exhibit identical dynamic behavior. These limits are summarized as: 1) The limit of complete phase separation occurs when  $p_r \rightarrow 0$  and  $E \rightarrow 0$  (HL),  $k_d \rightarrow \infty$  (CM), and  $b \rightarrow 0$  and  $\epsilon \rightarrow 0$  (HCS). 2) Microphase separation in the absence of natural interconversion occurs in the HL and HCS models when  $E \leq E_{\max}$  and  $\epsilon \leq \epsilon_{\max}$  at constant  $p_r$  or  $b$  and  $T$ . In the limit when  $p_r$  and  $b$  are small, while  $E \geq E_{\max}$  and  $\epsilon \geq \epsilon_{\max}$ , the dynamic behavior of the HL and HCS models becomes equivalent to the model of Glotzer *et al.* [207, 213, 216, 217, 235, 256, 257]. 3) The dynamic behavior of the CM model (imbalance of interaction forces) is a limiting case of the behavior of the HL and HCS models (external source of energy-carrying particles). 4) Limit of a homogeneous steady state occurs in all the models for  $T > T^{**}$ , when  $E > E^{**}$  (HL),  $k_d \rightarrow 0$  (CM), and  $\epsilon > \epsilon^{**}$  (HCS).

#### 4.5 Conclusion of Chapter 4

In summary, depending on the rate of interconversion and distance to the critical temperature, there are three possible scenarios that are observed in the behavior of the three microscopic models of mixtures that exhibit phase separation in the presence of both the natural and forced interconversions of species: (1) phase amplification or transient two-phase separation on the scale of the simulation box, (2) microphase separation, and (3) homogeneous steady state. Unlike the modulated phases and bicontinuous microemulsion structures observed in equilibrium conditions or the patterns formed in “frozen” spinodal decomposition states [9, 103–107], the steady-state dissipative structures investigated here are the result of the continuous energy supply to the system. The three physically different microscopic models considered here, as well as the nonequilibrium model of Glotzer *et al.* [207, 213, 216, 217, 235, 256, 257], demonstrate identical behavior

under appropriate limits. This behavior is quantitatively unified by the generalized Cahn-Hilliard theory presented in Chapter 3.

## Chapter 5: Overall Conclusion

In this thesis, it has been demonstrated that there are two major effects of molecular interconversion on the thermodynamics and kinetics of phase transitions: if the system relaxes to equilibrium, then the growth of one of the alternative phases may result in the destruction of phase coexistence. This phenomenon is referred to as phase amplification. In contrast, if the system evolves to a nonequilibrium state, the phase domain growth could be restricted at a mesoscopic length scale. This phenomenon is referred to as microphase separation. A nonequilibrium-thermodynamic approach has been developed, the generalized Cahn-Hilliard theory and the generalized Cook-Binder theory, to quantitatively describe the interplay between the dynamics of interconversion and phase separation. The theory has been verified with the results of simulations of several microscopic models of interconverting systems.

There is a variety of applications and broader impacts for the developed approach. As discussed in Chapter 2, molecular or supramolecular interconversion may be a generic cause of fluid polyamorphism. The possibility of phase amplification occurring in both simulations and experiments has rarely been discussed in the literature, while this phenomenon may explain the conflicting reports on the existence or non-existence of a fluid-fluid phase separation in polyamorphic substances (such as supercooled water [9, 13, 55, 56, 72–80] and high-pressure hydrogen [21, 34–45, 48, 59, 119–123]). In addition, one may hypothesize that phase amplification

could have been the trigger for the biological evolution into the current existence of the unique chirality in all living organisms [97, 112, 266, 293–295, 295, 296, 296, 297, 297–310].

Nonequilibrium microphase separation could exist in a wide class of systems, including “active matter systems,” a recent focus of theoretical and experimental studies [311, 312], as well as biomolecular condensates (*e.g.* membraneless organelles), where natural interconversion could be caused by mechanisms like polymerization, protein folding-unfolding, and self-assembly, while forced interconversion could be generated by the nonequilibrium environment [220, 221, 312–320]. The developed approach could be applicable to understanding and quantitatively describing these phenomena. In addition, microphase separation could also exist in other supramolecular structures, *e.g.* polymer solutions in the presence of photochemical reactions [110, 321]. The developed approach can be linked to other dissipative phenomena, like hydrodynamic instabilities and bifurcations in chemical reactions [322].

## Appendix A: Comparison of Exact Solution with Phenomenological Ansatzes

In this appendix<sup>1</sup>, a variety of different ansatzes are considered that would minimize the interfacial tension, Eqs. (2.54) to (2.61), in Sec. 2.4.3.1. It is found that there were no single free-parameter ansatzes that were able to minimize the interfacial tension with sufficient accuracy, while several ansatzes with three free parameters were sufficient. In Sec. 2.4.3, the Fisher-Wortis ansatz is considered, which has two free parameters (the shift,  $\hat{\delta}$ , and the interfacial thickness,  $\hat{\zeta}$ ). In this appendix, the two-parameter Fisher-Wortis ansatz is compared to an alternative symmetric three-parameter ansatz and the exact solution of the interfacial tension equilibrium condition, Eq. (2.53).

The symmetric three-parameter ansatz is given in normalized form by

$$\hat{\rho}_{\text{sym}}(\hat{z}) = \frac{\rho(\hat{z}) - \rho_V}{\rho_L - \rho_V} = \frac{1}{2} \left[ \tanh \left( \frac{\hat{z}}{\hat{\zeta}_\rho} \right) - 1 \right] \quad (\text{A.1})$$

$$\hat{x}_{\text{sym}}(\hat{z}) = \frac{x(\hat{z}) - x_V}{x_L - x_V} = \frac{1}{2} \left[ \tanh \left( \frac{\hat{z} + \hat{\delta}}{\hat{\zeta}_x} \right) - 1 \right] \quad (\text{A.2})$$

in which the three parameters are the shift between the concentration and density profiles,  $\hat{\delta}$ , and the interfacial thicknesses of the density,  $\hat{\zeta}_\rho$ , and concentration,  $\hat{\zeta}_x$  profiles. A comparison of the liquid-vapor interfacial tension between the Fisher-Wortis (FW) and the symmetric ansatzes

---

<sup>1</sup>This appendix was reproduced from Thomas J. Longo, Sergey V. Buldyrev, Mikhail A. Anisimov, and Frédéric Caupin, *J. Phys. Chem. B*, **127**, 3079 (2023); <https://doi.org/10.1021/acs.jpcc.2c08901>, with the permission of ACS Publications.

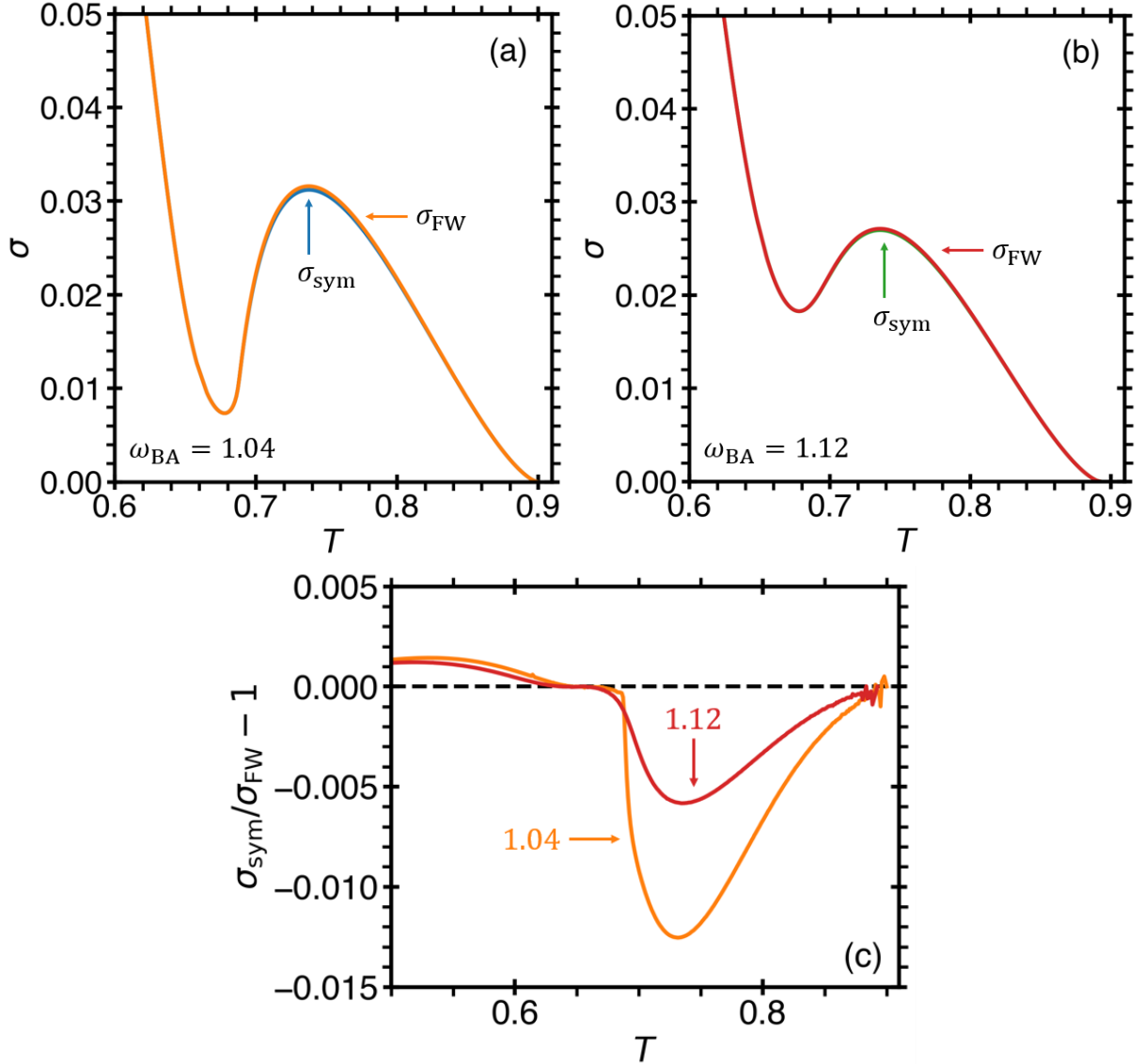


Figure A.1: Comparison between the Fisher-Wortis (FW) and an alternative symmetric ansatz (sym). obtained for the liquid-vapor coexistence, for two systems with  $\varepsilon_{BA} = 1.04$  (a) and  $\varepsilon_{BA} = 1.12$  (b) with  $\varepsilon_{AA} = 1.6$ ,  $\varepsilon_{BB} = 2.0$ ,  $\hat{e} = 3$ , and  $\hat{s} = 4$ . (c) The relative deviation between the symmetric and FW ansatzes.

of Eqs. (A.1) and (A.2) is presented in Fig. A.1. It is found that the FW ansatz describes the LV interfacial tension with sufficient accuracy everywhere except near the maximum of  $\sigma_{LV}$ . However, in this region, the symmetric ansatz differs from the FW ansatz by  $\simeq 1\%$  or less. Therefore, it was deemed that the FW ansatz is the most sufficient way to describe the interfacial properties, since it has only two free parameters.

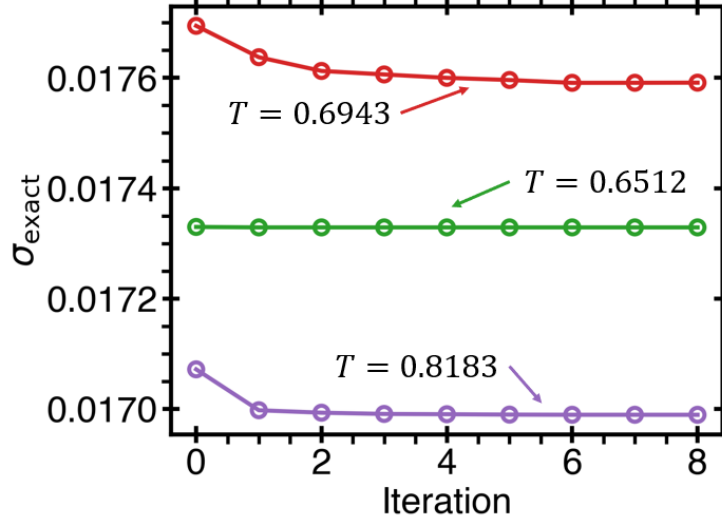


Figure A.2: Numerical calculations of the liquid-vapor surface tension for three temperatures in the system with  $\varepsilon_{\text{BA}} = 1.04$ ,  $\varepsilon_{\text{AA}} = 1.60$ ,  $\varepsilon_{\text{BB}} = 2.00$ ,  $\hat{e} = 3$ , and  $\hat{s} = 4$ . The FW ansatz is given at iteration 0. The temperatures were chosen based on surface tensions with similar values, as predicted by the FW ansatz.

In addition to the ansatz method, the interfacial properties were also calculated numerically by solving the interfacial tension equilibrium condition. It was found that the Euler-Lagrange derivatives, Eqs. (2.51) and (2.52), were highly unstable, as one would need to know both a coordinate position of both the density and concentration profiles as well as their derivative at this position. Thus, to solve these two equations for the density and concentration profiles, would require the adjustment of four unknown variables. Instead, Eq. (2.53) was numerically solved using the integral of Eqs. (2.51) and (2.52), which requires two functions,  $\rho(z)$  and  $x(z)$ , and two coordinate positions. Using one of the ansatzes for one of the unknown functions, one alternates between solving Eq. (2.53) for  $\rho(z)$  and  $x(z)$  in an iterative process to determine the exact solution. Figure A.2 illustrates the iterative solution method for three temperatures in the system with  $\varepsilon_{\text{BA}} = 1.04$ . The solutions for the profiles using the iterative method are presented in comparison to the FW ansatz in Fig. A.3. It is noted the asymmetric shape of the exact solution also serves to justify our choice of the FW ansatz, which more closely matches the shape of the

Table A.1: The degree of asymmetry for each profile of the system with  $\varepsilon_{\text{BA}} = 1.04$  at  $T = 0.6943$ , determined from the symmetric ansatz (sym), the Fisher-Wortis ansatz (FW), or the exact solution as calculated from Eq. (A.3).

Ansatz	$\rho$ -Profile	$x$ -Profile
Sym	0	0
FW	0.016	0.103
Exact	0.104	-0.060

exact solution for the profiles than the symmetric ansatz. To discuss the amount of asymmetry in each profile, let  $\phi(z)$  represent either the density or concentration profiles, and  $z_{1/2}$  be the  $z$ -value where  $\phi(z)$  reaches its midpoint,  $\phi(z) = [\phi(+\infty) + \phi(-\infty)]/2$ . The degree of asymmetry  $D_{\text{Asym}}$  is defined via

$$D_{\text{Asym}} = D_0 \sqrt{\frac{\int_0^{+\infty} \{ [\phi(+\infty) - \phi(z_{1/2} + z')] + [\phi(-\infty) - \phi(z_{1/2} - z')] \}^2 dz'}{\int_0^{+\infty} \{ [\phi(+\infty) - \phi(z_{1/2} + z')]^2 + [\phi(-\infty) - \phi(z_{1/2} - z')]^2 \} dz'}} \quad (\text{A.3})$$

where the prefactor,  $D_0$ , may be  $-1$  or  $1$ , as given by

$$D_0 = \text{Sign} \left[ \int_0^{+\infty} [\phi(+\infty) - \phi(z_{1/2} + z')] + [\phi(-\infty) - \phi(z_{1/2} - z')] dz' \right] \quad (\text{A.4})$$

$D_{\text{Asym}} = 0$ , if and only if the profile is symmetric; otherwise,  $D_{\text{Asym}}$  adopts values from  $-1$  to  $1$  depending on whether the profile spreads more towards the low or high values of  $\phi$ , respectively. A summary of the asymmetry for the system with  $\varepsilon_{\text{BA}} = 1.04$  at  $T = 0.6943$  is provided in Table A.1 below. Thus, it was found that the exact solution is indeed asymmetric. Ultimately, since the exact solution differs from the FW ansatz by a fraction of a percent (see Fig. A.2), it was determined that the FW ansatz was the most efficient way to describe the interfacial properties with sufficient accuracy.

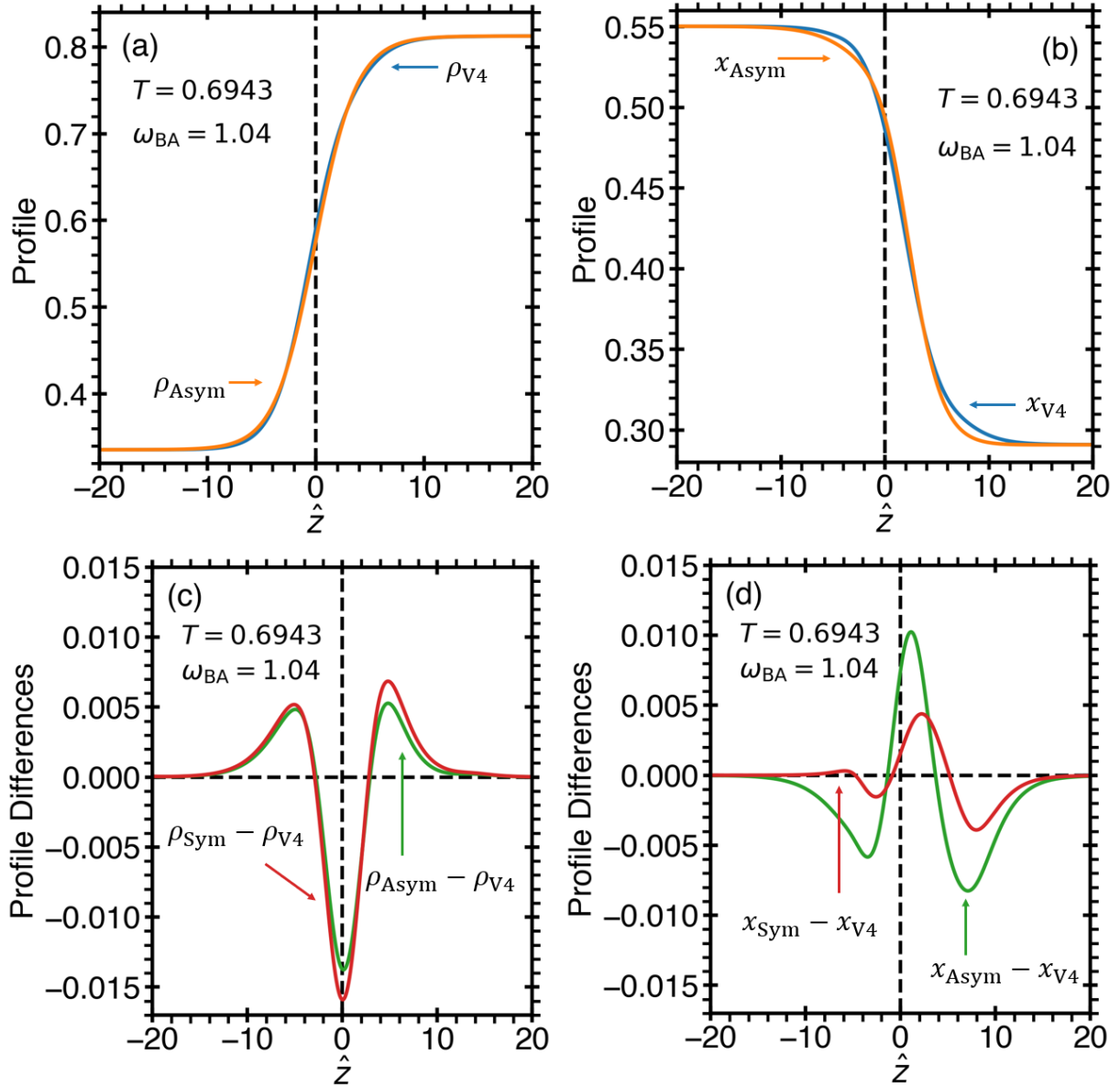


Figure A.3: Comparison of the liquid-vapor density (a) and concentration (b) interfacial profiles, as obtained from numerical calculations after eight iterations,  $\rho_{V4}$  and  $x_{V4}$ , and for the FW ansatz,  $\rho_{V0}$  and  $x_{V0}$ , for the system with  $\varepsilon_{BA} = 1.04$ ,  $\varepsilon_{AA} = 1.60$ ,  $\varepsilon_{BB} = 2.00$ ,  $\hat{e} = 3$ , and  $\hat{s} = 4$  at temperature,  $T = 0.6943$  (red curve in Fig. A.2). (c,d) The difference between the exact solution for the density and concentration profiles and the FW and symmetric ansatzes. In (a-d), the different profiles were aligned along their Gibbs dividing surface, such that the excess density is zero for all profiles.

## Bibliography

- [1] Nathaniel R. Fried, Thomas J. Longo, and Mikhail A. Anisimov. Thermodynamic modeling of fluid polyamorphism in hydrogen at extreme conditions. *J. Chem. Phys.*, 157:101101, 2022.
- [2] Nikolay A. Shumovskyi, Thomas J. Longo, Sergey V. Buldyrev, and Mikhail A. Anisimov. Modeling fluid polyamorphism through a maximum-valence approach. *Phys. Rev. E*, 106:015305, 2022.
- [3] Thomas J. Longo, Sergey V. Buldyrev, Mikhail A. Anisimov, and Frédéric Caupin. Interfacial properties of fluids exhibiting liquid polyamorphism and water-like anomalies. *J. Phys. Chem. B*, 127:3079-3090, 2023.
- [4] Thomas J. Longo and Mikhail A. Anisimov. Phase transitions affected by natural and forceful molecular interconversion. *J. Chem. Phys.*, 156:084502, 2022.
- [5] Thomas J. Longo, Nikolay A. Shumovskyi, Salim M. Asadov, Sergey V. Buldyrev, and Mikhail A. Anisimov. Structure factor of a phase separating binary mixture with natural and forceful interconversion of species. *J. Non-Cryst. Solids: X*, 13:100082, 2022.
- [6] Nikolay A. Shumovskyi, Thomas J. Longo, Sergey V. Buldyrev, and Mikhail A. Anisimov. Phase amplification in spinodal decomposition of immiscible fluids with interconversion of species. *Phys. Rev. E*, 103:L060101, 2021.
- [7] Betül Uralcan, Thomas J. Longo, Mikhail A. Anisimov, Frank H. Stillinger, and Pablo G. Debenedetti. Interconversion-controlled liquid-liquid phase separation in a molecular chiral model. *J. Chem. Phys.*, 155:204502, 2021.
- [8] Thomas J. Longo, Nikolay A. Shumovskyi, Betül Uralcan, Sergey V. Buldyrev, Mikhail A. Anisimov, and Pablo G. Debenedetti. Formation of dissipative structures in microscopic models of mixtures with species interconversion. *Proc. Natl. Acad. Sci.*, 120(1):e2215012120, 2023.
- [9] Mikhail A. Anisimov, Michal Duška, Frédéric Caupin, Lauren E. Amrhein, Amanda Rosenbaum, and Richard J. Sadus. Thermodynamics of fluid polyamorphism. *Phys. Rev. X*, 8:011004, 2018.
- [10] F. Caupin and M. A. Anisimov. Minimal microscopic model for liquid polyamorphism and waterlike anomalies. *Phys. Rev. Lett.*, 127:185701, 2021.

- [11] Osamu Mishima. *Liquid-Phase Transition in Water*. NIMS Monographs. Springer, Tokyo, Japan, 2021.
- [12] Pablo G. Debenedetti. *Metastable Liquids: Concepts and Principles*. Princeton University Press, Princeton, New Jersey, 1996.
- [13] Frédéric Caupin and Mikhail A. Anisimov. Thermodynamics of supercooled and stretched water: Unifying two-structure description and liquid-vapor spinodal. *J. Chem. Phys.*, 151:034503, 2019.
- [14] V. Diatschenko, C. W. Chu, D. H. Liebenberg, D. A. Young, M. Ross, and R. L. Mills. Melting curves of molecular hydrogen and molecular deuterium under high pressures between 20 and 373 K. *Phys. Rev. B*, 32:381–389, 1985.
- [15] Frédéric Datchi, Paul Loubeyre, and René LeToullec. Extended and accurate determination of the melting curves of argon, helium, ice (H<sub>2</sub>O), and hydrogen (H<sub>2</sub>). *Phys. Rev. B*, 61:6535–6546, 2000.
- [16] Eugene Gregoryanz, Alexander F. Goncharov, Kiyoto Matsuishi, Ho-kwang Mao, and Russell J. Hemley. Raman spectroscopy of hot dense hydrogen. *Phys. Rev. Lett.*, 90:175701, 2003.
- [17] Chang-sheng Zha, Hanyu Liu, John S. Tse, and Russell J. Hemley. Melting and high P–T transitions of hydrogen up to 300 GPa. *Phys. Rev. Lett.*, 119:075302, 2017.
- [18] Y. Fukai. *The Metal–Hydrogen System Basic Bulk Properties*. Materials Science. Springer, Berlin, Germany, 2 edition, 2005.
- [19] Vladimir V. Kechin. Melting curve equations at high pressure. *Phys. Rev. B*, 65:052102, 2001.
- [20] Philip Dalladay-Simpson, Ross T. Howie, and Eugene Gregoryanz. Evidence for a new phase of dense hydrogen above 325 gigapascals. *Nature*, 529:63–67, 2016.
- [21] Bingqing Cheng, Guglielmo Mazzola, Chris J. Pickard, and Michele Ceriotti. Evidence for supercritical behaviour of high-pressure liquid hydrogen. *Nature*, 585:217–220, 2020.
- [22] Eugene Gregoryanz, Philip Dalladay-Simpson Cheng Ji, Bing Li, Ross T. Howie, and Ho-Kwang Mao. Everything you always wanted to know about metallic hydrogen but were afraid to ask. *Matter Radiat. Extremes*, 5:038101, 2020.
- [23] Hua Y. Geng. Public debate on metallic hydrogen to boost high pressure research. *Matter Radiat. Extremes*, 2:275, 2017.
- [24] A. P. Drozdov M.I. Erements. Comments on the claimed observation of the Wigner-Huntington transition to metallic hydrogen. *ArXiv*, 1702.05125, 2017.
- [25] Paul Loubeyre, Florent Occelli, and Paul Dumas. Comment on: Observation of the Wigner-Huntington transition to metallic hydrogen. *ArXiv*, 1702.07192, 2017.

- [26] Alexander F. Goncharov and Viktor V. Struzhkin. Comment on observation of the Wigner-Huntington transition to metallic hydrogen. *Science*, 357(6353):eaam9736, 2017.
- [27] Isaac F. Silvera and Ranga Dias. Response to comment on observation of the Wigner-Huntington transition to metallic hydrogen. *Science*, 357(6353):eaan2671, 2017.
- [28] Lorenzo Monacelli, Michele Casula, Kosuke Nakano, Sandro Sorella, and Francesco Mauri. Quantum phase diagram of high-pressure hydrogen. *ArXiv*, 2202.05740, 2022.
- [29] E. Wigner and H. B. Huntington. On the possibility of a metallic modification of hydrogen. *J. Chem. Phys.*, 3:764, 1935.
- [30] Ranga P. Dias and Isaac F. Silvera. Observation of the Wigner-Huntington transition to metallic hydrogen. *Science*, 355(6326):715–718, 2017.
- [31] Isaac F. Silvera and Ranga Dias. Metallic hydrogen. *J. Phys.: Condens. Matter*, 30:254003, 2018.
- [32] M. I. Eremets, A. P. Drozdov, P. P. Kong, and H. Wang. Semimetallic molecular hydrogen at pressure above 350 GPa. *Nature Physics*, 15:1246–1249, 2019.
- [33] Paul Loubeyre, Florent Occelli, and Paul Dumas. Synchrotron infrared spectroscopic evidence of the probable transition to metal hydrogen. *Nature*, 577:631–635, 2020.
- [34] Vasily Dzyabura, Mohamed Zaghoo, and Isaac F. Silvera. Evidence of a liquid-liquid phase transition in hot dense hydrogen. *Proc. Natl. Acad. Sci.*, 110(20):8040–8044, 2013.
- [35] Mohamed Zaghoo, Ashkan Salamat, and Isaac F. Silvera. Evidence of a first-order phase transition to metallic hydrogen. *Phys. Rev. B*, 93:155128, 2016.
- [36] Mohamed Zaghoo and Isaac F. Silvera. Conductivity and dissociation in liquid metallic hydrogen and implications for planetary interiors. *Proc. Natl. Acad. Sci.*, 114(45):11873–11877, 2017.
- [37] R. Stewart McWilliams, D. Allen Dalton, Mohammad F. Mahmood, and Alexander F. Goncharov. Optical properties of fluid hydrogen at the transition to a conducting state. *Phys. Rev. Lett.*, 116:255501, 2016.
- [38] Kenji Ohta, Kota Ichimaru, Mari Einaga, Sho Kawaguchi, Katsuya Shimizu, Takahiro Matsuoka, Naohisa Hirao, and Yasuo Ohishi. Phase boundary of hot dense fluid hydrogen. *Sci. Rep.*, 5(16560), 2015.
- [39] Winfried Lorenzen, Bastian Holst, and Ronald Redmer. First-order liquid-liquid phase transition in dense hydrogen. *Phys. Rev. B*, 82:195107, 2010.
- [40] Jeffrey M. McMahon, Miguel A. Morales, Carlo Pierleoni, and David M. Ceperley. The properties of hydrogen and helium under extreme conditions. *Rev. Mod. Phys.*, 84:1607–1653, 2012.

- [41] Carlo Pierleoni, Miguel A. Morales, Giovanni Rillo, Markus Holzmann, and David M. Ceperley. Liquid-liquid phase transition in hydrogen by coupled electron-ion Monte Carlo simulations. *Proc. Natl. Acad. Sci.*, 113(18):4953–4957, 2016.
- [42] Guglielmo Mazzola, Ravit Helled, and Sandro Sorella. Phase diagram of hydrogen and a hydrogen-helium mixture at planetary conditions by quantum Monte Carlo simulations. *Phys. Rev. Lett.*, 120:025701, 2018.
- [43] Hua Y. Geng, Q. Wu, Miriam Marqués, and Graeme J. Ackland. Thermodynamic anomalies and three distinct liquid-liquid transitions in warm dense liquid hydrogen. *Phys. Rev. B*, 100:134109, 2019.
- [44] Joshua Hinz, Valentin V. Karasiev, S. X. Hu, Mohamed Zaghoo, Daniel Mejía-Rodríguez, S. B. Trickey, and L. Calderín. Fully consistent density functional theory determination of the insulator-metal transition boundary in warm dense hydrogen. *Phys. Rev. Research*, 2:032065, 2020.
- [45] Valentin V. Karasiev, Joshua Hinz, S. X. Hu, and S. B. Trickey. On the liquid–liquid phase transition of dense hydrogen. *Nature*, 600:E12–E14, 2021.
- [46] Andrea Tirelli, Giacomo Tenti, Kousuke Nakano, and Sandro Sorella. High-pressure hydrogen by machine learning and quantum Monte Carlo. *ArXiv*, 2112.11099, 2022.
- [47] Stanimir A. Bonev, Eric Schwegler, Tadashi Ogitsu, and Giulia Galli. A quantum fluid of metallic hydrogen suggested by first-principles calculations. *Nature*, 431:669–672, 2004.
- [48] Miguel A. Morales, Carlo Pierleoni, Eric Schwegler, and D. M. Ceperley. Evidence for a first-order liquid-liquid transition in high-pressure hydrogen from ab initio simulations. *Proc. Natl. Acad. Sci.*, 107(29):12799–12803, 2010.
- [49] V.V Brazhkin, S.V Popova, and R.N Voloshin. Pressure–temperature phase diagram of molten elements: selenium, sulfur and iodine. *Physica B*, 265(1):64–71, 1999.
- [50] A.G.M. Ferreira and L.Q. Lobo. The low-pressure phase diagram of sulfur. *J. Chem. Thermodyn.*, 43(2):95–104, 2011.
- [51] Laura Henry, Mohamed Mezouar, Gaston Garbarino, David Sifré, Gunnar Weck, and Frédéric Datchi. Liquid–liquid transition and critical point in sulfur. *Nature*, 584:382–386, 2020.
- [52] A. A. Povodyrev, M. A. Anisimov, and J. V. Sengers. Crossover Flory model for phase separation in polymer solutions. *Physica A*, 264(3):345–369, 1999.
- [53] Young C. Kim, Mikhail A. Anisimov, Jan V. Sengers, and Erik Luijten. Crossover critical behavior in the three-dimensional Ising model. *J. Stat. Phys.*, 110(3):591–609, 2003.
- [54] H.-O. Heuer. Critical crossover phenomena in disordered Ising systems. *J. Phys. A*, 26:1333–1339, 1993.

- [55] H. E. Stanley. Liquid polyamorphism. In Stuart A. Rice and Aaron R. Dinner, editors, *Advances in Chemical Physics*, volume 152. John Wiley & Sons, 2013.
- [56] H. Tanaka. Liquid–liquid transition and polyamorphism. *J. Chem. Phys.*, 153:130901, 2020.
- [57] D. Vollhardt and P. Wölfle. *The Superfluid Phases of Helium 3*. Taylor and Francis, London, UK, 1990.
- [58] A. Schmitt. *Introduction to Superfluidity*, volume 888 of *Lecture Notes in Physics*. Springer International Publishing, Cham, 2015.
- [59] G. E. Norman and I. M. Saitov. Plasma phase transition. *Phys. Usp.*, 64:1094, 2021.
- [60] Yoshinori Katayama, Takeshi Mizutani, Wataru Utsumi, Osamu Shimomura, Masaaki Yamakata, and Ken ichi Funakoshi. A first-order liquid–liquid phase transition in phosphorus. *Nature*, 403:170–173, 2000.
- [61] Yoshinori Katayama, Yasuhiro Inamura, Takeshi Mizutani, Masaaki Yamakata, Wataru Utsumi, and Osamu Shimomura. Macroscopic separation of dense fluid phase and liquid phase of phosphorus. *Science*, 306(5697):848–851, 2004.
- [62] J. N. Glosli and F. H. Ree. Liquid-liquid phase transformation in carbon. *Phys. Rev. Lett.*, 82:4659–4662, 1999.
- [63] Srikanth Sastry and C. Austen Angell. Liquid–liquid phase transition in supercooled silicon. *Nature Mater*, 2:739–743, 2003.
- [64] Martin Beye, Florian Sorgenfrei, William F. Schlotter, Wilfried Wurth, and Alexander Föhlisch. The liquid-liquid phase transition in silicon revealed by snapshots of valence electrons. *Proc. Natl. Acad. Sci.*, 107(39):16772–16776, 2010.
- [65] Vishwas V. Vasisht, Shibu Saw, and Srikanth Sastry. Liquid–liquid critical point in supercooled silicon. *Nat. Phys.*, 7:549–553, 2011.
- [66] Francesco Sciortino. Liquid–liquid transitions: Silicon in silico. *Nat. Phys.*, 7:523–524, 2011.
- [67] Ivan Saika-Voivod, Francesco Sciortino, and Peter H. Poole. Computer simulations of liquid silica: Equation of state and liquid–liquid phase transition. *Phys. Rev. E*, 63:011202, 2000.
- [68] Erik Lascaris, Mahin Hemmati, Sergey V. Buldyrev, H. Eugene Stanley, and C. Austen Angell. Search for a liquid-liquid critical point in models of silica. *J. Chem. Phys.*, 140:224502, 2014.
- [69] Y Tsuchiya and E F W Seymour. Thermodynamic properties of the selenium-tellurium system. *J. Phys. C Solid State Phys.*, 15(22):L687–L695, 1982.

- [70] V. V. Brazhkin, S. V. Popova, and R. N. Voloshin. Pressure-temperature phase diagram of molten elements: selenium, sulfur and iodine. *Physica B*, 265:64–71, 1999.
- [71] A. Cadien, Q. Y. Hu, Y. Meng, Y. Q. Cheng, M. W. Chen, J. F. Shu, H. K. Mao, and H. W. Sheng. First-order liquid-liquid phase transition in cerium. *Phys. Rev. Lett.*, 110:125503, 2013.
- [72] C. Austen Angell. Two-state thermodynamics and transport properties for water as zeroth-order results of a “bond lattice” model. *J. Phys. Chem.*, 75(24):3698, 1971.
- [73] C. Austen Angell. Amorphous water. *Annual Review of Physical Chemistry*, 55(1):559–583, 2004.
- [74] P. H. Poole, F. Sciortino, U. Essmann, and H. E. Stanley. Phase behavior of metastable water. *Nature*, 360:324–328, 1992.
- [75] Pablo G. Debenedetti. One substance, two liquids? *Nature*, 392:127–128, 1998.
- [76] V. Holten and M. A. Anisimov. Entropy-driven liquid–liquid separation in supercooled water. *Sci. Rep.*, 2:713, 2012.
- [77] V. Holten, J. C. Palmer, P. H. Poole, P. G. Debenedetti, and M. A. Anisimov. Two-state thermodynamics of the ST2 model for supercooled water. *J. Chem. Phys.*, 140:104502, 2014.
- [78] Paola Gallo, Katrin Amann-Winkel, Charles Austen Angell, Mikhail Alexeevich Anisimov, Frédéric Caupin, Charusita Chakravarty, Erik Lascaris, Thomas Loerting, Athanasios Zois Panagiotopoulos, John Russo, Jonas Alexander Sellberg, Harry Eugene Stanley, Hajime Tanaka, Carlos Vega, Limei Xu, and Lars Gunnar Moody Pettersson. Water: A tale of two liquids. *Chem. Rev.*, 116:7463–7500, 2016.
- [79] John W. Biddle, Rakesh S. Singh, Evan M. Sparano, Francesco Ricci, Miguel A. González, Chantal Valeriani, José L. F. Abascal, Pablo G. Debenedetti, Mikhail A. Anisimov, and Frédéric Caupin. Two-structure thermodynamics for the TIP4P/2005 model of water covering supercooled and deeply stretched regions. *J. Chem. Phys.*, 146:034502, 2017.
- [80] Michal Duška. Water above the spinodal. *J. Chem. Phys.*, 152:174501, 2020.
- [81] Vincent Holten, Chen Qiu, Emmanuel Guillermin, Max Wilke, Jaroslav Rička, Martin Frenz, and Frédéric Caupin. Compressibility anomalies in stretched water and their interplay with density anomalies. *J. Phys. Chem. Lett.*, 8(22):5519–5522, 2017.
- [82] Kyung Hwan Kim, Alexander Späh, Harshad Pathak, Fivos Perakis, Daniel Mariedahl, Katrin Amann-Winkel, Jonas A. Sellberg, Jae Hyuk Lee, Sangsoo Kim, Jaehyun Park, Ki Hyun Nam, Tetsuo Katayama, and Anders Nilsson. Maxima in the thermodynamic response and correlation functions of deeply supercooled water. *Science*, 358(6370):1589–1593, 2017.

- [83] Harshad Pathak, Alexander Späh, Niloofar Esmaeildoost, Jonas A. Sellberg, Kyung Hwan Kim, Fivos Perakis, Katrin Amann-Winkel, Marjorie Ladd-Parada, Jayanath Koliyadu, Thomas J. Lane, Cheolhee Yang, Henrik Till Lemke, Alexander Roland Oggenfuss, Philip J. M. Johnson, Yunpei Deng, Serhane Zerdane, Roman Mankowsky, Paul Beaud, and Anders Nilsson. Enhancement and maximum in the isobaric specific-heat capacity measurements of deeply supercooled water using ultrafast calorimetry. *Proc. Natl. Acad. Sci.*, 118(6):e2018379118, 2021.
- [84] Václav Vinš, Jan Hrubý, Radim Mareš, Jiří Hykl, and Jana Kalová. Surface tension of supercooled water: No inflection point down to  $-25$  °C. *J. Phys. Chem. Lett.*, 5(3):425–428, 2014.
- [85] Václav Vinš, Maurice Fransen, Jiří Hykl, and Jan Hrubý. Surface tension of supercooled water determined by using a counterpressure capillary rise method. *J. Phys. Chem. B*, 119(17):5567–5575, 2015.
- [86] Václav Vinš, Jan Hošek, Jiří Hykl, and Jan Hrubý. Surface tension of supercooled water: Inflection point-free course down to 250 K confirmed using a horizontal capillary tube. *J. Chem. Eng. Data*, 62(11):3823–3832, 2017.
- [87] Václav Vinš, Jiří Hykl, Jan Hrubý, Aleš Blahut, David Celný, Miroslav Čenský, and Olga Prokopová. Possible anomaly in the surface tension of supercooled water: New experiments at extreme supercooling down to  $-31.4$  degree C. *J. Phys. Chem. Lett.*, 11(11):4443–4447, 2020.
- [88] Miguel A. González, Chantal Valeriani, Frédéric Caupin, and José L. F. Abascal. A comprehensive scenario of the thermodynamic anomalies of water using the TIP4P/2005 model. *J. Chem. Phys.*, 145:054505, 2016.
- [89] Jingxiang Guo, Rakesh S. Singh, and Jeremy C. Palmer. Anomalous scattering in supercooled ST2 water. *Molecular Physics*, 116(15-16):1953–1964, 2018.
- [90] Rakesh S. Singh, Jeremy C. Palmer, Athanassios Z. Panagiotopoulos, and Pablo G. Debenedetti. Thermodynamic analysis of the stability of planar interfaces between co-existing phases and its application to supercooled water. *J. Chem. Phys.*, 150:2224503, 2019.
- [91] Pablo G. Debenedetti, Francesco Sciortino, and Gül H. Zerze. Second critical point in two realistic models of water. *Science*, 369(6501):289–292, 2020.
- [92] Osamu Mishima and H. Eugene Stanley. Decompression-induced melting of ice IV and the liquid–liquid transition in water. *Nature*, 392:164–168, 1998.
- [93] Kyung Hwan Kim, Katrin Amann-Winkel, Nicolas Giovambattista, Alexander Späh, Fivos Perakis, Harshad Pathak, Marjorie Ladd Parada, Cheolhee Yang, Daniel Mariedahl, Tobias Eklund, Thomas J. Lane, Seonju You, Sangmin Jeong, Matthew Weston, Jae Hyuk Lee, Intae Eom, Minseok Kim, Jaeku Park, Sae Hwan Chun, Peter H. Poole, and Anders Nilsson. Experimental observation of the liquid-liquid transition in bulk supercooled water under pressure. *Science*, 370(6519):978–982, 2020.

- [94] Sanjay Puri. Kinetics of phase transitions. *Phase Transit.*, 77:407–431, 2004.
- [95] Joaquin Marro and Ronald Dickman. *Nonequilibrium Phase Transitions in Lattice Models*. Cambridge University Press, Cambridge, United Kingdom, 1999.
- [96] Mukkish Acharyya. Nonequilibrium phase transitions in model ferromagnets: A review. *Int. J. Mod. Phys. C*, 16(11):1631–1670, 2005.
- [97] T. G. Lombardo, F. H. Stillinger, and P. G. Debenedetti. Thermodynamic mechanism for solution phase chiral amplification via a lattice model. *Proc. Natl. Acad. Sci.*, 106(36):15131–15135, 2009.
- [98] Folarin Latinwo, Frank H. Stillinger, and Pablo G. Debenedetti. Molecular model for chirality phenomena. *J. Chem. Phys.*, 145(15):154503, 2016.
- [99] Nikolai D. Petsev, Frank H. Stillinger, and Pablo G. Debenedetti. Effect of configuration-dependent multi-body forces on interconversion kinetics of a chiral tetramer model. *J. Chem. Phys.*, 155:084105, 2021.
- [100] P. C. Hohenberg and B. I. Halperin. Theory of dynamic critical phenomena. *Rev. Mod. Phys.*, 49:435–479, 1977.
- [101] A. Onuki. *Phase Transition Dynamics*. Cambridge University Press, Cambridge, UK, 2002.
- [102] John W. Cahn. Phase separation by spinodal decomposition in isotropic systems. *J. Chem. Phys.*, 42(1):93–99, 1965.
- [103] G. Gompper and M. Schick. Lattice theories of microemulsions. In William M. Gelbart, Avinoam Ben-Shaul, and Didier Roux, editors, *Micelles, Membranes, Microemulsions, and Monolayers*, chapter 8, pages 395–426. Springer, New York, NY, 1994.
- [104] David Andelman and Ronald E. Rosensweig. Modulated phases: Review and recent results. *J. Phys. Chem. B*, 113(12):3785–3798, 2009.
- [105] Richard A. L. Jones. *Soft Condensed Matter*. Oxford University Press, Oxford, UK, 2002.
- [106] Itamar Borukhov, David Andelman, Michel Cloitre Regis Borrega, Ludwik Leibler, and Henri Orland. Polyelectrolyte titration: Theory and experiment. *J. Phys. Chem. B*, 104:11027–11034, 2000.
- [107] Yuting I. Li and Michael E. Cates. Non-equilibrium phase separation with reactions: A canonical model and its behaviour. *J. Stat. Mech. Theory Exp.*, 2020:053206, 2020.
- [108] Dimitri D. Vvedensky. *Transformations of Materials*. Morgan and Claypool Publishers, San Rafael, California, 2019.
- [109] Brent Fultz. *Phase Transitions in Materials*. Cambridge University Press, Cambridge, UK, 2 edition, 2020.

- [110] D. H. Kim, W. T. Kim, E. S. Park, N. Mattern, and J. Eckert. Phase separation in metallic glasses. *Prog. Mater. Sci.*, 58:1103–1172, 2013.
- [111] C. Lin, C. Bocker, and C. Russel. Nanocrystallization in oxyfluoride glasses controlled by amorphous phase separation. *Nano Lett.*, 15:6764–6769, 2015.
- [112] F. Ricci, F. H. Stillinger, and P. G. Debenedetti. A computational investigation of attrition-enhanced chiral symmetry breaking in conglomerate crystals. *J. Chem. Phys.*, 139, 2013.
- [113] Anthony A. Hyman, Christoph A. Weber, and Frank Jülicher. Liquid-liquid phase separation in biology. *Annu. Rev. Cell Dev.*, 30(1):39–58, 2014.
- [114] Steven Boeynaems, Simon Alberti, Nicolas L. Fawzi, Tanja Mittag, Magdalini Polymenidou, Joost Schymkowitz Frederic Rousseau, James Shorter, Benjamin Wolozin, Ludo Van Den Bosch, Peter Tompa, and Monika Fuxreiter. Protein phase separation: A new phase in cell biology. *Trends Cell Biol.*, 28:420–435, 2018.
- [115] B. A. Huberman. Striations in chemical reactions. *J. Chem. Phys.*, 65(5):2013–2019, 1976.
- [116] J. Verdasca, P. Borckmans, and G. Dewel. Chemically frozen phase separation in an adsorbed layer. *Phys. Rev. E*, 52:R4616–R4619, 1995.
- [117] Daniele Carati and René Lefever. Chemical freezing of phase separation in immiscible binary mixtures. *Phys. Rev. E*, 56:3127–3136, 1997.
- [118] A. G. Lamorgese and R. Mauri. Liquid mixture convection during phase separation in a temperature gradient. *Phys. Fluids*, 23:034102, 2011.
- [119] S. T. Weir, A. C. Mitchell, and W. J. Nellis. Metallization of fluid molecular hydrogen at 140 GPa (1.4 Mbar). *Phys. Rev. Lett.*, 76:1860–1863, 1996.
- [120] E. Yu Tonkov, Dmitry G. Eskin, J. N. Fridlyander, and E.G. Ponyatovsky. *Phase Transformations of Elements Under High Pressure*. CRC Press, Boca Raton, USA, 2004.
- [121] V. V. Brazhkin, S. V. Popova, and R. N. Voloshin. High-pressure transformations in simple melts. *High Press. Res.*, 15(5):267–305, 2006.
- [122] Sandro Scandolo. Liquid-liquid phase transition in compressed hydrogen from first-principles simulations. *Proc. Natl. Acad. Sci.*, 100(6):3051–3053, 2003.
- [123] Jeremy McMinis, Raymond C. Clay, Donghwa Lee, and Miguel A. Morales. Molecular to atomic phase transition in hydrogen under high pressure. *Phys. Rev. Lett.*, 114:105305, 2015.
- [124] Renzhong Li, Ji Chen, Xinzheng Li, Enge Wang, and Limei Xu. Supercritical phenomenon of hydrogen beyond the liquid–liquid phase transition. *New J. Phys.*, 17:063023, 2015.
- [125] Shanti Deemyad and Isaac F. Silvera. Melting line of hydrogen at high pressures. *Phys. Rev. Lett.*, 100:155701, 2008.

- [126] M. I. Eremets and I. A. Trojan. Evidence of maximum in the melting curve of hydrogen at megabar pressures. *JETP Letters*, 89:174–179, 2009.
- [127] Natarajan Subramanian, Alexander F. Goncharov, Viktor V. Struzhkin, Maddury Somayazulu, and Russell J. Hemley. Bonding changes in hot fluid hydrogen at megabar pressures. *Proc. Natl. Acad. Sci.*, 108(15):6014–6019, 2011.
- [128] Claudio Attaccalite and Sandro Sorella. Stable liquid hydrogen at high pressure by a novel ab initio molecular-dynamics calculation. *Phys. Rev. Lett.*, 100:114501, 2008.
- [129] Hanyu Liu, Li Zhu, Wenwen Cui, and Yanming Ma. Room-temperature structures of solid hydrogen at high pressures. *J. Chem. Phys.*, 137:074501, 2012.
- [130] Anatoly B. Belonoshko, Muhammad Ramzan, Ho kwang Mao, and Rajeev Ahuja. Atomic diffusion in solid molecular hydrogen. *Sci. Rep.*, 3(2340), 2013.
- [131] Alexander F. Goncharov and Zachary M. Geballe. Comment on “Evidence of a first-order phase transition to metallic hydrogen”. *Phys. Rev. B*, 96:157101, 2017.
- [132] Ross T. Howie, Philip Dalladay-Simpson, and Eugene Gregoryanz. Comment on “Evidence of a first-order phase transition to metallic hydrogen”. *Phys. Rev. B*, 96:157102, 2017.
- [133] Isaac F. Silvera, Mohamed Zaghoo, and Ashkan Salamat. Reply to “Comment on ‘Evidence of a first-order phase transition to metallic hydrogen’”. *Phys. Rev. B*, 96:237102, 2017.
- [134] G.E. Norman, I.M. Saitov, and R.A. Sartan. Metastable molecular fluid hydrogen at high pressures. *Contributions to Plasma Physics*, 59:e201800173, 2019.
- [135] M. A. Anisimov, E. E. Gorodetskii, V. D. Kulikov, and J. V. Sengers. Crossover between vapor-liquid and consolute critical phenomena. *Phys. Rev. E*, 51:1199–1215, 1995.
- [136] Mikhail A. Anisimov and Jingtao Wang. Nature of asymmetry in fluid criticality. *Phys. Rev. Lett.*, 97:025703, 2006.
- [137] Jingtao Wang and Mikhail A. Anisimov. Nature of vapor-liquid asymmetry in fluid criticality. *Phys. Rev. E*, 75:051107, 2007.
- [138] Betul Uralcan, Folarin Latinwo, Pablo G. Debenedetti, and Mikhail A. Anisimov. Pattern of property extrema in supercooled and stretched water models and a new correlation for predicting the stability limit of the liquid state. *J. Chem. Phys.*, 150:064503, 2019.
- [139] National Bureau of Standards. Bond dissociation energies in simple molecules. Technical Report Nat. Stand. Ref. Data Ser., Nat. Bur. Stand. (U.S.), 31, U.S. Department of Commerce, Washington, D.C., 1970.
- [140] G. E. Sauer and L. B. Borst. Lambda transition in liquid sulfur. *Science*, 158(3808):1567–1569, 1967.

- [141] R Bellissent, L Descotes, and P Pfeuty. Polymerization in liquid sulphur. *J. Phys.: Condens. Matter*, 6(23A):A211–A216, 1994.
- [142] V. F. Kozhevnikov, W. B. Payne, J. K. Olson, C. L. McDonald, and C. E. Inglesfield. Physical properties of sulfur near the polymerization transition. *J. Chem. Phys.*, 121, 2004.
- [143] Arthur V. Tobolsky and Adi Eisenberg. Equilibrium polymerization of sulfur. *J. Am. Chem. Soc.*, 81(4):780–782, 1959.
- [144] Adi Eisenberg and Arthur V. Tobolsky. Equilibrium polymerization of selenium. *J. Pol. Sci.*, 46, 1960.
- [145] E. Zaccarelli, S. V. Buldyrev, E. La Nave, A. J. Moreno, I. Saika-Voivod, F. Sciortino, and P. Tartagliae. Model for reversible colloidal gelation. *Phys. Rev. Lett.*, 94:218301, 2005.
- [146] R. J. Speedy and P. G. Debenedetti. The entropy of a network crystal, fluid and glass. *Mol. Phys.*, 81(1):237–249, 1994.
- [147] R. J. Speedy and P. G. Debenedetti. The distribution of tetravalent network glasses. *Mol. Phys.*, 88(5):1293–1316, 1996.
- [148] G. Stell and P. C. Hemmer. Phase transitions due to softness of the potential core. *J. Chem. Phys.*, 56:4274, 1972.
- [149] F. H. Stillinger and T. Head-Gordon. Perturbational view of inherent structures in water. *Phys. Rev. E*, 47:2484–2490, 1993.
- [150] E. A. Jagla. Liquid-liquid equilibrium for monodisperse spherical particles. *Phys. Rev. E*, 63:061501, 2001.
- [151] G. Franzese, G. Malescio, A. Skibinsky, S. V. Buldyrev, and H. E. Stanley. Generic mechanism for generating a liquid-liquid phase transition. *Nature*, 409, 2001.
- [152] H. M. Gibson and N. B. Wilding. Metastable liquid-liquid coexistence and density anomalies in a core-softened fluid. *Phys. Rev. E*, 73:061507, 2006.
- [153] A. Skibinsky, S. V. Buldyrev, G. Franzese, G. Malescio, and H. E. Stanley. Liquid-liquid phase transitions for soft-core attractive potentials. *Phys. Rev. E*, 69:61206–15, 2004.
- [154] S. V. Buldyrev, P. Kumar, S. Sastry, H. E. Stanley, and S. Weiner. Hydrophobic collapse and cold denaturation in the Jagla model of water. *J. Phys.: Condens. Matter*, 22:284109, 2010.
- [155] Paul J. Flory. Thermodynamics of high polymer solutions. *J. Chem. Phys.*, 9:660, 1941.
- [156] Maurice L. Huggins. Solutions of long chain compounds. *J. Chem. Phys.*, 9:440, 1941.
- [157] Philip K. Chan and Alejandro D. Rey. Polymerization-induced phase separation. 1. Droplet size selection mechanism. *Macromolecules*, 29(27):8934–8941, 1996.

- [158] Kaifu Luo. The morphology and dynamics of polymerization-induced phase separation. *European Polymer Journal*, 42(7):1499–1505, 2006.
- [159] J.H. Hildebrand and R.L. Scott. *Regular Solutions*. Prentice-Hall international series in chemistry. Prentice-Hall, 1962.
- [160] B. J. Alder and T. E. Wainwright. Studies in molecular dynamics. i. general method. *J. Chem. Phys.*, 31:459, 1959.
- [161] D. C. Rapaport. *The Art of Molecular Dynamics Simulation*. Cambridge University Press, Cambridge, UK, 2 edition, 2004.
- [162] S.V. Buldyrev. Application of discrete molecular dynamics to protein folding and aggregation. In G. Franzese and M. Rubi, editors, *Aspects of Physical Biology*, volume 752 of *Lecture Notes in Physics*, pages 97–132. Springer-Verlag, Berlin, Heidelberg, 2009.
- [163] H. J. C. Berendsen, J. P. M. Postma, W. F. van Gunsteren, A. DiNola, and J. R. Haak. Molecular-dynamics with coupling to an external bath. *J. Chem. Phys.*, 81(8):3684–3690, 1984.
- [164] J. Luo, Limei Xu, C. A. Angell, H. E. Stanley, and S. V. Buldyrev. Physics of the Jagla model as the liquid-liquid coexistence line slope varies. *J. Chem. Phys.*, 142:224501, 2015.
- [165] D. R. Lide. *CRC Handbook of Chemistry and Physics*. CRC Press, Boca Raton, FL, 85 edition, 2003.
- [166] Renjie Chen, Erik Lascaris, and Jeremy C. Palmer. Liquid–liquid phase transition in an ionic model of silica. *J. Chem. Phys.*, 146:234503, 2017.
- [167] Nikolay A. Shumovskyi and Sergey V. Buldyrev. Generic maximum-valence model for fluid polyamorphism. *ArXiv*, 2210.01968, 2022. Submitted to *Phys. Rev. E*.
- [168] Srikanth Sastry, Pablo G. Debenedetti, Francesco Sciortino, and H. E. Stanley. Singularity-free interpretation of the thermodynamics of supercooled water. *Phys. Rev. E*, 53:6144–6154, 1996.
- [169] J. Hrubý and V. Holten. A two-structure model of thermodynamic properties and surface tension of supercooled water. *Proceedings of the 14th International Conference on the Properties of Water and Steam, Maruzen*, pages 241–246, 2004.
- [170] Alina Ciach, Wojciech Gózdź, and Aurélien Perera. Simple three-state lattice model for liquid water. *Phys. Rev. E*, 78:021203, 2008.
- [171] Peter H. Poole, Francesco Sciortino, Tor Grande, H. Eugene Stanley, and C. Austen Angell. Effect of hydrogen bonds on the thermodynamic behavior of liquid water. *Phys. Rev. Lett.*, 73:1632–1635, 1994.
- [172] C. Austen Angell. Insights into phases of liquid water from study of its unusual glass-forming properties. *Science*, 319(5863):582–587, 2008.

- [173] L. D. Landau and E. M. Lifshitz. In *Statistical Physics: Part 2*, volume 9 of *Course of Theoretical Physics*. Pergamon Press, Oxford, London, 2 edition, 1981.
- [174] S. S. Leung and Robert B. Griffiths. Thermodynamic properties near the liquid-vapor critical line in mixtures of  $\text{He}^3$  and  $\text{He}^4$ . *Phys. Rev. A*, 8:2670–2683, 1973.
- [175] G.X. Jin, S. Tang, and J.V. Sengers. Thermodynamic behavior of fluid mixtures in the critical region. *Fluid Phase Equilibria*, 75:1–10, 1992.
- [176] M.A. Anisimov and J.V. Sengers. On the choice of a hidden field variable near the critical point of fluid mixtures. *Physics Letters A*, 172(3):114–118, 1992.
- [177] Paul T. Hacker. Experimental values of the surface tension of supercooled water. *NASA Tech. Note*, 2510:1, 1951.
- [178] M. A. Floriano and C. A. Angell. Surface tension and molar surface free energy and entropy of water to  $-27.2\text{ }^\circ\text{C}$ . *J. Phys. Chem.*, 94(10):4199–4202, 1990.
- [179] E. H. Trinh and K. Ohsaka. Measurement of density, sound velocity, surface tension, and viscosity of freely suspended supercooled liquids. *Int. J. Thermophys.*, 16:545–555, 1995.
- [180] Melissa R. Feeney and Pablo G. Debenedetti. A theoretical study of the interfacial properties of supercooled water. *Ind. Eng. Chem. Res.*, 42(25):6396–6405, 2003.
- [181] Y. J. Lü and B. Wei. Second inflection point of water surface tension. *Appl. Phys. Lett.*, 89:164106, 2006.
- [182] Xiaoxiang Wang, Kurt Binder, Chuchu Chen, Thomas Koop, Ulrich Pöschl, Hang Su, and Yafang Cheng. Second inflection point of water surface tension in the deeply supercooled regime revealed by entropy anomaly and surface structure using molecular dynamics simulations. *Phys Chem. Chem. Phys.*, 21:3360–3369, 2019.
- [183] T. Ryan Rogers, Kai-Yang Leong, and Feng Wang. Possible evidence for a new form of liquid buried in the surface tension of supercooled water. *Sci. Rep.*, 6(33284):1–6, 2016.
- [184] Shahrazad M. A. Malek, Peter H. Poole, and Ivan Saika-Voivod. Surface tension of supercooled water nanodroplets from computer simulations. *J. Chem. Phys.*, 150:234507, 2019.
- [185] Alexander Gorfer, Christoph Dellago, and Marcello Sega. High-density liquid (HDL) adsorption at the supercooled water/vapor interface and its possible relation to the second surface tension inflection point. *ArXiv*, 2211.08865, 2022.
- [186] Peter Debye. Angular dissymmetry of the critical opalescence in liquid mixtures. *J. Chem. Phys.*, 31:680, 1959.
- [187] Arthur J. M. Yang, Paul D. Fleming, and Julian H. Gibbs. Molecular theory of surface tension. *J. Chem. Phys.*, 64:3732, 1976.

- [188] Bo Qiao Lu, R. Evans, and M.M. Telo da Gama. The form of the density profile at a liquid-gas interface. *Molecular Physics*, 55(6):1319–1338, 1985.
- [189] H. Kahl and S. Enders. Interfacial properties of binary mixtures. *Phys. Chem. Chem. Phys.*, 4:931–936, 2002.
- [190] Simon Stephan and Hans Hasse. Molecular interactions at vapor-liquid interfaces: Binary mixtures of simple fluids. *Phys. Rev. E*, 101:012802, 2020.
- [191] J. D. van der Waals. Thermodynamische theorie de capillariteit in de onderstelling van continue dichtheidsverandering. *Verhand. Konink. Akad. Wetensch. Amsterdam. (Sect. I)*, 1:56, 1893.
- [192] J. S. Rowlinson and B. Widom. *Molecular Theory of Capillarity*. Oxford University Press, Oxford, UK, 1982.
- [193] John W. Cahn and John E. Hilliard. Free energy of a nonuniform system. I. Interfacial free energy. *J. Chem. Phys.*, 28:258, 1958.
- [194] Claudia I Poser and Isaac C Sanchez. Surface tension theory of pure liquids and polymer melts. *J. Colloid Interface Sci.*, 69(3):539–548, 1979.
- [195] Claudia I. Poser and Isaac C. Sanchez. Interfacial tension theory of low and high molecular weight liquid mixtures. *Macromol.*, 14:361–370, 1981.
- [196] Manuel Schwartz, Simon Green, and W. A. Rutledge. *Vector Analysis with applications to geometry and physics*. Harper & Row, 1960.
- [197] Matthew P. A. Fisher and Michael Wortis. Curvature corrections to the surface tension of fluid drops: Landau theory and a scaling hypothesis. *Phys. Rev. B*, 29:6252–6260, 1984.
- [198] M. A. Anisimov and C. E. Bertrand. Thermodynamics of fluids at meso and nano scales. In Anthony R. Goodwin, Cor J Peters, and Jan Sengers, editors, *Applied Thermodynamics of Fluids*, chapter 7, pages 172–214. Royal Society of Chemistry, Cambridge, UK, 2010.
- [199] Frédéric Caupin. Liquid-vapor interface, cavitation, and the phase diagram of water. *Phys. Rev. E*, 71:051605, 2005.
- [200] M.A Anisimov, E.E Gorodetskii, V.D Kulikov, A.A Povodyrev, and J.V Sengers. A general isomorphism approach to thermodynamic and transport properties of binary fluid mixtures near critical points. *Physica A*, 220(3):277–324, 1995.
- [201] C. E. Bertrand and M. A. Anisimov. Complete scaling for inhomogeneous fluids. *Phys. Rev. Lett.*, 104:205702, 2010.
- [202] José L. F. Abascal and Carlos Vega. Widom line and the liquid-liquid critical point for the TIP4P/2005 water model. *J. Chem. Phys.*, 133:234502, 2010.

- [203] John W. Biddle, Rakesh S. Singh, Evan M. Sparano, Francesco Ricci, Miguel A. González, Chantal Valeriani, José L. F. Abascal, Pablo G. Debenedetti, Mikhail A. Anisimov, and Frédéric Caupin. Two-structure thermodynamics for the TIP4P/2005 model of water covering supercooled and deeply stretched regions. *J. Chem. Phys.*, 146:034502, 2017.
- [204] R. de Groot and P. Mazur. *Non-Equilibrium Thermodynamics* Dover. Dover Publications, New York City, NY, 1984.
- [205] A. G. Lamorgese and R. Mauri. Mixing of macroscopically quiescent liquid mixtures. *Phys. Fluids*, 18:044107, 2006.
- [206] R. Mauri. Balance equations. In Wenbing Hu, Roland Netz, Roberto Piazza, Peter Schall, and Gerard C.L. Wong, editors, *Non-Equilibrium Thermodynamics in Multiphase Flows*, Soft and Biological Matter, chapter 7, pages 73–86. Springer, Dordrecht, NL, 2013.
- [207] A. Lamorgese and R. Mauri. Spinodal decomposition of chemically reactive binary mixtures. *Phys. Rev. E*, 94:022605, 2016.
- [208] Roberto Mauri, Reuel Shinnar, and George Triantafyllou. Spinodal decomposition in binary mixtures. *Phys. Rev. E*, 53:2613–2623, 1996.
- [209] Natalia Vladimirova, Andrea Malagoli, and Roberto Mauri. Two-dimensional model of phase segregation in liquid binary mixtures. *Phys. Rev. E*, 60:6968–6977, 1999.
- [210] L. D. Landau and E. M. Lifshitz. Statistical Physics Part 1. volume 5 of *Course of Theoretical Physics*. Pergamon Press, Oxford, London, 3 edition, 1980.
- [211] J. W. Cahn and S. M. Allen. A microscopic theory for domain wall motion and its experimental verification in Fe-Al alloy domain growth kinetics. *J. phys., Colloq.*, 38(C7):C751–C754, 1977.
- [212] T. Ohta and K. Kawasaki. Equilibrium morphology of block copolymer melts. *Macromol.*, 19:2621, 1986.
- [213] Sharon C. Glotzer and Antonio Coniglio. Self-consistent solution of phase separation with competing interactions. *Phys. Rev. E*, 50:4241–4244, 1994.
- [214] Raúl A. Enrique and Pascal Bellon. Compositional patterning in immiscible alloys driven by irradiation. *Phys. Rev. B*, 63:134111, 2001.
- [215] Q Tran-Cong-Miyata and H. Nakanishi. Phase separation of polymer mixtures driven by photochemical reactions: current status and perspectives. *Polym. Int.*, 66:213–222, 2017.
- [216] Sharon C. Glotzer, Dietrich Stauffer, and Naeem Jan. Monte Carlo simulations of phase separation in chemically reactive binary mixtures. *Phys. Rev. Lett.*, 72(26):4109–4112, 1994.
- [217] Sharon C. Glotzer, Edmund A. Di Marzio, and M. Muthukumar. Reaction-controlled morphology of phase-separating mixtures. *Phys. Rev. Lett.*, 74(11):2034–2037, 1995.

- [218] R. Lefever, D. Carati, and N. Hassani. Comment on “Monte Carlo simulations of phase separation in chemically reactive binary mixtures”. *Phys. Rev. Lett.*, 75(8):1674–1674, 1995.
- [219] Tobias Grafke, Michael E. Cates, and Eric Vanden-Eijnden. Spatiotemporal self-organization of fluctuating bacterial colonies. *Phys. Rev. Lett.*, 119:188003, 2017.
- [220] Jan Kirschbaum and David Zwicker. Controlling biomolecular condensates via chemical reactions. *J. R. Soc. Interface*, 18:20210255, 2021.
- [221] Yuting I. Li and Michael E. Cates. Hierarchical microphase separation in non-conserved active mixtures. *Eur. Phys. J. E*, 44:119, 2021.
- [222] J. S. Langer and M. Bar-on. Theory of early-stage spinodal decomposition. *Ann. Physics*, 78(2):421–452, 1973.
- [223] C. Billotet and K. Binder. Dynamic correlation of fluctuations during spinodal decomposition. *Phys. A: Stat. Mech. Appl.*, 103(1):99–118, 1980.
- [224] Gene F. Mazenko and Oriol T. Valls. Theory of domain growth in an order-disorder transition. *Phys. Rev. B*, 30:6732–6748, 1984.
- [225] J. F. Marko and G. T. Barkema. Phase ordering in the Ising model with conserved spin. *Phys. Rev. E*, 52:2522–2534, 1995.
- [226] H. E Cook. Brownian motion in spinodal decomposition. *Acta Metallurgica*, 18:297–306, 1970.
- [227] K. Binder, C. Billotet, and P. Miold. On the theory of spinodal decomposition in solid and liquid binary mixtures. *Z. Phys., B Condens.*, 30(2):183–195, 1978.
- [228] A. J. Bray. Theory of phase-ordering kinetics. *Adv. Phys.*, 51(2):481–587, 2002.
- [229] J. S. Langer, M. Bar-on, and Harold D. Miller. New computational method in the theory of spinodal decomposition. *Phys. Rev. A*, 11(4):1417–1429, 1975.
- [230] Antonio Coniglio and Marco Zannetti. Multiscaling in growth kinetics. *EPL*, 10(6):575–580, 1989.
- [231] Antonio Coniglio and Marco Zannetti. Novel dynamical scaling in kinetic growth phenomena. *Physica A Stat. Mech. Appl.*, 163(1):325–333, 1990.
- [232] K. Binder. Collective diffusion, nucleation, and spinodal decomposition in polymer mixtures. *J. Chem. Phys.*, 79:6387, 1983.
- [233] Gert R. Strobl. Structure evolution during spinodal decomposition of polymer blends. *Macromol.*, 18:559–563, 1985.
- [234] John W. Cahn. The later stages of spinodal decomposition and the beginnings of particle coarsening. *Acta Metallurgica*, 14:1685–1692, 1966.

- [235] Jacob J. Christensen, Ken Elder, and Hans C. Fogedby. Phase segregation dynamics of a chemically reactive binary mixture. *Phys. Rev. E*, 54:R2212–R2215, 1996.
- [236] William H. Press, Saul A. Teukolsky, William T. Vetterling, and Brian P. Flannery. *Numerical Recipes: The Art of Scientific Computing*. Cambridge University Press, Cambridge, UK, 3 edition, 2007.
- [237] Rakesh S. Singh, John W. Biddle, Pablo G. Debenedetti, and Mikhail A. Anisimov. Two-state thermodynamics and the possibility of a liquid-liquid phase transition in supercooled TIP4P/2005 water. *J. Chem. Phys.*, 144:144504, 2016.
- [238] Kyohei Takae and Hajime Tanaka. Role of hydrodynamics in liquid-liquid transition of a single-component substance. *Proc. Natl. Acad. Sci.*, 117(9):4471–4479, 2020.
- [239] T. D. Lee and C. N. Yang. Statistical theory of equations of state and phase transitions. II. Lattice gas and Ising model. *Phys. Rev.*, 87(3):410–419, 1952.
- [240] Michael E. Fisher. Scaling, universality and renormalization group theory. In F. J. W. Hahne, editor, *Critical Phenomena*, Lecture Notes in Physics, pages 1–139. Springer, Berlin, Heidelberg, 1983.
- [241] John B. Kogut. An introduction to lattice gauge theory and spin systems. *Rev. Mod. Phys.*, 51(4):659–713, 1979.
- [242] T. Senthil and Matthew P. A. Fisher. Z<sub>2</sub> gauge theory of electron fractionalization in strongly correlated systems. *Phys. Rev. B*, 62(12):7850–7881, 2000.
- [243] T. Ohta and K. Kawasaki. Mode coupling theory of dynamic critical phenomena for classical liquids. I: Dynamic critical exponents. *Prog.*, 55, 1971.
- [244] Mikhail A. Anisimov. *Critical Phenomena in Liquids and Liquid Crystals*. Gordon and Breach Science Publishers, Philadelphia, PA, 1991.
- [245] Nigel Goldenfeld. Lectures on phase transitions and the renormalization group. volume 85 of *Frontiers in Physics*. Addison-Wesley Publishing Company, New York City, New York, 1992.
- [246] Kenneth G. Wilson and J. Kogut. The renormalization group and the epsilon expansion. *Phys. Rep.*, 12(2):75–199, 1974.
- [247] Kenneth G. Wilson and Michael E. Fisher. Critical exponents in 3.99 dimensions. *Phys. Rev. Lett.*, 28:240–243, 1972.
- [248] M. A. Anisimov, A. T. Berestov, L. S. Veksler, B. A. Koval’chuk, and V. A. Smirnov. Scaling theory and the equation of state of argon in a wide region around the critical point. *Sov. Phys.-JETP*, 39(2):359–365, 1974.
- [249] V. A. Agayan, M. A. Anisimov, and J. V. Sengers. Crossover parametric equation of state for Ising-like systems. *Phys. Rev. E*, 64:026125, 2001.

- [250] A. F. Kostko, M. A. Anisimov, and J. V. Sengers. Dynamics of critical fluctuations in polymer solutions. *Phys. Rev. E*, 76:021804, 2007.
- [251] B. I. Halperin, P. C. Hohenberg, and E. D. Siggia. Renormalization-group calculations of divergent transport coefficients at critical points. *Phys. Rev. Lett.*, 32:1289–1292, 1974.
- [252] E. D. Siggia, B. I. Halperin, and P. C. Hohenberg. Renormalization-group treatment of the critical dynamics of the binary-fluid and gas-liquid transitions. *Phys. Rev. B*, 13:2110–2123, 1976.
- [253] J. V. Sengers. Transport properties of fluids near critical points. *Int. J. Thermophys.*, 6:203, 1985.
- [254] Kyozi Kawasaki. Mode coupling and critical dynamics. In C. Domb and M. S. Green, editors, *Phase transitions and critical phenomena*, volume 5A. Academic Press, New York City, New York, 1976.
- [255] Subir K. Das, Jürgen Horbach, Kurt Binder, Michael E. Fisher, and Jan V. Sengers. Static and dynamic critical behavior of a symmetrical binary fluid: A computer simulation. *J. Chem. Phys.*, 125(024506), 2006.
- [256] Sharon C. Glotzer. Computer simulations of spinodal decomposition in polymer blends. In Dietrich Stauffer, editor, *Annual Reviews of Computational Physics*, volume 2, chapter 1, pages 1–46. World Scientific, Berlin, Germany, 1995.
- [257] Raishma Krishnan and Sanjay Puri. Molecular dynamics study of phase separation in fluids with chemical reactions. *Phys. Rev. E*, 92:052316, 2015.
- [258] N. Metropolis and R. L. Ashenurst. Basic operations in an unnormalized arithmetic system. *IEEE Trans. Comput.*, EC-12(6):896–904, 1963.
- [259] Kyozi Kawasaki. Diffusion constants near the critical point for time-dependent Ising models. I. *Phys. Rev.*, 145(1):224–230, 1966.
- [260] Roy J. Glauber. Time-dependent statistics of the Ising model. *J. Math. Phys.*, 4(2):294–307, 1963.
- [261] Kerson Huang. *Statistical Mechanics*. John Wiley and Sons, Inc., 2 edition, 1987.
- [262] Pradeep Kumar, Sergey V. Buldyrev, Francesco Sciortino, Emanuela Zaccarelli, and H. Eugene Stanley. Static and dynamic anomalies in a repulsive spherical ramp liquid: Theory and simulation. *Phys. Rev. E*, 72:021501, 2005.
- [263] Hermann Amandus Schwarz. *Gesammelte mathematische Abhandlungen*. Springer, Berlin, Heidelberg, 1972.
- [264] Samuel M. Allen and John W. Cahn. A microscopic theory for antiphase boundary motion and its application to antiphase domain coarsening. *Acta Metallurgica*, 27(6):1085–1095, 1979.

- [265] M. Teubner and R. Strey. Origin of the scattering peak in microemulsions. *J. Chem. Phys.*, 87:3195, 1987.
- [266] Von Albert Guijarro and Miguel Yus. *The Origin of Chirality in the Molecules of Life*. The Royal Society, Cambridge, UK, 2009.
- [267] Laurence D. Barron. Biochirality: Origins, evolution and molecular recognition. edited by pedro cintas. *Orig. Life Evol. Biosph.*, 44:61–62, 2014.
- [268] A. N. Collins, G. N. Sheldrake, and J. Crosby. Chirality in industry: The commercial manufacture and applications of optically active compounds. *J. Chem. Educ.*, 70(7):A199, 1993.
- [269] Hans-Ulrich Blaser. Industrial asymmetric catalysis: Approaches and results. *Rendiconti Lincei*, 18(4):281–304, 2007.
- [270] Hans-Ulrich Blaser. Chirality and its implications for the pharmaceutical industry. *Rendiconti Lincei*, 24(3):213–216, 2013.
- [271] Guo-Qiang Lin, Jian-Ge Zhang, and Jie-Fei Cheng. Overview of chirality and chiral drugs. In *Chiral Drugs*, pages 3–28. John Wiley & Sons, Inc., 2011.
- [272] Guang Yang and Hai-Zhi Bu. Toxicology of chiral drugs. In *Chiral Drugs*, pages 381–399. John Wiley & Sons, Inc., 2011.
- [273] Naveen Chhabra, MadanL Aseri, and Deepak Padmanabhan. A review of drug isomerism and its significance. *Int. J. Appl. Basic Med. Res.*, 3(1):16, 2013.
- [274] D. Sutton, J. L. Stanford, and A. J. Ryan. Reaction-induced phase-separation in polyoxyethylene/polystyrene blends. II. Structure development. *J. Macromol. Sci. Phys.*, 43(1):233–251, 2004.
- [275] Gang Zhang, Guiwu Liu, Zhongqi Shi, and Guanjun Qiao. Dynamics of spinodal decomposition coupled with chemical reaction in thermosetting phenol-formaldehyde resin-based solutions and its application in monolithic porous materials. *RSC Adv.*, 4:7068–7078, 2014.
- [276] Ileana A. Zucchi, MarÃa J. Galante, Julio Borrajo, and Roberto J. J. Williams. A model system for the thermodynamic analysis of reaction-induced phase separation: Solutions of polystyrene in bifunctional epoxy/amine monomers. *Macromol. Chem. and Phys.*, 205(5):676–683, 2004.
- [277] Roberto J. J. Williams, Boris A. Rozenberg, and Jean-Pierre Pascault. *Reaction-induced phase separation in modified thermosetting polymers*, pages 95–156. Springer, Berlin, Heidelberg, 1997.
- [278] Kam-Wa D. Lee, Philip K. Chan, and Xianshe Feng. A computational study of the polymerization-induced phase separation phenomenon in polymer solutions under a temperature gradient. *Macromol. Theory Sim.*, 12(6):413–424, 2003.

- [279] Katsunari Kataoka, Osamu Urakawa, Hiroya Nishioka, and Qui Tran-Cong. Directional phase separation of binary polymer blends driven by photo-cross-linking with linearly polarized light. *Macromol.*, 31(25):8809–8816, 1998.
- [280] Asuka Harada and Qui Tran-Cong. Experimental verification of a scaling law for phase separation kinetics of reacting polymer mixtures. *Macromol.*, 29(13):4801–4803, 1996.
- [281] Qui Tran-Cong, Takashi Ohta, and Osamu Urakawa. Soft-mode suppression in the phase separation of binary polymer mixtures driven by a reversible chemical reaction. *Phys. Rev. E*, 56:R59–R62, 1997.
- [282] Qui Tran-Cong, Junji Kawai, Yukihiro Nishikawa, and Hiroshi Jinnai. Phase separation with multiple length scales in polymer mixtures induced by autocatalytic reactions. *Phys. Rev. E*, 60:R1150–R1153, 1999.
- [283] Rowena Ball and John Brindley. The life story of hydrogen peroxide III: Chirality and physical effects at the dawn of life. *Orig. Life Evol. Biosph.*, 46(1):81–93, 2015.
- [284] S. C. Abrahams, R. L. Collin, and W. N. Lipscomb. The crystal structure of hydrogen peroxide. *Acta Crystallographica*, 4(1):15–20, 1951.
- [285] William R. Busing and Henri A. Levy. Crystal and molecular structure of hydrogen peroxide: A neutron-diffraction study. *J. Chem. Phys.*, 42(9):3054–3059, 1965.
- [286] Cristobal Viedma. Enantiomeric crystallization from DL-aspartic and DL-glutamic acids: implications for biomolecular chirality in the origin of life. *Orig. Life Evol. Biosph.*, 31(6):501–509, 2001.
- [287] Heloisa N. Bordallo, Boris A. Kolesov, Elena V. Boldyreva, and Fanni Juranyi. Different dynamics of chiral and racemic (l- and dl-) serine crystals: Evidenced by incoherent inelastic neutron and raman scattering. *J. Am. Chem. Soc.*, 129(36):10984–10985, 2007.
- [288] Christian Dressel, Tino Reppe, Marko Prehm, Marcel Brautzsch, and Carsten Tschierske. Chiral self-sorting and amplification in isotropic liquids of achiral molecules. *Nature Chem.*, 6:971–977, 2014.
- [289] Steve Plimpton. Fast parallel algorithms for short-range molecular dynamics. *J. Comp. Phys.*, 117:1–19, 1995.
- [290] B. J. Alder and T. E. Wainwright. Studies in molecular dynamics. I. General method. *J. Chem. Phys.*, 31:459, 1959.
- [291] D. C. Rapaport. *The Art of Molecular Dynamics Simulation*. Cambridge University Press, Cambridge, UK, 2 edition, 2004.
- [292] H. J. C. Berendsen, J. P. M. Postma, W. F. van Gunsteren, A. DiNola, and J. R. Haak. Molecular dynamics with coupling to an external bath. *J. Chem. Phys.*, 81:3684, 1984.
- [293] Ronald Breslow. A likely possible origin of homochirality in amino acids and sugars on prebiotic earth. *Tetrahedron Letters*, 52(17):2028–2032, 2011.

- [294] D. K. Kondepudi and G. W. Nelson. Weak neutral currents and the origin of biomolecular chirality. *Nature*, 314(6010):438–441, 1985.
- [295] Donna G. Blackmond. Asymmetric autocatalysis and its implications for the origin of homochirality. *Proc. Natl. Acad. Sci.*, 101(16):5732–5736, 2004.
- [296] Donna G. Blackmond. The origin of biological homochirality. *Cold Spring Harb. Perspect. Biol.*, 101(a032540), 2019.
- [297] Wim L. Noorduin, Toshiko Izumi, Alessia Millemaggi, Michel Leeman, Hugo Meekes, Willem J. P. Van Enkevort, Richard M. Kellogg, Bernard Kaptein, Elias Vlieg, and Donna G. Blackmond. Emergence of a single solid chiral state from a nearly racemic amino acid derivative. *J. Am. Chem. Soc.*, 130(4):1158—1159, 2008.
- [298] F.C. Frank. On spontaneous asymmetric synthesis. *Biochimica et Biophysica Acta*, 11:459–463, 1953.
- [299] Kenso Soai, Takanori Shibata, Hiroshi Morioka, and Kaori Choji. Asymmetric autocatalysis and amplification of enantiomeric excess of a chiral molecule. *Nature*, 378(6559):767–768, 1995.
- [300] Takanori Shibata, Hiroshi Morioka, Tadakatsu Hayase, Kaori Choji, and Kenso Soai. Highly enantioselective catalytic asymmetric automultiplication of chiral pyrimidyl alcohol. *J. Am. Chem. Soc.*, 118(2):471–472, 1996.
- [301] Gábor Lente. The effect of parity violation on kinetic models of enantioselective autocatalysis. *Phys. Chem. Chem. Phys.*, 9(46):6134, 2007.
- [302] Harold W. Hatch, Frank H. Stillinger, and Pablo G. Debenedetti. Chiral symmetry breaking in a microscopic model with asymmetric autocatalysis and inhibition. *J. Chem. Phys.*, 133(22):224502, 2010.
- [303] M. Cao and P. A. Monson. A study of the phase behavior of a simple model of chiral molecules and enantiomeric mixtures. *J. Chem. Phys.*, 122(5):054505, 2005.
- [304] Frank H. Stillinger. Critical point confluence phenomenon. *J. Phys. Chem. B*, 122(13):3441–3446, 2017.
- [305] S. F. Mason and G. E. Tranter. The electroweak origin of biomolecular handedness. *Proc. R. Soc. Lond. A*, 397(1812):45–65, 1985.
- [306] Jeffrey L. Bada. Origins of homochirality. *Nature*, 374(6523):594–595, 1995.
- [307] P. G. H. Sandars. A toy model for the generation of homochirality during polymerization. *Orig. Life Evol. Biosph.*, 33(6):575–587, 2003.
- [308] Gabin Laurent, David Lacoste, and Pierre Gaspard. Emergence of homochirality in large molecular systems. *Proc. Natl. Acad. Sci.*, 118(3), 2021.

- [309] Farshid Jafarpour, Tommaso Biancalani, and Nigel Goldenfeld. Noise-induced mechanism for biological homochirality of early life self-replicators. *Phys. Rev. Lett.*, 115:158101, 2015.
- [310] Farshid Jafarpour, Tommaso Biancalani, and Nigel Goldenfeld. Noise-induced symmetry breaking far from equilibrium and the emergence of biological homochirality. *Phys. Rev. E*, 95:032407, 2017.
- [311] Christoph A Weber, David Zwicker, Frank Jülicher, and Chiu Fan Lee. Physics of active emulsions. *Rep. Prog. Phys.*, 82(6):064601, 2019.
- [312] Sriram Ramaswamy. The mechanics and statistics of active matter. *Annu. Rev. Condens. Matter Phys.*, 1(1):323–345, 2010.
- [313] Hong Joo Kim, Nam Chul Kim, Yong-Dong Wang, Emily A. Scarborough, Jennifer Moore, Zamia Diaz, Kyle S. MacLea, Brian Freibaum, Songqing Li, Amandine Mollieux, Anderson P. Kanagaraj, Robert Carter, Kevin B. Boylan, Aleksandra M. Wojtas, Rosa Rademakers, Jack L. Pinkus, Steven A. Greenberg, John Q. Trojanowski, Bryan J. Traynor, Bradley N. Smith, Simon Topp, Athina-Soragia Gkazi, Jack Miller, Christopher E. Shaw, Michael Kottlors, Janbernd Kirschner, Alan Pestronk, Yun R. Li, Alice Flynn Ford, Aaron D. Gitler, Michael Benatar, Oliver D. King, Virginia E. Kimonis, Eric D. Ross, Conrad C. Wehl, James Shorter, and J. Paul Taylor. Mutations in prion-like domains in hnRNPA2B1 and hnRNPA1 cause multisystem proteinopathy and ALS. *Nature*, 495(7442):467–473, 2013.
- [314] Yi-Hsuan Lin, Julie D. Forman-Kay, and Hue Sun Chan. Theories for sequence-dependent phase behaviors of biomolecular condensates. *Biochemistry*, 57:2499–2508, 2018.
- [315] R. Ranganathan and E. Shakhnovich. Dynamic metastable long-living droplets formed by sticker-spacer proteins. *eLife*, 9:e56159, 2020.
- [316] Furqan Dar and Rohit Pappu. Phase separation: Restricting the sizes of condensates. *eLife*, 9:e59663, 2020.
- [317] Kiersten M. Ruff, Furqan Dar, and Rohit V. Pappu. Ligand effects on phase separation of multivalent macromolecules. *Proc. Natl. Acad. Sci.*, 118(10):e2017184118, 2021.
- [318] Tanja Mittag and Rohit V. Pappu. A conceptual framework for understanding phase separation and addressing open questions and challenges. *Mol. Cell*, 82(12):2201–2214, 2022.
- [319] Srivastav Ranganathan and Eugene Shakhnovich. The physics of liquid-to-solid transitions in multi-domain protein condensates. *Biophysical Journal*, 121(14):2751–2766, 2022.
- [320] Marina Feric, Azadeh Sarfallah, Furqan Dar, Dmitry Temiakov, Rohit V. Pappu, and Tom Misteli. Mesoscale structure-function relationships in mitochondrial transcriptional condensates. *Proc. Natl. Acad. Sci.*, 119(41):e2207303119, 2022.

- [321] Fei Wang, Patrick Altschuh, Lorenz Ratke, Haodong Zhang, Michael Selzer, and Britta Nestler. Progress report on phase separation in polymer solutions. *Adv. Mater.*, 31(26):1806733, 2019.
- [322] Gregoire Nicolis and Ilya Prigogine. *Self-Organization in Nonequilibrium Systems: From Dissipative Structures to Order through Fluctuations*. Wiley, New York, 1977.